Ph.D. in Chemical Sciences, XXXIV cycle

Next Generation Energy Storage Systems based on Sulfur

University of Ferrara

Department of Chemical, Pharmaceutical and Agricultural Sciences

SDS CHIM/02

2018 – 2021

Candidate: Supervisor:

Vittorio Marangon   Prof. Jusef Hassoun

Coordinator: Prof. Carlo Cavazzini

Index

Chapter 1.

Introduction and aim of the work

1.1 Lithium-ion and lithium-sulfur batteries

Lithium-ion batteries are today the technology of choice to power a wide array of devices, from portable electronic systems such as smartphones and laptops, to the electric vehicles (EVs) and renewable energy production plants.[1] The first rechargeable energy storage system based on the intercalation of alkali metal in electrodes relying on transition metals was developed by Michael Stanley Whittingham, who successfully combined a lithium metal anode with a titanium sulfide cathode in 1976 to obtain the first Li/TiS_2 battery.[2] Afterwards, great efforts have been made to enhance this new technology until the actual commercialization of the first lithium-ion battery in 1991, which was awarded in 2019 by the Nobel Prize in Chemistry assigned to Michael Stanley Whittingham, John B. Goodenough and Akira Yoshino.[3] The diffusion of the lithium-ion battery was possible thank to the substitution of the lithium metal which, despite being characterized by considerable theoretical specific capacity and the lowest standard reduction potential (*i.e.*, 3861 mAh g^{-1} and -3.04 V *vs* standard hydrogen electrode, respectively), is dangerously reactive in presence of water and easily forms dendritic structures on its surface due to uneven lithium plating upon cycling that cause shortcircuits and thermal runaways.[4,5] Indeed, the typical lithium-ion battery exploits a graphite anode (C_6) and a $LiCoO_2$ cathode, resulting in a specific energy of about 200 Wh kg^{-1}.[6] In this configuration, the electrodes communicates through an electrolyte based on a carbonate solvent and a lithium salt (Fig. 1.1.1) which mediates the exchange of Li^+ ions in according with equation 1.1.1:[6]

$$C_6 + LiCoO_2 \rightleftarrows Li_xC_6 + Li_{1-x}CoO_2 \qquad\qquad (1.1.1)$$

where x is the fraction of Li^+ ions that (de-)intercalates in the electrodes structures and is about 0.6. On the other hand, the graphite/$LiCoO_2$ battery is affected by several issues, that is, the relatively low intercalation ability of graphite, the poor thermal stability of the $Li_{1-x}CoO_2$ phase, and the intrinsic toxicity of the Co element.[7,8] Therefore, numerous viable alternatives have been proposed to achieve an efficient and, at the same time, sustainable lithium-ion battery configuration.
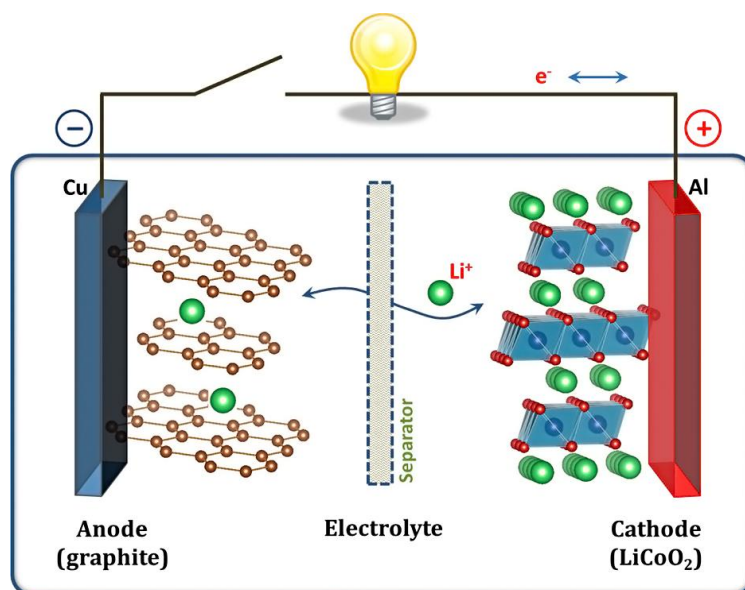
Figure 1.1.1. Scheme of a common Li-ion battery using a LiCoO$_2$ cathode and a graphite anode.[9]

Regarding the cathode side, an accredited strategy involves the partial substitution of Co in the LiCoO$_2$ material to achieve lower toxicity and cost, and, at the same time, superior performances. Accordingly, the LiNi$_{1/3}$Mn$_{1/3}$Co$_{1/3}$O$_2$ (NMC) and LiNi$_{0.8}$Co$_{0.15}$Al$_{0.05}$O$_2$ (NCA) layered compounds offer a lower content of Co, higher delivered capacity (between 180 and 185 mAh g^{-1} with respect to 150 mAh g^{-1}) and improved thermal stability of the de-lithiated phase.[10,11] Another suitable alternative is represented by the olivine structured LiFePO$_4$ (LFP) cathode, which, despite the relatively low working potential (3.45 V *vs* Li$^+$/Li) and reversible capacity (170 mAh g^{-1}), is a low cost and environmentally friendly material with enhanced chemical, electrochemical, and thermal stability with respect to the LiCoO$_2$ material and respective variants.[12] The numerous advantages involved in these chemistries allowed the substitution of the LiCoO$_2$ cathode in the present lithium-ion technology and the achievement of more reliable batteries.[13] Concerning the anode materials, lithium titanium oxide (Li$_4$Ti$_5$O$_{12}$, LTO) is commercially employed thank to the safety content provided, allowed by relevant thermal stability and by the working voltage of 1.5 V *vs* Li$^+$/Li that avoids lithium plating upon charge.[14] Furthermore, Sn, Si and their oxides are naturally abundant and the electrodes based on their Li-alloys allow the exchange of multiple Li$^+$ ions per molar unit of metal, leading to capacity values ranging from 500 to 1000 mAh g^{-1} with respect to the limited 372 mAh g^{-1} related to graphite.[15–17]

On the other hand, the results achieved on the lithium-ion technology led to an energy density of about 250 Wh kg^{-1}, which may be insufficient for the actual world-wide application of emergent technologies such as the EVs.[18] Indeed, the ever growing massive exploitation of carbon fuels and

consequent emission of greenhouse gases posed in the recent years the urgency to develop more efficient and sustainable energy systems beyond the lithium-ion battery to promote the actual application of a carbon-neutral mobility and contrast the global climate change.[19–21]

One of the most promising devices that may represent a step forward with respect to the lithium-ion technology is the lithium-sulfur (Li-S) battery, which relates on the reversible multi-electron conversion process between sulfur and lithium centered at about 2.2 V that leads to the final product Li_2S,[8] as reported by equation 1.1.2:

$$S_8 + 16Li^+ + 16e^- \rightleftarrows 8Li_2S \hspace{4cm} (1.1.2)$$

The exchange of multiple charges per mole of active material represents one of the key advantages of the Li-S battery with respect to the lithium-ion one, which instead (de-)intercalates only a limited x fraction of Li^+ ions in the layered electrodes structures ($0 < x < 1$).[9] Indeed, the Li-S conversion electrochemical process allows a theoretical energy density of 3730 Wh kg^{-1} referring to sulfur mass, while the maximum one associated to the lithium-ion devices is about 900 Wh kg^{-1} ($x = 0.8$) referring to the intercalated cathode.[8,9] Furthermore, the Li-S system offers a modest environmental impact of the materials employed and an expected low cost. Nevertheless, the practical application of this device is still hindered by several issues. The simple reaction reported in equation 1.1.2 actually evolves through a multi-step process involving the formation of lithium polysulfides intermediates (Li_2S_x, $2 \leq x \leq 8$) at different potential values as schematized in Figure 1.1.2, with the long-chained ones being able to dissolve into the electrolyte solution.[22]
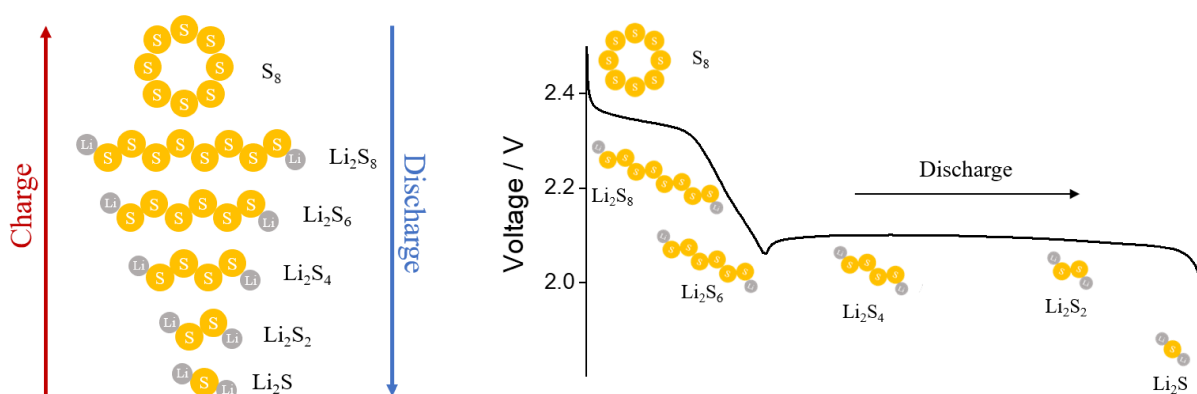

Figure 1.1.2. Graphical scheme of the species involved in the Li-S battery electrochemical conversion process and their evolution through the discharge step.[8]

3

These species can migrate through the electrolyte solution during discharge, reduce on the anode surface and subsequently move back to the cathode upon charge where they end up being newly oxidized, giving rise to a continuous "shuttle" mechanism (Fig. 1.1.3) that causes loss of active material, poor coulombic efficiency, electrodes degradation and, eventually, cell failure.[23,24]
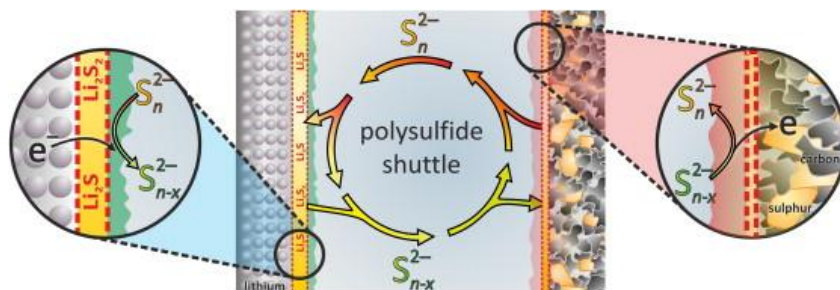
Figure 1.1.3. Representation of the polysulfides parasitic "shuttle" mechanism in a Li-S battery.[23]

The employment of *in situ* ^{7}Li nuclear magnetic resonance (^{7}Li NMR) technique suggested that the formation of the lithium polysulfides actually occurs through a complex chemical environment involving mixed species such as charged free radicals rather than discrete step-by-step reactions.[22] In support of these results, *in situ* electron paramagnetic resonance (EPR) allowed the direct observation of sulfur radicals ($S_3^{\cdot-}$) throughout the whole cycling (Fig. 1.1.4), indicating a temporal equilibrium between polysulfides rather than the formation of specific intermediates at different potential values.[25] The presence of radical species poses serious concern on the choice of the electrolyte, as a high stability towards sulfur radicals is required to achieve long-term cycling.
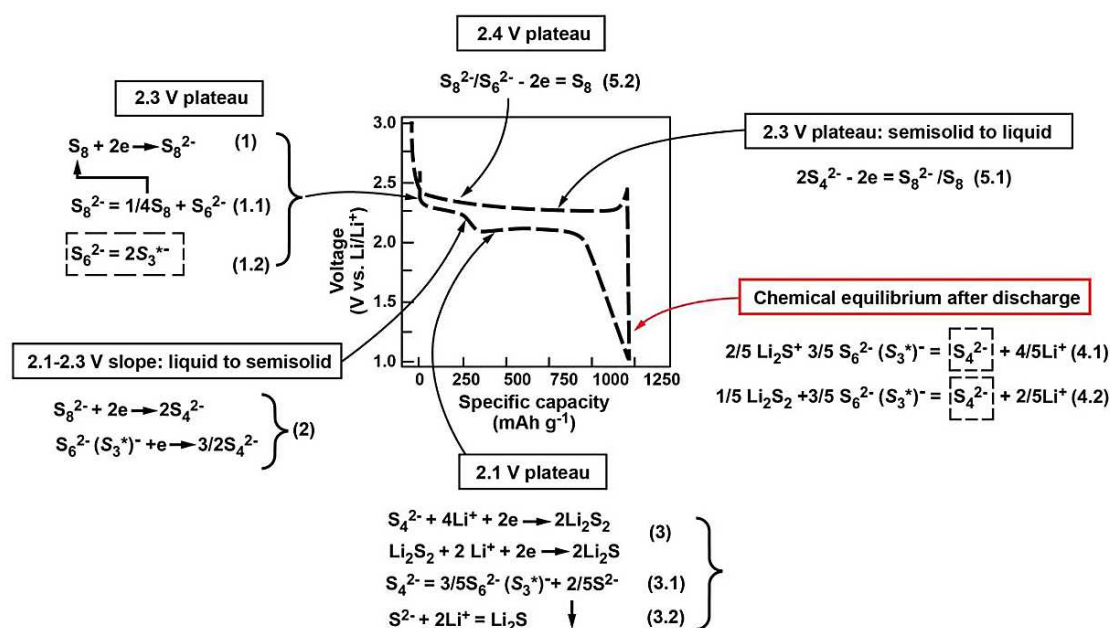
Figure 1.1.4. Proposed reaction mechanism for Li-S batteries based on the employment of *in situ* EPR technique.[25]

Further issues related to the Li-S device are represented by the insulant character of sulfur and by the safety hazards deriving from the use of the reactive lithium metal anode. In order to overcome these shortcomings, various strategies were proposed to safely and efficiently exploit the energetic conversion process of the Li-S battery, such as the enhancement of the sulfur electrode conductivity and the concomitant retention and entrapment of the polysulfide intermediates at the cathode side through the addition of carbonaceous additives.[26,27] Moreover, alternative and suitable electrolyte configurations were deeply studied to achieve stable cycling of the Li-S devices,[28] as well as energy storage systems based on sulfur employing more sustainable and/or safer anodic materials.[29,30] The next sections will elucidate in details some of the most accredited approaches to achieve sulfur-based batteries of practical interests.

1.2 Optimizations for the sulfur cathode

The insulating character of sulfur, *i.e.,* the active material in sulfur-based energy storage systems, is one of the numerous challenges posed by these devices. The addition of conductive carbons to the sulfur cathode revealed remarkable improvements of the cycling behavior of the Li-S batteries due to a favorable combination between the enhancement of the electrode conductivity and the storing of active material in the porous structures of the carbon frames, which mitigates the dissolution of lithium polysulfides into the electrolyte (Fig. 1.2.1).[26]

Previous studies demonstrated that the porosity of carbon materials provides several advantages according to the size of the pores, which can be classified as micropores (< 2 nm), mesopores (between 2 and 50 nm) and macropores (> 50 nm).[31] Micropores are usually employed as they can easily accommodate lithium polysulfides and prevent the penetration of solvent molecules, thus mitigating the intermediates dissolution and hinder the "shuttle" effect;[32] mesopores favor sulfur encapsulation, ease the Li^+ ions transportation and allow higher sulfur loading due to the larger size;[33,34] macropores, achievable through interwoven carbon nanostructures, allow electrolyte immersion and may prevent polysulfide dissolution due to high electrolyte absorbability.[35] Following this trend, suitable cathodes based on encapsulation of sulfur were obtained by exploiting hollow carbons, that provide large internal volume allowing high sulfur loading and alleviating volume changes of the active material,[36] as well as hierarchical porous carbons which combine different porosities.[37–39] Alternative carbon frameworks were obtained by employing graphene, that possesses high electrical conductivity, notable mechanical stability, and large theoretical surface (2630 m^2 g^{-1}), as well as surface functional groups (C=O, C-O-C, -OH) that promote the polysulfides anchoring.[40,41]
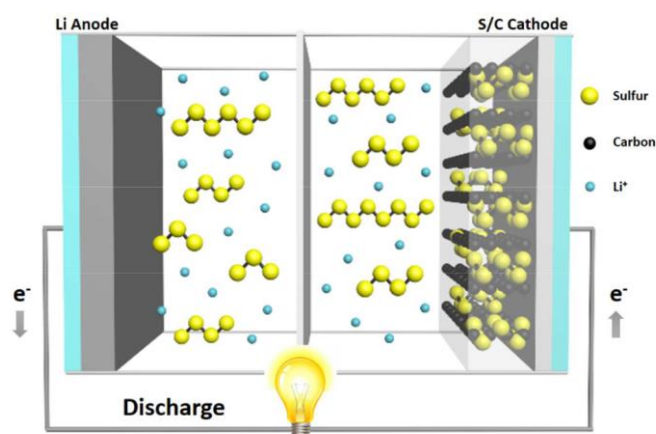
Figure 1.2.1. Graphical scheme of a Li-S battery employing a sulfur-carbon composite as cathode.[42]

Suitable carbon additives were also identified in nanotubes,[43,44] nanosheets,[45] nanospherules,[46] and other morphologies,[47,48] as well as in carbons doped with heteroatoms such as N, B, or S which provide additional polysulfide-retaining functional groups.[49–51] Moreover, the issues related to the climate change risen in the recent years focused the attention on the necessity to develop eco-friendly materials for the new energy devices,[52] encouraging the research to develop carbons from the recycle of bio-waste products.[53,54] Concerning Li-S batteries, sustainable conductive additives were derived by crab shells,[55] cherry pits,[56] bamboo,[57] coconut shells[58] and jellyfish umbrellas.[59]

A further improvement for lithium polysulfides retention is represented by the addition of metal organic frameworks (MOFs) and metal oxides. MOFs present several advantages, including a porous structure to cage sulfur and related products, and metal ions that provide binding interactions.[60] The first applications of these compounds in Li-S battery were achieved through the chromium trimesate metal-organic framework named MIL-101 (Cr),[61] which is represented in Figure 1.2.2.
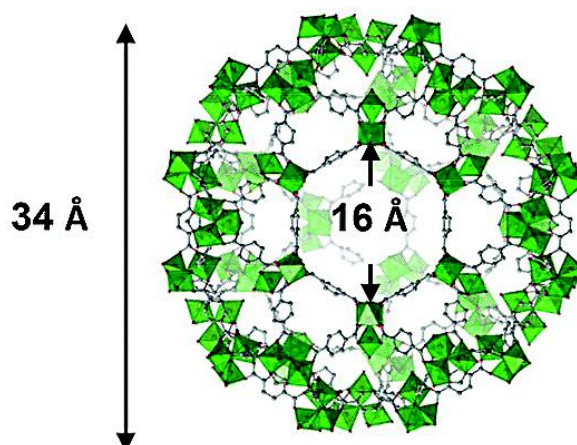
Figure 1.2.2. Schematic representation of the MIL-101 (Cr) composite structure.[62]

Despite the promising results, MOFs suffer from poor electrical conductivity and the oxidation of the infiltrated sulfur leads to drops of the delivered capacity.[63] Thus, improved performances were obtained by using conductive additives such as graphene,[64] carbon nanotubes[65] and conductive polymers.[66] Subsequently, intensive studies have been carried out on the MOFs derivatives due to the enhanced characteristics revealed by these composites upon treatment of the pristine MOFs. In particular, efficient sulfur-carbon composites were synthesized by Zn, Co, Cu and graphene oxide-based MOFs,[67–71] while MOF-derived metal oxides such as Co_3O_4 and TiO_2 allowed stable capacity

values.[72,73] On the other hand, bare metal oxides are widely studied as sulfur cathode additives due to the remarkable polysulfides adsorption enabled by the numerous polar active sites.[74] Early reports on $Mg_{0.6}Ni_{0.4}O$ and SiO_2 risen the attention on the suitability of these species,[75,76] leading to the optimization of sulfur cathodes containing various titanium oxides (TiO_2, Ti_4O_7),[77–79] MnO_2,[80] $NiFe_2O_4$,[81] and many others.

The inclusion of metal centers in the cathode formulation was recently proposed to strongly enhance the charge transfer kinetics and, possibly, catalyze the polysulfides conversion thank to the increased affinity between them and the electrode surface.[82–84] An additional advantage of this strategy resides in the higher conductivity of metals with respect to carbon, which may allow the use of a lower amount of inactive material and boost the practical energy density of the cell.

The performance of a sulfur cathode is also strongly influenced by the electrode support. Aluminum is the substrate of choice for the high voltage-operating cathodes in lithium-ion batteries and sulfur electrodes due to its low reduction potential. However, recent studies suggested the substitution of aluminum with a porous carbon paper, i.e., a gas diffusion layer (GDL), due to its more suitable characteristics. In particular, GDL benefits from a macroporous texture with respect to conventional aluminum (Fig. 1.1.3) that homogeneously accommodates the active material particles, leading to enhanced ionic and electronic conductivity, as well as to better electrode wettability.[85] Thus, the sulfur electrodes employing GDL shown improved cyclability with enhanced kinetics and higher delivered capacity values than the respective ones using aluminum.[85] These promising data suggest that the use of porous current collectors may be fundamental to achieve sulfur batteries with sufficient energy density for actual commercialization.
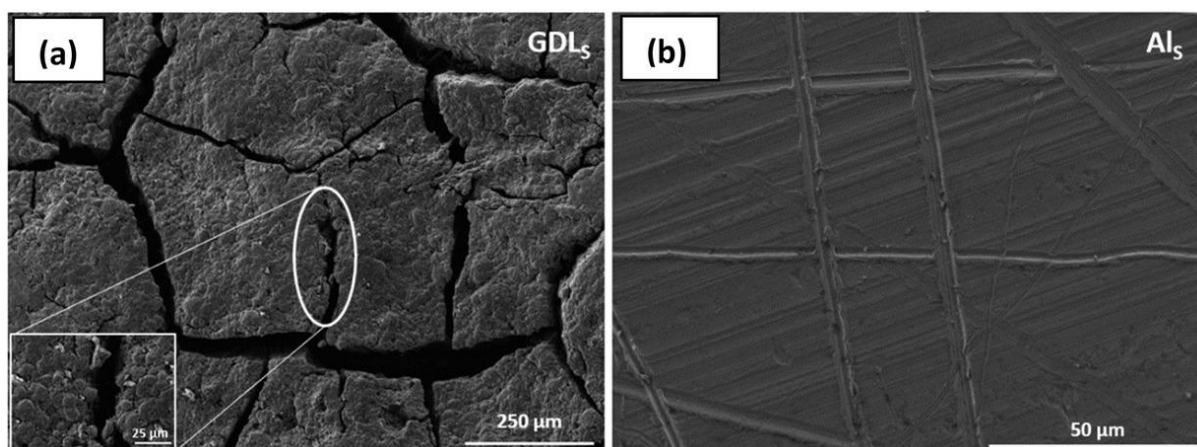
Figure 1.1.3. Images captured by scanning electron microscope (SEM) of **(a)** GDL and **(b)** Al current collectors.[85]

In summary, the performance of a Li-S battery is strongly influenced by the cathode formulation. The experimental techniques used to investigate the role played by each component usually include electron microscopy to study the electrode morphology and its evolution, both by scanning (SEM) and transmission (TEM) mode, and X-ray diffraction (XRD) to obtain details on the structural features.[31] Following this trend, X-ray computed tomography (CT) was employed in recent works to reconstruct a three-dimensional representation of the cathode that allows the identification of the single phases due to different attenuation of the X-ray incident beam associated to the density of each component (Fig. 1.1.4a).[86] The unique features of this technique may shed light on the actual microstructural reorganization of the positive electrode promoted by the electrochemical conversion process, revealing the behavior of the sulfur particles during both discharge (Figure 1.1.4b-d) and charge (Fig. 1.1.4e-g) processes and allowing *ad hoc* engineering of the sulfur cathode and its optimization.[87]
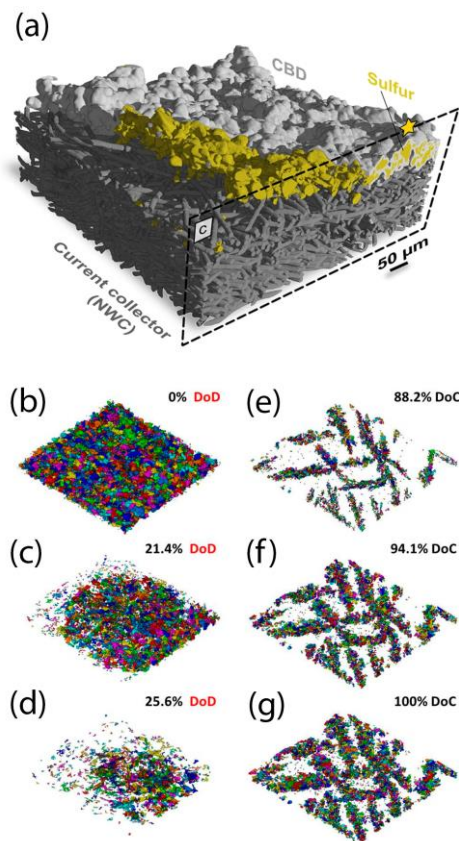
Figure 1.1.4. (a) 3D reconstruction of a pristine sulfur electrode employing a nonwoven C current collector from an X-ray CT data set.[86] Panels **(b-d)** and **(e-g)** show the volume renderings of individually labelled S particles at various depth of discharge (DoD) and depth of charge (DoC) percentages, respectively.[87]

1.3 Efficient electrolyte formulations

Compatibility with lithium metal and chemical stability towards the polysulfide intermediates are fundamental requirements for electrolytes to drive safe and efficient Li-S battery operation. In this regard, electrolytes commonly used in Li-ion batteries based on carbonate solvents as diethyl carbonate (DEC) and ethylene carbonate (EC) cannot be considered for application in Li-S batteries due to the marked reactivity with lithium polysulfides that lead to their deterioration (Fig. 1.3.1).[88]
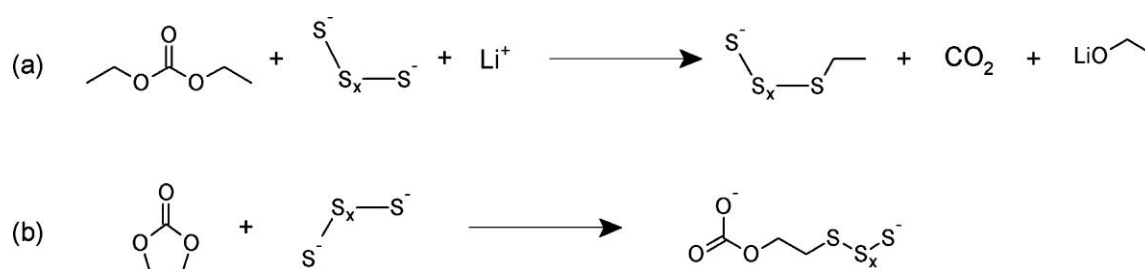
Figure 1.3.1. Proposed reactions between polysulfides and either **(a)** DEC or **(b)** EC solvents.[88]

In view of these issues, ethers were identified as potential candidate for application in Li-S batteries thank to their higher stability towards the polysulfide intermediates.[89] Furthermore, the limited electrochemical stability window of these solvents (oxidation at around 4.0 V *vs* Li^+/Li) is compatible with Li-S battery operation (< 3.0 V *vs* Li^+/Li), while prevents their application in high-voltage lithium-ion batteries.[28] Nowadays, the binary mixture of 1,3-dioxolane (DOL, Fig. 1.3.2a) and 1,2-dimethoxyethane (DME, Fig. 1.3.2b) combined by the 1:1 volume ratio is considered as the baseline electrolyte solvent for Li-S battery due to low viscosity, suitable stability towards both lithium and polysulfides, and compatibility with lithium salts.[28] In particular, lithium bis(trifluoromethanesulfonyl)imide (LiTFSI, $LiN(SO_2)_2(CF_3)_2$), lithium bis(fluorosulfonyl)imide (LiFSI, $LiN(SO_2)_2F_2$) and lithium trifluoromethanesulfonate (lithium triflate, $LiSO_3CF_3$) conductive salts are commonly used in efficient electrolytes for Li-S batteries due to their high ionic conductivity and stability of the respective anions.[90,91]

Despite the premises, a highly conductive and stable electrolyte is not sufficient to allow stable cycling of Li-S batteries due to the "shuttle" mechanism of the polysulfides and their parasitic reactions at the lithium metal anode.[23,24] In this regard, a major breakthrough was achieved through the acknowledgement of the solid electrolyte interphase (SEI) concept, that is, a passivation layer that forms on the lithium surface due to partial reduction of the electrolyte components, protects the anode from undesired reactions and hinders the formation of dendrites.[92,93] The cleavage of the cyclic structure of the DOL solvent is reported to promote the formation of a stable SEI,[94] however, the

addition of sacrificial agents to the electrolyte solution is by now a consolidated strategy to form a SEI layer through reduction on lithium surface.[95] Indeed, the addition of controlled amounts of SEI forming species to the electrolyte proven remarkable enhancements in the performance of Li-S systems, such as nitrates (LiNO$_3$, KNO$_3$, CsNO$_3$, LaNO$_3$), sulfides (P$_2$S$_5$, CS$_2$, lithium polysulfides) and even water.[95] LiNO$_3$ received particular attention since it was firstly proposed and several studies led to the understanding of its simple and effective SEI formation mechanism by reduction at the lithium surface that involves the precipitation of several LiN$_x$O$_y$ species, making it nowadays the most common additive for Li-S batteries electrolytes.[94,96–98]

The safety hazards linked to the use of lithium metal can be further limited by employment of lowly flammable electrolyte solvent. End-capped ethers called "glymes" with CH$_3$O(CH$_2$CH$_2$O)$_n$CH$_3$ formula and low n value (Fig. 1.3.2c-f) are liquid at room temperature and are characterized by higher flash point with respect to the flammable and volatile DOL and DME.[44] This class of solvents presents suitable compatibility with the common conductive lithium salts, and lithium metal batteries combining glyme-based electrolytes and cathodes exploiting different chemistries such as LiFePO$_4$, LiCoO$_2$, NMC or graphite revealed promising performances.[99–103]
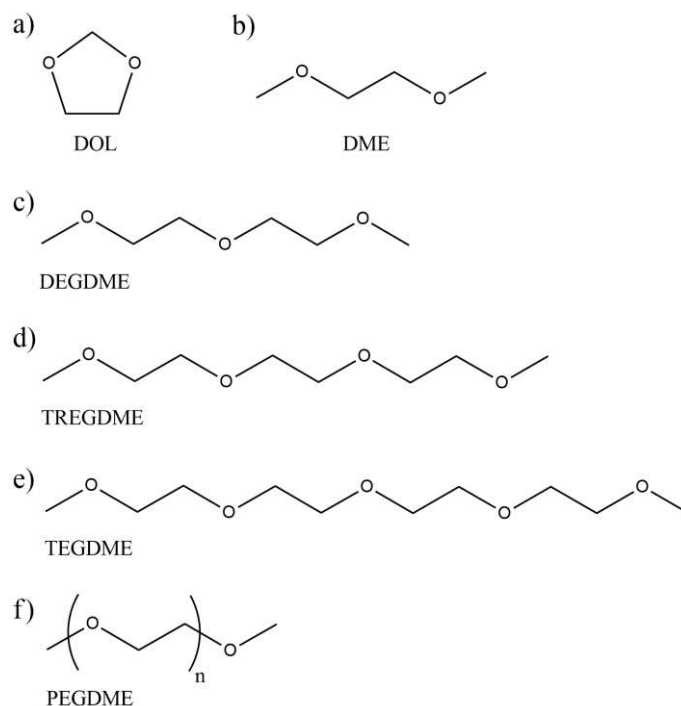
Figure 1.3.2. Molecule structures of various ether solvents employed for Li-S battery electrolytes. In particular: **(a)** 1,3-dioxolane (DOL), **(b)** 1,2-dimethoxyethane (DME), **(c)** diethylene glycol dimethyl ether (DEGDME, $n = 2$), **(d)** triethylene glycol dimethyl ether (TREGDME, $n = 3$), **(e)** tetraethylene glycol dimethyl ether (TEGDME, $n = 4$) and **(f)** polyethylene glycol dimethyl ether (PEGDME).

Beside reasonably high flash point, fast Li$^+$ ions transport, wide electrochemical stability window and thermal stability, glyme-based solutions demonstrated remarkable stability towards lithium polysulfides which make them attractive candidates for application in Li-S batteries,[89,104,105] and effective suppression of the infinite charge process caused by "shuttle" mechanism (Fig. 1.3.3a) was achieved through formation of a stable SEI by exploiting the LiNO$_3$ additive (Fig. 1.3.3b).[110]

Intensive work has been recently devoted to the study of the interaction between the Li$^+$ ions and the glyme molecules, as the study of glyme-based electrolytes exploiting high concentrations of lithium salts, usually described as solvent-in-salt solutions or solvate ionic liquids (SILs), revealed superior transport properties, high oxidative and thermal stability, and formation of an improved SEI.[106–109] The high Li$^+$ concentration leads to the formation of [Li(glyme)]$^+$ molten complexes through the chelation of the Li$^+$ ions by the glyme molecules with formation of crown-like structures, which were detected by Raman spectroscopy and *ab initio* molecular orbital calculations.[110,111] Moreover, the use of high concentrations of lithium salts in electrolytes for Li-S battery was successfully proposed to suppress sulfur dissolution from the cathode,[112] and the consequent application of glyme-based SIL solutions to Li-S batteries shown promising cycling behavior.[113–115]
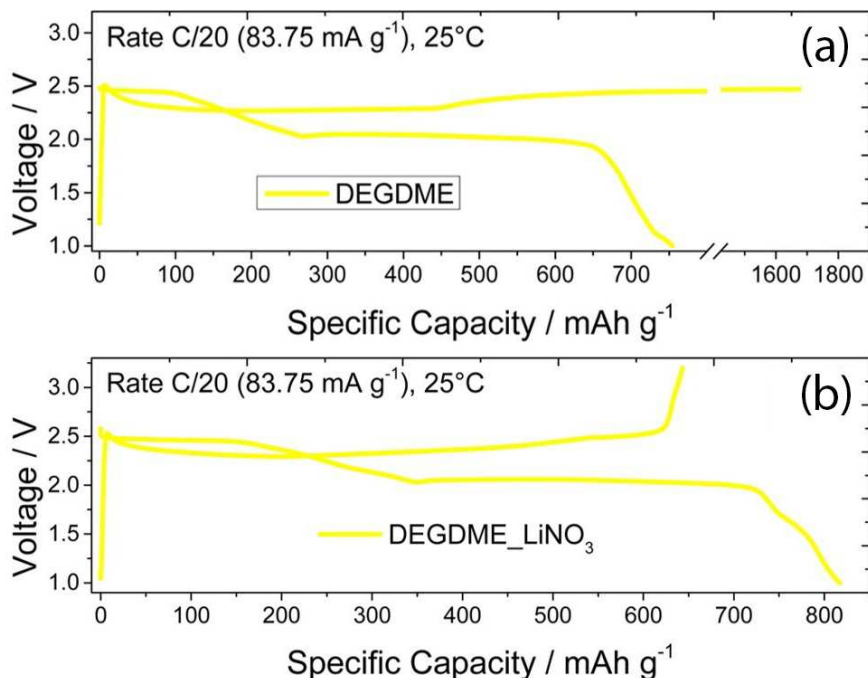
Figure 1.3.3. Electrochemical performances of a Li-S battery employing a glyme-based electrolytes either **(a)** without or **(b)** including LiNO$_3$ additive.

The unique characteristics of these solvents also allow notable performance of semi-liquid Li-S batteries exploiting "catholytes", that is, lithium polysulfides-enriched conductive solutions which act as both cathode and electrolyte.[116–119] This innovative formulation prevents dissolution of sulfur from the cathode and may efficiently operate as active material with no need of solid sulfur at the positive side thank to the electrochemical activity of the dissolved polysulfides.[116–119]

Solid polymer electrolytes are also of great interest to achieve safe rechargeable lithium batteries. In particular, solid polymer electrolytes based on polyethylene oxide (PEO) exhibit excellent thermal, mechanical and electrochemical stability, negligible volatility, efficient dendrites suppression, and their compatibility with conductive lithium salts lead to suitable Li^+ transport characteristics.[120] Nevertheless, the high molecular weight of PEO causes excessive crystallinity at room temperature that forces its application only at temperatures above 65 °C, that is, when PEO amorphous state is reached and adequate ionic conductivity (10^{-4} S cm^{-1}) is obtained.[121] Ceramic fillers such as TiO_2, SiO_2, Al_2O_3 or ZrO_2 are widely employed to promote the polymer amorphous state, however, operative temperatures around 60 °C are still needed.[121–123] Liquid plasticizers and ionic liquids greatly enhance ionic conductivity and Li^+ ions transport, although the electrolyte mechanical stability is put at risk and the introduction of volatile and flammable species may compromise the safety content of the battery.[124–126] Thus, more effort is required to optimize solid-state polymer electrolytes, especially upon the promising results of lithium batteries exploiting both insertion[127–130] and sulfur-based conversion electrodes.[131–137]

1.4 Possible alternatives to lithium metal anode

As discussed above, a safe use of lithium metal anode in a rechargeable sulfur-based battery is made possible by adopting safe electrolyte media containing sacrificial additives that form a protective SEI on the lithium surface which mitigates the parasitic "shuttle" mechanism and hinders the growth of dangerous metallic dendrites.[94,95,97] Despite the notable improvements, the reactivity of lithium metal may still pose relevant safety issues that could prevent the actual use of high-energy sulfur-based devices. Furthermore, lithium is a geo-localized element and its high price heavily affects the production of lithium batteries.[138] Thus, the replacement of the lithium anode is an argument of particular interest and several efforts are invested to design safer and more affordable configurations.

In this regard, the application of the Li-ion battery concept through the employment of a non-reactive anode may allow safe operation of the Li-S electrochemical conversion process.[139] Encouraging results were achieved by using graphite-based anodes, as graphite can be easily pre-lithiated to host Li^+ ions and forms a suitable SEI that ensures long cycle life and stable cycling behavior of the Li-S ion battery (Fig. 1.4.1a).[140–143] Nevertheless, the higher electrochemical potential and the lower theoretical capacity (372 mAh g^{-1}) of graphite-based intercalation anodes with respect to lithium lead to a limited energy density of the Li-S full battery.[144] Compared to graphite, Li-alloying materials such as tin and silicon offer much higher theoretical capacity values, that is, 990 and 4200 mAh g^{-1}, respectively,[145] that would lead to a satisfying energy content of the device. One of the first successful applications of a Li-alloying-based anode in Li-S battery was accomplished through the embedment of Sn nanometric particles in an amorphous carbon matrix that was demonstrated to effectively alleviate the volume changes of the electrode caused by the alloying process between Sn and Li (Figure 1.4.1b).[146,147] These pioneering results drawn the attention on this promising configuration and led to the optimization of a Li-S full cell using a Sn-C anode and common carbonate-based electrolyte.[148] Abrupt volume changes are also involved in the Si-based anodes alloying process, as indicated by the first results on silicon-sulfur full batteries which displayed a short cycle life despite the encouraging capacity values.[149] Notable improvements on the cycling behavior were achieved through pre-lithiation of silicon anodes that strongly mitigates the formation of lithium dendrites.[150,151] Nevertheless, as reported for the Sn-based anodes, the employment of carbon structures to alleviate the Si volume change upon repeated alloying and de-alloying was found to be determinant to achieve high-performance silicon-sulfur batteries with satisfactory capacity retention.[152–154] Following this trend, a further strategy to safely exploit the Li-Si alloying process consists in using silicon oxide (SiO_x) as anode rather than elemental Si. Indeed,

14

the oxide structure buffers the volume changes, and its combination with a carbon matrix (SiO$_x$-C) ensures suitable conductivity and structural retention.[17,155] Indeed, the balanced combination of a pre-lithiated SiO$_x$-C anode (Li$_y$SiO$_x$-C) and a sulfur cathode displayed notable performance in Li-ion-sulfur battery in terms of specific capacity and long cycle life (Fig. 1.4.1c).[156]
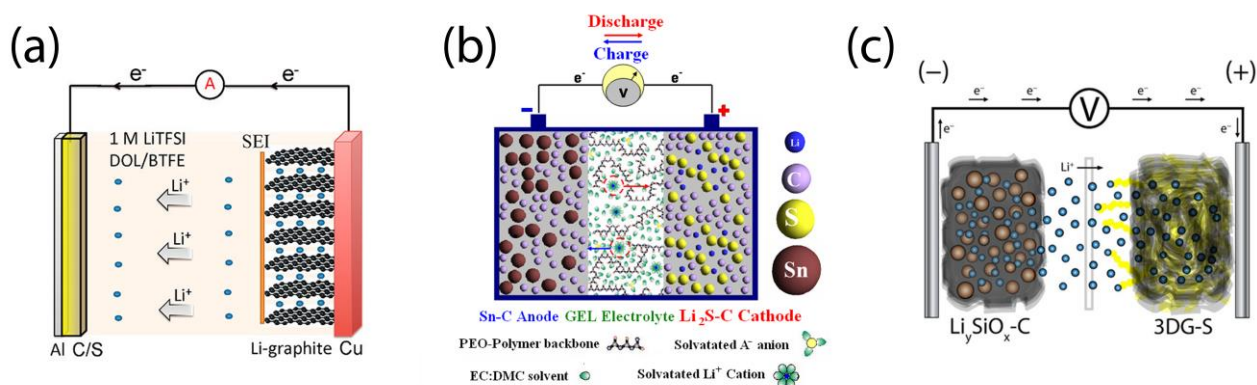
Figure 1.4.1. Configurations of Li-ion-sulfur batteries employing different anodes, that is, **(a)** pre-lithiated graphite,[141] **(b)** a tin-carbon (Sn-C) composite,[146] and **(c) a** pre-lithiated silicon oxide-carbon (Li$_y$SiO$_x$-C) electrode.[156]

Despite the undeniable steps made towards a safe use of the Li-S conversion electrochemical process in the last years, the use of lithium heavily increases the price of the battery, whether it be elemental or in the form of Li$^+$ ions in composite electrodes. In this scenario, the sodium-sulfur (Na-S) battery offers at the same time a promising theoretical energy density of 1274 Wh kg^{-1} thank to the Na-S conversion process analogue to that of Li-S configuration, and an expected lower cost.[138] Indeed, sodium is one of the most abundant element in the earth crust and is less geo-localized with respect to lithium, leading to the price being 1/25th of that of lithium.[138,157] Nevertheless, the Na-S technology is affected by issues similar to those of the Li-S battery, that is, the low conductivity of elemental sulfur, the safety hazards posed by the reactivity of sodium metal, the "shuttle" mechanism caused by the formation and dissolution of sodium polysulfides with various chain length (Na$_2$S$_x$, 2 $\leq x \leq$ 8) and consequent volume change in the sulfur cathode (Fig. 1.4.2).[158] Enhanced performance of the Na-S battery can be achieved by confining sulfur into carbon matrices with various structures to mitigate the dissolution of the polysulfide intermediates and increase the electron conductivity of the cathode.[159–162] Furthermore, the inclusion of functional groups and polar species in the carbon hosts such as –OH, N$_2$, NiS$_2$ and metal particles may lead to a more efficient anchoring of the polysulfides and improved kinetics of the conversion process.[163–166] Safe electrolyte media were prepared by employing SEI-forming agents such as fluoroethylene carbonate (FEC) and trimethyl phosphate (TMP), which allow stable cycling performance by preventing formation of sodium dendrites on the anode surface and limiting parasitic reactions caused by the "shuttle" mechanism,

even in presence of reactive carbonate species.[167,168] On the other hand, glyme-based electrolytes may represent a viable solution due to promising characteristics in terms of conductivity, sodium transport number, electrochemical stability and low flammability.[169,170] As seen for the Li-S system, glyme species are particularly suitable to prepare high-performance catholyte solutions, where the polysulfides dissolved into the electrolyte act both as active material and as a buffer against sulfur dissolution from the cathode.[171,172]
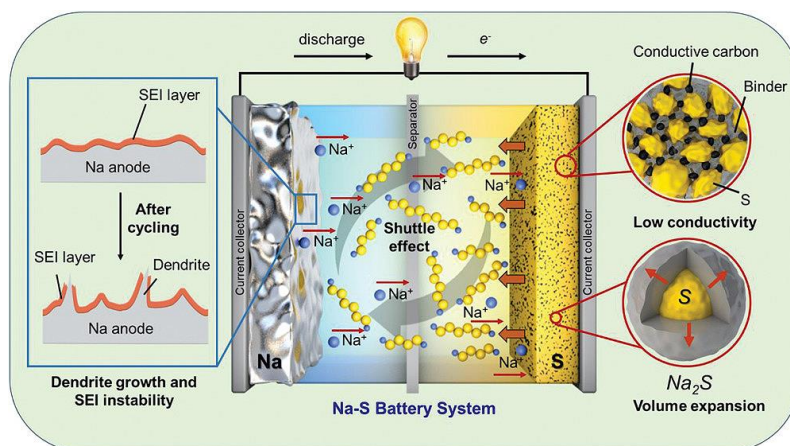
Figure 1.4.2. Graphical representation of a Na-S battery illustrating functioning and practical issues affecting this device.[138]

1.5 Aim of the work

Lithium-ion battery is today one of the most reliable energy storage systems to power a vast selection of electronic devices and sustainable transports such as EVs. However, the ever increasing energy demand requires novel technologies to surpass lithium-ion batteries in terms of various aspects, including energy density, lifespan, and sustainability of the materials employed. In this regard, intensive research work was dedicated to sulfur-based batteries in the recent years due to their superior theoretical characteristics, with particular attention to the Li-S devices which have shown the most promising performance in view of a possible commercialization. On the other hand, various practical issues linked but not limited to the insulant character of sulfur and the polysulfide intermediates "shuttle" mechanism are still to be solved.[173] The work presented herein explores various strategies to achieve performance of practical interest from sulfur-based batteries, with particular focus on the Li-S system and the characteristics of its main components, that is, cathode, electrolyte and anode.

Chapter 2 proposes a novel multidisciplinary analysis approach to understand the actual behavior of the sulfur cathode during operation in Li-S battery and applies it to alternative, scalable and high-performance electrodes to evaluate their applicability in advanced electrochemical systems. In particular, X-ray computed tomography (CT) is used in section *2.1* to study the role of the synthesis pathway on the morphological features of various sulfur-carbon composites and the microstructural modifications that occur in the corresponding electrodes upon cycling in lithium cell. The study reveals substantial morphological differences between electrodes with same compositions but different synthesis methods, which also influence their electrochemical performance. Moreover, scanning electron microscopy (SEM) coupled with energy dispersion X-ray spectroscopy (EDS), X-ray diffraction (XRD) and galvanostatic cycling tests are employed to thoroughly characterize the sulfur-carbon electrodes. Section *2.2* displays the investigation of a novel sulfur-tin composite for application in lithium batteries synthetized with a scalable method and characterized by a relatively low content of electrochemically inactive Sn conductive nanoparticles (S:Sn 80:20 w/w). The low amount of conductive additive is expected to improve the energy density of the Li-S battery with respect to the ones employing sulfur-carbon-based electrodes, which usually employs an inactive carbon content not lower than 30wt%. The study involves the use of XRD, transmission electron microscopy (TEM), SEM and EDS techniques to observe structure, morphology and elemental distribution of the composite and related electrode, respectively, while the electrochemical behavior is evaluated through cyclic voltammetry (CV), electrochemical impedance spectroscopy (EIS) and galvanostatic cycling measurements. The data show optimal stability of the electrode and the

application in Li battery reveals fast conversion kinetics, low interphase resistance, notable rate capability and long cycle life, suggesting the inclusion of metal nanoparticles as effective strategy to achieve scalable composites with high sulfur content. In section *2.3*, the metal content is lowered to 15wt% and two sulfur composites benefiting of either tin or nickel nanoparticles (S:Sn 85:15 w/w and S:Ni 85:15 w/w, respectively) are investigated through the same techniques employed for the S:Sn 80:20 w/w composite including, in addition, X-ray CT. The two composites exhibit remarkable electrochemical performance in Li cell, while CT studies elucidate the crucial benefits deriving from the porous structure of the carbon-based electrode support (*i.e.*, gas diffusion layer, GDL) used for the cathode that allows infiltration of sulfur upon charge and substantially improves the kinetics of the Li-S conversion process. This multidisciplinary approach is further exploited in section *2.4* to investigate a sulfur electrode benefiting from GDL and a sulfur-metal composite consisting of sulfur bulk doped by a content of Au nanoparticles as low as 3wt% (S:Au 97:3 w/w) showing impressive electrochemical performance.

Chapter 3 focuses on the study and application of glyme-based electrolytes with alternative configurations for Li-S battery. Prior to application in Li-S battery, the chemical and electrochemical properties of the solutions are evaluated in terms of thermal stability, ionic conductivity, Li^+ ions transport number and stripping/deposition overvoltage, electrochemical stability window, and electrode/electrolyte interphase resistance. The characterization is carried out by employing thermogravimetric analyses (TGA), chronoamperometry, EIS, galvanostatic measurements, linear sweep voltammetry (LSV) and CV. Section *3.1* reports the study of concentrated electrolytes based on either DEGDME or TREGDME dissolving LiTFSI conductive salt and lithium nitrate $LiNO_3$ in concentrations approaching the saturation limits. The use of high lithium salts concentration leads to an improved thermal stability and X-ray photoelectron spectroscopy (XPS) carried out on lithium foils soaked with the electrolytes reveals the formation of a suitable SEI composed of multiple layers with variegated composition. Thus, the application in Li-S battery shows suitable electrochemical performance and long cycle life that may represent a step forward for the realization of Li-S cells with high safety content. The fundamental importance of the safety content is also considered in section *3.2*, where a novel solid composite polymer electrolyte is proposed. The membrane is synthetized by using crystalline polyethylene glycol dimethyl ether (PEGDME, average molecular weight of 2000 g mol^{-1}), LiTFSI, $LiNO_3$ and SiO_2 as ceramic filler. The relatively low molecular weight of the selected crystalline PEGDME allows Li^+ ions conductivity properties suitable for battery application already at 50 °C, while the operative temperature usually related to standard polymer electrolytes based heavy polyethylene oxide (PEO) exceeds 65°C. This new solid electrolyte configuration demonstrates excellent performance at 50 °C in Li battery when combined with an

olivine-structured LiFePO$_4$ cathode, and its application in Li-S cell at the same low temperature reveals the formation of a suitable electrode/electrolyte interphase and fine cycling behavior. Semi-liquid sulfur cells using DEGDME-based catholytes dissolving Li$_2$S$_8$, LiNO$_3$ and either LiTFSI or LiCF$_3$SO$_3$ are investigated in section *3.3*. The solutions exhibit remarkable thermal stability and Li$^+$ transport properties that allow notable performance in Li battery driven by the dissolved Li$_2$S$_8$ with no necessity of solid sulfur at the cathode side. The catholyte using LiTFSI is successively combined with a Cr$_2$O$_3$-based electrode that favors the retention of the lithium polysulfides produced during discharge and promotes suitable cycling of the Li cell.

Sulfur-based systems using alternative and more sustainable anodes are considered in Chapter 4. Section *4.1* illustrates the study of two activated carbons derived from bio-mass residues activated with either H$_3$PO$_4$ or KOH for application as anode in lithium-ion battery and, then, as conductive matrix for sulfur composites employed in a sustainable lithium-ion-sulfur battery using a silicon oxide-based anode. The applicability of activated carbons is preliminarily evaluated through XRD, Raman spectroscopy, TGA, FT-IR measurements, elemental analysis, porosimetry, and SEM-EDS. The samples exhibit suitable characteristics and low presence of impurities due to the activation process. CV and EIS carried out on Li batteries show reversible (de-)insertion of Li$^+$ and low electrode/electrolyte interphase resistance, and cycling tests in lithium half-cell and in Li-ion battery employing a LiFePO$_4$ cathode reveal stable capacity values and long cycle life. The carbon activated with H$_3$PO$_4$ is then selected to synthetize a sulfur-carbon composite with an active material content as high as 75wt%, as indicated by TGA. However, galvanostatic cycling tests in lithium half-cell reveals poor cycling stability probably caused by undesired reactions between lithium metal and impurities dissolved in the ether-based electrolyte deriving from the activated carbon matrix. Thus, the lithium anode is substituted by a sustainable, non-reactive lithiated silicon oxide-based electrode (Li$_y$SiO$_x$-C) that allows long cycle life of the full Li-S battery. In section *4.2*, a promising Na-S battery exploiting a glyme-based electrolyte and a sulfur-carbon cathode enhanced with a GDL support is presented. TREGDME dissolving sodium trifluoromethanesulfonate (NaCF$_3$SO$_3$) conductive salt shows negligible flammability when directly exposed to flame and suitable properties in terms of transport properties and electrochemical stability window. Furthermore, comparison of galvanostatic cycling measurements of sulfur cathodes with same composition but different current collectors displays more stable cycling of the electrode configuration using porous GDL with respect to the one using standard aluminum. Thus, the results suggest a viable and safe configuration of sulfur battery to exploit the highly energetic, yet challenging, Na anode.

1.6 References

[1] B. Scrosati, *J. Solid State Electrochem.* **2011**, *15*, 1623.

[2] M. S. Whittingham, *Science (80-.).* **1976**, *192*, 1126.

[3] J.-L. Brédas, J. M. Buriak, F. Caruso, K.-S. Choi, B. A. Korgel, M. R. Palacín, K. Persson, E. Reichmanis, F. Schüth, R. Seshadri, M. D. Ward, *Chem. Mater.* **2019**, *31*, 8577.

[4] W. Xu, J. Wang, F. Ding, X. Chen, E. Nasybulin, Y. Zhang, J. G. Zhang, *Energy Environ. Sci.* **2014**, *7*, 513.

[5] D. Lin, Y. Liu, Y. Cui, *Nat. Nanotechnol.* **2017**, *12*, 194.

[6] K. M. Abraham, *J. Phys. Chem. Lett.* **2015**, *6*, 830.

[7] L. Croguennec, M. R. Palacin, *J. Am. Chem. Soc.* **2015**, *137*, 3140.

[8] B. Scrosati, J. Hassoun, Y.-K. Sun, *Energy Environ. Sci.* **2011**, *4*, 3287.

[9] J. B. Goodenough, K.-S. Park, *J. Am. Chem. Soc.* **2013**, *135*, 1167.

[10] P. Rozier, J. M. Tarascon, *J. Electrochem. Soc.* **2015**, *162*, A2490.

[11] J. S. Weaving, F. Coowar, D. A. Teagle, J. Cullen, V. Dass, P. Bindin, R. Green, W. J. Macklin, *J. Power Sources* **2001**, *97–98*, 733.

[12] K. Zaghib, A. Guerfi, P. Hovington, A. Vijh, M. Trudeau, A. Mauger, J. B. Goodenough, C. M. Julien, *J. Power Sources* **2013**, *232*, 357.

[13] L. S. Martins, L. F. Guimarães, A. B. Botelho Junior, J. A. S. Tenório, D. C. R. Espinosa, *J. Environ. Manage.* **2021**, *295*, 113091.

[14] N. Takami, H. Inagaki, T. Kishi, Y. Harada, Y. Fujita, K. Hoshina, *J. Electrochem. Soc.* **2009**, *156*, A128.

[15] L. Liu, F. Xie, J. Lyu, T. Zhao, T. Li, B. G. Choi, *J. Power Sources* **2016**, *321*, 11.

[16] M. Ge, C. Cao, G. M. Biesold, C. D. Sewell, S. Hao, J. Huang, W. Zhang, Y. Lai, Z. Lin, *Adv. Mater.* **2021**, *33*, 2004577.

[17] J. Ge, Q. Tang, H. Shen, F. Zhou, H. Zhou, W. Yang, J. Hong, B. Xu, J. Saddique, *Appl. Surf. Sci.* **2021**, *552*, 149446.

[18] R. Van Noorden, *Nature* **2014**, *507*, 26.

[19] P. Poizot, F. Dolhem, *Energy Environ. Sci.* **2011**, *4*, 2003.

[20] C. D. Thomas, A. Cameron, R. E. Green, M. Bakkenes, L. J. Beaumont, Y. C. Collingham, B. F. N. Erasmus, M. F. de Siqueira, A. Grainger, L. Hannah, L. Hughes, B. Huntley, A. S. van Jaarsveld, G. F. Midgley, L. Miles, M. a Ortega-Huerta, A. Townsend Peterson, O. L. Phillips, S. E. Williams, *Nature* **2004**, *427*, 145.

[21] C. McGlade, P. Ekins, *Nature* **2015**, *517*, 187.

[22] J. Xiao, J. Z. Hu, H. Chen, M. Vijayakumar, J. Zheng, H. Pan, E. D. Walter, M. Hu, X. Deng,

J. Feng, B. Y. Liaw, M. Gu, Z. D. Deng, D. Lu, S. Xu, C. Wang, J. Liu, *Nano Lett.* **2015**, *15*, 3309.

[23] M. R. Busche, P. Adelhelm, H. Sommer, H. Schneider, K. Leitner, J. Janek, *J. Power Sources* **2014**, *259*, 289.

[24] L. E. Camacho-Forero, T. W. Smith, S. Bertolini, P. B. Balbuena, *J. Phys. Chem. C* **2015**, *119*, 26828.

[25] Q. Wang, J. Zheng, E. Walter, H. Pan, D. Lv, P. Zuo, H. Chen, Z. D. Deng, B. Y. Liaw, X. Yu, X. Yang, J.-G. Zhang, J. Liu, J. Xiao, *J. Electrochem. Soc.* **2015**, *162*, A474.

[26] A. Manthiram, Y. Fu, S.-H. Chung, C. Zu, Y.-S. Su, *Chem. Rev.* **2014**, *114*, 11751.

[27] Z.-J. Zheng, H. Ye, Z.-P. Guo, *Energy Environ. Sci.* **2021**, *14*, 1835.

[28] S. Zhang, K. Ueno, K. Dokko, M. Watanabe, *Adv. Energy Mater.* **2015**, *5*, 1500117.

[29] R. Kumar, J. Liu, J.-Y. Hwang, Y.-K. Sun, *J. Mater. Chem. A* **2018**, *6*, 11582.

[30] T. Li, J. Xu, C. Wang, W. Wu, D. Su, G. Wang, *J. Alloys Compd.* **2019**, *792*, 797.

[31] F. Li, Q. Liu, J. Hu, Y. Feng, P. He, J. Ma, *Nanoscale* **2019**, *11*, 15418.

[32] Z. Li, L. Yuan, Z. Yi, Y. Sun, Y. Liu, Y. Jiang, Y. Shen, Y. Xin, Z. Zhang, Y. Huang, *Adv. Energy Mater.* **2014**, *4*, 1301473.

[33] X. Ji, K. T. Lee, L. F. Nazar, *Nat. Mater.* **2009**, *8*, 500.

[34] Z. Li, Y. Jiang, L. Yuan, Z. Yi, C. Wu, Y. Liu, P. Strasser, Y. Huang, *ACS Nano* **2014**, *8*, 9295.

[35] Y.-S. Su, Y. Fu, A. Manthiram, *Phys. Chem. Chem. Phys.* **2012**, *14*, 14495.

[36] Z. Li, H. Bin Wu, X. W. (David) Lou, *Energy Environ. Sci.* **2016**, *9*, 3061.

[37] C. Liang, N. J. Dudney, J. Y. Howe, *Chem. Mater.* **2009**, *21*, 4724.

[38] K. Xi, S. Cao, X. Peng, C. Ducati, R. Vasant Kumar, A. K. Cheetham, *Chem. Commun.* **2013**, *49*, 2192.

[39] N. Moreno, A. Caballero, J. Morales, M. Agostini, J. Hassoun, *Mater. Chem. Phys.* **2016**, *180*, 82.

[40] G. Hu, C. Xu, Z. Sun, S. Wang, H.-M. Cheng, F. Li, W. Ren, *Adv. Mater.* **2016**, *28*, 1603.

[41] Q. Shao, Z.-S. Wu, J. Chen, *Energy Storage Mater.* **2019**, *22*, 284.

[42] Z. Lin, C. Liang, *J. Mater. Chem. A* **2015**, *3*, 936.

[43] J. Guo, Y. Xu, C. Wang, *Nano Lett.* **2011**, *11*, 4288.

[44] L. Carbone, T. Coneglian, M. Gobet, S. Munoz, M. Devany, S. Greenbaum, J. Hassoun, *J. Power Sources* **2018**, *377*, 26.

[45] J. Guo, J. Zhang, F. Jiang, S. Zhao, Q. Su, G. Du, *Electrochim. Acta* **2015**, *176*, 853.

[46] J. Kim, D.-J. Lee, H.-G. Jung, Y.-K. Sun, J. Hassoun, B. Scrosati, *Adv. Funct. Mater.* **2013**,

23, 1076.

[47] M. Wang, X. Xia, Y. Zhong, J. Wu, R. Xu, Z. Yao, D. Wang, W. Tang, X. Wang, J. Tu, *Chem. – A Eur. J.* **2019**, *25*, 3710.

[48] H. Shi, W. Lv, C. Zhang, D.-W. Wang, G. Ling, Y. He, F. Kang, Q.-H. Yang, *Adv. Funct. Mater.* **2018**, *28*, 1800508.

[49] G. Zhou, E. Paek, G. S. Hwang, A. Manthiram, *Adv. Energy Mater.* **2016**, *6*, 1501355.

[50] S. S. Zhang, *Inorg. Chem. Front.* **2015**, *2*, 1059.

[51] M. Inagaki, M. Toyoda, Y. Soneda, T. Morishita, *Carbon N. Y.* **2018**, *132*, 104.

[52] S. Dühnen, J. Betz, M. Kolek, R. Schmuch, M. Winter, T. Placke, *Small Methods* **2020**, *4*, 2000039.

[53] J. Wang, P. Nie, B. Ding, S. Dong, X. Hao, H. Dou, X. Zhang, *J. Mater. Chem. A* **2017**, *5*, 2411.

[54] F. Wang, D. Ouyang, Z. Zhou, S. J. Page, D. Liu, X. Zhao, *J. Energy Chem.* **2021**, *57*, 247.

[55] H. Yao, G. Zheng, W. Li, M. T. McDowell, Z. Seh, N. Liu, Z. Lu, Y. Cui, *Nano Lett.* **2013**, *13*, 3385.

[56] C. Hernández-Rentero, R. Córdoba, N. Moreno, A. Caballero, J. Morales, M. Olivares-Marín, V. Gómez-Serrano, *Nano Res.* **2018**, *11*, 89.

[57] Y. Yan, M. Shi, Y. Wei, C. Zhao, M. Carnie, R. Yang, Y. Xu, *J. Alloys Compd.* **2018**, *738*, 16.

[58] Z.-H. Chen, X.-L. Du, J.-B. He, F. Li, Y. Wang, Y.-L. Li, B. Li, S. Xin, *ACS Appl. Mater. Interfaces* **2017**, *9*, 33855.

[59] J. Han, X. Chen, B. Xi, H. Mao, J. Feng, S. Xiong, *ChemistrySelect* **2018**, *3*, 10175.

[60] Y. Zheng, S. Zheng, H. Xue, H. Pang, *J. Mater. Chem. A* **2019**, *7*, 3469.

[61] R. Demir-Cakan, M. Morcrette, F. Nouar, C. Davoisne, T. Devic, D. Gonbeau, R. Dominko, C. Serre, G. Férey, J.-M. Tarascon, *J. Am. Chem. Soc.* **2011**, *133*, 16154.

[62] W. Salomon, F.-J. Yazigi, C. Roch-Marchal, P. Mialane, P. Horcajada, C. Serre, M. Haouas, F. Taulelle, A. Dolbecq, *Dalt. Trans.* **2014**, *43*, 12698.

[63] P. M. Shanthi, P. J. Hanumantha, B. Gattu, M. Sweeney, M. K. Datta, P. N. Kumta, *Electrochim. Acta* **2017**, *229*, 208.

[64] Z. Zhao, S. Wang, R. Liang, Z. Li, Z. Shi, G. Chen, *J. Mater. Chem. A* **2014**, *2*, 13509.

[65] H. Zhang, W. Zhao, M. Zou, Y. Wang, Y. Chen, L. Xu, H. Wu, A. Cao, *Adv. Energy Mater.* **2018**, *8*, 1800013.

[66] H. Jiang, X.-C. Liu, Y. Wu, Y. Shu, X. Gong, F.-S. Ke, H. Deng, *Angew. Chemie Int. Ed.* **2018**, *57*, 3916.

[67] Y. Jiang, H. Liu, X. Tan, L. Guo, J. Zhang, S. Liu, Y. Guo, J. Zhang, H. Wang, W. Chu, *ACS Appl. Mater. Interfaces* **2017**, *9*, 25239.

[68] J. He, Y. Chen, W. Lv, K. Wen, C. Xu, W. Zhang, Y. Li, W. Qin, W. He, *ACS Nano* **2016**, *10*, 10981.

[69] X. Yang, Y. Yu, N. Yan, H. Zhang, X. Li, H. Zhang, *J. Mater. Chem. A* **2016**, *4*, 5965.

[70] Y. Liu, G. Li, J. Fu, Z. Chen, X. Peng, *Angew. Chemie Int. Ed.* **2017**, *56*, 6176.

[71] W. Bao, Z. Zhang, W. Chen, C. Zhou, Y. Lai, J. Li, *Electrochim. Acta* **2014**, *127*, 342.

[72] J. Xu, W. Zhang, Y. Chen, H. Fan, D. Su, G. Wang, *J. Mater. Chem. A* **2018**, *6*, 2797.

[73] C. Li, Z. Li, Q. Li, Z. Zhang, S. Dong, L. Yin, *Electrochim. Acta* **2016**, *215*, 689.

[74] X. Liu, J.-Q. Huang, Q. Zhang, L. Mai, *Adv. Mater.* **2017**, *29*, 1601759.

[75] M.-S. Song, S.-C. Han, H.-S. Kim, J.-H. Kim, K.-T. Kim, Y.-M. Kang, H.-J. Ahn, S. X. Dou, J.-Y. Lee, *J. Electrochem. Soc.* **2004**, *151*, A791.

[76] X. Ji, S. Evers, R. Black, L. F. Nazar, *Nat. Commun.* **2011**, *2*, 325.

[77] Q. Li, Z. Zhang, K. Zhang, L. Xu, J. Fang, Y. Lai, J. Li, *J. Solid State Electrochem.* **2013**, *17*, 2959.

[78] K. Xie, K. Zhang, Y. Han, K. Yuan, Q. Song, J. Wang, C. Shen, X. Liu, B. Wei, *Electrochim. Acta* **2016**, *210*, 415.

[79] X. Tao, J. Wang, Z. Ying, Q. Cai, G. Zheng, Y. Gan, H. Huang, Y. Xia, C. Liang, W. Zhang, Y. Cui, *Nano Lett.* **2014**, *14*, 5288.

[80] X. Liang, L. F. Nazar, *ACS Nano* **2016**, *10*, 4192.

[81] Q. Fan, W. Liu, Z. Weng, Y. Sun, H. Wang, *J. Am. Chem. Soc.* **2015**, *137*, 12946.

[82] H. Al Salem, G. Babu, C. V. Rao, L. M. R. Arava, *J. Am. Chem. Soc.* **2015**, *137*, 11542.

[83] C.-Y. Fan, P. Xiao, H.-H. Li, H.-F. Wang, L.-L. Zhang, H.-Z. Sun, X.-L. Wu, H.-M. Xie, J.-P. Zhang, *ACS Appl. Mater. Interfaces* **2015**, *7*, 27959.

[84] W. Zhang, C. Yang, B. Ding, J. Peng, F. Xu, M. Zheng, H. Hu, Y. Xiao, Y. Liu, Y. Liang, *Chem. Commun.* **2020**, *56*, 1215.

[85] A. Benítez, Á. Caballero, E. Rodríguez-Castellón, J. Morales, J. Hassoun, *ChemistrySelect* **2018**, *3*, 10371.

[86] L. Zielke, C. Barchasz, S. Waluś, F. Alloin, J.-C. Leprêtre, A. Spettl, V. Schmidt, A. Hilger, I. Manke, J. Banhart, R. Zengerle, S. Thiele, *Sci. Rep.* **2015**, *5*, 10921.

[87] C. Tan, T. M. M. Heenan, R. F. Ziesche, S. R. Daemi, J. Hack, M. Maier, S. Marathe, C. Rau, D. J. L. Brett, P. R. Shearing, *ACS Appl. Energy Mater.* **2018**, *1*, 5090.

[88] J. Gao, M. A. Lowe, Y. Kiya, H. D. Abruña, *J. Phys. Chem. C* **2011**, *115*, 25132.

[89] C. Barchasz, J.-C. Leprêtre, S. Patoux, F. Alloin, *Electrochim. Acta* **2013**, *89*, 737.

[90] L. Wang, Y. Ye, N. Chen, Y. Huang, L. Li, F. Wu, R. Chen, *Adv. Funct. Mater.* **2018**, *28*, 1800919.

[91] K. Xu, *Chem. Rev.* **2004**, *104*, 4303.

[92] D. Aurbach, *J. Power Sources* **2000**, *89*, 206.

[93] E. Peled, S. Menkin, *J. Electrochem. Soc.* **2017**, *164*, A1703.

[94] D. Aurbach, E. Pollak, R. Elazari, G. Salitra, C. S. S. Kelley, J. Affinito, *J. Electrochem. Soc.* **2009**, *156*, A694.

[95] H. Zhang, G. G. Eshetu, X. Judez, C. Li, L. M. Rodriguez-Martínez, M. Armand, *Angew. Chemie Int. Ed.* **2018**, *57*, 15002.

[96] S. S. Zhang, *Electrochim. Acta* **2012**, *70*, 344.

[97] S. Xiong, K. Xie, Y. Diao, X. Hong, *J. Power Sources* **2014**, *246*, 840.

[98] A. Rosenman, R. Elazari, G. Salitra, E. Markevich, D. Aurbach, A. Garsuch, *J. Electrochem. Soc.* **2015**, *162*, A470.

[99] T. Tamura, T. Hachida, K. Yoshida, N. Tachikawa, K. Dokko, M. Watanabe, *J. Power Sources* **2010**, *195*, 6095.

[100] S. Seki, K. Takei, H. Miyashiro, M. Watanabe, *J. Electrochem. Soc.* **2011**, *158*, A769.

[101] Y. Gambe, Y. Sun, I. Honma, *Sci. Rep.* **2015**, *5*, 8869.

[102] D. Shanmukaraj, S. Lois, S. Fantini, F. Malbosc, M. Armand, *Chem. Mater.* **2018**, *30*, 246.

[103] S. Wei, Z. Li, K. Kimura, S. Inoue, L. Pandini, D. Di Lecce, Y. Tominaga, J. Hassoun, *Electrochim. Acta* **2019**, *306*, 85.

[104] S. Kim, Y. Jung, H. S. Lim, *Electrochim. Acta* **2004**, *50*, 889.

[105] L. Carbone, M. Gobet, J. Peng, M. Devany, B. Scrosati, S. Greenbaum, J. Hassoun, *ACS Appl. Mater. Interfaces* **2015**, *7*, 13859.

[106] Y. Yamada, A. Yamada, *J. Electrochem. Soc.* **2015**, *162*, A2406.

[107] J.-D. Xie, W.-J. Liu, C. Li, J. Patra, Y. A. Gandomi, Q.-F. Dong, J.-K. Chang, *Electrochim. Acta* **2019**, *319*, 625.

[108] I. Ruggeri, A. La Monaca, F. De Giorgio, F. Soavi, C. Arbizzani, V. Berbenni, C. Ferrara, P. Mustarelli, *ChemElectroChem* **2019**, *6*, 4002.

[109] P. Jankowski, M. Dranka, W. Wieczorek, P. Johansson, *J. Phys. Chem. Lett.* **2017**, *8*, 3678.

[110] R. Kido, K. Ueno, K. Iwata, Y. Kitazawa, S. Imaizumi, T. Mandai, K. Dokko, M. Watanabe, *Electrochim. Acta* **2015**, *175*, 5.

[111] K. Ueno, R. Tatara, S. Tsuzuki, S. Saito, H. Doi, K. Yoshida, T. Mandai, M. Matsugami, Y. Umebayashi, K. Dokko, M. Watanabe, *Phys. Chem. Chem. Phys.* **2015**, *17*, 8248.

[112] L. Suo, Y.-S. Hu, H. Li, M. Armand, L. Chen, *Nat. Commun.* **2013**, *4*, 1481.

[113] B. D. Adams, E. V. Carino, J. G. Connell, K. S. Han, R. Cao, J. Chen, J. Zheng, Q. Li, K. T. Mueller, W. A. Henderson, J.-G. Zhang, *Nano Energy* **2017**, *40*, 607.

[114] S. Seki, N. Serizawa, K. Takei, Y. Umebayashi, S. Tsuzuki, M. Watanabe, *Electrochemistry* **2017**, *85*, 680.

[115] Z. Li, S. Zhang, S. Terada, X. Ma, K. Ikeda, Y. Kamei, C. Zhang, K. Dokko, M. Watanabe, *ACS Appl. Mater. Interfaces* **2016**, *8*, 16053.

[116] S. S. Zhang, J. A. Read, *J. Power Sources* **2012**, *200*, 77.

[117] M. Agostini, S. Xiong, A. Matic, J. Hassoun, *Chem. Mater.* **2015**, *27*, 4604.

[118] P. Chiochan, S. Kosasang, N. Ma, S. Duangdangchote, P. Suktha, M. Sawangphruk, *Carbon N. Y.* **2020**, *158*, 244.

[119] D. J. Lee, M. Agostini, J. W. Park, Y. K. Sun, J. Hassoun, B. Scrosati, *ChemSusChem* **2013**, *6*, 2245.

[120] Z. Xue, D. He, X. Xie, *J. Mater. Chem. A* **2015**, *3*, 19218.

[121] F. Croce, G. B. Appetecchi, L. Persi, B. Scrosati, *Nature* **1998**, *394*, 456.

[122] X.-L. Wang, A. Mei, X.-L. Li, Y.-H. Lin, C.-W. Nan, *J. Power Sources* **2007**, *171*, 913.

[123] G. Derrien, J. Hassoun, S. Sacchetti, S. Panero, *Solid State Ionics* **2009**, *180*, 1267.

[124] Y. T. Kim, E. S. Smotkin, *Solid State Ionics* **2002**, *149*, 29.

[125] E. Simonetti, M. Carewska, G. Maresca, M. De Francesco, G. B. Appetecchi, *J. Electrochem. Soc.* **2017**, *164*, A6213.

[126] D. Di Girolamo, S. Panero, M. A. Navarra, J. Hassoun, *J. Electrochem. Soc.* **2016**, *163*, A1175.

[127] W. Lyu, G. He, T. Liu, *ChemistryOpen* **2020**, *9*, 713.

[128] D. Lin, W. Liu, Y. Liu, H. R. Lee, P. C. Hsu, K. Liu, Y. Cui, *Nano Lett.* **2016**, *16*, 459.

[129] R. Lei, Y. Yang, C. Yu, Y. Xu, Y. Li, J. Li, *Sustain. Energy Fuels* **2021**, *5*, 1538.

[130] B. W. Zewde, S. Admassie, J. Zimmermann, C. S. Isfort, B. Scrosati, J. Hassoun, *ChemSusChem* **2013**, *6*, 1400.

[131] X. Judez, H. Zhang, C. Li, J. A. González-Marcos, Z. Zhou, M. Armand, L. M. Rodriguez-Martinez, *J. Phys. Chem. Lett.* **2017**, *8*, 1956.

[132] L. Zhong, S. Wang, M. Xiao, W. Liu, D. Han, Z. Li, J. Qin, Y. Li, S. Zhang, S. Huang, Y. Meng, *Energy Storage Mater.* **2021**, *41*, 563.

[133] A. Santiago, J. Castillo, I. Garbayo, A. Saenz de Buruaga, J. A. Coca Clemente, L. Qiao, R. Cid Barreno, M. Martinez-Ibañez, M. Armand, H. Zhang, C. Li, *ACS Appl. Energy Mater.* **2021**, *4*, 4459.

[134] X. Zhang, T. Zhang, Y. Shao, H. Cao, Z. Liu, S. Wang, X. Zhang, *ACS Sustain. Chem. Eng.*

2021, *9*, 5396.

[135] I. Gracia, H. Ben Youcef, X. Judez, U. Oteo, H. Zhang, C. Li, L. M. Rodriguez-Martinez, M. Armand, *J. Power Sources* **2018**, *390*, 148.

[136] L. Carbone, J. Hassoun, *Ionics (Kiel).* **2016**, *22*, 2341.

[137] X. Judez, H. Zhang, C. Li, G. G. Eshetu, Y. Zhang, J. A. González-Marcos, M. Armand, L. M. Rodriguez-Martinez, *J. Phys. Chem. Lett.* **2017**, *8*, 3473.

[138] A. Y. S. Eng, V. Kumar, Y. Zhang, J. Luo, W. Wang, Y. Sun, W. Li, Z. W. Seh, *Adv. Energy Mater.* **2021**, *11*, 2003493.

[139] H. Zhao, N. Deng, J. Yan, W. Kang, J. Ju, Y. Ruan, X. Wang, X. Zhuang, Q. Li, B. Cheng, *Chem. Eng. J.* **2018**, *347*, 343.

[140] S. Zheng, Y. Chen, Y. Xu, F. Yi, Y. Zhu, Y. Liu, J. Yang, C. Wang, *ACS Nano* **2013**, *7*, 10995.

[141] S. Chen, Z. Yu, M. L. Gordin, R. Yi, J. Song, D. Wang, *ACS Appl. Mater. Interfaces* **2017**, *9*, 6959.

[142] P. Zeng, Y. Han, X. Duan, G. Jia, L. Huang, Y. Chen, *Mater. Res. Bull.* **2017**, *95*, 61.

[143] X.-B. Cheng, H.-J. Peng, J.-Q. Huang, R. Zhang, C.-Z. Zhao, Q. Zhang, *ACS Nano* **2015**, *9*, 6373.

[144] R. Cao, W. Xu, D. Lv, J. Xiao, J.-G. Zhang, *Adv. Energy Mater.* **2015**, *5*, 1402273.

[145] W.-J. Zhang, *J. Power Sources* **2011**, *196*, 877.

[146] J. Hassoun, B. Scrosati, *Angew. Chemie Int. Ed.* **2010**, *49*, 2371.

[147] G. Derrien, J. Hassoun, S. Panero, B. Scrosati, *Adv. Mater.* **2007**, *19*, 2336.

[148] B. Duan, W. Wang, A. Wang, Z. Yu, H. Zhao, Y. Yang, *J. Mater. Chem. A* **2014**, *2*, 308.

[149] Y. Yang, M. T. McDowell, A. Jackson, J. J. Cha, S. S. Hong, Y. Cui, *Nano Lett.* **2010**, *10*, 1486.

[150] R. Elazari, G. Salitra, G. Gershinsky, A. Garsuch, A. Panchenko, D. Aurbach, *Electrochem. commun.* **2012**, *14*, 21.

[151] M. Hagen, E. Quiroga-González, S. Dörfler, G. Fahrer, J. Tübke, M. J. Hoffmann, H. Althues, R. Speck, M. Krampfert, S. Kaskel, H. Föll, *J. Power Sources* **2014**, *248*, 1058.

[152] J. Hassoun, J. Kim, D. J. Lee, H. G. Jung, S. M. Lee, Y. K. Sun, B. Scrosati, *J. Power Sources* **2012**, *202*, 308.

[153] Y. Yan, Y.-X. Yin, S. Xin, J. Su, Y.-G. Guo, L.-J. Wan, *Electrochim. Acta* **2013**, *91*, 58.

[154] A. Krause, S. Dörfler, M. Piwko, F. M. Wisser, T. Jaumann, E. Ahrens, L. Giebeler, H. Althues, S. Schädlich, J. Grothe, A. Jeffery, M. Grube, J. Brückner, J. Martin, J. Eckert, S. Kaskel, T. Mikolajick, W. M. Weber, *Sci. Rep.* **2016**, *6*, 27982.

[155] C. Gao, H. Zhao, P. Lv, C. Wang, J. Wang, T. Zhang, Q. Xia, *J. Electrochem. Soc.* **2014**, *161*, A2216.

[156] A. Benítez, D. Di Lecce, G. A. Elia, Á. Caballero, J. Morales, J. Hassoun, *ChemSusChem* **2018**, *11*, 1512.

[157] D. Kundu, E. Talaie, V. Duffort, L. F. Nazar, *Angew. Chemie Int. Ed.* **2015**, *54*, 3431.

[158] S. Zhang, Y. Yao, Y. Yu, *ACS Energy Lett.* **2021**, *6*, 529.

[159] R. Carter, L. Oakes, A. Douglas, N. Muralidharan, A. P. Cohn, C. L. Pint, *Nano Lett.* **2017**, *17*, 1863.

[160] Q. Guo, S. Li, X. Liu, H. Lu, X. Chang, H. Zhang, X. Zhu, Q. Xia, C. Yan, H. Xia, *Adv. Sci.* **2020**, *7*, 1903246.

[161] Q. Lu, X. Wang, J. Cao, C. Chen, K. Chen, Z. Zhao, Z. Niu, J. Chen, *Energy Storage Mater.* **2017**, *8*, 77.

[162] Y.-X. Wang, J. Yang, W. Lai, S.-L. Chou, Q.-F. Gu, H. K. Liu, D. Zhao, S. X. Dou, *J. Am. Chem. Soc.* **2016**, *138*, 16576.

[163] A. Ghosh, A. Kumar, T. Das, A. Ghosh, S. Chakraborty, M. Kar, D. R. MacFarlane, S. Mitra, *Adv. Funct. Mater.* **2020**, *30*, 2005669.

[164] Z. Yan, J. Xiao, W. Lai, L. Wang, F. Gebert, Y. Wang, Q. Gu, H. Liu, S.-L. Chou, H. Liu, S.-X. Dou, *Nat. Commun.* **2019**, *10*, 4793.

[165] N. Wang, Y. Wang, Z. Bai, Z. Fang, X. Zhang, Z. Xu, Y. Ding, X. Xu, Y. Du, S. Dou, G. Yu, *Energy Environ. Sci.* **2020**, *13*, 562.

[166] B. Zhang, T. Sheng, Y. Wang, S. Chou, K. Davey, S. Dou, S. Qiao, *Angew. Chemie Int. Ed.* **2019**, *58*, 1484.

[167] X. Zhao, Q. Zhu, S. Xu, L. Chen, Z. Zuo, X. Wang, S. Liu, D. Zhang, *J. Electroanal. Chem.* **2019**, *832*, 392.

[168] J. Wu, J. Liu, Z. Lu, K. Lin, Y.-Q. Lyu, B. Li, F. Ciucci, J.-K. Kim, *Energy Storage Mater.* **2019**, *23*, 8.

[169] H. Ryu, T. Kim, K. Kim, J.-H. Ahn, T. Nam, G. Wang, H.-J. Ahn, *J. Power Sources* **2011**, *196*, 5186.

[170] I. Kim, J.-Y. Park, C. H. Kim, J.-W. Park, J.-P. Ahn, J.-H. Ahn, K.-W. Kim, H.-J. Ahn, *J. Power Sources* **2016**, *301*, 332.

[171] X. Yu, A. Manthiram, *J. Phys. Chem. C* **2014**, *118*, 22952.

[172] A. Kumar, A. Ghosh, A. Roy, M. R. Panda, M. Forsyth, D. R. MacFarlane, S. Mitra, *Energy Storage Mater.* **2019**, *20*, 196.

[173] A. Bhargav, J. He, A. Gupta, A. Manthiram, *Joule* **2020**, *4*, 285.

Chapter 2.

High-energy sulfur composites

2.1 Alternative investigation of sulfur-carbon composites

2.1.1 Presentation

The use of carbon additives to increase conductivity in sulfur cathodes is by now a consolidated strategy to achieve high-capacity and stable Li-S batteries.[1] Consequently, electrode film optimization is gaining more attention[2,3] alongside the fine morphological engineering of sulfur-carbon composites widely investigated in the pioneering Li-S works.[4,5] In spite of the outstanding performances reported in the literature that benefit from a cathode nanoengineering,[6] sulfur impregnation pathways based on melting,[7,8] crystallization from an organic solution,[9] and solvothermal permeation[10] into commercial carbons offer the advantage of being relatively straightforward and ensuring adequate electrochemical results in optimized configurations. Hence, understanding the interplay between the carbon morphology,[8,11] the cathodic film microstructure,[3] and the battery performance appears to be a crucial step to mitigate the various shortcomings in the current Li-S cell aiming at practical applications.[12]

In this regard, multiscale X-ray computed tomography sheds light on the spatial distribution of the sulfur particles within the composite electrode by providing qualitative data associated with the attenuation of the incident beam by the various materials.[13] This technique allows a volume reconstruction of the electrode at the nano- and micro-scale and enables a quantitative analysis of the morphological parameters.[14] In this section, the role of synthesis pathway on sulfur-carbon cathode microstructure, which drives the Li-S cell performance in terms of rate capability and capacity retention, is investigated. Sulfur particles are detected and their size distribution in the electrode film is analyzed. In detail, sulfur-carbon mixtures in the 70:30 wt ratio prepared by versatile approaches involving either the direct mixing of carbon with molten sulfur or the dispersion of the solid precursors in alcohol are comparatively studied. Scalable electrodes are obtained by using commercially available carbon sources (*i.e.*, carbon black and multiwalled carbon nanotubes) and are thoroughly investigated by combining X-ray diffraction, electron microscopy, and energy-dispersive X-ray spectroscopy results with X-ray CT imaging at the nano- and micro-scale.

2.1.2 Experimental

Elemental sulfur (≥99.5 %, Riedel-de Haën) and either super P carbon black (SPC, Timcal) or multi walled carbon nanotubes (MWCNTs, >90 % carbon basis, D × L 110–170 nm × 5–9 μm, Sigma-Aldrich) were mixed in the weight ratio of 70:30, respectively, and heated in a silicon oil thermostatic bath at 120 °C to melt sulfur. The mixture was vigorously stirred for ca. 2 h at 120 °C, cooled to room temperature to achieve a solid composite, and subsequently ground in an agate mortar to obtain a fine black powder. The composites prepared via melting procedure (MP) using super P carbon and multi walled carbon nanotubes are indicated as S@SPC-MP and S@MWCNTs-MP, respectively.

Elemental sulfur (≥99.5 %, Riedel-de Haën) and either super P carbon black (SPC, Timcal) or multi walled carbon nanotubes (MWCNTs, >90 % carbon basis, D × L 110–170 nm × 5–9 μm, Sigma-Aldrich) were dispersed in 2-propanol (≥99.8 %, Sigma-Aldrich) under magnetic stirring in the weight ratio of 70:30, respectively (the solubility of S in low-molecular weight alcohols at room temperature has been reported to be < 0.1wt%).[15] Afterwards, the mixtures were heated up to the boiling point of 2-propanol until full evaporation of the liquid phase, cooled to room temperature, and dried at room temperature under vacuum for 3 h to remove any possible trace of solvent. Subsequently, the sulfur-carbon precursors were pressed for 30 s at ca. 3 t cm^{-2} to obtain 14 mm diameter pellets, which were heated at 120 °C for 3 h under air and then ground in an agate mortar after cooling to room temperature. The composites prepared via solvent-assisted procedure (SAP) using super P carbon and multi walled carbon nanotubes are indicated as S@SPC-SAP and S@MWCNTs-SAP, respectively.

Electrode slurries were prepared by dispersing the sulfur-carbon composites (80wt%), super P carbon as conductive agent (Timcal, 10wt%), and polyvinilidene fluoride as binder (PVDF 6020, Solef Solvay, 10wt%) in *N*-methyl-2-pyrrolidone (NMP, anhydrous, 99.5 %, Sigma- Aldrich) through an agate mortar and a pestle. The homogenized slurries were cast on a carbon-cloth foil (GDL ELAT 1400, MTI Corp.) by means of a doctor blade. Afterwards, the slurries were heated at 50 °C under air for about 3 h to evaporate NMP, cut into disks with a diameter of 14 mm, and dried overnight at 45 °C under vacuum. The electrode disks had a sulfur loading between 1.7 and 2.9 mg cm^{-2}.

X-ray diffraction (XRD) patterns of the sulfur-carbon (S-C) composite powders were collected in the 2θ range between 10° and 70° with a scan rate of 0.4° min^{-1} and a step size of 0.01°, through a Rigaku SmartLab diffractometer using a Cu-Kα source. The powders were spread on a glass sample holder for XRD. Phase identification was performed by comparing the experimental XRD patterns with the reference data of the Inorganic Crystal Structure Database (ICSD). Scanning

electron microscopy (SEM) and energy dispersive X-ray spectroscopy (EDS) analyses of the powders were carried out by means of a Zeiss EVO MA10 employing a tungsten thermionic electron gun and an INCA X-ACT Oxford Instrument analyzer.

X-ray nano-CT imaging of the S-C materials was performed using a Zeiss Xradia 810 Ultra instrument (Carl Zeiss Inc.) equipped with a micro-focus rotating Cr anode with characteristic energy at 5.4 keV (Cr- Kα, MicroMax-007HF, Rigaku) set at 35 kV and 25 mA. Samples for X-ray nano-CT were prepared by securing the powder on stainless steel (SS) needles by epoxy [2,4,6-tris(dimethylaminomethyl)phenol, Devcon] with the aid of an optical microscope. The X-ray beam was focused onto the sample by a condenser lens in an elliptical capillary hosted inside a He-filled chamber (condenser chamber). A Fresnel zone plate inside a further He-filled chamber (optics chamber) focused the X-ray beam coming from the specimen onto a charge-coupled device (CCD) detector. An optional Au ring inside the optics chamber was used to achieve Zernike phase contrast by utilizing phase shifts across the incident X-ray beam. Thus, two different CT scans in absorption-contrast and Zernike phase-contrast modes,[16] respectively, have been performed for each sample by recording radiographs (from 901 to 1201 projections, with exposure times from 10 to 16 s for the former mode and from 40 to 50 s for the latter mode) through 180° in a field of view of 65 μm, with a 2 voxel binning. The acquisition parameters led to a voxel size of ca. 126 nm. Absorption-contrast and Zernike phase-contrast datasets were reconstructed by the Zeiss XMReconstructor software (Carl Zeiss Inc.) using a filtered back-projection algorithm, and then visualized and merged through the Avizo 2019.4 software (Visualization Sciences Group, FEI Company).[16] The merged tomographic data were further processed by applying a non-local means filter, segmented, and imaged through the Avizo 2019.4 software (Visualization Sciences Group, FEI Company). Three domains with increasing X-ray attenuation were identified by employing grayscale thresholding[14,17] and watershed[18] methods, that is, *i)* exterior, *ii)* carbon, and *iii)* sulfur.

X-ray micro-CT imaging of the electrodes was carried out using a Zeiss Xradia 520 Versa instrument (Carl Zeiss Inc.) equipped with a polychromatic micro-focus source (tungsten target) set either at 80 kV and 88 μA or at 90 kV and 89 μA. Samples with a size of about 1 × 1 mm were cut from each electrode sheet and stuck to a SS dowel by epoxy [2,4,6-tris(dimethylaminomethyl)phenol, Devcon]. Tomographic scans were performed by taking 1601 projections through 360° and acquiring images through a 40× objective lens with an X-ray exposure between 40 and 50 s and a 1 voxel binning. Source-specimen and detector-specimen distances were set in the ranges from 12.0 to 15.0 mm and from 8.8 to 11.8 mm, respectively. The experimental conditions were carefully tuned to ensure suitable X-ray transmission values as well as a voxel size within the 192–198 nm range and a field of view within the 358–385 μm range, depending on the sample. Tomographic datasets were

reconstructed by the Scout-and-Scan Control System Reconstructor software (Carl Zeiss Inc.) using a filtered back-projection algorithm, and then processed by applying a non-local means filter, segmented, visualized, and analyzed through the Avizo 2019.4 software (Visualization Sciences Group, FEI Company). Four domains with increasing X-ray attenuation were identified by employing grayscale thresholding[14,17] and watershed[18] methods: *i)* exterior, *ii)* carbon/binder, *iii)* carbon-cloth fibers, and *iv)* sulfur. Binary datasets were produced for the sulfur domain, processed by particle separation tools through the Avizo 2019.4 software (Visualization Sciences Group, FEI Company) and further analyzed by means of the ImageJ plugin XLib[19] and the Avizo 2019.4 software to calculate the discrete particle size distribution (PSD) and sphericity (shape factor) distribution according to equation (2.1.1):

$$(Sphericity) = \pi^{\frac{1}{3}} \frac{(6V)^{\frac{2}{3}}}{A} \qquad\qquad (2.1.1)$$

where V and A are the estimated volume and surface of the particles.

1,3-Dioxolane (DOL, anhydrous, containing ca. 75 ppm of butylated hydroxytoluene, i.e., BHT, as inhibitor, 99.8%, Sigma-Aldrich) and 1,2-dimethoxyethane (DME, anhydrous, inhibitor-free, 99.5%, Sigma- Aldrich) were dried under molecular sieves (3 Å, rod, size 1/16 in., Honeywell Fluka) until the water content was below 10 ppm according to a Karl Fischer titration (899 Coulometer, Metrohm). Lithium bis(trifluoromethanesulfonyl)imide (LiTFSI, 99.95% trace metals basis, Sigma-Aldrich) and lithium nitrate (LiNO$_3$, 99.99% trace metals basis, Sigma-Aldrich) were dried under vacuum at 110 and 80 °C, respectively, for 3 days. An electrolyte solution was prepared by dissolving LiTFSI and LiNO$_3$ in a 1:1 (w:w) DOL:DME mixture in a concentration of either salts with respect to the solvent mass of 1 mol kg^{-1}.

CR2032 coin-cells (MTI Corp.) were assembled by stacking a lithium disk with a diameter of 14 mm, a Celgard 2400 separator with a diameter of 16 mm soaked by 50 μL of electrolyte solution, and the sulfur-carbon composite electrode. Electrolyte preparation and coin-cell assembly were carried out in an Ar-filled glovebox (MBraun, O$_2$ and H$_2$O content below 1 ppm). The rate capability of the coin cells was tested by galvanostatic cycling at a current rate increasing every 5 cycles, that is, at C/10, C/8, C/5, C/3, C/2, 1C and 2C, and decreasing back to the initial value (C/10) at the 36th cycle (1C = 1675 mA g$_S^{-1}$). The cycle life of the coin cells was evaluated by galvanostatic measurements at a current rate of C/3 (1C = 1675 mA g$_S^{-1}$). The cycling tests were carried out within voltage ranges of 1.9–2.8 V from C/10 to C/2 and of 1.8–2.8 V from 1C to 2C, by using a MACCOR series 4000 battery test system.

All the measurements were carried out at room temperature (25 °C).

2.1.3 Results

Viable approaches to achieve composite cathodes for Li-S batteries include simple pathways according to which elemental sulfur is thoroughly mixed with carbon,[7] such as those adopted herein by directly employing molten sulfur (S@SPC-MP and S@MWCNTs-MP composites) or by benefitting from an alcohol dispersion as the synthesis precursor (S@SPC-SAP and S@MWCNTs-SAP composites). In this regard, the microstructure of the positive electrode, depending on both the carbon nature and the synthesis condition, may certainly affect the electrochemical characteristics,[11] although a careful optimization of the various cell components is crucial for favoring a reversible sulfur conversion over long cycling.[3,20,21] The XRD patterns of the four composites reported in Figure 2.1.1 reveal the expected structure of the orthorhombic sulfur (ICSD # 63082) for all the materials (see *2.1.2 Experimental* section for acronyms) and a small peak at about 26° (2θ) for both S@MWCNTs-MP and S@MWCNTs-SAP due to the graphitic character of MWCNTs.[7] On the other hand, S@SPC-MP and S@SPC-SAP do not show significant crystalline phases besides sulfur due to the predominantly amorphous nature of SPC. The full width at half maximum (FWHM) of the sulfur phase indicates relatively large crystal domains for all the powders, thereby suggesting the possible formation of heterogeneous mixtures of carbon and micrometric sulfur particles, rather than S-embedded into the carbons.
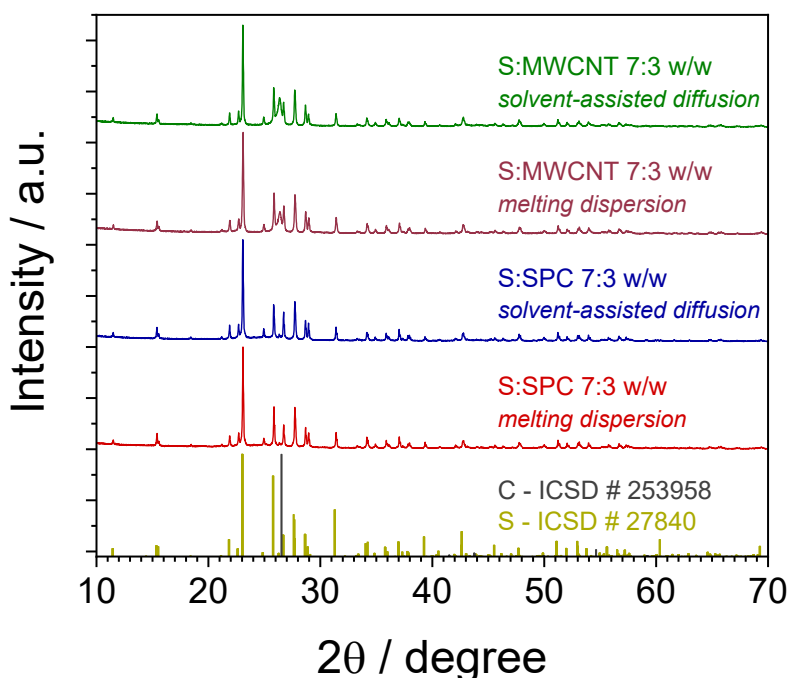

Fig. 2.1.1. XRD patterns of the S-C powders with reference reflections of hexagonal graphite (ICSD # 253958, space group *P*63/*mmc*, No. 194) and orthorhombic sulfur (ICSD # 63082, space group *Fddd*, No. 70).

A detailed morphological analysis combining SEM, EDS and X-ray nano-CT (see Figs. 2.1.2 and 2.1.3) corroborates the hypothesis drawn from XRD, showing that all the composites consist of discrete, irregular sulfur particles with a size ranging from a few micrometers to about 50 μm surrounded by carbon. Despite the similarities, the materials reveal different morphological features depending on both the carbon nature and the preparation route. Accordingly, the SEM images at low magnification (Fig. 2.1.2a, e, i, and m) indicate that the MP ensures a better dispersion of the electrode components and smaller sulfur particles than the SAP, as indeed evidenced by EDS mapping (Fig. 2.1.2b–c, f–g, j–k, and n–o), while a detail of samples at high magnification (Fig. 2.1.2d, h, l, and p) clearly shows micrometric aggregates of C nanoparticles for S@SPC-MP and S@SPC-SAP and randomly oriented C fibers with nanometric width and micrometric length for S@MWCNTs-MP and S@MWCNTs-SAP.
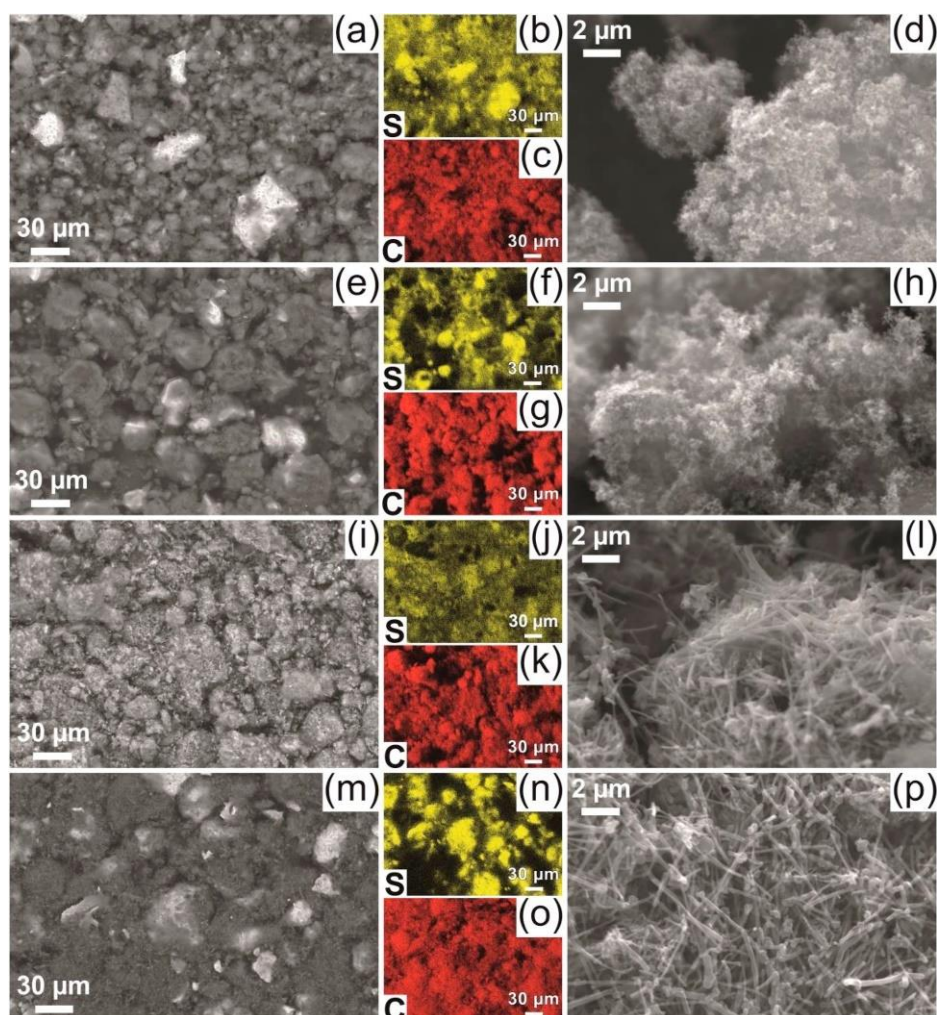
Fig. 2.1.2. Morphological analysis of **(a–d)** S@SPC-MP, **(e–h)** S@SPC-SAP, **(i–l)** S@MWCNTs-MP, and **(m–p)** S@MWCNTs-SAP. In detail: **(a and d, e and h, i and l, m and p)** SEM images at two different magnifications in **(a, e, i, m)** backscattered and **(d, h, l, p)** secondary electron modes; **(b and c, f and g, j and k, n and o)** EDS maps of **(b, f, j, n)** S and **(c, g, k, o)** C on the samples.

Even though SEM-EDS may be a powerful tool to investigate the composite morphology, nanoscale imaging of the bulk by X-ray CT advantageously provides a 3D reconstruction of sulfur-carbon agglomerates in a field of view of about 65 μm, thereby allowing to further appreciate the effect of the carbon and synthesis procedure on the material microstructure. High-resolution datasets, gathering complementary information on both the X-ray attenuation and the submicrometric features due to edge enhancement, have been obtained by combining tomographic reconstructions of scans in absorption-contrast and Zernike phase-contrast modes, respectively.[16] The corresponding images produced by merging phase and absorption contrast data, shown in Figure 2.1.3a–d, suggest that the MP may give rise to a lower degree of sulfur aggregation than the SAP (compare panels a and c with panels b and d, respectively). Interestingly, the sulfur agglomerates contain micro- and nanopores in S@SPC-MP and S@MWCNTs-MP; in contrast, S@SPC-SAP and S@MWCNTs-SAP are characterized by large sulfur particles with low porosity and relatively high attenuation of the incident beam. Further processing by image segmentation according to grayscale threshold[14,17] and watershed[18] methods has been carried out to get a volume rendering of the specimens (see Fig. 2.1.3e–h). The images illustrate the 3D distribution at the nanoscale (voxel size of 126 nm) of the sulfur particles (yellow phase) surrounded by carbon domains (gray phase), thus providing a visual representation supporting the above reported observations.
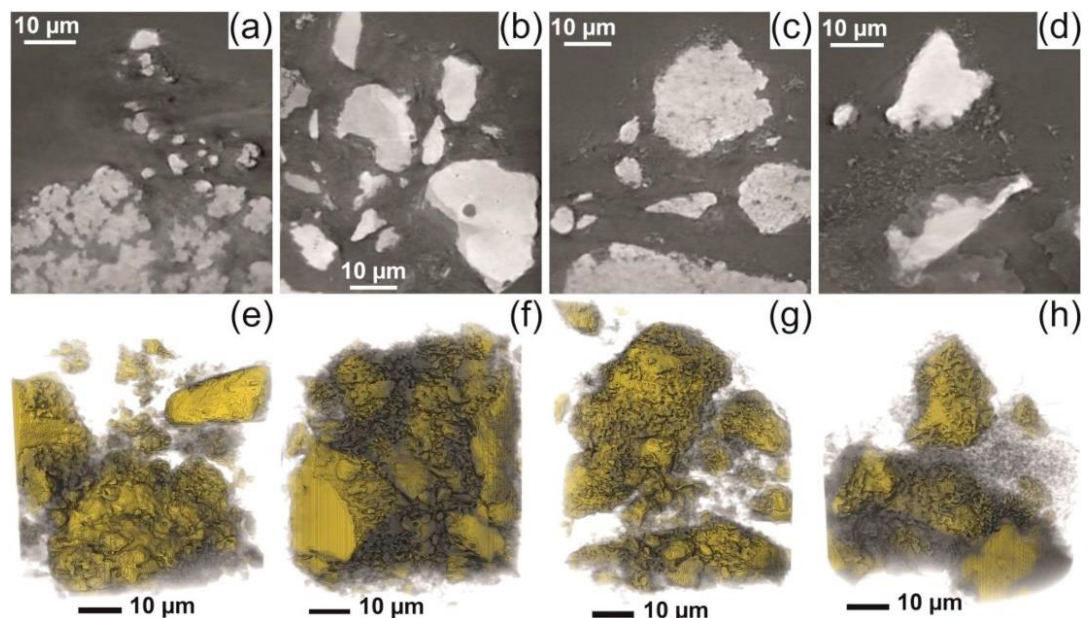

Figure 2.1.3. X-ray nano-CT imaging of **(a, e)** S@SPC-MP, **(b and f)** S@SPC-SAP, **(c, g)** S@MWCNTs-MP, and **(d, h)** S@MWCNTs-SAP, as **(a−d)** cross-sectional slices extracted in the xz plane parallel to the rotation axis (X-ray attenuation depicted through a grayscale) and **(e, f, g, h)** corresponding three-phase segmented volume renderings (S: yellow; C: gray; exterior: transparent); each dataset has been reconstructed from two different CT acquisitions in absorption-contrast and Zernike phase-contrast modes, respectively.

As already mentioned, the electrode substrate and the microstructure of the deposited electrode film may play a crucial role in determining optimal performances besides the structural and morphological features of the sulfur-based material.[3,21] On the other hand, the sulfur particle size and shape distributions, as well as the carbon nature, might reasonably affect key characteristics of the electrode coating. Therefore, X-ray micro-CT was employed to study the positive electrodes supported on a carbon-cloth current collector, which has been widely investigated as a promising alternative to conventional aluminum, benefiting from suitable porosity and surface properties.[22] Compared to the tomographic surveys at the nanoscale in Figure 2.1.3, X-ray micro-CT has a lower resolution but it ensures a much larger field of view (between 358 and 385 μm in the experimental conditions exploited), which may allow us to build the 3D reconstruction of a more representative volume for a quantitative analysis of the sulfur phase. Moreover, the carbon cloth is a particularly suitable support for tomography due to its lower X-ray attenuation with respect to aluminum, which enables an unambiguous sulfur detection and facilitates the segmentation by thresholding.[23] Relevant features are exhibited by Figure 2.1.4, showing the reconstructed images of the electrodes in terms of a cross-sectional slice extracted in the xz plane (where z is the rotation axis orthogonal to the X-ray beam and to the electrode plane, panels a, d, g, and j) and represented by a grayscale indicating the X-ray attenuation, along with the corresponding segmented slice (panels b, e, h, and k) and volume rendering (panels c, f, i, and l).[14] The left-hand side panels (Fig. 2.1.4a, d, g, and j) reveal *i*) highly attenuating sulfur particles with size and shape distributions apparently depending on both the carbon nature in the S-C composite (SPC and MWCNTs) and the synthesis procedure (MP and SAP), *ii*) the moderately attenuating cloth fibers, and *iii*) a lowly attenuating carbon/binder domain. Furthermore, X-ray CT clearly shows the carbon coating of the cloth, having similar attenuation to the carbon/binder domain, which is mostly located between the electrode film and the fibers. The corresponding segmented slices (Fig. 2.1.4b, e, h, and k) depict *i*) the sulfur particles in yellow, *ii*) the carbon fibers in light gray, *iii)* the carbon/binder phases in dark gray, and *iv*) the exterior/pores in black, whereas the right-hand side panels (Fig. 2.1.4c, f, i, and l) display the related 3D renderings using the same color map except for the exterior/pore which is not considered. Notably, Fig. 2.1.4 shows that the S@SPC-MP electrode is mostly formed by sulfur particles having a size of a few micrometers, besides large agglomerates approaching 50 μm (see panels a–c), while the other samples mainly contain sulfur domains of approximately 10–50 μm (see panels d–l). Therefore, the carbon nature remarkably affects the electrode microstructure when using the MP (compare Fig. 2.1.4a–c with Fig. 2.1.4g–i) but has only a minor influence on the sulfur particle size when SAP is employed (compare Fig. 2.1.4d–f with Fig. 2.1.4j–l). Moreover, X-ray micro-CT suggests that the MP might

35

favor the mixing between the electrode components with respect to the SAP (compare Fig. 2.1.4a–c and g–i with Fig. 2.1.4d–f and j–l, respectively).

A quantitative evaluation of the effect of carbon additive and synthesis pathway may be achieved through a comparison of the sulfur PSD in the various samples, which has been calculated herein by processing binary 3D images reconstructed from the micro-CT datasets of Figure 2.1.4. The particle size, quantified in Figure 2.1.5a, c, e, and g by the radius of related spheres with equivalent volume,[17] reveals that the MP actually ensures smaller sulfur domains than the SAP as previously supposed (compare panels a and e with panels c and g, respectively). S@SMWCNTs-MP (Fig. 2.1.5e) exhibits a narrower distribution than S@SPC-MP (Fig. 2.1.5a), with about the 90% of
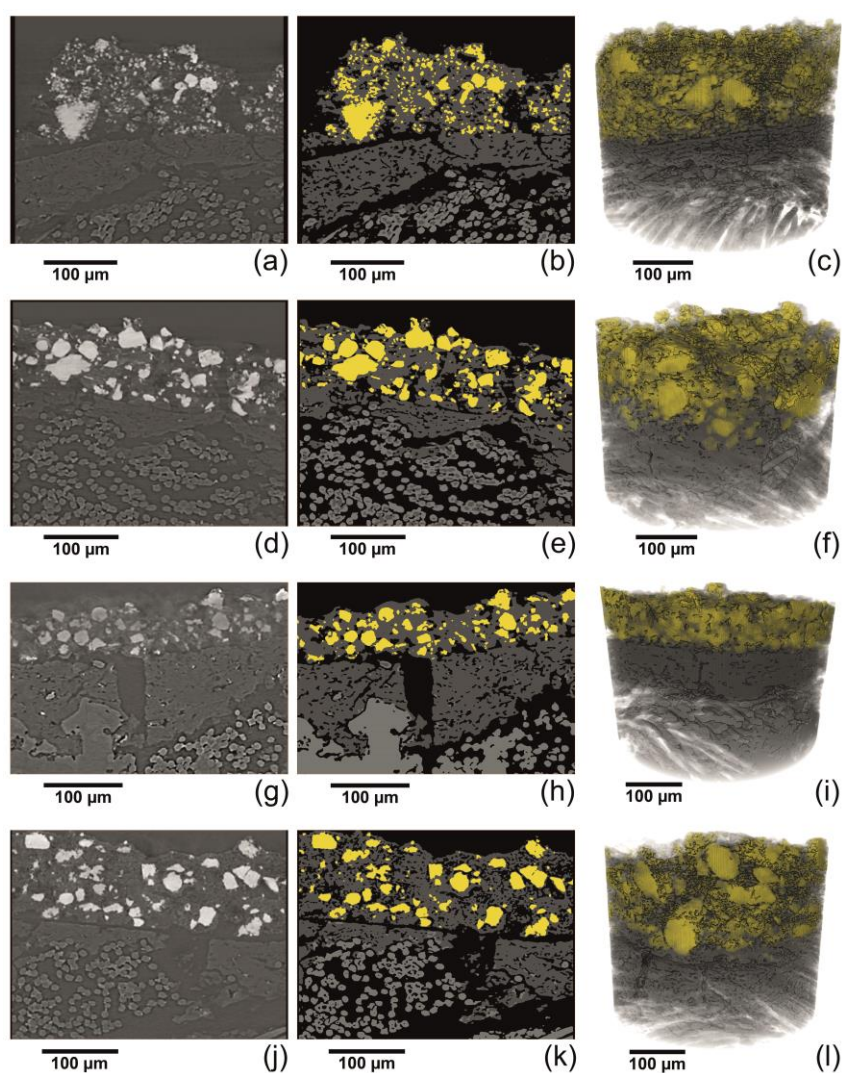
Figure 2.1.4. X-ray micro-CT imaging of **(a–c)** S@SPC-MP, **(d–f)** S@SPC-SAP, **(g–i)** S@MWCNTs-MP, and **(j–l)** S@MWCNTs-SAP electrode samples. In detail: **(a, d, g, j)** cross-sectional slices extracted in the xz plane parallel to the rotation axis and orthogonal to the electrode plane (X-ray attenuation depicted through a grayscale), **(b, e, h, k)** corresponding segmentations (S: yellow; carbon-cloth fibers: light gray; C/PVDF: dark gray; exterior: black), and **(c, f, i, l)** segmented volume renderings (S: yellow; carbon-cloth fibers: light gray; C/PVDF: dark gray; exterior: transparent).

the phase being dispersed in particles of equivalent radius below 13 μm, although a large number of sulfur domains in the latter electrode (about 50%) have an equivalent radius smaller than 7 μm, whereas S@SPC-SAP (Fig. 2.1.5c) and S@SMWCNTs-SAP (Fig. 2.1.5g) have similar distributions and significantly larger average size. A shape factor analysis quantifying the deviation from the spherical shape according to equation (2.1.1) (see the *2.1.2 Experimental* section for further details) indicates for S@SPC-MP (Fig. 2.1.5b) a relatively wide distribution with small average values compared to the other samples (Fig. 2.1.5d, f, and h).
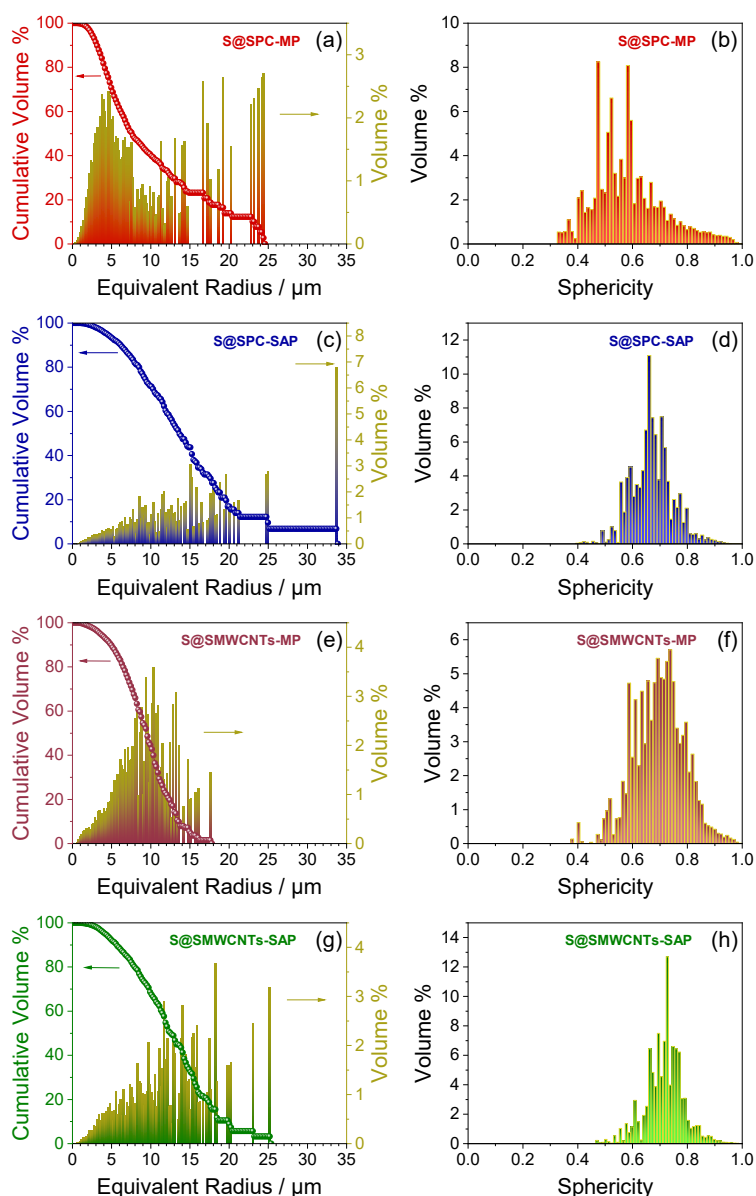
Figure 2.1.5. Analysis of the S phase in the X-ray micro-CT datasets of **(a–b)** S@SPC-MP, **(c–d)** S@SPC-SAP, **(e–f)** S@MWCNTs-MP, and **(g–h)** S@MWCNTs-SAP (see the related imaging of Fig. 2.1.4 and the 2.1.1 Experimental section for further information). In detail: **(a, c, e, g)** discrete particle size distribution (PSD)[19] and **(b, d, f, h)** sphericity (shape factor) distribution.

The above observations might be attributed to a high sulfur nucleation rate by crystallization using the MP, which can lead to small sulfur particles and large domains with low sphericity perhaps formed by coalescence, particularly enabled by the SPC due to its sub-micrometric or nanometric morphology.[24] On the other hand, the similar microstructure of S@SPC-SAP and S@SMWCNTs-SAP might imply that the SAP, which includes thermal treatment of pelletized precursors obtained from the alcohol dispersions, decreases the number of sulfur crystallization centers, mitigates the specific S-C interaction, slows down the nucleation, and favors the particle growth rate (see the *2.1.2 Experimental* section for the synthetic procedures). The sulfur particle size and the carbon morphology generally have a remarkable effect on the electrochemical reaction kinetics in Li/S batteries,[8,10] as indeed demonstrated for the four composites studied herein. Figure 2.1.6 reports the responses of rate capability tests in lithium cells of the S-C electrodes in terms of voltage profiles (panels a–d) and cycling behavior (panel e) at current rates increasing from C/10 to 2C (1C = 1675 mA g_S^{-1}). All the cells exhibit the typical plateaus at about 2.3 and 2.1 V during discharge, and at about 2.4 and 2.2 V during charge (see Fig. 2.1.6a–d), reflecting the well-known conversion of elemental sulfur to soluble polysulfides (Li_2S_x, where $4 \leq x \leq 8$), as well as to solid Li_2S_2 and possibly Li_2S.[25] The voltage curves reveal a high reversibility and the effective mitigation of the polysulfide shuttling by $LiNO_3$,[26] although the extent of the expected increase in cell polarization by raising the current may suggest faster kinetics for S@SPC-MP and S@MWCNTs-MP when compared to the corresponding materials prepared by SAP, *i.e.*, S@SPC-SAP and S@MWCNTs-SAP. Indeed, S@SPC-MP and S@MWCNTs-MP ensure a suitable process up to 1C and C/2 rates, while the increasing overvoltage of S@SPC-SAP and S@MWCNTs-SAP hinders the second plateau above C/2 and C/3 rates, respectively (compare Fig. 2.1.6a and c with Fig. 2.1.6b and d). As for the effect of carbon, the SPC-based electrodes have enhanced rate capability and a lower cell polarization than the MWCNTs-containing counterparts (compare Fig. 2.1.6a and b with Fig. 2.1.6c and d, respectively). Accordingly, S@SPC-MP demonstrates the highest rate capability among the investigated configurations, with a reversible capacity ranging from about 1510 mAh g_S^{-1} at C/10 to about 1160 mAh g_S^{-1} at 1C, whereas S@MWCNTs-SAP delivers the lowest values, that is, ca. 1180 mAh g_S^{-1} at C/10 and ca. 1040 mAh g_S^{-1} at C/3 (see Fig. 2.1.6e). Besides, S@SPC-SAP exhibits values as high as 1560 and 1510 mAh g_S^{-1} at C/10 and C/8 but suffers from a more pronounced capacity decrease compared to S@SPC-MP as the rate further increases, while S@MWCNTs-MP ensures a capacity ranging from about 1340 mAh g_S^{-1} to about 1110 mAh g_S^{-1} within C/10 and C/2 (see Fig. 2.1.6e). On the other hand, all the cells recover the initial capacity when the C-rate reverts to C/10 at the 36th cycle. Therefore, a significant correlation between the rate performance and the sulfur PSD as determined by X-ray CT (see Fig. 2.1.5) is observed. Notably, the MP can effectually

lead to smaller sulfur particles thereby possibly facilitating the Li/S conversion at high current,[27] and the nanometric morphology of SPC can further enhance the cell performance in terms of reaction kinetics. Furthermore, it is worth noticing that all the electrode formulations exhibit a satisfactory capacity ranging from 1030 to 1330 mAh g_S^{-1} at the C/3 rate.
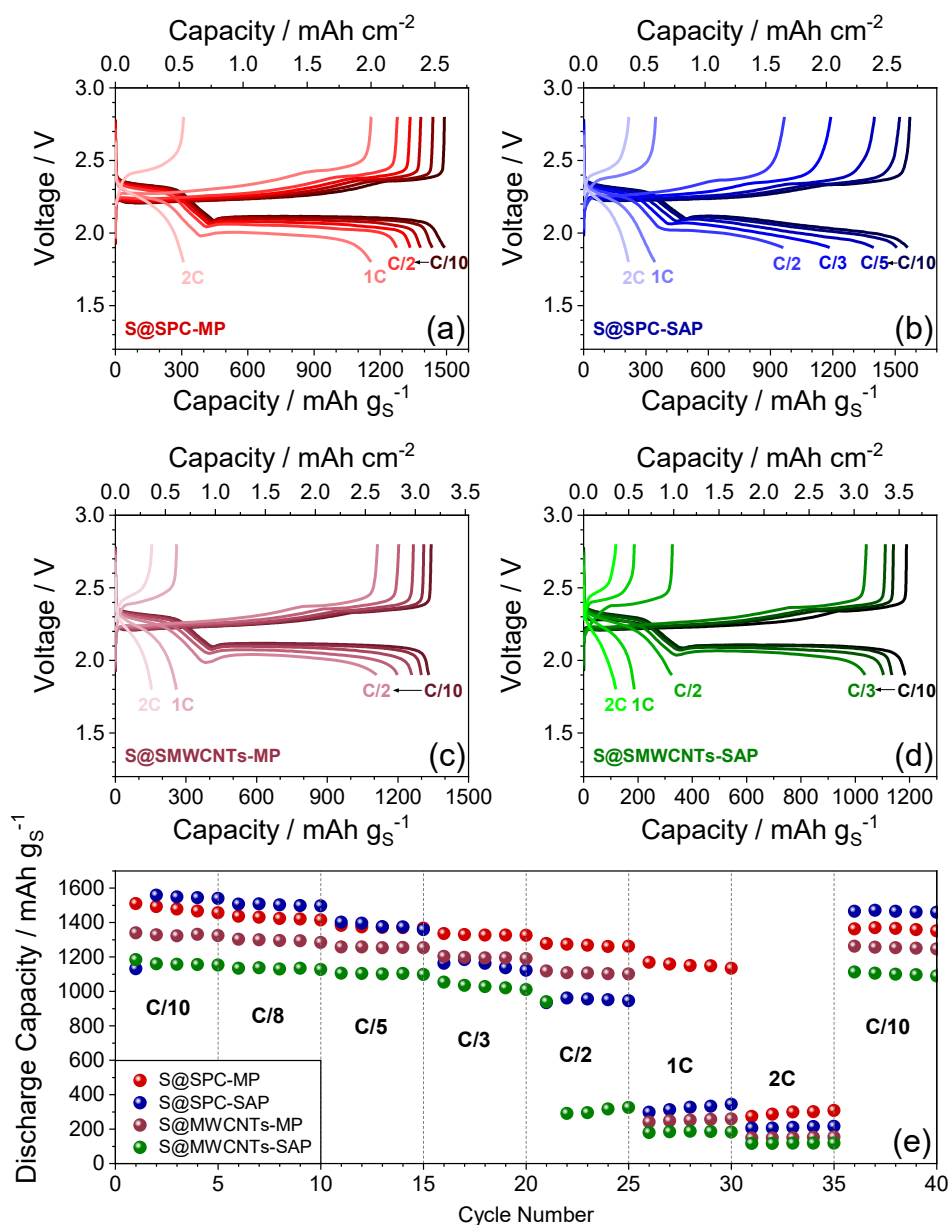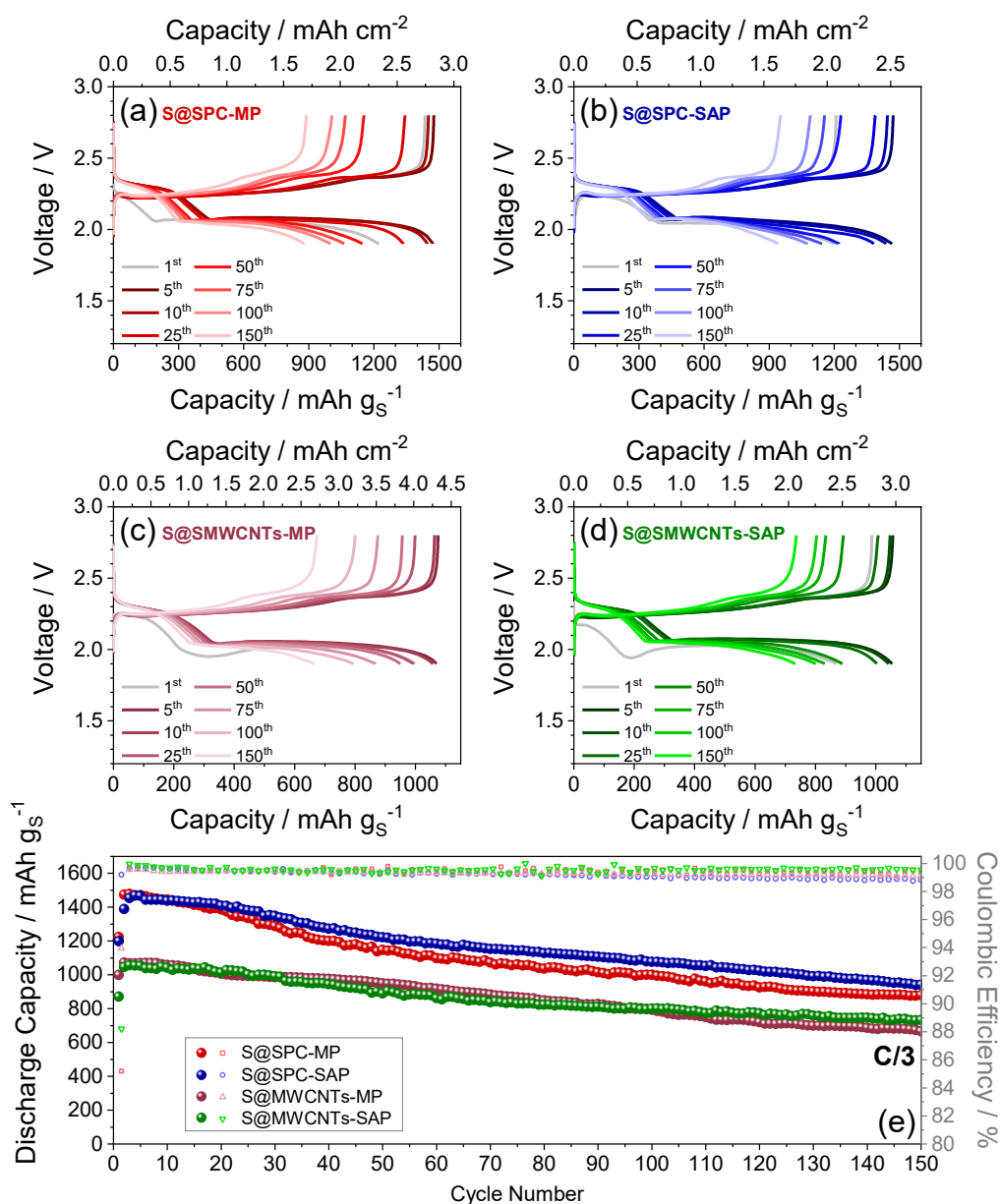

Figure 2.1.6. (a–d) Voltage profiles and **(e)** cycling behavior of the **(a)** S@SPC-MP, **(b)** S@SPC-SAP, **(c)** S@MWCNTs-MP, and **(d)** S@MWCNTs-SAP electrodes in Li coin-cells studied at current rates increasing from C/10 to 2C. Voltage range: 1.9–2.8 V from C/10 to C/2; 1.8–2.8 V from 1C to 2C. Temperature: 25 °C. Sulfur loading: from 1.7 to 2.4 mg cm^{-2}.

39

The cells have been tested at a constant current of C/3 over 150 cycles to evaluate possible effects of the electrode morphology on the capacity retention and the coulombic efficiency. Figure 2.1.7 shows the corresponding voltage curves (panels a–d) along with the capacity and efficiency trends (panel e). All the cells display an increase in reversible capacity after the first discharge reflecting an electrochemical activation promoted by the formation of a suitable electrode/electrolyte interphase,[28] and a subsequent response partially in agreement with Figure 2.1.6. Thus, the voltage profiles (Fig. 2.1.7a–d) reveal comparable overvoltage values, reversible capacities strongly depending on the carbon nature, and a capacity decay likely influenced by the synthesis procedure. In detail, the SPC ensures a higher reversible capacity than the MWCNTs as also shown in Figure 2.1.6 and discussed above, that is, ca. 1470 mAh g_S^{-1} compared to ca. 1060 mAh g_S^{-1}, whereas the SAP has beneficial effects on the capacity retention with respect to the MP (see Fig. 2.1.7e). It is worth noting that the cells employing S@MWCNTs electrodes deliver a higher geometric surface capacity (see top x-axes in Figs. 2.1.6a-d and 2.1.7a-d) due to the slightly higher sulfur loading which may influence the gravimetric capacity. On the other hand, the observed data suggest that large sulfur particles may mitigate the active material loss during cycling, in spite of adverse effect on the current capability,[27] while carbon nanoparticles may promote the electrochemical conversion of the various polysulfides. Indeed, S@SPC-MP suffers from a capacity fading to about 60% of the initial value after 150 cycles, although it has shown the best rate performance in Fig. 2.1.6 benefiting from the relatively small sulfur particles size (see Figs. 2.1.4 and 2.1.5),[27] while the large domains of electroactive material in S@SPC-SAP improve the retention to about 64%. A similar trend is observed for S@MWCNTs-MP and S@MWCNTs-SAP, which deliver at the end of the test about 62 and 69% of the initial capacity, respectively (see Fig. 2.1.7e). The figure also provides evidence that composite electrodes consisting of micrometric sulfur particles and carbons of various morphologies prepared according to relatively simple pathways may ensure a promising cycling behavior at a C/3 rate, with a coulombic efficiency above 98.8% indicating highly reversible conversion processes (see the right y-axis of Fig. 2.1.7e).

In summary, the obtained data show that electrodes using the same carbon additive with different sulfur particle size distribution in pristine condition have different response in terms of specific capacity, rate capability, and cycling stability. Certainly, a full elucidation of this phenomenon might require further *in situ* and/or *operando* X-ray CT analyses of cathodes of various chemical nature and morphology to track their evolution during cycling, although *ad hoc* cell geometries usually employed in these studies appear to be not suitable for a comparison of performance between different materials due to the use of small electrode samples and high E/S ratios as compared to the typical coin-cell configuration. In this regard, X-ray 3D imaging of a composite

cathode as a function of state of charge has revealed significant morphological changes occurring in the sulfur phase, while the carbon/ binder domain was relatively stable during discharging and subsequent charging.[13] In particular, elemental sulfur has been reported to grow preferentially along cracks within the carbon/binder framework as well as close to the electrode/separator interface. Based on these considerations, the observed effect of morphology suggest that pristine sulfur distribution influences the microstructure of the carbon/binder framework, the sulfur nucleation sites and the kinetics of sulfur electrodeposition and, therefore, the cycling response of the cell.

Figure 2.1.7. (a–d) Voltage profiles and **(e)** cycling behavior with coulombic efficiency of the **(a)** S@SPC-MP, **(b)** S@SPC-SAP, **(c)** S@MWCNTs-MP, and **(d)** S@MWCNTs- SAP electrodes in Li coin-cells studied at a constant current rate of C/3. Voltage range: 1.9–2.8 V. Temperature: 25 °C. Sulfur loading: from 1.7 to 2.9 mg cm^{-2}.

2.2 Tin nanoparticles as efficient conductive matrix

2.2.1 Presentation

As discussed in section *2.1*, simple approaches involving coating of molten sulfur on carbon appeared to be suitable for achieving materials with satisfactory performances in lithium cell, and at the same time modest expected cost which may favor the economical sustainability of the Li/S battery and hence its large-scale diffusion.[7] In particular, literature works demonstrated that the low electronic conductivity of the sulfur due to its insulating character represents the rate-determining step, which controls the cell polarization and hence the specific capacity and the energy density.[29] However, relatively high fractions of inert carbon matrices used for ensuring satisfactory electron conductivity actually affect both gravimetric and volumetric energy densities of the composite.[30] In this section, the energy density is enhanced by coating sulfur on nanometric tin particles adopting a weight ratio of 80:20. The nanometric metal is used to increase the conductivity of the S-Sn composite in view of the metallic nature that provides a relevant electron mobility, therefore lowering the resistance of the composite,[31] and to achieve a low electrode/electrolyte interphase resistance,[32] thus improving the electrode performance in lithium cell in terms of low charge/discharge polarization and high-rate capability.[33] Furthermore, the metallic tin nanoparticles are expected to support the active material, stabilize the sulfur electrode by weak interaction, and allow a highly efficient electrochemical process and relevant cycling stability of the Li/S cell.[32] Remarkably, the high sulfur loading in the S-Sn composite, that is, 80% w/w, allowed by the use of the electron conducting metal as the matrix (Sn) is expected to ensure a high practical capacity compared with several electrode materials with lower active material content.[34] Indeed, X-ray diffraction, scanning and transmission electron microscopy, selected area electron diffraction patterns, and energy dispersive X-ray spectroscopy are used to detect structure and morphology of the synthesized composite, whereas the study of the electrochemical performances in Li/S cell is carried out through cyclic voltammetry, electrochemical impedance spectroscopy, and galvanostatic cycling measurements.

2.2.2 Experimental

The composite was prepared by mixing elemental sulfur (≥99.5 %, Riedel-de Haën) and tin nanopowder (<150 nm, Sigma-Aldrich, ≥99 % trace metal basis) in a weight ratio of 80:20. The mixture was subsequently heated using a silicon oil bath at the temperature of 120 °C until the

complete melting of sulfur. The dispersion of tin into molten sulfur was stirred for 30 min and then quenched at room temperature until solidification. Subsequently, the solid composite was grinded in an agate mortar to obtain the final electrode powder (indicated in the manuscript by the acronym S-Sn).

The structure of the S-Sn composite was investigated by XRD, and the patterns were obtained through a Bruker D8 Advance diffractometer equipped with a Cu-Kα source by performing a scan in the 2θ range between 10° and 50° at a rate of 10 s per step with step size of 0.02°.

The morphology of the S-Sn material was studied using SEM and TEM techniques, performed using a Zeiss EVO 40 microscope equipped with a LaB_6 thermoionic electron gun and a Zeiss EM 910 microscope quipped with a tungsten thermoionic electron gun operating at 100 kV, respectively. EDS was recorded on the SEM images through a X-ACT Cambridge Instruments analyzer to study the element distribution into the S-Sn composite.

The electrodes were prepared by doctor blade casting of a slurry formed by the S-Sn composite (80wt%), Super P carbon (10wt%, Timcal, conducting agent), and polyvinylidene fluoride (10wt%, PVDF 6020, Solef Solvay, binder) in N-methyl-2-pyrrolidone (NMP, Sigma-Aldrich), on a GDL foil (ELAT, MTI corporation). The slurry was heated for 3 h at 50 °C to remove the solvent and finally cut into disks (14mm diameter), which were dried at 45 °C overnight under vacuum. The loading of the active material in the final electrode was ranging from 1 to 4 mg cm^{-2}.

The electrolyte used for this study is a solution of 1 mol of lithium bis(trifluoromethanesulfonyl)imide (LiTFSI, 99.95% trace metals basis, Sigma-Aldrich) and 1 mol of lithium nitrate ($LiNO_3$, 99.99% trace metals basis, Sigma-Aldrich) in 1 kg of a solvent formed by mixing 1,3-dioxolane (DOL, anhydrous, containing ca. 75 ppm of butylated hydroxytoluene, i.e., BHT, as inhibitor, 99.8%, Sigma-Aldrich) and 1,2-dimethoxyethane (DME, anhydrous, inhibitor-free, 99.5%, Sigma- Aldrich) in a 1:1 weight ratio, and indicated subsequently as DOL:DME 1:1 w/w, 1 mol kg^{-1} LiTFSI, 1 mol kg^{-1} $LiNO_3$.

To evaluate the electrochemical process characteristics and the performances of the composite in lithium cell, 2032-type coin cells were prepared exploiting the Li|DOL:DME 1:1 w/w, 1 mol kg^{-1} LiTFSI, 1 mol kg^{-1} $LiNO_3$|S-Sn configuration. The cells were prepared in an Ar-filled glove box (MBraun, O_2 and H_2O content below 1 ppm) by using the electrode disk as the cathode, a Celgard foil soaked in 50 μL of the electrolyte as the separator, and a lithium metal disk as the anode. The electrochemical process was studied through CV and EIS tests, which were performed using a VersaSTAT MC Princeton Applied Research (PAR) analyzer: CV measurements consisted of ten cycles in the 1.8 – 2.8 V range with a scan rate of 0.1 mV s^{-1}, while EIS measurements were taken at

the OCV, after the first, fifth, and tenth CV cycles in the 500 kHz – 100 mHz frequency range using a 10 mV amplitude signal.

The performances of the S-Sn composite in lithium cell were investigated through galvanostatic cycling (GC) tests using a MACCOR series 4000 battery test system: a rate capability measurement was performed using current values of C/10, C/8, C/5, C/3, C/2, 1C, and 2C in the 1.9 – 2.8 V range from C/10 to C/2, and in the 1.8 – 2.8 V range for 1C and 2C. Galvanostatic tests prolonged to 100 cycles were performed at constant rate of C/3, 1C, and 2C (1 C = 1675 mA g_S^{-1}) within the 1.9 – 2.8 V range at C/3 and 1C, and the 1.8 – 2.8 V range at 2C. Both specific current and specific capacity were referred to the sulfur mass, that is, the electrochemically active component in the S-Sn composite prepared by a S-to-Sn weight ratio of 80:20. An EIS test was performed on a lithium cell using a S-Sn electrode at the OCV, after 1 cycle and after 100 cycles using a current value of 2C in the 1.8 – 2.8 V range.

An *ex situ* XRD test was performed using a pristine S-Sn electrode, and an electrode collected from a cell after one galvanostatic cycle using a current value of C/10 in the 1.9 – 2.8 V range. The cell was disassembled in an Ar-filled glove box (MBraun, O_2 and H_2O content below 1 ppm), the electrode collected and dried for 30 min under vacuum, and the XRD pattern collected under air through a Bruker D8 Advance diffractometer equipped with a Cu Kα source by performing a scan in the 2θ range between 10° and 50° at a rate of 10 s per step with the step size of 0.02°.

2.2.3 Results

The structure and morphology of the electrode play a key role in determining its behavior in lithium cell, and therefore, they are subsequently determined by XRD, SEM, and TEM. Figure 2.2.1 shows the comparison between the experimental diffraction patterns of the S-Sn electrode and of the metallic Sn nanopowder used for material synthesis, as well as the theoretical data of elemental sulfur (red diagram) and metallic tin (blue diagram) indicated according to the powder diffraction file (PDF) numbers. The S-Sn pattern shows reflection peaks ascribable exclusively to orthorhombic sulfur (S_8, PDF # 85-0799) and tetragonal tin (Sn, PDF # 86-2265), without signs of Sn/S compounds such as SnS (tin sulfide),[35] thus suggesting only physical mixing between the two elements without chemical reaction or impurity, as indeed expected by the low temperature adopted for the material synthesis (i.e., 120 °C). This important result excludes possible side reactions of sulfide species during the electrochemical process in the lithium cell[36] which can affect the reversibility and the voltage shape of the material, expected instead to reflect only the reaction of sulfur with lithium.[37] The pattern of the S-Sn composite shows a different ratio between the peaks at 30.66°/32.05° and 43.91°/44.94°

with respect to those of metallic tin in the same 2θ position, as most likely due to the contribution of corresponding peaks related to sulfur (compare the theoretical diagrams of Sn and S_8 in Fig. 2.2.1). Furthermore, the pattern of the metallic tin nanopowder shows only minor traces of SnO_2, identified by two peaks at 30° and 33° (stars). In summary, the predominant presence of Sn metal with respect to SnO_2 may be reflected into high electron conductivity, and thus remarkable rate capability in lithium cell of the electrode, which contains only Sn metal as the support.[38]
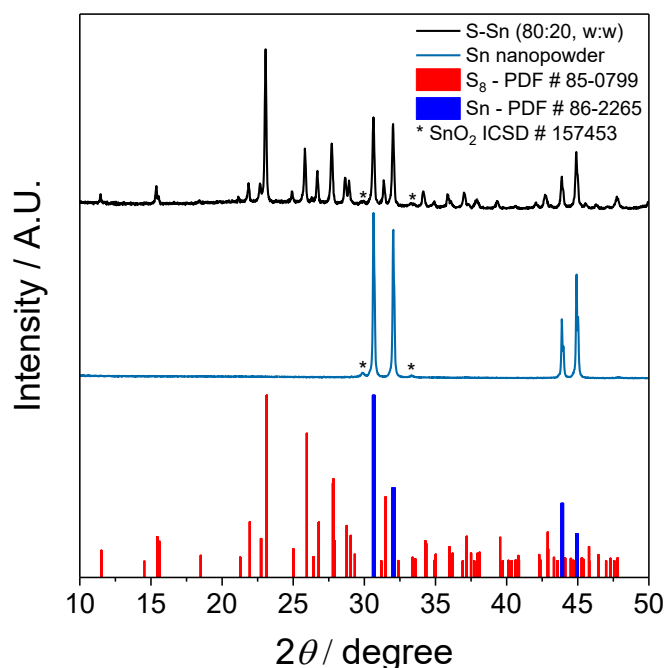
Figure 2.2.1. XRD patterns of the S-Sn composite (black) and metallic tin nanopowder used for the synthesis (light blue); reference data for elemental sulfur (red, PDF # 85-0799), metallic tin (blue, PDF # 86-2265) and SnO_2 (stars, ICSD #157453) are also reported.

Figure 2.2.2 shows the SEM-EDS and TEM images of the material exploited to study its morphology. The SEM-EDS images, displayed in panels a–e and inset, show that the S-Sn material is characterized by a uniform distribution of tin into the sulfur bulk. In particular, panels c and e indicate metal nanoparticles embedded into sulfur as expected by the synthetic pathway, which involves stirring of the metal particles and molten S. Therefore, Sn acts as a support for sulfur and forms spherical structures in which sulfur coats tin, as indeed suggested by the TEM images (panels f–h). The TEM images shown in Figure 2.2.2f–h collected in various regions of the sample evidence the presence of tin core particles (dark-colored spheres) interconnected by the sulfur shell (light-colored background); the inset of Figure 2.2.2f further highlights the distribution of the metallic tin (marked by light blue line) into sulfur (marked by a red line) in a spot of the material. The inset also

shows that the nanometric tin is hosted into the sulfur bulk to form a core–shell-like configuration. The crystallinity of the S-Sn composite is further confirmed by the distribution of electron diffraction spots of the SADEP measurement performed on the TEM image and reported in the inset of Figure 2.2.2h.[39] Such a composite morphology consisting of sulfur loaded by metal may actually confer to the S-Sn electrode a higher conductivity with respect to the insulating bulk sulfur[40] and an enhanced behavior in lithium cell, which requires an efficient ion and electron transport for lowering the electrode/electrolyte interphase resistance.[41] It is worth mentioning that the relatively limited content (20% w/w) of the electrochemically inactive Sn, within the exploited potential range of the Li/S battery, may be further lowered due to its metallic nature and high conductivity, thus increasing the practical capacity of the Li/S cell.[34]
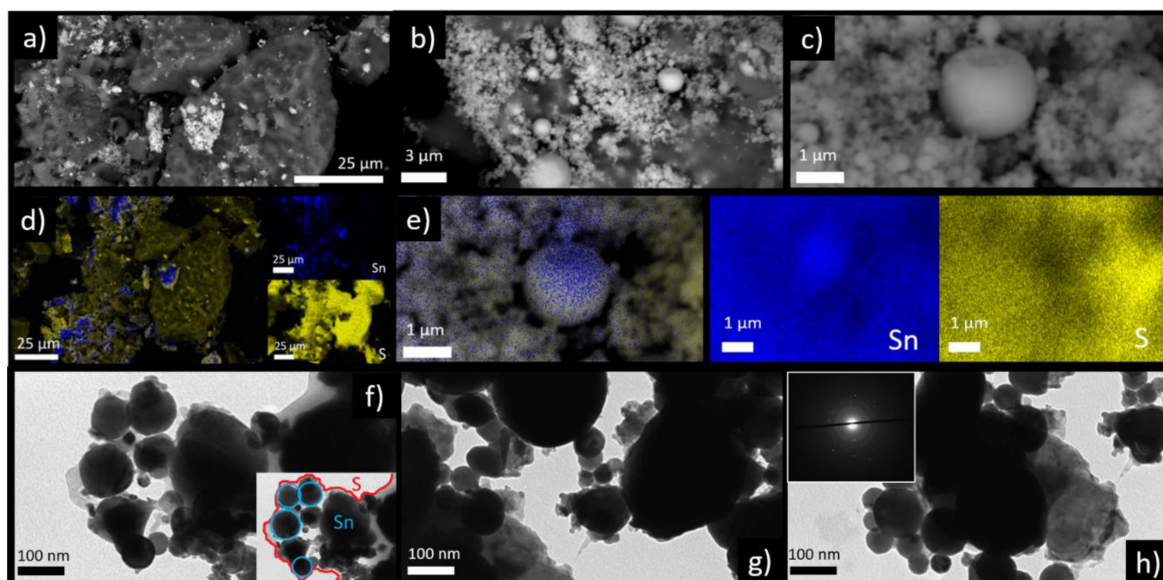

Figure 2.2.2. (a–c) SEM images of the S-Sn composite with various magnifications; **(d, e)** corresponding EDS maps for metallic tin (blue) and elemental sulfur (yellow), insets show the single maps for Sn and S; **(f–h)** TEM images of the S-Sn composite: inset in panel **(f)** highlights the distribution of the metallic tin (marked by light blue line) into sulfur (marked by a red line) in a spot of the material, while the inset in panel **(h)** shows the SAEDP.

The electrochemical process of the S-Sn composite has been characterized in lithium cells by CV, EIS, and galvanostatic cycling. Figure 2.2.3 shows the CV profiles performed within 1.8 and 2.8 V vs Li$^+$/Li (panel a) and the EIS Nyquist plots collected upon voltammetry (panel b). It is worth noting that the lower potential cutoff during voltammetry (1.8 V vs Li$^+$/Li, Figure 2.2.3a) has been chosen to minimize the formation of highly insulating species such as lithium sulfide (Li$_2$S). During the first cathodic scan, two peaks can be observed: the first one, at 2.2 V vs Li$^+$/Li, corresponds to the conversion of sulfur by reaction with lithium ions and reduction to long chain lithium polysulfides, such as Li$_2$S$_8$ and Li$_2$S$_6$, while the second one, at 2.0 V vs Li$^+$/Li, indicates the formation of short-

chain polysulfides Li_2S_x ($2 \leq x \leq 4$).[42] Instead, during the first anodic scan, the two oxidation peaks merge into a broad double peak, centered at about 2.4 and 2.45 V *vs* Li^+/Li, by the conversion of the lithium polysulfides to the Li and S_8 species, as already observed previously for this kind of materials.[42] The first CV cycle shows limited polarization and relevant reversibility, thus accounting for the fast kinetics of the electrochemical process compared with other electrodes,[7] which further enhances during the subsequent cycles showing a shift of the cathodic peaks to higher potential values (2.35 and 2.05 V *vs* Li^+/Li) and the anodic ones to lower values around 2.4 V *vs* Li^+/Li. This suitable process, usually occurring from first to second cycle, is indicated in the literature by the term *activation* as it leads to an increased energy efficiency.[11,28] This trend can be likely ascribed both to the formation of a stable SEI at the electrode surface by irreversible electrolyte degradation[26] and to suitable modifications of the electrode structure during the first cycle leading to its gradual lithiation with partial formation of polysulfide and a decrease of the electrode/electrolyte interphase resistance. [11,28] The SEI layer, which is additionally improved by the presence of $LiNO_3$ in the electrolyte,[43,44] favors the kinetics of the electrochemical process, protects the electrodes, and provides stability to the electrode/electrolyte interphase,[26] as suggested by the overlapping CV profiles reported in Figure 2.2.3a. However, the voltammograms show a small decrease in the peak intensity by cycles, most likely due to a minor loss of the active material by side reactions leading to the partial precipitation of lithium polysulfide at the anode or progressive formation of short-chain polysulfides such as Li_2S and Li_2S_2.[37] The reasons accounting for the aforementioned activation with the decrease in the cell polarization are investigated by EIS measurements during CV, and shown in Figure 2.2.3b, which displays the Nyquist plot at the open-circuit voltage (OCV), after 1, 5, and 10 cycles. The figure evidences a relevant change from the first to the subsequent CV cycles both of the plot shape and of the resistance values, which were studied by nonlinear least-squares fitting (NLLS) using a Boukamp tool[45,46] and shown in Table 2.2.1. It is worth mentioning that only fits with a χ^2 value of the order of 10^{-4} or lower were considered suitable for data analysis. The study shows that the cell is represented by an equivalent circuit of the type $R_e(R_1Q_1)(R_2Q_2)Q_w$ where, in addition to the electrolyte resistance R_e, the first two R_iQ_i elements represent medium-high frequency semicircles ascribed to the electrode/electrolyte interphase, including SEI film and charge transfer resistances and constant phase elements (CPEs).[47] At the OCV, the last element in the low-frequency region (Q_w) can actually account for the diffusion of lithium ions at the electrode/electrolyte interphase according to a depressed, loop-type Warburg profile, which is generally observed in the presence of inhomogeneous or porous structures in which some of the pores are filled by electrolyte.[48] After one CV cycle, the Nyquist plot drastically shrinks and the low-frequency element (Q_w) changes to a tilted line ascribed to the common Warburg diffusion of the lithium ions into the electrode/electrolyte interphase and

geometrical capacity of the cell.[45,46] The Nyquist profiles hardly change upon subsequent CV cycles, and the resistance values remain low and stable. The data of Table 2.2.1 indicate an overall resistance value (R) of the electrode/electrolyte interphase decreasing from about 370 Ω at the OCV to values as low as 5, 4, and 3 Ω after 1, 5, and 10 CV cycles, respectively.[49,50] This remarkable resistance reduction, mentioned earlier as electrode activation, as well as the relevant change of the Nyquist plot shape can account for a significant variation of the electrode structure and characteristic upon the first charge/discharge cycle, which certainly merits further insights by specific techniques, such as ex situ XRD, and possibly in situ XRD, in situ SEM, or tomography, to be fully clarified.[51,52] Such an activation process leads to very low electrode/electrolyte resistance values, which can actually allow optimal operation in lithium cell in terms of the delivered capacity and the rate capability.
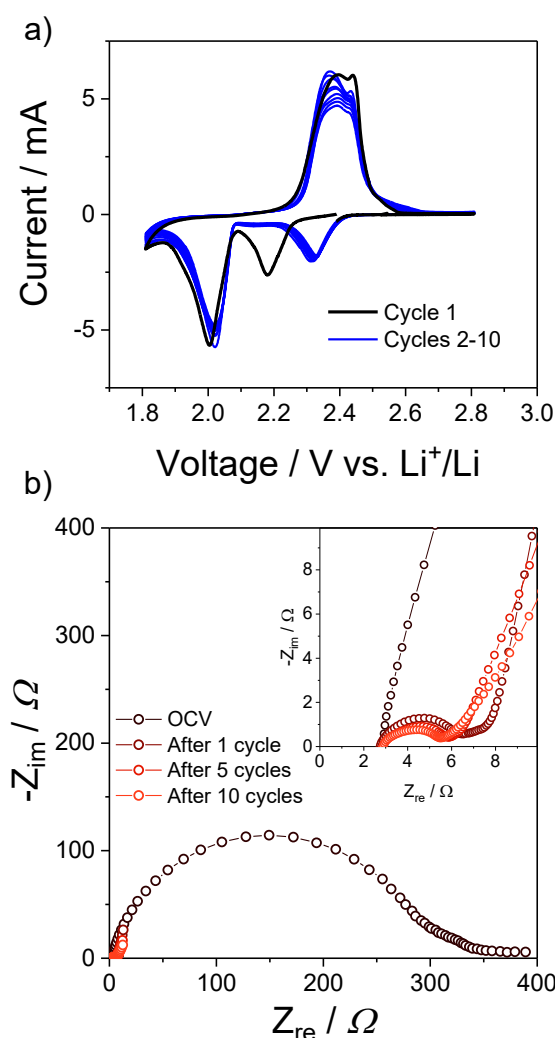

Figure 2.2.3. (a) CV profiles of the Li/S-Sn cell (potential range 1.8 – 2.8 V *vs* Li+/Li; scan rate 0.1 mV s-1; and **(b)** corresponding Nyquist plot obtained by EIS at the OCV, after 1, 5, and 10 CV cycles, inset shows a magnification in the low impedance region. EIS frequency range 500 kHz – 100 mHz; signal amplitude 10 mV.

Cell condition	Circuit	R_1 (Ω)	R_2 (Ω)	$R = R_1 + R_2$ (Ω)	χ^2
OCV	$R_e(R_1Q_1)(R_2Q_2)Q_w$	282.3 ± 8.5	84.9 ± 13.7	367.2 ± 11.4	5.0×10^{-4}
1 CV cycle	$R_e(R_1Q_1)(R_2Q_2)Q_w$	3.5 ± 0.1	1.7 ± 0.3	5.2 ± 0.2	1.8×10^{-4}
5 CV cycles	$R_e(R_1Q_1)(R_2Q_2)Q_w$	3.2 ± 0.1	0.3 ± 0.1	3.5 ± 0.1	6.1×10^{-5}
10 CV cycles	$R_e(R_1Q_1)(R_2Q_2)Q_w$	2.8 ± 0.1	0.3 ± 0.1	3.1 ± 0.1	1.2×10^{-4}

Table 2.2.1. NLLS analyses performed on the impedance spectra of Figure 2.2.3b, recorded upon CV of the S-Sn composite in the lithium cell.

The applicability of the S-Sn material in batteries is subsequently studied by galvanostatic cycling in lithium cell both at various currents, to determine the rate capability of the electrode, and at a constant rate to evaluate the cycle life. Figure 2.2.4 shows the steady-state voltage profiles (panel a) and the cycling trend (panel b) of a galvanostatic test performed at C/10, C/8, C/5, C/3, C/2, 1C, and 2C (1C = 1675 mA g_S^{-1}). The profiles of Figure 2.2.4a show at the lowest C-rate (C/10) the voltage signature expected by voltammetry upon the first cycle, with two plateaus clearly separated at about 2.35 and 2.05 V during discharge and two corresponding charge plateaus, which tend to merge at about 2.4 V due to the curve slope (compare Figure 2.2.3a and 2.2.4a). The cell delivers at C/10 a maximum capacity value of about 1200 mAh g_S^{-1}, which decreases only slightly and gradually to about 1120, 1080, 1040, 1010, and 950 mAh g_S^{-1} at C/8, C/5, C/3, C/2, and 1C, respectively, as demonstrated by the cycling trends of Figure 2.2.4b. This capacity decrease is expected by the increase in the cell polarization observed in Figure 2.2.4a due to the increase in the current during the test. Remarkably, upon a further increase in the current to a value as high as 2C, the cell holds a capacity of about 780 mAh g_S^{-1}, which is considered to be a very significant value taking into account the high current density, calculated to be of the order of 7 mA cm^{-2} (*vs* electrode geometric surface of 1.54 cm^2) taking into account the elevated 1C for the Li/S cell (1C = 1675 mA g_S^{-1}) and a possible sulfur loading of about 2 mg cm^{-2} (see *2.2.2* Experimental section for details). Therefore, Figure 2.2.4 shows relevantly high values of the specific capacity, well comparing at intermediate/low currents of those enhanced composites reported in the literature by more complex and cost-effective preparation techniques,[53,54] and even exceeding the typical results at the high C-rates.[55] This interesting performance is likely ascribed to a very low resistance achieved by the electrode/electrolyte interphase driven by the electrode composition, structure, and morphology in which Sn acts within
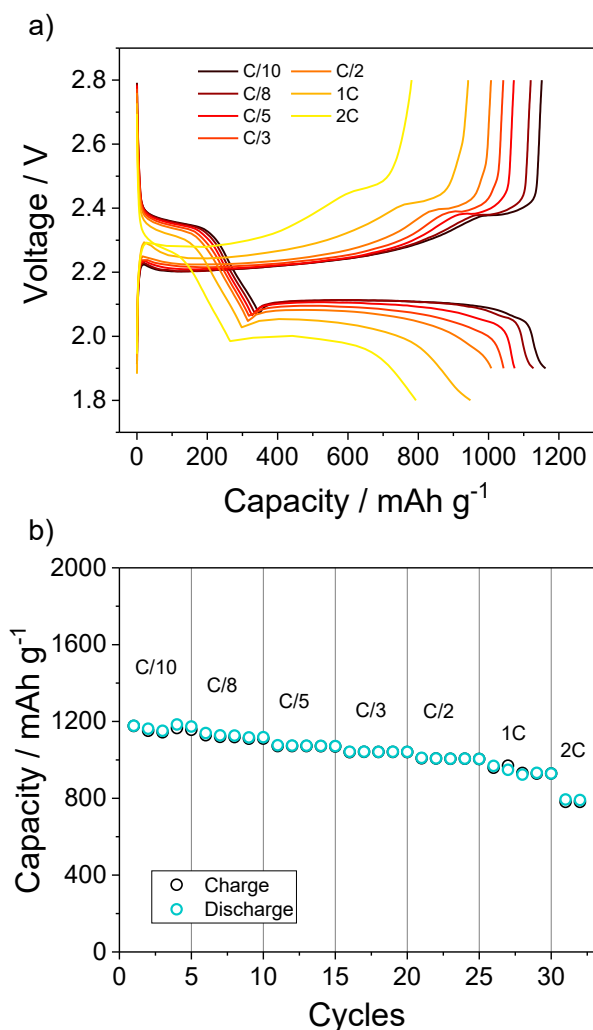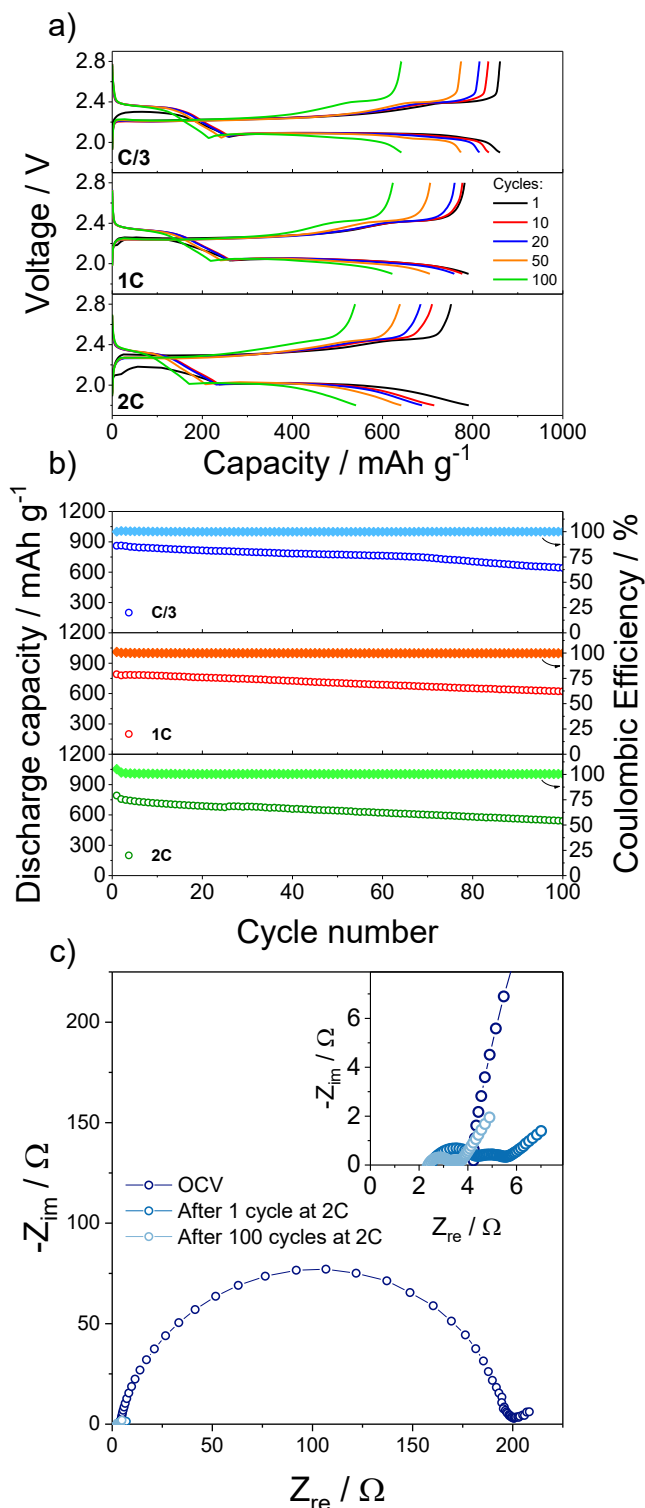
Figure 2.2.4 (a) Voltage profiles and **(b)** corresponding cycling trend of the galvanostatic measurement performed on Li/S-Sn cell at various current rates, that is, C/10, C/8, C/5, C/3, C/2, 1C, 2C. Voltage range of 1.9 – 2.8 V from C/10 to C/2 and of 1.8 – 2.8 V at 1C and 2C.

the exploited potentials as an electrochemically inactive metal, while providing highly conductive support, as already described.

The cycle life of the S-Sn electrode in lithium cell is characterized by galvanostatic measurements prolonged up to 100 cycles within the high C-rate region, that is, at C/3, 1C, and 2C. Figure 2.2.5 shows the voltage profiles of selected cycles (panel a), the trends of specific capacity and efficiency versus cycle number of cell (panel b), and the Nyquist plots obtained at the OCV, after 1 cycle, and after 100 cycles at the constant rate of 2C (panel c). After the first discharge process, which is characterized by the aforementioned SEI film formation and activation process,[26] the voltage profiles of Figure 2.2.5a overlap for all of the exploited currents with constantly limited polarization. During the initial cycles, the cells show a capacity of about 870, 800, and 790 mAh g$_S$-

[1] C/3, 1C, and 2C, respectively, which are slightly lower values than those of the rate capability test, mainly due to the different operating conditions.

Figure 2.2.5. (a) Voltage profiles and **(b)** corresponding cycling trends (left y-axis) with coulombic efficiency (right y-axis) of prolonged galvanostatic measurements performed using the Li/S-Sn cell at C/3, 1C and 2C rates. Voltage range of 1.9 – 2.8 V at C/3 and 1C, and of 1.8 – 2.8 V at 2C. **(c)** Nyquist plots of the EIS measurements performed at the OCV, after 1 and 100 cycles at the constant current rate of 2C; the inset shows a magnification in the low impedance region. EIS frequency range 500 kHz – 100 mHz; signal amplitude 10 mV.

Furthermore, Figure 2.2.5b shows a coulombic efficiency approaching 100% over the 100 cycles considered by the test, a steady state capacity of about 810, 780, and 700 mAh g_S^{-1}, and a capacity retention of about 77 %, 80 %, and 71 % at C/3, 1C, and 2C, respectively. These retention values may be likely attributed to the possible partial loss of sulfur caused by the irreversible formation of short-chained lithium polysulfides rather than to cell resistance increase.[1] To clarify this aspect, Figure 2.2.5c shows the EIS Nyquist plots of the S-Sn electrode in lithium cell performed at the OCV, after 1 cycle, and upon 100 cycles at a constant current rate of 2C. As already described during the discussion of Figure 2.2.3b, the plots were analyzed by NLLS through a Boukamp tool[45,46] and the results are shown in Table 2.2.2. Figure 2.2.5c and the results of Table 2.2.2 show a decrease in the interphase resistance (R) from a value of about 193 Ω at the OCV to 2.8 and 1.2 Ω after 1 and 100 cycles, respectively, thus confirming the effect of the above discussed activation process in stabilizing the electrode/electrolyte interphase. In summary, Figure 2.2.5 shows a very suitable cell performance in terms of cycle life, cell stability, and delivered capacity, particularly relevant at the high currents and a remarkable electrode/electrolyte interphase stability, thus suggesting the S-Sn material for application in high-performance Li-S batteries.

Cell condition	Circuit	R_1 (Ω)	R_2 (Ω)	$R= R_1+R_2$ (Ω)	χ^2
OCV	$R_e(R_1Q_1)Q_w$	192.8 ± 1.7	/	192.8 ± 1.7	4.4×10^{-4}
1 cycle at 2C	$R_e(R_1Q_1)(R_2Q_2)Q_w$	1.6 ± 0.1	1.2 ± 0.1	2.8 ± 0.1	1.0×10^{-4}
100 cycles at 2C	$R_e(R_1Q_1)(R_2Q_2)Q_w$	0.7 ± 0.05	0.5 ± 0.05	1.2 ± 0.05	1.0×10^{-4}

Table 2.2.2 NLLS analyses performed on the impedance spectra of Figure 2.2.5c, recorded upon galvanostatic cycling at the constant current rate of 2C of the S-Sn composite in the lithium cell.

To investigate the structural changes of the S-Sn material during the electrochemical process, Figure 2.2.6 reports an *ex situ* XRD study performed on the electrode upon one cycle in lithium cell at C/10. Figure 2.2.6a shows the voltage profile of the above cycle in which the states of charge corresponding to the XRD measurements are indicated by P1 (OCV) and P2 (after charge), while the related patterns are displayed in Figure 2.2.6b. The XRD of the electrode at the pristine state (black pattern in Figure 2.2.6b) clearly exhibits the reflections of sulfur and tin, as already observed for the material powder in Figure 2.2.1, with additional very broad signal between 20° and 30° due to the GDL carbon matrix used as the support.[22] This pattern confirms the expected retention of the S-Sn structure upon deposition on GDL support through doctor blade casting (see *2.2.2* Experimental

section). Relevantly, the XRD of the electrode collected from the cell after the whole cycle (orange pattern in Figure 2.2.6b) shows the diffraction peaks of Sn without significant changes, thus suggesting mechanical stability of the electrode and retention of the metal structure despite its relatively low mass ratio (*i.e.*, 20 %). Furthermore, the patterns upon one galvanostatic cycle show the reflections ascribed to sulfur and possibly to crystalline polysulfide species, which appear, however, broader and less intense with respect to the pristine electrode. This trend may be likely ascribed to an incomplete conversion during the charge of the lithium polysulfides formed by the initial discharge, as well as to the possible partial formation of amorphous sulfur instead of crystalline one.[56]
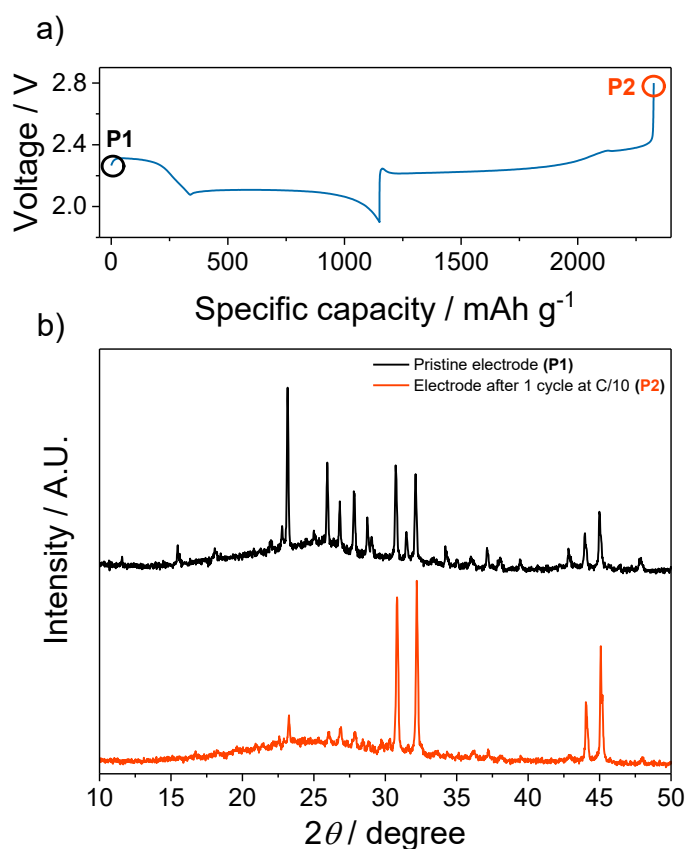
Figure 2.2.6. *Ex situ* XRD study of the S-Sn electrode upon cycling in lithium cell. **(a)** Voltage profile of one galvanostatic cycle performed at C/10: the states of charge corresponding to XRD measurements are indicated by the labels P1 (before cycling, OCV of the cell) and P2 (after the whole discharge/charge cycle). **(b)** *Ex situ* XRD patterns of the S-Sn electrode at the pristine state (black) and after the above galvanostatic cycle (orange). Voltage limits 1.9–2.8 V.

Hence, the above test clearly indicates the electrode reversibility and structural retention and suggests possible presence of dissolved polysulfide in the electrolyte at the electrode surface or in its proximity, even at the charged state of the cell. Furthermore, the patterns of Figure 2.2.6b exclude the formation of crystalline sulfides such as SnS_2 due to the absence of relevant signals indicating additional compounds and clearly show the retention of the metallic structure of the tin by cycling. However, partial electrolyte oxidation and minor loss of the active sulfur during the electrochemical process by polysulfide migration and direct reaction with the anode cannot be completely excluded.[57] These side reactions may actually contribute to the partial capacity fade observed in Figure 2.2.5. Hence, these important aspects certainly require further experiments to be fully clarified, including different electrode formulations and electrolyte compositions.

2.3 Enhanced Sn and Ni-enriched sulfur nanocomposites

2.3.1 Presentation

The study carried out in the previous section *2.2* demonstrated the suitability of a sulfur-tin nanocomposite supported on a carbon-cloth support (GDL) for application in lithium battery, where the high conductivity of metal nanoparticles allowed use of relevant active material amount (as high as 80wt% of sulfur in the composite). Beside the enhanced conductivity, sulfur–metal electrodes might possibly benefit from a higher expected tap density as compared to composite materials using porous carbon matrices[30,41,58,59] as well as by a simple preparation pathway. Hence, a comprehensive investigation of sulfur–metal composites may be worthwhile in order to shed light on the effect of nanoparticles on the multiphase sulfur conversion process in lithium cells. Accordingly, in the following section *2.3* an extended description of the electrochemical reorganization occurring in the positive electrode is provided by means of various experimental techniques. New electrode formulations including either tin or nickel nanometric powders and increasing the sulfur weight ratio to a value as high as 85% are considered. As seen in section *2.1*, X-ray computed tomography can be employed to reconstruct a three-dimensional representation of the electrode to actually observe the microstructural features of the sample and reveal substantial correlation between electrode design and electrochemical performance. Thus, the new materials are thoroughly described, including their electrochemical evolution in cells and the reaction kinetics through an interdisciplinary approach combining various experimental techniques, namely, X-ray computed tomography at the micro- and nanoscales, X-ray diffraction, electron microscopies, energy-dispersive X-ray spectroscopy, cyclic voltammetry, and electrochemical impedance spectroscopy. In particular, high-resolution tomographic datasets may elucidate the remarkable microstructural reorganization occurring upon reversible sulfur conversion in the battery (the above mentioned *activation* process) by enabling the three-dimensional reconstruction of the electrode.[13] Moreover, in-depth diffraction, microscopy, and electrochemical analyses may shed light on the evolution of the crystal structure, morphology, reaction potential, and electrode kinetics.

2.3.2 Experimental

Nanocomposites were prepared by physically mixing elemental sulfur (≥99.5 %, Riedel-de Haën) with either tin (<150 nm, Sigma-Aldrich, ≥99 % trace metal basis) or nickel (<100 nm, Sigma-Aldrich, ≥99 % trace metal basis) powders in a weight ratio of 85:15. The mixtures were heated in a

silicon oil bath at 120 °C under magnetic stirring until the complete melting of sulfur and subsequently quenched at room temperature until sulfur solidification. The materials thus obtained were ground in an agate mortar to obtain fine powders, which are represented as S:Sn 85:15 w/w and S:Ni 85:15 w/w.

The crystal structure of the nanocomposites was studied by XRD by means of a Bruker D8 ADVANCE diffractometer equipped with a Cu-Kα source by performing a scan in the 2θ range between 10° and 90° at a rate of 10 s per step with a step size of 0.02°. Powder morphology was obtained by scanning and transmission electron microscopies (SEM and TEM, respectively) through a Zeiss EVO 40 microscope with a LaB_6 thermionic electron gun and a Zeiss EM 910 microscope with a tungsten thermionic electron gun operating at 100 kV, respectively. The elemental distribution in the composites was determined by collecting EDS maps via the X-ACT Cambridge Instruments analyzer of the SEM equipment. Selected area electron diffraction (SAED) data were obtained from the abovementioned TEM.

The S:Sn 85:15 w/w and S:Ni 85:15 w/w powders were investigated by X-ray nano-CT by means of a Zeiss Xradia 810 Ultra instrument (Carl Zeiss Inc.) equipped with a microfocus rotating Cr anode with characteristic energy at 5.4 keV (Cr-Kα, MicroMax-007HF, Rigaku) set at 35 kV and 25 mA. The instrument had a capillary condenser located in a He-filled chamber concentrating the quasi-monochromatic and quasi-parallel X-ray beam onto the sample, a pinhole blocking the unwanted scattered X-rays from the sample stage, and a zone plate in a He-filled optics chamber that focused the X-ray beam on a CCD detector. Nano-CT scans were obtained in the X-ray absorption-contrast and large-field-of-view (65 mm) modes with 1 voxel binning by taking 1601 projections through 180° with exposure times of 46 and 55 s for S:Sn 85:15 w/w and S:Ni 85:15 w/w, respectively, thereby leading to a voxel size of about 63 nm. The nano-CT samples were prepared by attaching a small amount of powder on stainless steel (SS) needles by an epoxy glue [2,4,6-tris(dimethylaminomethyl)phenol, Devcon] with the support of an optical microscope. The tomographic datasets were reconstructed by the Zeiss XM reconstruction software (Carl Zeiss Inc.) by employing a filtered back-projection algorithm. The nano-CT data were processed by applying nonlocal means and unsharp masking filters and then getting segmented and imaged by using Avizo 2019.2 (Visualization Sciences Group, FEI Company). Three domains with increasing X-ray attenuations were identified by employing a grayscale threshold method:[14,17] *i)* exterior, *ii)* sulfur, and *iii)* metal nanoparticles.

Two composite electrodes were made by mixing the S:Sn 85:15 w/w or S:Ni 85:15 w/w powders (80wt%), Super P carbon as the conducting agent (10wt%, Timcal), and polyvinylidene fluoride (PVDF) as the binder (10wt%, Solef 6020, Solvay). The components were dispersed in *N*-

methyl-2-pyrrolidone (NMP, Sigma-Aldrich) to obtain a uniform slurry that was cast onto a carbon-cloth foil (GDL, ELAT 1400, MTI Corp.) by means of a doctor blade. The cast slurries were heated to 50 °C for about 3 h to remove the solvent and subsequently cut into 14 mm-diameter disks by using a punch. The electrode disks were dried at 45 °C under a vacuum overnight to eliminate the residual solvent and water traces; then, they were stored in an Ar-filled glovebox (MBraun, O_2 and H_2O content below 1 ppm). Two electrode batches with sulfur loading of about 2 mg cm^{-2} and within 6 and 7 mg cm^{-2}, respectively, were prepared for each sulfur–metal nanocomposite by properly adjusting the coating thickness (about 500 and 700 mm, respectively) as well as the solvent quantity.

CR2032 coin cells (MTI Corp. and Hohsen Corp.) were assembled in an Ar-filled glovebox (MBraun, O_2 and H_2O content below 1 ppm) by stacking a composite electrode, a Celgard 2400 separator filled by either 50 μL (sulfur loading: ~2 mg cm^{-2}) or 80 μL (sulfur loading: within 6 and 7 mg cm^{-2}) of electrolyte solution, and a 14 mm-diameter lithium disk. Cells for *ex situ* characterization were prepared by employing moderately low pressure than usual in order to facilitate disassembly after the tests. The electrolyte solution was prepared by dissolving lithium bis(trifluoromethanesulfonyl) imide (LiTFSI, 99.95% trace metals basis, Sigma-Aldrich) and lithium nitrate (LiNO$_3$, 99.99% trace metals basis, Sigma-Aldrich) in a mixture of 1,3-dioxolane (DOL, anhydrous, containing ca. 75 ppm of butylated hydroxytoluene, i.e., BHT, as inhibitor, 99.8%, Sigma-Aldrich) and 1,2-dimethoxyethane (DME, anhydrous, inhibitor-free, 99.5%, Sigma- Aldrich) in a weight ratio of 1:1. The final salt concentration with respect to the solvent mass was 1 mol kg^{-1} for LiTFSI and either 1 or 0.4 mol kg^{-1} for LiNO$_3$. The composition of DOL:DME 1:1 w/w, 1 mol kg^{-1} LiTFSI, and 1 mol kg^{-1} LiNO$_3$ was used for all the electrochemical measurements, while the composition of DOL:DME 1:1 w/w, 1 mol kg^{-1} LiTFSI, and 0.4 mol kg^{-1} LiNO$_3$ was employed for the *ex situ* characterization.

The electrochemical behaviors of the S:Sn 85:15 w/w and S:Ni 85:15 w/w electrodes in lithium cells were investigated by coupling the CV and EIS data. CV measurements were carried out within the 1.8 – 2.8 V *vs* Li$^+$/Li range at a constant scan rate of 0.1 mV s^{-1}. The impedance spectra were recorded upon voltammetry cycling, namely, under the open-circuit voltage (OCV) condition, after 1, 5, and 10 cycles by applying an alternating voltage signal (amplitude: 10 mV; frequency range: within 500 kHz and 100 mHz) to the cell. The impedance spectra were analyzed to evaluate the electrode/electrolyte interphase resistances by using the Boukamp software according to the nonlinear least-squares (NLLS) method.[45,46] The EIS responses were modelled by the $R_e(R_1Q_1)(R_2Q_2)Q_w$ equivalent circuit, where R_e represents the electrolyte resistance, R_iQ_i (i = 1, 2) elements correspond to the electrode/electrolyte interphase resistance and pseudocapacitance at high-intermediate frequencies (including passivation films and charge transfer), and Q_w represents a low-

frequency Li$^+$ diffusion process.[45,46] Here, χ^2 values of the order of 10^{-4} to 10^{-5} and low estimation errors with regard to the resistances (see Tables 2.3.1 and 2.3.2) suggest the accuracy of the analyses.

CV data at various scan rates, i.e., 0.05, 0.1, 0.15, 0.2, and 0.25 mV s^{-1}, within the 1.8 – 2.8 V *vs* Li$^+$/Li range were obtained to estimate the apparent Li$^+$ diffusion coefficient (D) upon the electrochemical reaction according to the Randles–Sevcik equation (2.3.1):[60,61]

$$I_p = 0.4463zFAC \left(\frac{zFvD}{RT}\right)^{\frac{1}{2}} \tag{2.3.1}$$

where I_p is the peak current (A), z is the number of exchanged electrons, F is the Faraday constant (96 485 C mol^{-1}), A is the geometric area of the electrodes (1.54 cm^2), C is the estimated volumetric concentration of Li$^+$ in the electrode volume (mol cm^{-3}), v is the scan rate (V s^{-1}), D is the diffusion coefficient (cm^2 s^{-1}), R is the gas constant (8.31451 J mol^{-1} K^{-1}), and T is the temperature (298 K). The CV and EIS measurements were performed by a VersaSTAT MC Princeton Applied Research (PAR) analyzer.

The electrochemical performances of the S:Sn 85:15 w/w and S:Ni 85:15 w/w nanocomposites in the lithium cell were assessed by galvanostatic cycling at various current rates (C/*x*), where 1C rate is 1675 mA g$_S^{-1}$ as referred to the sulfur mass in the electrode. These measurements were performed by using a MACCOR series 4000 battery test system. Li|DOL:DME 1:1 w/w, 1 mol kg^{-1} LiTFSI, and 1 mol kg^{-1} LiNO$_3$|cathode cells with sulfur loading of about 2 mg cm^{-2} were tested at constant rates of C/3, 1C, 2C, and 3C over 100 cycles by adjusting the voltage range to 1.9 – 2.8 V for C/3 and 1C rates and 1.8 – 2.8 V for 2C and 3C rates. Li|DOL:DME 1:1 w/w, 1 mol kg^{-1} LiTFSI, and 1 mol kg^{-1} LiNO$_3$|cathode cells with high sulfur loading (6.8 and 6.3 mg cm^{-2} for S:Sn 85:15 w/w and S:Ni 85:15 w/w, respectively) were cycled at a constant current rate of C/20 within the voltage range of 1.9 – 2.8 V. Two rate capability tests for each Li|DOL:DME 1:1 w/w, 1 mol kg^{-1} LiTFSI, and 1 mol kg^{-1} LiNO$_3$|cathode cell (sulfur loading: ~2 mg cm^{-2}) were carried out by increasing the current rate every 5 cycles from C/10 to 2C and from 1C to 10C and decreasing the current to the initial values after 35 cycles. In detail, the cells were tested at C/10, C/8, C/5, C/3, C/2, 1C, 2C, 3C, 4C, 5C, 8C, and 10C rates within the voltage ranges of 1.9 – 2.8 V (from C/10 to C/2) and 1.8 – 2.8 V (from 1C to 10C). Galvanostatic cycling tests of the S:Sn 85:15 w/w and S:Ni 85:15 w/w cathodes over about 300 cycles were carried out on Li|diethylene glycol dimethyl ether (DEGDME, 99.5%, Sigma-Aldrich), 1 mol kg^{-1} LiTFSI, and 1 mol kg^{-1} LiNO$_3$|cathode cells with sulfur loading of about 2 mg cm^{-2}. The cells were cycled at a 1C rate within the voltage range of 1.8 – 2.8 V.

The S:Sn 85:15 w/w and S:Ni 85:15 w/w electrodes were investigated before and after cycling by combining XRD, SEM, SEM-EDS, and X-ray micro-CT measurements. The electrodes were galvanostatically cycled in Li|DOL:DME 1:1 w/w, 1 mol kg^{-1} LiTFSI, and 0.4 mol kg^{-1} LiNO$_3$|cathode cells at a C/3 rate within the voltage range of 1.9 – 2.8 V through a MACCOR model 4300 battery test system. The cells were disassembled in an Ar-filled glovebox (MBraun, O$_2$ and H$_2$O content below 1 ppm); the cathodes were recovered and dried under a vacuum for 30 min in the glovebox antechamber. The electrode samples were exposed to the atmosphere when performing the XRD, SEM, SEM-EDS, and micro-CT measurements. The XRD patterns were collected through a Rigaku SmartLab instrument equipped with a Cu-Kα source by performing a scan in the 2θ range between 10° and 90° at a rate of 0.4° min^{-1} with a step size of 0.01°. SEM and SEM-EDS images were collected by means of a Zeiss EVO MA10 equipped with a tungsten thermionic electron gun and INCA X-ACT analyzer from Oxford Instruments.

X-ray micro-CT datasets were obtained from a Zeiss Xradia 520 Versa instrument (Carl Zeiss Inc.) employing a polychromatic microfocus source (tungsten target) set at 80 kV and 88 mA. The micro-CT samples were prepared by cutting out a 1 mm-size square from each electrode and attaching the specimen to a SS dowel by an epoxy glue [2,4,6-tris(dimethylaminomethyl)phenol, Devcon]. Source and detector distances from the sample stage and X-ray exposure time were adjusted in order to obtain suitable transmission values. Tomographic datasets were collected by using a 20× objective lens and taking 1601 projections through 360° with an exposure time from 22 to 40 s and 1 voxel binning. The experimental conditions led to a voxel size ranging from 288 to 373 nm and a field of view from about 570 to about 730 mm. The tomographic datasets were reconstructed by the scout-and-scan control system reconstruction software (Carl Zeiss Inc.) employing a filtered back-projection algorithm. The micro-CT data were processed by applying nonlocal means and unsharp masking filters and then segmented, imaged, and analyzed by using Avizo 2019.2 (Visualization Sciences Group, FEI Company). The adopted voxel size allowed the identification of five domains with increasing X-ray attenuations by employing a grayscale threshold method:[14,17] *i)* exterior, *ii)* carbon/binder/carbon cloth, *iii)* isolated sulfur, *iv)* sulfur–metal nanoparticle intimate mixture, and *v)* isolated metal domain. Binary datasets were produced after segmentation to evaluate the particle size distribution (PSD) of the domain formed by isolated sulfur and intimate mixture of sulfur and metallic nanoparticles. In detail, the sulfur and sulfur–metal nanoparticle intimate mixture domains (*iii* and *iv*) were merged into a single segmentation phase, which was processed by particle separation tools by Avizo 2019.2 (Visualization Sciences Group, FEI Company) and analyzed by XLib, an ImageJ software plug-in.[19] The sphericity (shape factor) of the particles was calculated by using equation (2.3.2):

$$(Sphericity) = \pi^{\frac{1}{3}} \frac{(6V)^{\frac{2}{3}}}{A}$$

(2.3.2)

where V and A are the estimated volume and surface of the particles, respectively.

All the measurements were carried out at 25 °C.

2.3.3 Results

Microstructural characteristics of the sulfur–metal nanocomposites are shown in Figure 2.3.1 and 2.3.2; they were obtained by combining the XRD, nano-CT, electron microscopy, and EDS data. The XRD patterns (Fig. 2.3.1) reveal the structural features of elemental sulfur and metal nanoparticles in both the samples, thereby suggesting the absence of impurities formed by parasitic reactions during the synthesis process,[38,62] such as metal sulfides, which might affect the electrochemical process in lithium cells.[35] These results suggest the mild-temperature mixing of sulfur and metallic nanopowders as a suitable approach for achieving pure nanocomposite materials, possibly benefiting from the dispersion of electronically conductive and crystalline tin and nickel particles within the sulfur matrix.[33,63] Fig. 2.3.2 shows the nanocomposite morphology formulated from the SEM-EDS, TEM, and X-ray nano-CT data for S:Sn 85:15 w/w and S:Ni 85:15 w/w. The former is mostly composed of nanometric tin particles (≤ 200 nm; inset in panel a shows the secondary electron image) that form 5–40 mm micrometric agglomerates, visible as bright domains in the backscattered-electrons image of panel a as well as the EDS map in panel c. Metallic tin is surrounded by a sulfur phase, observed in both panel a (as a dark-gray matrix) and EDS image of panel b. With regard to the latter sample, the secondary electron image (inset of panel d) indicates the presence of primary Ni particles ranging from about 100 nm to about 1 mm, which are arranged into secondary structures (ranging from 50 to 100 mm) beside micrometric sulfur, as shown by the backscattered-electrons and EDS images in panels d–f. Furthermore, panels g–n show rather different morphologies of the sulfur–metal agglomerates at the nanoscale, suggesting more intimate mixing between the two phases for S:Sn 85:15 w/w with respect to S:Ni 85:15w/w. TEM and X-ray nano-CT data may provide qualitative information on the sample composition as the density of the various phases forming the composite are directly reflected into the attenuation coefficient of the incident beam.[14] Accordingly, the relevant differences in the sulfur and metal densities (2.07, 7.31, and 8.9 g cm^{-3} at 25 °C for S, Sn, and Ni, respectively)[15] allow unambiguous phase identification: metal particles/agglomerates are, therefore, observed in the TEM images (Fig. 2.3.2g and k) and X-ray nano-CT reconstructions (Fig. 2.3.2h, l) as highly attenuating domains (dark and bright particles, respectively); however, sulfur

60

exhibits relatively low attenuation (gray phase in both TEM and X-ray nano-CT images). Interestingly, electron microscopy and X-ray tomography data successfully reveal that for S:Sn 85:15 w/w, the tin particles and aggregates are embedded into a sulfur matrix (Fig. 2.3.2g), which is a promising morphological feature for yielding suitable electrode performance, particularly at higher current rates, as observed in section *2.2*. On the other hand, S:Ni 85:15 w/w is formed by bigger and segregated metallic clusters beside micrometric sulfur particles (Fig. 2.3.2k), thereby suggesting a possibly lower rate capability mostly due to increased average electron paths.[63] The nano-CT datasets have been segmented based on the X-ray attenuation by using a grayscale threshold method,[14,17] as shown by the slices in panels h, i, l and m in Fig. 2.3.2, where the exterior, sulfur, tin, and nickel are depicted in black, yellow, blue, and green, respectively. Hence, the segmented volume renderings of a single sulfur–metal agglomerate shown in panels j and n with the related insets reporting only the metal domains clearly show that tin is mostly embedded within the sulfur phase, while nickel is hosted on the surface. Moreover, the SAED insets of panels g and k confirm the crystalline nature of metals in agreement with the XRD data.[39,64] The in-depth material characterization discussed above (by using XRD, electron microscopy, and X-ray nano-CT methods) advantageously reveals a detailed sketch of the composite microstructure, which is expected to strongly affect the electrode behavior in lithium cells according to a complex Li–S conversion mechanism.
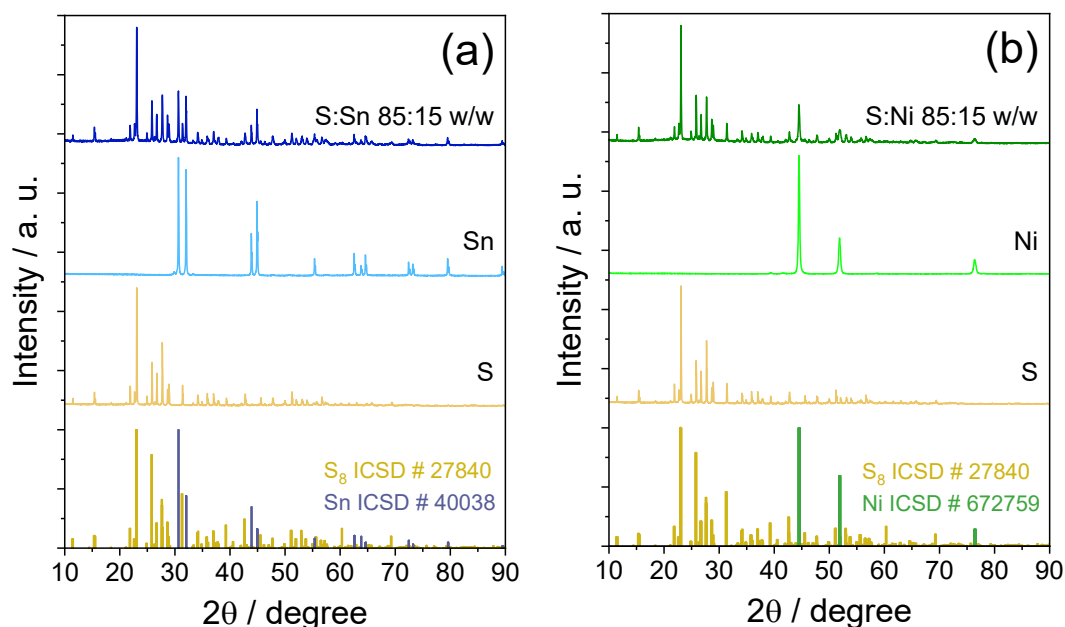
Figure 2.3.1. XRD patterns of the S:Sn 85:15 w/w and S:Ni 85:15 w/w powders as well as the related components: **(a)** S:Sn 85:15 w/w composite (blue), tin (light blue) and sulfur (yellow); **(b)** S:Ni 85:15 w/w composite (green), nickel (light green) and sulfur (yellow). Reference data for elemental sulfur (yellow bars, ICSD # 27840), metallic tin (blue bars, ICSD # 40038) and metallic nickel (green bars, ICSD # 672759).
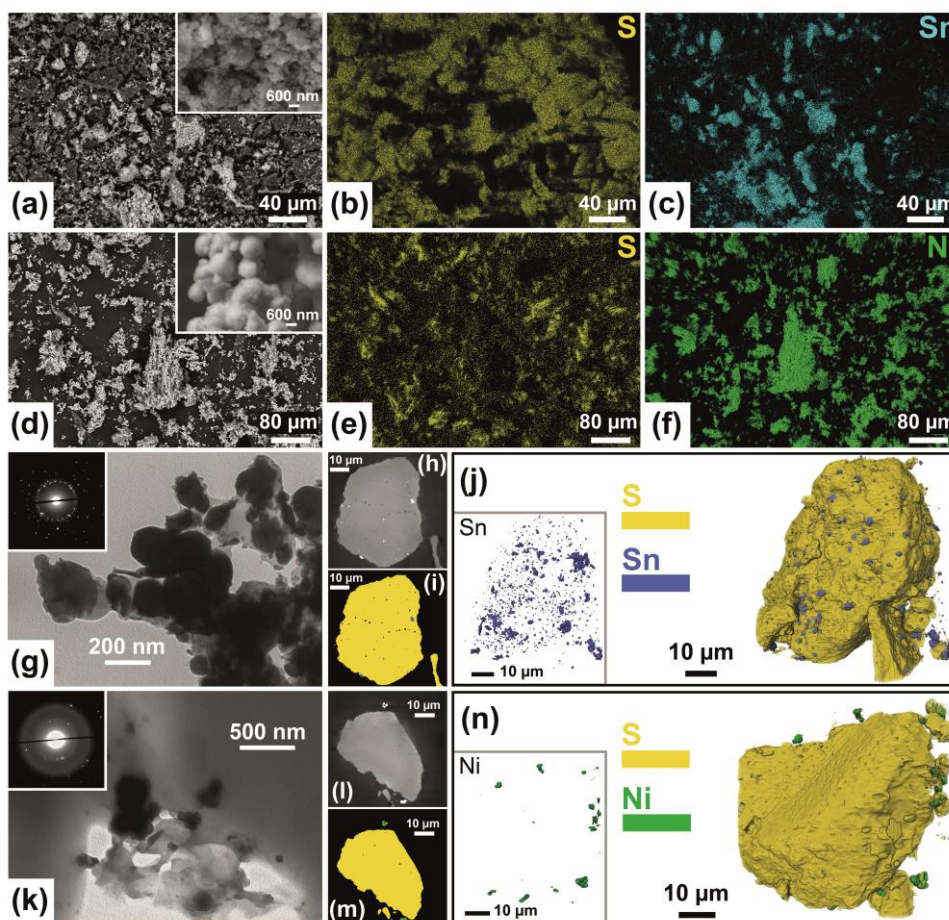
Figure 2.3.2. Electron and X-ray microscopy study of the composite powders. In detail: **(a, d)** SEM images of **(a)** S:Sn 85:15 w/w and **(d)** S:Ni 85:15 w/w (insets show magnified views), and (**(b, c)** and **(e, f)**) corresponding EDS elemental maps of **(b, e)** sulfur, **(c)** tin, and **(f)** nickel; **(g, k)** TEM images of **(g)** S:Sn 85:15 w/w and **(k)** S:Ni 85:15 w/w (insets show the corresponding SAED patterns); (**(h–j)** and **(l–n)**) X-ray nano-CT study of **(h–j)** S:Sn 85:15 w/w and **(l–n)** S:Ni 85:15 w/w in terms of **(h, l)** slices extracted in the yz plane (X-ray attenuation depicted through grayscale), **(i, m)** corresponding three-phase segmentation (S: yellow; Sn: blue; Ni: green; exterior: black), and **(j, n)** segmented volume rendering including and (inset) excluding the S phase (S: yellow; Sn: blue; Ni: green).

CV and EIS upon discharge/charge cycles are employed to determine the reaction potentials and electrode kinetics in a Li–S cell using a typical ether-based electrolyte comprising LiTFSI and LiNO₃ salts dissolved in a DOL/DME mixture. Fig. 2.3.3 shows the voltammograms obtained at a scan rate of 0.1 mV s⁻¹ for S:Sn 85:15 w/w (panel a) and S:Ni 85:15 w/w (panel b), revealing well-defined reduction and oxidation peaks as well as overlapping profiles over 10 cycles. This figure indicates the reversible electrochemical processes characterized by remarkable stability, while a slightly different CV response during the first cathodic and anodic scans suggests electrode reorganizations promoted by the multiphase reaction mechanism along with the formation of an adequate electrode/electrolyte interphase.[13] In detail, the first reduction is characterized by the presence of two peaks at about 2.25 and 2.00 V *vs* Li⁺/Li for S:Sn 85:15 w/w and at 2.25 and 2.05 V

62

vs Li^{+}/Li for S:Ni 85:15 w/w, which can be attributed to the gradual formation of long-chain and short-chain lithium polysulfides, *i.e.*, Li_2S_x with $x \geq 6$ and $2 \leq x \leq 4$, respectively, and possibly Li_2S.[42,51,65] However, the subsequent anodic scan reveals a broad double peak between 2.30 and 2.45 V *vs* Li^{+}/Li, corresponding to the oxidation of Li_2S and lithium polysulfides with the electrodeposition of Li metal at the anode and probably S_8 at the cathode.[42] The two electrodes exhibit moderate cell polarization, suggesting low charge transfer resistance and fast kinetics of the electrochemical process.[7] A shift in the first cathodic peak to higher potential values during subsequent cycles, that is, from 2.25 to 2.35 V *vs* Li^{+}/Li, as well as the slight overvoltage decrease for the oxidation reactions further reflects the abovementioned electrode rearrangements. These phenomena have already been observed in the data presented in section *2.2*, along with an enhancement in the electrode kinetics by cycling, which leads to an increase in sulfur utilization. In this regard, EIS measurements have shown a remarkable decrease in the electrode/electrolyte interphase resistance, suggesting favorable modifications of the cathode microstructure upon the progressive lithiation of the active material and perhaps a minor irreversible reaction of the electrolyte species to form suitable electrode passivation layers.[26] In addition, the voltammograms shown in Fig. 2.3.3a and b show gradually decreasing peak currents due to cycling, which might be related to the partial loss of active material during the electrochemical process.[51] The impedance spectra obtained from the CV measurements, namely, at the OCV and after 1, 5, and 10 cycles, confirm the previous observations by revealing a massive drop in the electrode/electrolyte interphase resistance after the first cycle. Accordingly, the related Nyquist plots (Fig. 2.3.3c and d for S:Sn 85:15 w/w and S:Ni 85:15 w/w, respectively) reveal a remarkable decrease in the overlapped high-intermediate frequency semicircles after the first cycle, which reflects overall resistance values falling from 26 and 138 Ω for S:Sn 85:15 w/w and S:Ni 85:15 w/w, respectively, to about 2 Ω (see the Experimental section and Tables 2.3.1 and 2.3.2 for further details about the NLLS analysis).[45,46] It is worth noting that a higher initial electrode/electrolyte interphase resistance in S:Ni 85:15 w/w as compared to that in S:Sn 85:15 w/w may be expected considering the better nanometric metal dispersion of the latter composite indicated by the analysis shown in Fig. 2.3.2. The remarkable decrease in the resistance is in line with the beneficial electrode activation observed by CV, occurring upon the electrodissolution of elemental sulfur *via* the formation of long-chain polysulfides, subsequent precipitation of Li_2S_x species $(x \leq 2)$,[42,51,65] and sulfur electrodeposition during charging, which gradually enhances Li^{+} and electron transfers at the cathode/electrolyte interphase. In this scenario, earlier studies have demonstrated a change in the electrode morphology with respect to pristine conditions by cycling in lithium cells due to the growth of sulfur clusters during charging on the preferred sites acting as nucleation points.[13]

| Cell condition	Equivalent circuit	R_1 (Ω)	R_2 (Ω)	$R_1 + R_2$ (Ω)	χ^2
OCV	$R_e(R_1Q_1)(R_2Q_2)$	19.9 ± 0.7	5.7 ± 1.6	26 ± 2	2.0×10^{-4}
1 CV cycle	$R_e(R_1Q_1)(R_2Q_2)Q_w$	1.04 ± 0.06	0.88 ± 0.14	1.92 ± 0.2	9.9×10^{-5}
5 CV cycles	$R_e(R_1Q_1)(R_2Q_2)Q_w$	1.78 ± 0.05	0.27 ± 0.06	2.05 ± 0.11	8.3×10^{-5}
10 CV cycles	$R_e(R_1Q_1)(R_2Q_2)Q_w$	2.22 ± 0.05	0.16 ± 0.05	2.38 ± 0.10	5.3×10^{-5}

Table 2.3.1. Electrode/electrolyte interphase resistances calculated through NLLS analyses of the impedance spectra (shown in Fig. 2.3.3c), recorded upon CV (Fig. 2.3.3a) of a Li|S:Sn 85:15 w/w cell.

| Cell condition	Equivalent circuit	R_1 (Ω)	R_2 (Ω)	$R_1 + R_2$ (Ω)	χ^2
OCV	$R_e(R_1Q_1)$	137.5 ± 0.9	/	137.5 ± 0.9	5.2×10^{-4}
1 CV cycle	$R_e(R_1Q_1)(R_2Q_2)Q_w$	1.22 ± 0.04	0.80 ± 0.08	2.02 ± 0.12	5.5×10^{-5}
5 CV cycles	$R_e(R_1Q_1)(R_2Q_2)Q_w$	1.88 ± 0.05	0.36 ± 0.09	2.24 ± 0.14	6.6×10^{-5}
10 CV cycles	$R_e(R_1Q_1)(R_2Q_2)Q_w$	2.25 ± 0.05	0.24 ± 0.05	2.49 ± 0.10	5.9×10^{-5}

Table 2.3.2. Electrode/electrolyte interphase resistances calculated through NLLS analyses of the impedance spectra (shown in Fig. 2.3.3c), recorded upon CV (Fig. 2.3.3a) of a Li|S:Ni 85:15 w/w cell.

CV measurements at various scan rates were obtained to calculate the apparent value of D within the electrode according to equation (2.3.1) (Fig. 2.3.3e and f; see the *2.3.2 Experimental* section for further details).[60,61] Although the assumptions of the diffusion-limited model proposed by Randles and Sevcik[60,61] might not completely describe the complex multistep and multiphase sulfur conversion mechanism, this method has been widely employed in the literature to formulate a suitable figure of merit for the electrode reaction rate.[66–68] Herein, the linear relation of the peak current (I_p) and the square root of the scan rate ($v^{1/2}$, see Fig. 2.3.4) actually suggests an electrochemical process controlled by diffusion, which is in agreement with equation (2.3.1). Therefore, D was calculated by assigning one electron to each cathodic peak (at about 2.3 and 2.0 V *vs* Li$^+$/Li, respectively) and two electrons to the broad anodic double peak (at 2.4 V *vs* Li$^+$/Li) based on the formal reaction in the cell, i.e., $S + 2Li+ + 2e^- \rightleftarrows Li_2S$ (Table 2.3.3 shows the obtained D values). The plots of the apparent value of D as a function of the potential *vs* Li$^+$/Li reported in the

bottom panels shown in Fig. 2.3.3e and f reveal that the D values for both S:Sn 85:15 w/w and S:Ni 85:15 w/w range from 10^{-8} to 10^{-7} cm^2 s^{-1}, which gradually decrease upon discharging and subsequent charging, thereby reflecting the already observed high-power capability of the sulfur conversion to long-chain polysulfides (mostly Li_2S_8 and Li_2S_6, perhaps along with minor amounts of Li_2S_4).[69] The high apparent coefficients[66–68] observed in the voltammetry data possibly suggest a fast electrochemical process benefiting from the metal particles, which ensure low electrode/electrolyte interphase resistance and high reversibility.
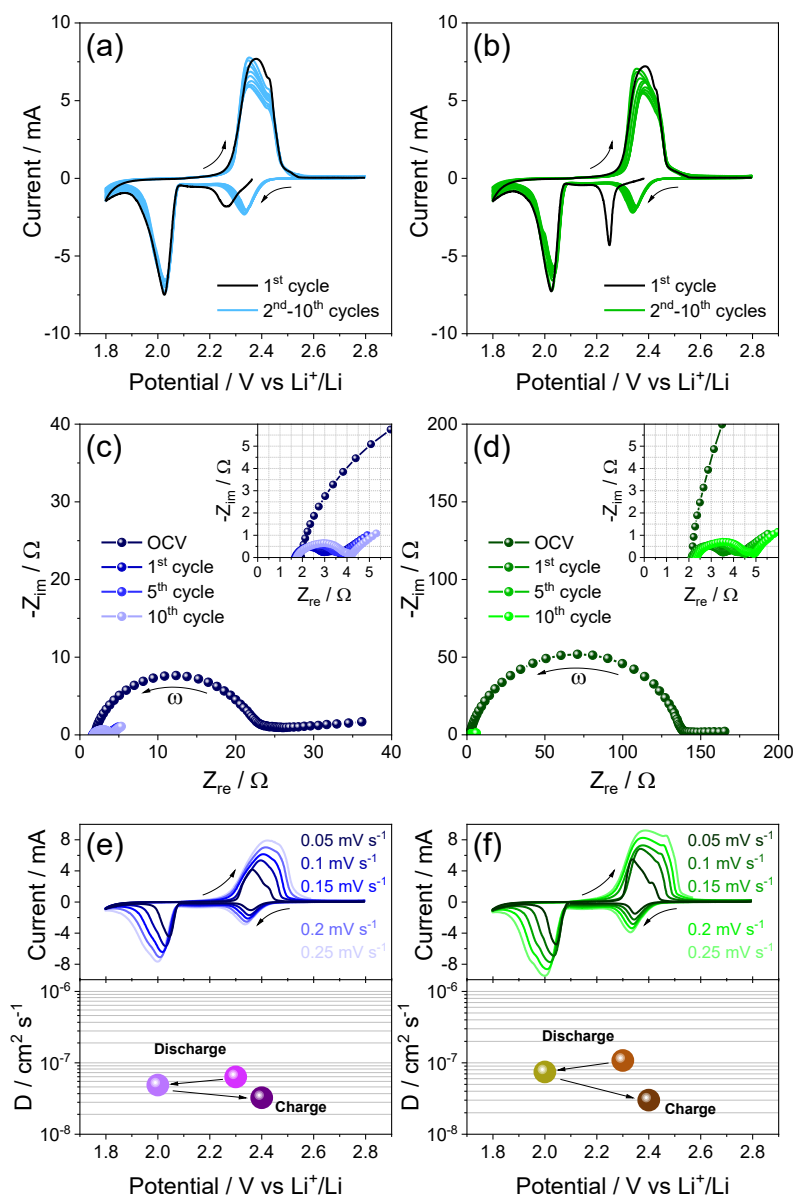
Figure 2.3.3. (a, b) CV profiles (potential range: 1.8 – 2.8 V *vs* Li$^+$/Li; scan rate: 0.1 mV s^{-1}) and **(c, d)** corresponding Nyquist plots (inset shows the magnified view) of EIS measurements performed at the OCV and after 1, 5, and 10 cycles (frequency range: 500 kHz to 100 mHz; signal amplitude: 10 mV) for Li cells using **(a, c)** S:Sn 85:15 w/w and **(b, d)** S:Ni 85:15 w/w electrodes. **(e, f)** CV profiles at various scan rates (0.05, 0.1, 0.15, 0.2, and 0.25 mV s^{-1}; potential range: 1.8 – 2.8 V *vs* Li$^+$/Li; top panels) of Li cells using **(e)** S:Sn 85:15 w/w and **(f)** S:Ni 85:15 w/w electrodes and corresponding apparent Li$^+$ diffusion coefficient (*D*) values (bottom panels) according to the Randles–Sevcik equation.[60,61]
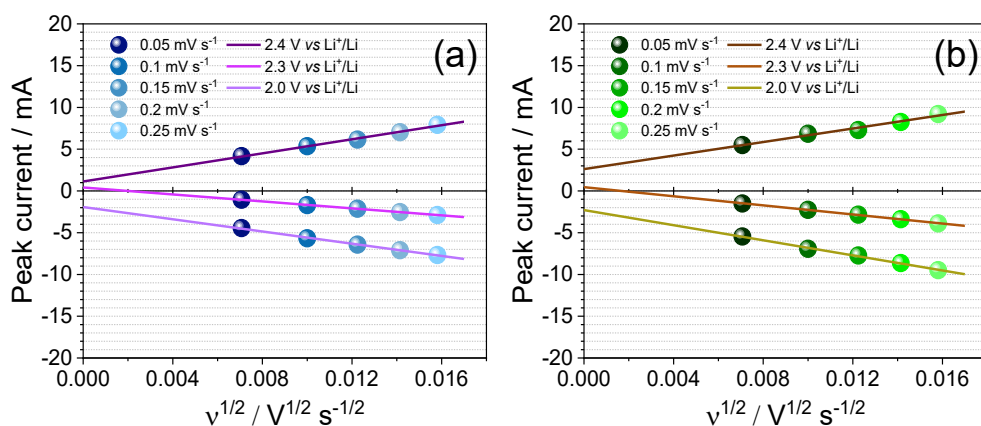
Figure 2.3.4. Peak current (I_p) vs the square root of the scan rate ($v^{1/2}$) for the voltammograms of Figure 2.3.3e-f (top panels) with related linear fits. CV measurements were performed on Li cells using the **(a)** S:Sn 85:15 w/w and **(b)** S:Ni 85:15 w/w electrodes.

| Material	State of charge	Intercept (A)	Slope (A $s^{1/2}$ $V^{-1/2}$)	*D* (cm^2 s^{-1})
	2.3 V *vs* Li$^+$/Li (disch.)	$(4.2\pm0.3)\times10^{-4}$	-0.209 ± 0.003	6.4×10^{-8}
S:Sn 85:15 w/w	2.0 V *vs* Li$^+$/Li (disch.)	$(-1.93\pm0.12)\times10^{-3}$	-0.366 ± 0.010	4.9×10^{-8}
	2.4 V *vs* Li$^+$/Li (ch.)	$(1.1\pm0.2)\times10^{-3}$	0.42 ± 0.02	3.2×10^{-8}
	2.3 V *vs* Li$^+$/Li (disch.)	$(4.5\pm0.7)\times10^{-4}$	-0.272 ± 0.006	1.1×10^{-7}
S:Ni 85:15 w/w	2.0 V *vs* Li$^+$/Li (disch.)	$(-2.3\pm0.2)\times10^{-3}$	-0.452 ± 0.014	7.5×10^{-8}
	2.4 V *vs* Li$^+$/Li (ch.)	$(2.6\pm0.4)\times10^{-3}$	0.41 ± 0.03	3.0×10^{-8}

Table 2.3.3. Li$^+$ diffusion coefficient (D) values at various states of charge for Li cells using the S:Sn 85:15 w/w and S:Ni 85:15 w/w electrodes.

The aforementioned material reorganization, occurring upon cycling and accounting for the electrochemical behavior observed in Fig. 2.3.3, is actually investigated in Figures 2.3.5 and 2.3.6 by SEM-EDS, *ex situ* XRD and X-ray micro-CT measurements performed on the S:Sn 85:15 w/w and S:Ni 85:15 w/w electrodes before and after cycling in lithium cells (see the *2.3.2 Experimental* section for further details).

Figure 2.3.5 shows the SEM-EDS images of the electrodes before and after 1 and 10 cycles. The pristine samples (panels a–f for S:Sn 85:15 w/w and panels g–l for S:Ni 85:15 w/w) are characterized by a rather uniform distribution of large micrometric sulfur particles and metal

agglomerates, while more apparent segregation is observed for S:Ni 85:15 w/w, which is in agreement with the results shown in Figure 2.3.2. Furthermore, the samples reveal homogeneous dispersions of C and F attributable to the conductive agent and PVDF binder used for electrode preparation. Secondary-electron SEM images detected with higher magnification (panels f and l) confirm the same morphological features of Figure 2.3.2 for the Sn and Ni particles. The micrographs shown in Figure 2.3.5 reveal huge morphological changes after 1 cycle (panels m–r for S:Sn 85:15 w/w and panels s–x for S:Ni 85:15 w/w), mainly exhibiting a decrease in the sulfur particle size and deposition of oxygen-containing species at the surface, which can be reasonably attributed both to the electrolyte and to the thin passivation layers. This analysis indicates the formation of large, irregular sulfur particles approaching 80 mm less intimately mixed with the other electrode components in S:Sn 85:15 w/w, while few small sulfur particles (from about 30 to about 70 mm) are detected in S:Ni 85:15 w/w. Besides the micrometric sulfur particles, EDS reveals the homogenous dispersion of elemental S over the samples, suggesting the possible presence of lithiated sulfide species over the electrode as well as submicrometric sulfur domains. The images after 10 cycles (panels y–di for S:Sn 85:15 w/w and panels ei–ji for S:Ni 85:15 w/w) show a further decrease in the average sulfur particle size, while the other electrode components appear unaltered due to cycling.

Panels a and b in Figure 2.3.6 show the XRD patterns of the S:Sn 85:15 w/w and S:Ni 85:15 w/w electrodes, respectively, in pristine condition and after 1 and 10 galvanostatic cycles at a C/3 rate. The patterns of pristine samples exhibit the expected reflections of orthorhombic sulfur (α-S$_8$, ICSD #27840) and metals (where tin and nickel references are ICSD #40038 and ICSD #672759, respectively), which is in full agreement with the already discussed XRD data on the related powders (Fig. 2.3.1), along with the broad peak centered at about 26° (2θ) due to the carbon-cloth support.[70] Notably, the XRD data after 1 and 10 cycles indicate a substantial decrease in crystallinity for the sulfur phase, while the diffraction peaks of metallic tin (panel a) and nickel (panel b) are clearly unaffected by the electrochemical process. Hence, the sulfur peaks of S:Sn 85:15 w/w are relevantly broader and less intense after 1 cycle than that in pristine conditions (panel a), thereby suggesting either an incomplete conversion during charging or perhaps a deposition of amorphous - rather than crystalline – sulfur, which is in complete agreement with the decrease of sulfur particles size observed in Figure 2.3.5.[56] Such a loss in crystallinity is even more evident in the patterns of S:Ni 85:15 w/w (panel b). After 10 cycles, these patterns reveal further minor reorganizations, namely, a marginal change in the relative peak intensities within the sulfur phase in S:Sn 85:15 w/w, which might be ascribed to the possible deposition of crystalline long-chain polysulfides after electrode drying (see the *2.3.2 Experimental* section for further details about cell disassembly), as well as a minor decrease in crystallinity for both the electrodes (see Fig. 2.2.6 in section *2.2*).
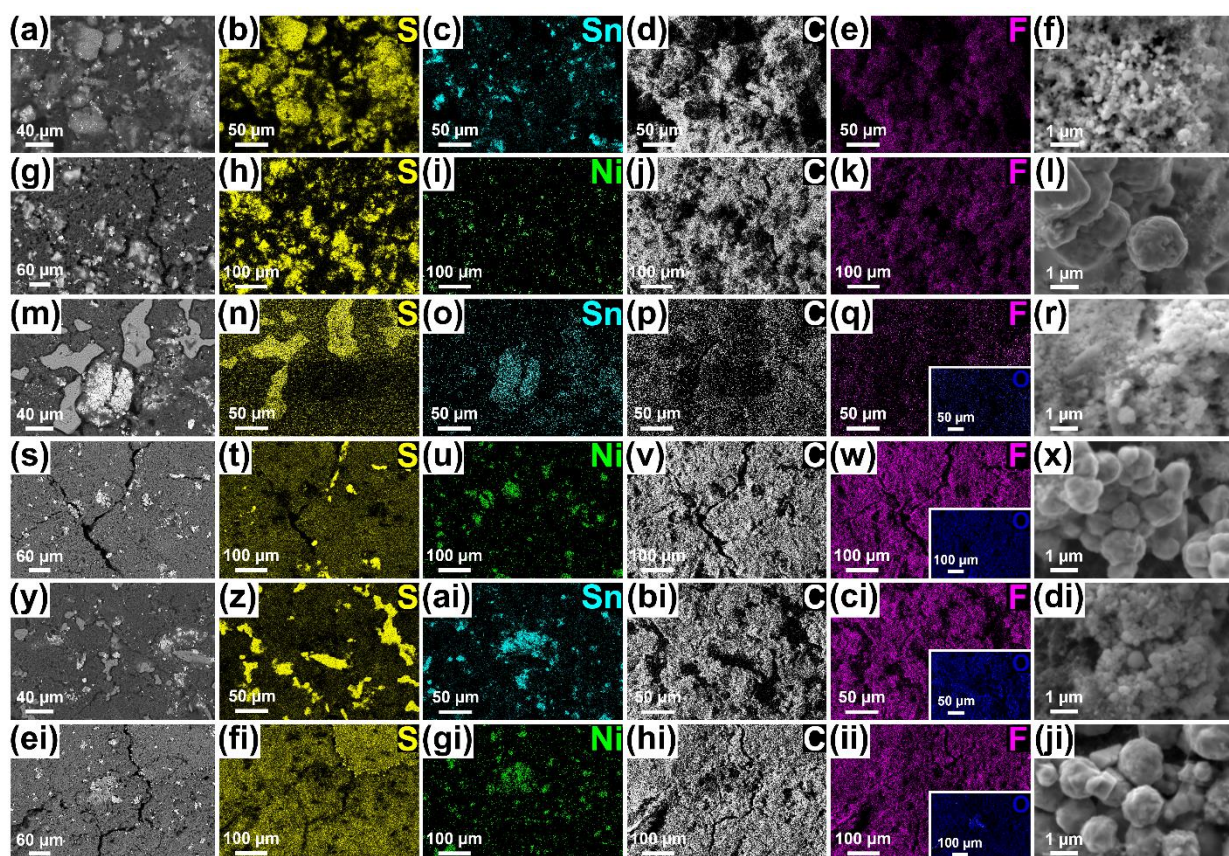
Figure 2.3.5. SEM-EDS images of the **(a-f, m-r, y-di)** S:Sn 85:15 w/w and **(g-l, s-x, ei-ji)** S:Ni 85:15 w/w electrodes **(a-l)** in the pristine state, **(m-x)** after 1 cycle, and **(y-ji)** after 10 cycles. In detail: **(a, g, m, s, y, ei, f, l, r, x, di, ji)** SEM images at different magnifications; **(b-e, h-k, n-q, t-w, z-ci, fi-ii)** EDX maps of S, Sn, Ni, C, F, and O over the electrode. Galvanostatic cycling was performed at a C/3 rate (1C = 1675 mA g_s^{-1}) and 25 °C on Li/DOL:DME 1:1 w/w, 1 mol kg^{-1} LiTFSI, 0.4 mol kg^{-1} LiNO$_3$/cathode cells employing S:Sn 85:15 w/w and S:Ni 85:15 w/w electrodes within the voltage range from 1.9 and 2.8 V.

Although SEM-EDS and XRD effectively prove the presence of significant morphological and structural changes occurring during the first cycle, X-ray CT may provide further insights into the spatial rearrangement of the various components within the bulk by three-dimensional imaging. Earlier works have investigated the Li–S process by tomography in order to reveal the morphological evolution and related degradation phenomena occurring in cells.[13,23,71,72] However, these papers have mostly focused on the fundamental characterization of the electrochemical reactions in ad hoc cell geometries using small samples of composite S–C electrodes and having a very short cycle life (a few cycles). On the other hand, the aim is to provide a comprehensive description of the cathode microstructural reorganizations in high-performance coin cells. Therefore, panels c, e, g and i in Figure 2.3.6 show the volume rendering of micro-CT datasets for S:Sn 85:15 w/w (c and g) and S:Ni 85:15 w/w (e and i) performed by using a grayscale representation, which reflects X-ray attenuation

within the sample. Metallic clusters are clearly visible in the pristine electrodes (panels c and e) as bright domains (highly attenuating phase) laid on the carbon-cloth surface (lowly attenuating phase) together with larger gray-colored sulfur particles (moderate attenuating phase) and a lowly attenuating carbon/binder mixture. Further domain with moderately high attenuation coefficient is detected in the S:Sn 85:15 w/w sample (panel c) and can be attributed to the intimate mixture between S and Sn particles, as shown in Fig. 2.3.2. In this regard, it is noteworthy that the relatively high voxel size of the micro-CT datasets (of the order of 300 nm) prevents the clear visualization of smaller S–metal agglomerates, which appear as a continuous single phase. Interestingly, the absence of a moderately high attenuating domain in S:Ni 85:15 w/w suggests the partial segregation of metal clusters, which is in agreement with the data shown in Fig. 2.3.2. Panels d and f in Figure 2.3.6 show the segmentation based on the grayscale thresholding[14,17] of cross-sectional slices extracted in a plane orthogonal to the pristine electrode surface. As per the X-ray tomography data, electrodes are formed by a dense mixture of metallic clusters and sulfur deposited over a light and highly porous carbon-cloth current collector. In addition, the data confirm the different microstructures of the S–metal agglomerates in both S:Sn 85:15 w/w and S:Ni 85:15 w/w, as already suggested by the TEM and nano-CT data, revealing a more intimate mixture for the former nanocomposite.

The X-ray images in panels g–j show that S:Sn 85:15 w/w (Fig. 2.3.6g and h) and S:Ni 85:15 w/w (Fig. 2.3.6i and j) electrodes undergo comparable microstructural reorganizations upon the first cycle, which lead to the electrodeposition of sulfur particles within the porosity of the carbon cloth as well as next to the metal clusters to form moderately high attenuating domains, i.e., S–Sn and S–Ni intimate mixtures. These observations conform with the *ex situ* SEM-EDS data (Fig. 2.3.5), showing a drop in the amount of sulfur located on the electrode surface by cycling, as well as with the earlier results on similar composite electrodes indicating sulfur migration within the carbon-based support during cycling.[23] Therefore, X-ray CT and SEM-EDS data reveal that sulfur preferably deposits *i)* close to the metal centers and *ii)* within the current-collector bulk (i.e., not in proximity to the metals). Such a remarkable rearrangement may actually account for electrochemical activation, which is unequivocally observed from the data shown in Figure 2.3.3. Apparently, sulfur electrodeposition easily occurs close to the electron-conducting surfaces, which suitably act as nucleation centers and possibly as chemisorption sites.[73] Therefore, it is reasonable to assume that newly electrodeposited sulfur has higher electric contact with the current collector than that obtainable with pristine sulfur,[73] thereby accounting for the remarkable decrease in the electrode/electrolyte interphase resistance, as shown by the EIS data (Fig. 2.3.3c and d).
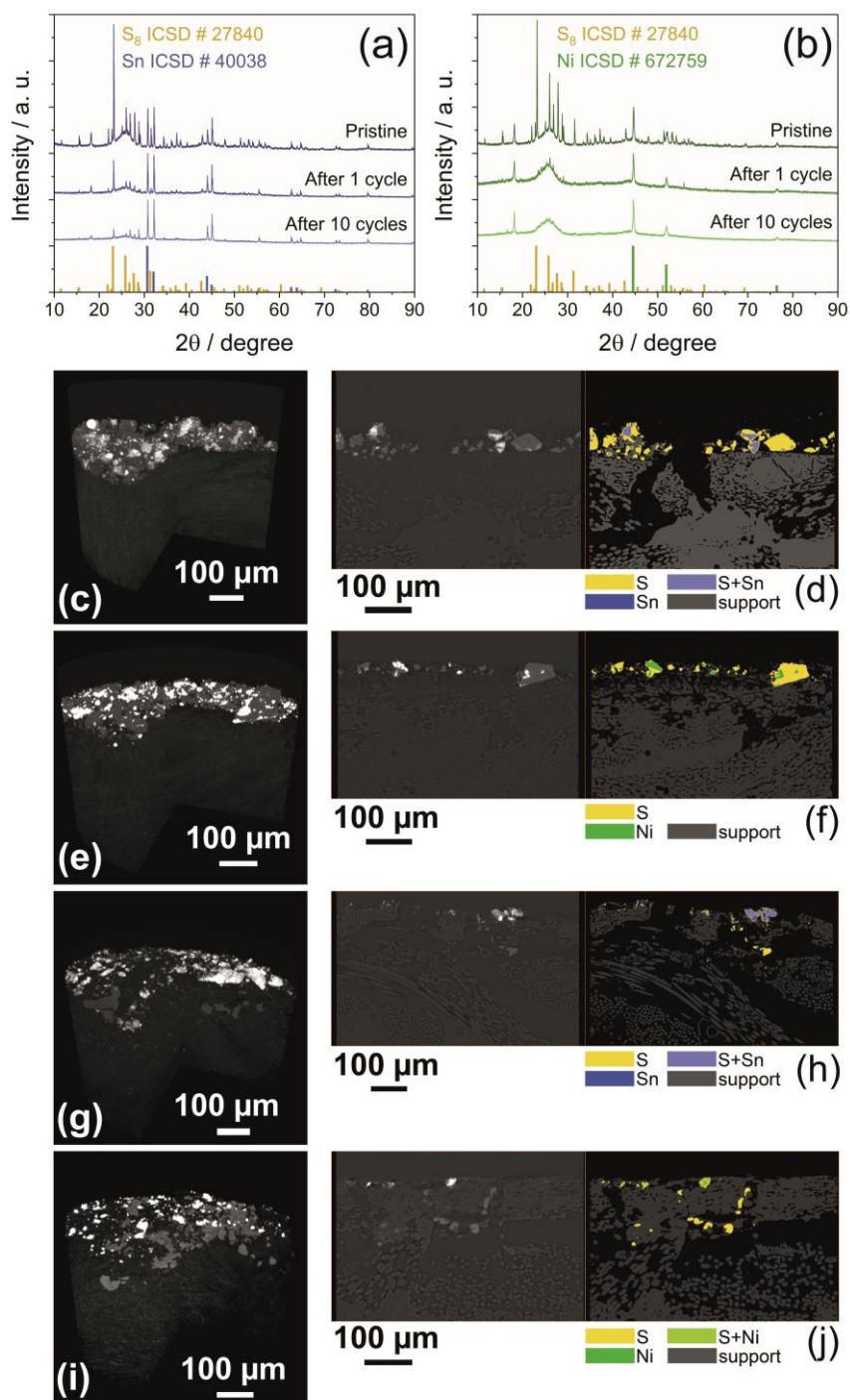
Figure 2.3.6. XRD and X-ray micro-CT analyses of S:Sn 85:15 w/w and S:Ni 85:15 w/w electrode samples before and after cycling at a constant current rate of C/3 in Li cells (voltage range: 1.9 – 2.8 V). **(a, b)** XRD patterns of **(a)** S:Sn 85:15 w/w and **(b)** S:Ni 85:15 w/w electrodes collected under the pristine condition and *ex situ* after 1 and 10 discharge/charge cycles; reference data for elemental sulfur (yellow bars, ICSD #27840), metallic tin (blue bars, ICSD #40038), and metallic nickel (green bars, ICSD #672759). **(c–j)** X-ray micro-CT analysis of ((**c, d**) and **(g, h)**) S:Sn 85:15 w/w and ((**e, f**) and **(i, j)**) S:Ni 85:15 w/w electrode samples **(c–f)** before and **(g–j)** after 1 discharge/charge cycle in terms of **(c, e, g, i)** volume rendering using grayscale (X-ray attenuation depicted through grayscale) and **(d, f, h, j)** slice extracted along a plane orthogonal to the electrode surface with corresponding segmentation (S: yellow; Sn: blue; S–Sn intimate mixture: light blue; Ni: green; S–Ni intimate mixture: light green; carbon/binder/carbon cloth: gray; exterior: black).

The X-ray micro-CT datasets were further analyzed (Figure 2.3.7) to determine the PSD of the sulfur domains along with their sphericity (shape factor), including the moderately high attenuating phase formed by the intimate mixture of sulfur and metal clusters (light blue and light green for S:Sn 85:15 w/w and S:Ni 85:15 w/w, respectively). The segmented volume renderings in panels a, c, e and g in Figure 2.3.7 show the migration of sulfur from the carbon-cloth surface in pristine condition (panels a and c for S:Sn 85:15 w/w and S:Ni 85:15 w/w, respectively) toward the support bulk after 1 cycle (panels e and g for S:Sn 85:15 w/w and S:Ni 85:15 w/w, respectively), along with the growth of the moderately high attenuating domains (light blue and light green, respectively). This suggests that sulfur electrodeposition is preferred next to Sn and Ni as well as within the carbon cloth. The related PSD analyses (Fig. 2.3.7b, d, f and h) are obtained by processing the datasets of S and S–metal mixture domains in order to obtain discrete particles approximated to spheres with equivalent radius along the x-axis. The data reveal a decreasing trend from the pristine to the cycled electrode, which is in complete agreement with the *ex situ* XRD and SEM-EDS results. However, it should be pointed out that the assumption of spherical particles represents the first approximation adopted herein to simplify the discussion, since the actual shape of these particles may significantly differ. Panels b and d in Figure 2.3.7 suggest that about 80% of the analyzed phase in both S:Sn 85:15 w/w and S:Ni 85:15 w/w is distributed within the particles of equivalent radii below 25 mm (left y-axis), while the remaining volume fraction is composed of particles slightly larger than 30 mm (right y-axis). A substantial reorganization leads to a particle size decrease after the first cycle (Fig. 2.3.7f and h) according to radius values below 17 and 15 mm for about 80% of the phase volume of S:Sn 85:15 w/w and S:Ni 85:15 w/w, respectively.

Although X-ray CT data cannot reveal the actual Li–S mechanism by detecting the various reaction intermediates, this multi-technique approach suggests an important role played by Sn and Ni clusters in the sulfur nanocomposites, as well as that of the porous current collector, for suitably enhancing the conversion reaction by steering massive microstructural rearrangement within the electrode bulk during the electrochemical process. It was observed that the metal centers and the conductive carbon-cloth support may act as preferred S nucleation sites, possibly improving the reaction kinetics. This important result is fully supported by the galvanostatic tests in lithium cells over 100 cycles at C/3, 1C, 2C, and 3C rates (1C = 1675 mA g$_s^{-1}$), as shown in Figure 2.3.8, in terms of voltage profiles (panels a and b) and cycling trends (panels c and d). The data indicate an initial capacity increase promoted by the abovementioned particle reorganization with the formation of suitable electrode/electrolyte interphases.[26,28]

71
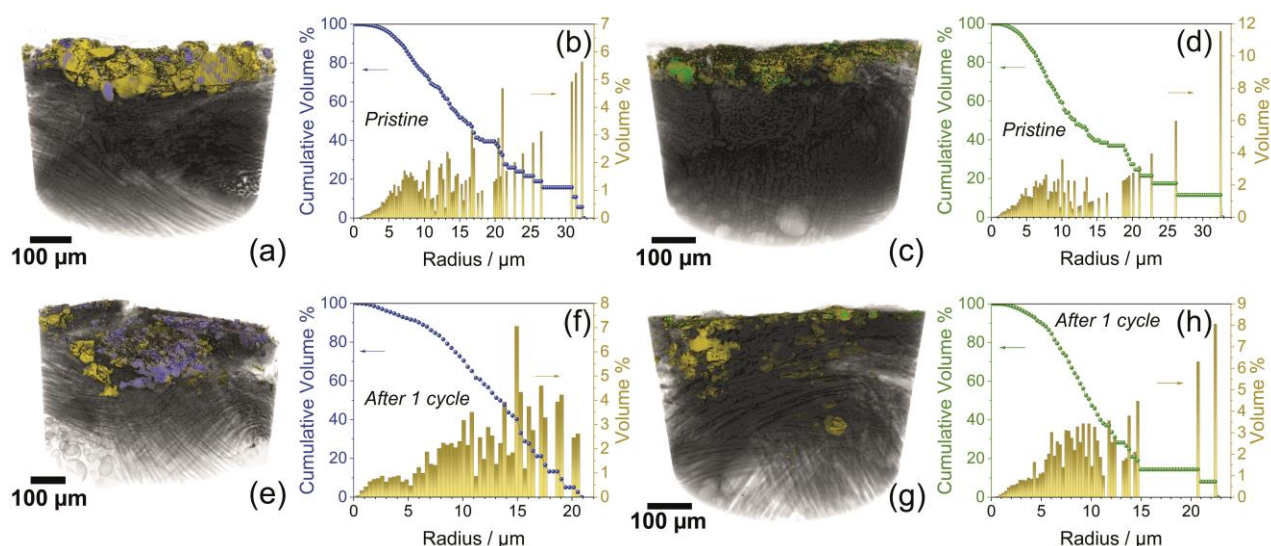
Figure 2.3.7. X-ray micro-CT analysis of (**(a, b)** and **(e, f)**) S:Sn 85:15 w/w and (**(c, d)** and **(g, h)**) S:Ni 85:15 w/w electrode samples **(a–d)** before and **(e–g)** after 1 discharge/charge cycle at a constant current rate of C/3 in Li cells (voltage range: 1.9 – 2.8 V). In detail: **(a, c, e, g)** segmented volume rendering (S: yellow; Sn: blue; S–Sn intimate mixture: light blue; Ni: green; S–Ni intimate mixture: light green; carbon/binder/carbon cloth: gray) and **(b, d, f, h)** discrete particle size distribution[19] (PSD) of the S and S–metal domains as determined by the analysis of micro-CT datasets.

This trend is more relevant in cells using S:Ni 85:15 w/w (Fig. 2.3.8b and d) rather than those using S:Sn 85:15 w/w (Fig. 2.3.8a and c) as most likely due to the less uniform mixture between S and Ni as compared to Sn in the pristine condition observed by XRD, SEM-EDS, and X-ray CT data. Therefore, cells deliver a higher reversible capacity in the subsequent cycles through voltage profiles (Fig. 2.3.8a and b) having efficient overlapping with each other, reflecting the multiphase conversion signature observed in the voltammetry data (Fig. 2.3.3). In detail, the two cells exhibit a comparable galvanostatic response characterized by two discharge plateaus at about 2.3 and 2.0 V reversed into two charge plateaus at about 2.2 and 2.4 V, as well as by low polarization that moderately increases at a higher current rate. The cycling trends for S:Sn 85:15 w/w (Fig. 2.3.8c) yield maximum reversible capacities of about 1000, 840, 820, and 600 mAh g_S^{-1} and those for S:Ni 85:15 w/w (Fig. 2.3.8d) of 1390, 960, 910, and 740 mAh g_S^{-1} at C/3, 1C, 2C, and 3C rates, respectively. Furthermore, the coulombic efficiency approaches 100% for the entire test after the first cycle and capacity retention after 100 cycles increases from about 87% and 80% at the lowest rate to values exceeding 90% at the highest rate. These responses indicate high-performing electrode materials as well as efficient mitigation of the shuttle effect by the sacrificial LiNO₃ additive,[74] thereby demonstrating the suitability of sulfur–metal composites obtained by an innovative approach advantageously replacing conventional carbon-based additives with relatively low amounts of metal nanopowders. This can increase the material density while maintaining the improved performance. Indeed, the decrease in

metal fraction as compared to that obtained in section *2.2* actually enhances both gravimetric energy density and cycling behavior, while a detailed comparative investigation of the cathode microstructural reorganizations including different metals most importantly accounts for the cell response. Notably, according to the *ex situ* measurements, the metal particles and carbon-cloth current collector lead to remarkable cell operation. In this regard, it is worth mentioning that carbon-containing woven supports may significantly improve the electrochemical performance.[69] In particular, a comparative study has revealed that a carbon-cloth support may ensure higher reversible capacity and lower polarization than those obtained from conventional aluminum owing to the enhanced charge transfer at the electrode/electrolyte interphase.[22] This beneficial effect can be attributed to the better electric contact of the active material particles with the current collector, as well as higher electrode wetting enabled by the relevant porosity and favorable chemical nature of the carbon cloth.[22]
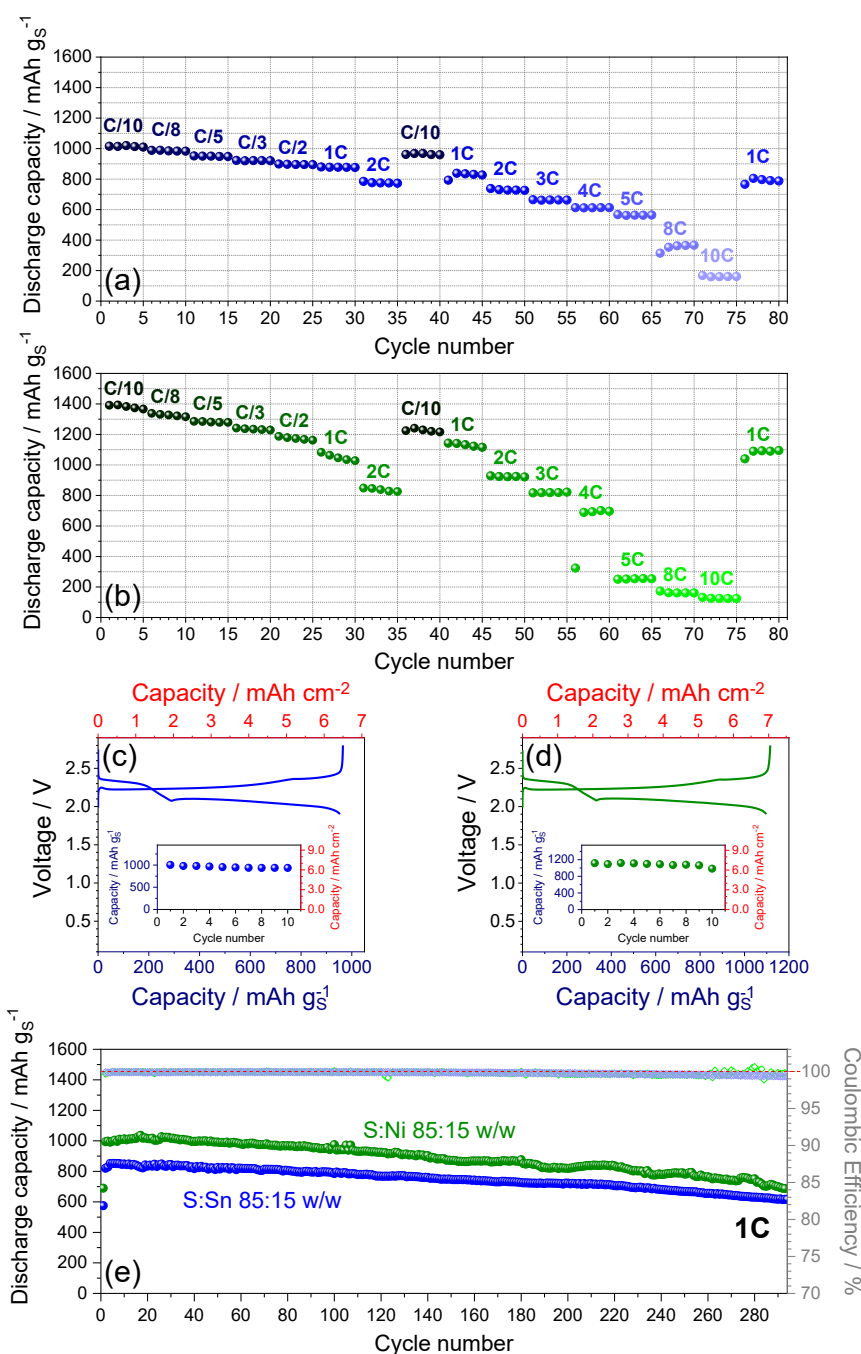
Although both S:Sn 85:15 w/w and S:Ni 85:15 w/w nanocomposites demonstrate high performances in the optimized cell configuration adopted in this study, the latter material exhibits higher capacity values, particularly at the relatively low rate of C/3, although with more pronounced decrease by increasing the current. This behavior may be related to the sulfur–metal arrangements observed by XRD, SEM-EDS, and X-ray CT data in addition to the different intrinsic characteristics of tin and nickel clusters. Further investigations were conducted to clarify this aspect by performing rate capability tests within a wide current range from C/10 to 10C. Figure 2.3.9 shows the rate performances of S:Sn 85:15 w/w (panel a) and S:Ni 85:15 w/w (panel b) in terms of discharge capacity, while panels a and b in Figure 2.3.10 show the related voltage profiles of the steady-state cycles. The profiles shown in Figure 2.3.10 reveal the increase in polarization expected by raising the current and accompanied by a decrease in specific capacity. The S:Ni 85:15 w/w nanocomposite exhibits higher capacity within the range from C/10 to 2C rate than that by the S:Sn 85:15 w/w one, namely, about 1380, 1330, 1280, 1235, 1170, 1045, and 840 mAh g_S^{-1} at C/10, C/8, C/5, C/3, C/2, 1C, and 2C versus the corresponding values of 1020, 985, 950, 920, 900, 875, and 775 mAh g_S^{-1}, respectively (Fig. 2.3.9a and b). On the other hand, the latter electrode has higher rate capability, that is, a lower capacity decrease by increasing the current, which is in good agreement with the electrochemical results (Fig. 2.3.8) as well as the microstructural features detected by electron microscopy and X-ray tomography (Figs. 2.3.2, 2.3.5, 2.3.6 and 2.3.7). In addition, the S:Sn 85:15 w/w electrode fully recovers the initial capacity when the current is decreased to C/10 at the 36th cycle, while the S:Ni 85:15 w/w one shows slight fading to 1240 mAh g_S^{-1}.
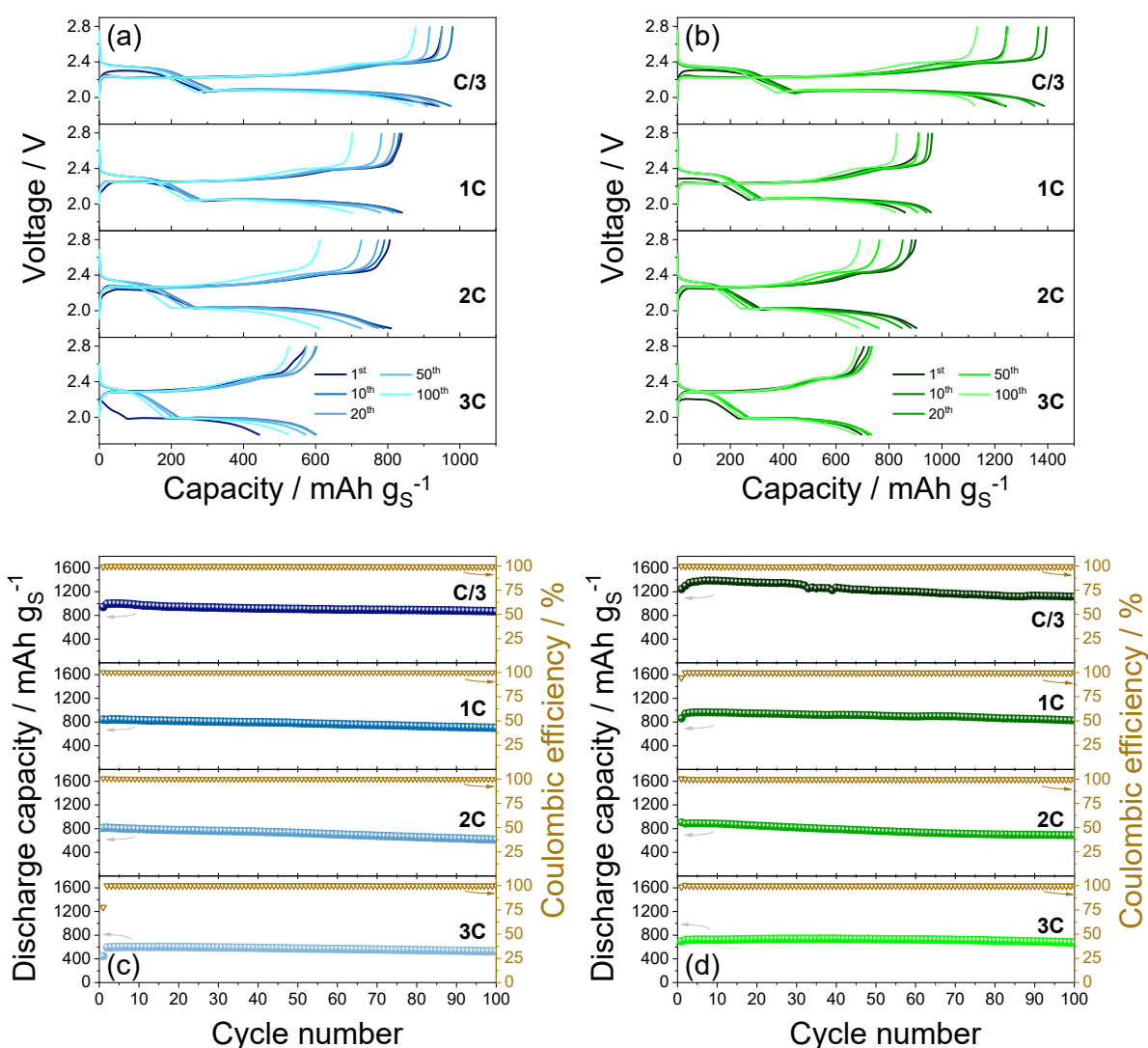
Figure 2.3.8. (a, b) Voltage profiles and **(c, d)** corresponding cycling trends with coulombic efficiency (right y-axis) of galvanostatic measurements performed on Li cells employing **(a, c)** S:Sn 85:15 w/w and **(b, d)** S:Ni 85:15 w/w composites. Tests performed at C/3, 1C, 2C, and 3C current rates within the voltage ranges of 1.9 – 2.8 V for C/3 and 1C and 1.8 – 2.8 V for 2C and 3C rates.

Significant differences in rate performances of the electrodes are further evidenced by changing the current from 1C to a value as high as 10C. Indeed, S:Ni 85:15 w/w exhibits discharge capacities of 1130, 920, 820, and 690 mAh g_S^{-1} while S:Sn 85:15 w/w delivers 830, 725, 660, and 610 mAh g_S^{-1} at 1C, 2C, 3C, and 4C rates, respectively. However, the first cycle at 4C of S:Ni 85:15 w/w (Fig. 2.3.9b) is characterized by an abrupt drop in the specific capacity to 320 mAh g_S^{-1}, which is not observed in the case of S:Sn 85:15 w/w (Fig. 2.3.9a). The better rate capability of the tin-based nanocomposite as compared to the nickel-based one is clearly revealed by cycling at 5C, 8C, and 10C rates, which indicates capacity values of 560, 360, and 160 mAh g_S^{-1} for the former (Fig. 2.3.9a), whereas 250,

160, and 120 mAh g$_S$$^{-1}$ for the latter (Fig. 2.3.9b). Importantly, both these electrodes recover the initial capacity almost completely, i.e., 795 mAh g$_S$$^{-1}$ for S:Sn 85:15 w/w and 1095 mAh g$_S$$^{-1}$ for S:Ni 85:15 w/w, as the current is decreased to 1C at the end of the test.
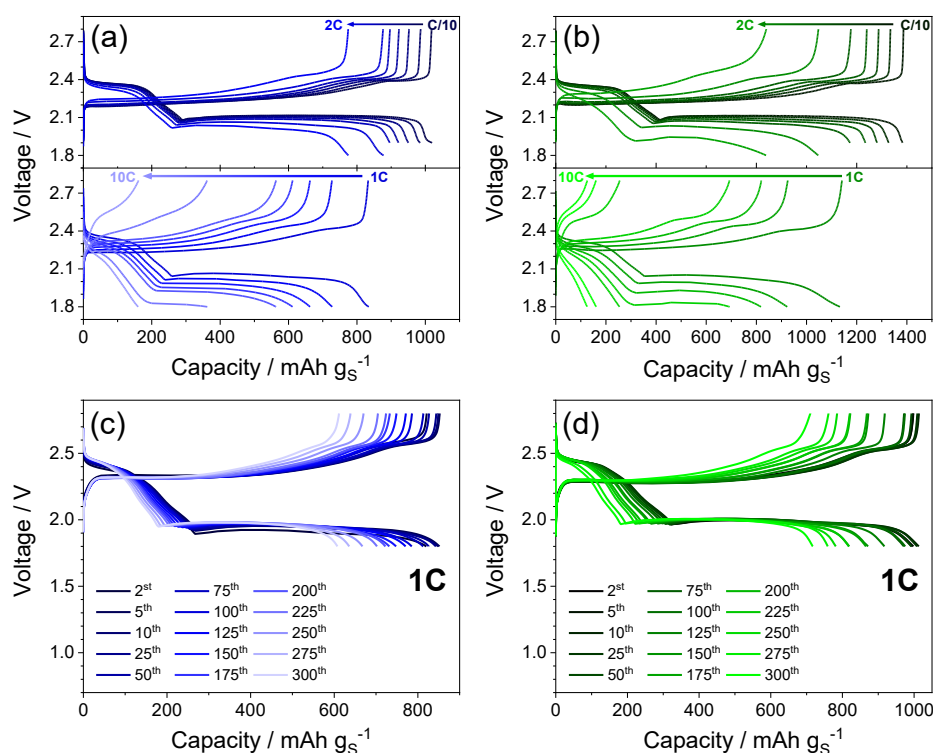

Figure 2.3.9. (a, b) Rate capability test on Li cells employing **(a)** S:Sn 85:15 w/w and **(b)** S:Ni 85:15 w/w composites at C/10, C/8, C/5, C/3, C/2, 1C, 2C, 3C, 4C, 5C, 8C, and 10C. Voltage range: 1.9 – 2.8 V from C/10 to C/2 and 1.8 – 2.8 V from 1C to 10C. **(c, d)** Steady-state voltage profile and (inset) discharge capacity trend upon the first 10 discharge/charge cycles of Li cells employing **(c)** S:Sn 85:15 w/w and **(d)** S:Ni 85:15 w/w composites with sulfur loading values of 6.8 and 6.3 mg cm^{-2}, respectively. Tests performed at a constant current rate of C/20 within the voltage range of 1.9 – 2.8 V. **(e)** Cycling trends with coulombic efficiency (right y-axis) of galvanostatic measurements performed on Li cells employing S:Sn 85:15 w/w and S:Ni 85:15 w/w composites and a DEGDME-based electrolyte. Tests performed at a 1C rate within the voltage range of 1.8 – 2.8 V.

These results reveal higher performances in terms of specific capacity for the nickel-based electrode, while higher rate capability for the tin-based one. However, both the nanocomposites can be considered as promising candidates for applications in high-energy Li–S batteries based on state-of-the-art data.[12,75]

It is worth considering that crucial parameters such as electrode loading and thickness, electrolyte/sulfur mass ratio (E/S), and lithium-metal excess may significantly affect the actual energy density, leading to maximum practical values between 400 and 600 Wh kg^{-1} with respect to the entire cell mass.[75,76] Therefore, the active material loading was further increased, aiming to match some of the expected requirements for commercial applications.[76] Panels c and d in Figure 2.3.9 show the preliminary cycling results for S:Sn 85:15 w/w and S:Ni 85:15 w/w electrodes with loading values increased from the typical value used for material characterization (about $2 – 3 mg_S$ cm^{-2}) to 6.8 and 6.3 mg$_S$ cm^{-2}, respectively, in lithium coin cells using 80 µL electrolyte solution (see the *2.3.2 Experimental* section for further details regarding cell assembly). These cells respectively deliver capacities as high as 6.4 and 6.9 mAh cm^{-2}, referred to the electrode geometric area (1.54 cm^2), at a C/20 rate, as shown by the top x-axis of the voltage profiles (Fig. 2.3.8c and d) as well as the right y-axis of the capacity trends (insets of panels c and d), which correspond to about 1000 and 1100 mAh g$_S^{-1}$ (bottom x-axis of the voltage profiles and left y-axis of the cycling trends). Such relevant performance actually suggests that the metal–nanocomposite approach is a viable strategy to achieve high-energy Li–S batteries, although additional work is imperative to conform to the strict demands of the battery market.[76] Further engineering of the electrode support, along with the careful optimization of cell design, might fit the various figures of merit, possibly promoting practical applications.[75,76] Based on the X-ray CT data, a large volume fraction of the carbon-cloth foil is not involved in sulfur electrodeposition. Therefore, a much thinner carbon-cloth foil might reasonably increase the practical gravimetric energy density of the cell without compromising the performance.

Cycle life is considered to be a key parameter that currently limits the actual transition of Li–S technology from the laboratory to market applications.[75] Therefore, a stable electrode behavior over about 300 galvanostatic cycles is demonstrated at a 1C rate, that is, a current value close to practical requirements,[76] by employing a diglyme solution. On the other hand, the electrolyte formulation may alter the ionic conductivity and lithium-ion transport within the electrolyte, as well as the passivation layer over the lithium metal anode.[47] Accordingly, DOL-DME-based electrolytes may decrease the cell polarization and enhance the rate capability of the cell, while diglyme-based solutions may mitigate lithium dendrite formation at the anode side, which is a suitable characteristic for allowing long-term cycling tests.[77] Furthermore, various cell components that have been optimized herein (such as sulfur-based composite, binder, current collector, electrolyte formulation,

E/S ratio, and lithium anode) may affect the performance of such a complex system.[3,74] Fig. 2.3.9e, 2.3.10c and d show the relevant cycling trends and voltage profiles, respectively. The cells reveal a remarkable response characterized by moderate polarization (Fig. 2.3.10c and d) and coulombic efficiency approaching 100% (Fig. 2.3.9e). In particular, S:Sn 85:15 w/w exhibits lower specific capacity and higher retention than those exhibited by S:Ni 85:15 w/w, which is in full agreement with the results shown in Figure 2.3.8, thereby suggesting a significant effect of the chemical characteristics and morphology of the metal clusters on the cycling ability of the material. Relevantly, S:Sn 85:15 w/w and S:Ni 85:15 w/w deliver the maximum capacities of about 850 and 1030 mAh g_S^{-1} with retention of about 72 and 70% after 300 cycles. Such promising results indicate an alternative way to get high-performance Li–S cells matching the best results in the literature.[74]

Figure 2.3.10. (a and **b)** Voltage profiles of the rate capability tests reported in Figure 2.3.8. Tests performed on Li cells using the **(a)** S:Sn 85:15 w/w and **(b)** S:Ni 85:15 w/w composites at C/10, C/8, C/5, C/3, C/2, 1C, 2C, 3C, 4C, 5C, 8C and 10C rates. Voltage range: 1.9 – 2.8 V from C/10 to C/2 and 1.8 – 2.8 V from 1C to 10C. **(c, d)** Voltage profiles of galvanostatic measurements performed on Li cells employing the **(c)** S:Sn 85:15 w/w and **(d)** S:Ni 85:15 w/w composites. Tests performed at a 1C rate within the voltage range of 1.8 – 2.8 V.

2.4 A gold-doped sulfur electrode

2.4.1 Presentation

Sections *2.2* and *2.3* revealed the advantages deriving from the use of conductive metal nanoparticles and a porous carbon electrode support (GDL) to prepare high-performing sulfur cathodes. Indeed, a simple and scalable approach allows to synthetize sulfur composites where the active material is loaded by conductive additives in weight percentage as low as 15%, thereby ensuring a high sulfur loading. On the other hand, the incorporation of noble metal centers in the cathode has been indicated to favor the conversion reaction by possibly increasing the affinity of the electrode surface toward lithium polysulfides and/or its bulk electronic conductivity.[78–80] In addition, X-ray computed tomography CT analyses supported by electron microscopy have suggested in section *2.3* favorable interactions between the metal sites and polysulfides, promoting electrodeposition of sulfur on the porous cathode framework upon charging. Bearing in mind these findings, the suitable characteristics of a gold-doped sulfur electrode for application in a lithium battery are studied in the following section. Accordingly, a scalable composite is prepared by melting sulfur in the presence of Au nanoparticles, which allow an active material loading as high as 97wt% thank to the higher tap density than that of common carbon additives. The novel sulfur composite is comprehensively investigated via X-ray computed tomography, electron microscopy, and X-ray diffraction, while the corresponding cathode cast on a GDL current collector is characterized in lithium cell by combining various electrochemical techniques, including voltammetry, electrochemical impedance spectroscopy, and galvanostatic cycling. X-ray CT analyses at the microscale are further used to shed light on the crucial role of cathode microstructure in enhancing sulfur conversion kinetics and cell performance.

2.4.2 Experimental

Elemental sulfur (≥99.5%, Riedel-de Haën) and gold nanopowder (<100 nm, 99.9% trace metal basis, Sigma-Aldrich) were mixed in the weight ratio of 97:3 and heated under magnetic stirring in a silicon oil bath at 120 °C until melting of sulfur and homogeneous blending of the two components was achieved. Subsequently, the mixture was cooled to room temperature and ground in an agate mortar after solidification. The resulting composite is indicated as S:Au 97:3 w/w.

The structure of the S:Au 97:3 w/w powder was investigated by means of XRD through a Bruker D8 Advance diffractometer equipped with a Cu-Kα source (8.05 keV) with a scan in the 2θ

range between 10° and 90° at a rate of 10 s step^{-1} with a step size of 0.02°. Morphology and elemental composition of the S:Au 97:3 w/w powder were inspected by SEM, EDS, transmission electron microcopy TEM, and X-ray CT at the nanoscale. SEM-EDS was carried out through a Zeiss EVO MA10 using a tungsten thermionic electron source and equipped with an INCA X-ACT Oxford Instrument analyzer. TEM images were collected by a Zeiss EM 910 microscope employing a tungsten thermionic electron source operating at 100 kV. The X-ray CT analysis at the nanoscale was performed through a Zeiss Xradia 810 Ultra instrument (Carl Zeiss Inc.), employing a micro-focus rotating Cr anode (Cr-Kα of 5.4 keV, MicroMax-007HF, Rigaku). The X-ray source of the CT microscope was set at 35 kV and 25 mA. The specimen for X-ray nano-CT consisted of a small amount of S:Au 97:3 w/w powder secured on the tip of a stainless steel (SS) needle by epoxy [2,4,6-tris(dimethylaminomethyl)phenol, Devcon]. The X-ray nano-CT instrument comprised a He-filled chamber housing a condenser capillary that focused the beam onto the specimen and an He-filled optics chamber containing a Fresnel zone plate that focused the beam coming from the specimen onto a charge-coupled device (CCD) detector. A tomographic scan was carried out in absorption-contrast and large-field-of view (65 μm) mode by taking 901 radiographs of the sample through 180° rotation. Each radiograph was collected with an X-ray exposure time of 45 s and binning 1. The resulting voxel size was ca. 63 nm. The tomographic dataset was reconstructed through the Zeiss XMReconstructor software (Carl Zeiss Inc.) employing a filtered back-projection algorithm. The 3D reconstructed image was visualized, processed by applying nonlocal means and unsharp masking filters, and segmented through the Avizo 2020.2 software (Visualization Sciences Group, FEI SAS, Thermo Fisher Scientific). Three phases with increasing X-ray attenuation coefficient were identified by segmentation using grayscale[14] and watershed[18] methods: *i)* exterior, *ii)* sulfur, and *iii)* gold.

S:Au 97:3 w/w electrodes were prepared by doctor-blade casting (MTI Corp.) of a slurry containing the S:Au 97:3 w/w composite, conductive carbon black (Super P, Timcal), and polyvinilidenefluoride (Solef ® 6020 PVDF) in the weight ratio of 8:1:1, respectively. This slurry was prepared by dispersing the components in *N*-methyl-2-pyrrolidone (NMP, Sigma-Aldrich) by means of an agate mortar and a pestle, and then cast on a carbon-cloth foil (GDL ELAT 1400, MTI Corp.). The wet electrode film was heated on a hot plate at 50 °C under air for about 3 h to evaporate the solvent. Cathode disks with a diameter of 14 mm (geometric area of 1.54 cm^2) were cut out from the dry coated foil and then heated overnight at 40 °C under vacuum before being transferred in an Ar-filled glovebox (MBraun, O_2 and H_2O content below 1 ppm). Three batches of electrodes having different sulfur loading were prepared, that is, *i)* in the range from 1.6 to 2.4 mg cm^{-2}, *ii)* in the range from 4.1 to 5.7 mg cm^{-2}, and *iii)* 1.4 mg cm^{-2}.

CR2032 coin cells were assembled in an Ar-filled glovebox (MBraun, O_2 and H_2O content below 1 ppm) by stacking a lithium disk with diameter of 14 mm, a Celgard 2400 separator with diameter of 16 mm soaked by the electrolyte solution, and a S:Au 97:3 w/w electrode. The electrolyte solution was obtained by dissolving lithium bis(trifluoromethanesulfonyl)imide (LiTFSI, 99.95% trace metals basis, Sigma-Aldrich) and lithium nitrate ($LiNO_3$, 99.99% trace metals basis, Sigma-Aldrich) in a mixture of 1,3-dioxolane (DOL, anhydrous, contains ca. 75 ppm BHT as inhibitor, 99.8%, Sigma-Aldrich) and 1,2-dimethoxyethane (DME, anhydrous, 99.5%, inhibitor-free, Sigma-Aldrich) in the 1:1 w/w ratio. Prior to use, LiTFSI and $LiNO_3$ were dried at 110 and 80 °C, respectively, under vacuum for 3 days, while DOL and DME were dried under molecular sieves (3 Å, rod, size 1/16 in., Honeywell Fluka) until the water content was lower than 10 ppm, as measured by a Karl Fischer 899 Coulometer (Metrohm). The final concentration of each salt in the electrolyte solution was 1 mol kg^{-1} as referred to the weight of solvent.

Cyclic voltammetry (CV) measurements were carried out at a scan rate of 0.1 mV s^{-1} in the 1.8 – 2.8 V vs Li$^+$/Li potential range. Electrochemical impedance spectra were collected at the open circuit voltage (OCV) condition of the cell, as well as after 1, 5 and 10 voltammetry cycles, and analyzed by the non-linear least squares (NLLS) fitting method via the Boukamp software (χ^2 values of the order of 10^{-5}).[45,46] EIS was performed by applying to the cell an alternate voltage signal with amplitude of 10 mV within the frequency range from 500 kHz to 100 mHz. Further CV scans in the 1.8 – 2.8 V vs Li$^+$/Li potential range at increasing scan rates, i.e., 0.05, 0.1, 0.15, 0.2 and 0.25 mV s^{-1}, were performed to estimate the apparent Li$^+$ diffusion coefficient (D) according to the Randles-Sevcik equation (2.4.1):[60,61]

$$I_p = 0.4463zFAC \left(\frac{zFvD}{RT}\right)^{½} \tag{2.4.1}$$

where I_p is the peak current (A), z is the number of exchanged electrons, F is the Faraday constant (96 485 C mol^{-1}), A is the geometric area of the S:Au 97:3 w/w electrode (1.54 cm^2), C is the estimated Li$^+$ concentration in the electrode volume (mol cm^{-3}), v is the scan rate (mV s^{-1}), D is the Li$^+$ diffusion coefficient (cm^2 s^{-1}), R is the gas constant (8.31451 J mol^{-1} K^{-1}) and T is the room temperature (298 K). Herein, a number of 1 exchanged electron ($z = 1$) was considered for each discharge peak (occurring at about 2.3 and 2.0 V vs Li$^+$/Li), while a number of 2 exchanged electrons ($z = 2$) was taken into account for the charge peak (occurring at about 2.4 V vs Li$^+$/Li). The CV and EIS measurements were performed through a VersaSTAT MC Princeton Applied Research (PAR–AMETEK) analyzer.

Galvanostatic cycling measurements were carried out using a MACCOR series 4000 battery test system. Coin cells with a S loading between 1.9 and 2.2 mg cm^{-2} over the electrode and an electrolyte/sulfur (E/S) ratio of 15 µL mg^{-1} were tested within the current rate ranging from C/10 to 1C (1C = 1675 mA g$_S$$^{-1}$). In detail, galvanostatic measurements over 100 cycles were carried out at C/3 and 1C rates within the 1.9 – 2.8 V and 1.8 – 2.8 V voltage ranges, respectively. The rate capability of the electrode was assessed by applying current rates of C/10, C/8, C/5, C/3 and 1C, increasing every 5 cycles and decreasing back to the initial value of C/10 at the 26th cycle. Voltage ranges of 1.9 – 2.8 V from C/10 to C/3 and of 1.8 – 2.8 V at 1C were set for this rate capability test. Coin cells with a S loading of 5.7 mg cm^{-2} and an E/S ratio of 5 µL mg^{-1} were cycled at a constant current rate of C/20 rate between 1.8 and 2.8 V. A further Li|S:Au 97:3 w/w coin cell with a sulfur loading over the electrode of 1.4 mg cm^{-2} and an E/S ratio of 15 µL mg^{-1} was subjected to prolonged cycling at the 2C rate between 1.8 and 2.8 V.

The S:Au 97:3 w/w electrode, the lithium-metal anode, and the separator were imaged before and after cycling in the lithium cell by X-ray CT at the microscale using a Zeiss Xradia 620 Versa microscope (Carl Zeis Inc.) employing a polychromatic microfocus source (tungsten target). Cathode samples for X-ray micro-CT were prepared by cutting out portions with approximate size of 1mm × 1 mm from each electrode and securing these to SS dowels by epoxy [2,4,6-tris(dimethylaminomethyl)phenol, Devcon]. Tomographic scans of the cathodes were performed using a 40× lens and collecting 1601 radiographs of the specimen through 360° rotation with binning 1. Voltage and current of the X-ray source, time of exposure for each projection, as well as source–specimen and detector–specimen distances, were adjusted to obtain suitable transmission values. In detail, electrodes with a sulfur loading from 1.6 to 2.4 mg cm^{-2} were investigated by setting the source in the 80 – 90 kV and 87 – 89 µA ranges, while electrodes with a sulfur loading from 4.1 to 4.2 mg cm^{-2} were studied setting the source at 120 kV and 83 µA. The exposure time varied from 44 to 47 s, while the source–specimen and detector–specimen distances were in the ranges of 9.77 – 9.81 and 8.95 – 9.05 mm, respectively, thereby leading to a voxel size between 176 and 177 nm in a field of view of about 330 µm. The anode and separator samples were recovered from two Li|S:Au 97:3 w/w coin-cells, which were held at OCV and discharged/charged at a 2C rate upon 300 cycles, respectively. Both cells had a sulfur loading over the electrode of 1.4 mg cm^{-2} and an E/S ratio of 15 µL mg^{-1}. Cell disassembling was carried out in an Ar-filled glovebox (MBraun, O$_2$ and H$_2$O content below 1 ppm). Afterwards, lithium and separator samples were cut out and sealed inside Swagelok-type cells having polyether ether ketone (PEEK) housing SS pins, which had an inner diameter of 0.8 mm, in order to avoid air exposure during the X-ray CT scans. These scans were performed by collecting 901 radiographs of the specimen through 360° rotation and using a 20× lens and binning

1. The source was set at 60 kV and 83 µA, the exposure time was 30 s, and source–specimen and detector–specimen distances were adjusted to obtain suitable transmission values and a voxel size of 301 nm. The micro-CT datasets were reconstructed through the Scout-and-Scan Control System Reconstructor software (Carl Zeiss Inc.) employing either a filtered back-projection algorithm (cathode) or the Optirecon algorithm (anode and separator). The 3D reconstructed images were visualized, processed by applying nonlocal means and unsharp masking filters, segmented, and quantitatively analyzed through the Avizo 2020.2 software (Visualization Sciences Group, FEI SAS, Thermo Fisher Scientific). Four domains with increasing X-ray attenuation coefficient were identified in the cathode by segmentation using grayscale[14] and watershed[18] methods: *i)* exterior, *ii)* a domain including carbon, PVDF and carbon-cloth support, *iii)* sulfur, and *iv)* gold. For cathode analysis, binary datasets were produced by selecting the segmented sulfur domain, and the phase fraction of sulfur along the Z axis, i.e., the specimen rotation axis orthogonal to the electrode plane, was calculated. Electrodes used for X-ray CT with a sulfur loading from 1.6 to 2.4 mg cm^{-2} were cycled at a 1C rate, while the those with a sulfur loading from 4.1 to 4.2 mg cm^{-2} were cycled at a C/10 rate.

2.4.3 Results

Figure 2.4.1 shows the structural and morphological characteristics of the S:Au 97:3 w/w powder as studied by combining XRD, electron microscopy, and X-ray CT techniques. XRD reveals the patterns of orthorhombic sulfur (α-S$_8$) and metallic gold, with relative peak intensities reflecting the volume ratio between the two phases and suggesting large crystal domains for sulfur (Fig. 2.4.1a). The absence of reflections attributed to additional phases confirms that the mild conditions adopted to prepare the composite, along with the well-known inert nature of metallic gold,[81] actually prevent the formation of impurities or side products. SEM images at various magnifications (Fig. 2.4.1b, c and g) and EDS maps (Fig. 2.4.1f and h) display sub-micrometric Au agglomerates laying on sulfur particles with size from about 5 µm to about 50 µm, as well as segregated larger Au clusters with maximum size approaching 30 µm. Each metal aggregate is mostly formed by nanometric primary particles below 100 nm, as evidenced by the TEM image in Figure 2.4.1i. X-ray CT at the nanoscale enables a three-dimensional reconstruction of a portion of the composite of about 60 µm. The related cross-sectional slice with corresponding three-phase segmentation (Fig. 2.4.1d and e) and the volume rendering (Fig. 2.4.1j) reveal a large sulfur cluster with irregular shape containing few Au domains below 1 µm. It is worth noting that the dispersion of a low fraction of noble metal into a bulk of active material evidenced in Figure 2.4.1 may actually lead to an increased energy density of the electrode and mitigate the insulating character of sulfur to boost the conversion in lithium cell. Indeed, gold is

expected to enhance the reaction kinetics at the electrode/electrolyte interphase and favor the electrodeposition of sulfur and possibly the formation of Li_2S.
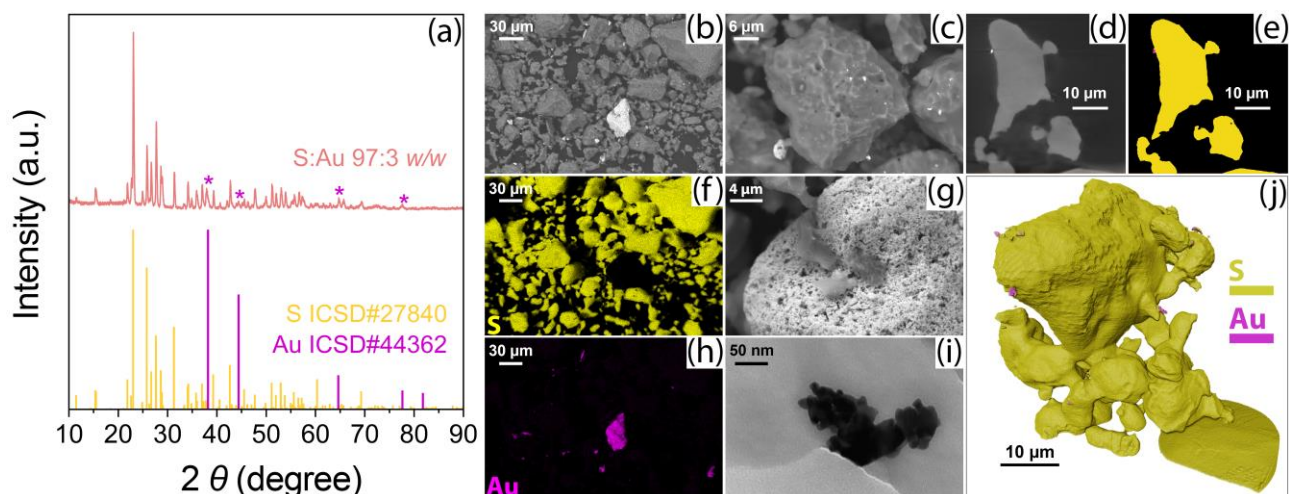
Figure 2.4.1. (a) XRD pattern of the S:Au 97:3 w/w powder (top) and reference data (bottom) for elemental sulfur (yellow, ICSD #27840) and metallic gold (magenta, ICSD #44362). **(b–j)** Morphological analysis of the S:Au 97:3 w/w powder by electron microscopy and X-ray CT. In detail: **(b, c, g)** SEM images at various magnifications in **(b, c)** backscattered and **(g)** secondary electron modes; **(f, h)** EDS maps of **(f)** S and **(h)** Au; **(i)** TEM image; **(d, e** and **j)** X-ray CT imaging at the nanoscale, as **(d)** cross-sectional slice extracted in a plane along the rotation axis (beam attenuation represented through a grayscale), **(e)** corresponding three-phase segmented slice (Au: magenta, S: yellow, exterior: black), and **(j)** three-phase segmented volume rendering (Au: magenta, S: yellow, exterior: not represented).

The electrochemical process of the S:Au 97:3 w/w cathode in the cell has been characterized by voltammetry and impedance spectroscopy measurements (Fig. 2.4.2). The first reduction scan of Figure 2.4.2a reveals two peaks at about 2.20 and 2.00 V vs Li^+/Li, which can be associated with the formation of long-chain and short-chain lithium polysulfides, i.e., Li_2S_x with $6 \leq x \leq 8$ and $2 \leq x \leq 4$, and possibly Li_2S.[42,51,82] The subsequent oxidation scan is instead characterized by a broad double peak with maximum centered at 2.35 and 2.40 V vs Li^+/Li, reflecting the reversible reaction of Li_2S_x species ($1 \leq x \leq 8$) with eventual electrodeposition of S_8 at high potential.[42,82] After the initial cycle, Figure 2.4.2a shows a notable shift of the first discharge peak from 2.20 V vs Li^+/Li to 2.30 V vs Li^+/Li, and a slight decrease in polarization for the second discharge peak. This electrochemical behavior suggests an improvement of the charge transfer at the electrode/electrolyte interphase along with microstructural rearrangements in the cathode upon multiphase conversion of sulfur, in good agreement with data reported in previous sections and earlier reports.[13,26] These modifications lead to an additional shoulder in the potential range of 2.5 – 2.7 V vs Li^+/Li during the oxidation scans, thus suggesting a change in the conversion kinetics. This phenomenon likely involves sulfur precipitation during charge on preferred locations over the electrode according to an electrochemical

activation which increases the active material utilization enabling suitable reaction sites on the cathode surface. This hypothesis is in part supported by the different signature of the first CV scan compared to the overlapping profiles of the subsequent cycles (Fig. 2.4.2a).
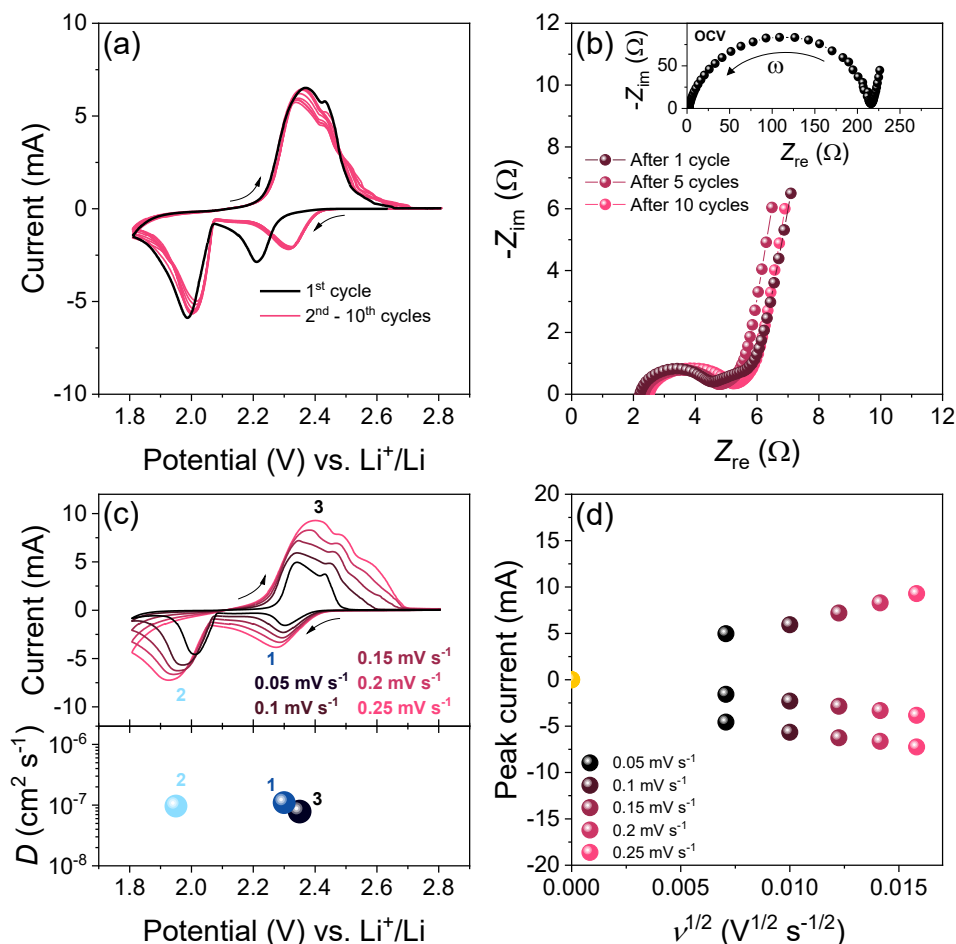
Figure 2.4.2. (a) CV profiles of the Li|S:Au 97:3 w/w cell at a scan rate of 0.1 mV s^{-1} within the potential range from 1.8 to 2.8 V *vs* Li$^+$/Li and **(b)** Nyquist plot of impedance spectra of the same cell at the OCV and after 1, 5 and 10 voltammetry cycles; EIS carried out by applying to the cell an alternate voltage signal with amplitude of 10 mV within the frequency range from 500 kHz to 100 mHz. **(c)** CV profiles (upper panel) of the Li|S:Au 97:3 w/w cell at various scan rates, i.e., 0.05, 0.1, 0.15, 0.2 and 0.25 mV s^{-1} within the potential range from 1.8 to 2.8 V *vs* Li$^+$/Li and apparent Li$^+$ diffusion coefficient (D, bottom panel) calculated by applying the Randles-Sevcik equation to the CV data (see equation (2.4.1) in the *2.4.2 Experimental* section and Table 2.4.2). **(d)** Peak current as a function of the square root of the scan rate (v$^{1/2}$) extracted from the CV profiles of panel **(c)**; the yellow point indicates the axes origin.

Furthermore, EIS indicates a significant drop in electrode/electrolyte interphase resistance (R$_i$) after the first scan and a steady response for the subsequent 10 cycles (see the related Nyquist plots in Fig. 2.4.2b). Table 2.4.1 reports the results of an NLLS fitting of the impedance data performed by modeling the cell response with the R$_e$(R$_i$Q$_i$)$_n$Q$_g$ equivalent circuit (n = 1, 2), where the high-middle

frequency sub-circuit containing pseudo-capacitive and resistive elements arranged in parallel [*i.e.*, $(R_iQ_i)_n$] reproduces the electrode/electrolyte interphase, while R_e and Q_g simulate the electrolyte resistance and the cell capacitance, respectively.[45,46] This analysis suggests a decrease of R_i from 216 ± 1 Ω at the OCV condition (inset of Fig. 2.4.2b) to values fluctuating between 3.4 ± 0.3 Ω and 4.0 ± 0.2 Ω during the subsequent cycles (main panel of Fig. 2.4.2b), and reflects a remarkable improvement of the charge transfer kinetics due to the above mentioned activation.

Cell condition	Equivalent circuit	R_1 (Ω)	R_2 (Ω)	$R_1 + R_2$ (Ω)	χ^2
OCV	$R_e(R_1Q_1)Q_g$	216 ± 1	/	216 ± 1	8×10^{-5}
After 1 CV cycle	$R_e(R_1Q_1)(R_2Q_2)Q_g$	2.1 ± 0.1	01.9 ± 0.2	4.0 ± 0.2	8×10^{-5}
After 5 CV cycles	$R_e(R_1Q_1)(R_2Q_2)Q_g$	2.4 ± 0.1	1.0 ± 0.3	3.4 ± 0.3	2×10^{-5}
After 10 CV cycles	$R_e(R_1Q_1)(R_2Q_2)Q_g$	2.8 ± 0.1	0.8 ± 0.2	3.6 ± 0.2	3×10^{-5}

Table 2.4.1. Results of NLLS analysis of impedance spectra of the Li|S:Au 97:3 w/w cell (Fig. 2.4.2b) collected upon a CV measurement (Fig. 2.4.2a).

CV at various scan rates have been carried out to estimate the apparent Li^+ diffusion coefficient (*D*) according to the Randles-Sevcik equation (2.4.1).[60,61] The related voltammetry profiles, shown in top panel of Figure 2.4.2c, display the expected raise in polarization and peak current intensity (I_p) as the scan rate increases from 0.05 to 0.25 mV s^{-1}, along with the appearance of the abovementioned additional shoulder during charging from 2.6 to 2.7 V *vs* Li^+/Li. Notably, the linear relation between the I_p and the square root of the scan rate ($v^{1/2}$) evidenced by Figure 2.4.2d suggests an electrochemical process controlled by diffusion, despite the substantial difference between the Randles-Sevcik system[60,61] and the cell herein investigated. Therefore, a *D* value is calculated for each reduction peak as well as for the double oxidation peak, and reported in Table 2.4.2 and in the bottom panel of Fig. 2.4.2c. The apparent diffusion coefficient ranges between 7.8×10^{-8} and 1.1×10^{-7} cm^2 s^{-1} at the various states of charge of the cell (Table 2.4.2) and decreases at the end of discharge, thus in agreement with the extensively described reaction kinetics which hinder the final steps of sulfur conversion to short-chain lithium polysulfides and possibly to Li_2S.[69] An additional slight decrease of *D* during charging reflects the partially limited ion diffusion into the insulating sulfur electrode, which may actually be enhanced by providing proper electrodeposition sites that allow a reversible process at high current rates.[40] In this regard, the dispersion of metal

nanoparticles within the cathode has proven to be an effective strategy to enhance the multiphase conversion reactions, as observed in sections *2.2* and *2.3.* Herein, this approach has been further improved by exploiting the highly conductive gold nano-powder, which has enabled satisfactory electrode kinetics despite a metal amount as low as 3%, thus leading to a final sulfur ratio into the cathode film of 78wt% and, possibly, high energy density.

State of charge	D $(cm^2\ s^{-1})$
2.30 V *vs* Li⁺/Li (disch.)	1.1×10^{-7}
1.95 V *vs* Li⁺/Li (disch.)	9.6×10^{-8}
2.35 V *vs* Li⁺/Li (ch.)	7.8×10^{-8}

Table 2.4.2. Li⁺ diffusion coefficient (D) calculated by applying the Randles-Sevcik equation to CV data (equation (2.4.1) in the *2.4.2 Experimental* section).[60,61] Fig. 2.4.2c displays the corresponding CV (upper panel) and the D coefficients (bottom panel). Fig. 2.4.2d shows the corresponding peak current trends.

Figure 2.4.3 reports the features in lithium cells of the S:Au 97:3 w/w electrode by exploiting an average sulfur loading typically used in Li-S battery studies (i.e., of about 2 mg cm^{-2}). The cells are galvanostatically cycled at various currents in order to verify the rate capability of the electrode (Fig. 2.4.3a and d), as well as at a constant rate of C/3 (Fig. 2.4.3b and e) and 1C (Fig. 2.4.3c and f) to evaluate the cycle life (1C = 1675 mA g$_S^{-1}$). In detail, the battery reveals suitable response characterized by a moderate increase in polarization (Fig. 2.4.3a) and a limited decrease in capacity by gradually raising the C-rate from C/10 to 1C (Fig. 2.4.3d). The voltage profiles at C/10 show two plateaus centered at about 2.35 and 2.10 V during discharge, and at 2.40 and 2.20 V during charge (Fig. 2.4.3a), in agreement with the CV curves already shown in Fig. 2.4.2. In spite of the abovementioned overvoltage increase with the raise in C-rate, the cell almost fully restores its maximum capacity as the current is lowered back to the initial value of C/10 at the end of the test. Indeed, Fig. 2.4.3d shows capacity values of about 1314, 1237, 1156, 1039 and 890 mAh g$_S^{-1}$ at the rates of C/10, C/8, C/5, C/3 and 1C, respectively, as well as a capacity of 1260 mAh g$_S^{-1}$ when the current is lowered back to C/10 after the 25th cycle, which reflects a 96% retention. Additionally, galvanostatic tests prolonged over 100 cycles at the constant current rates of C/3 (Fig. 2.4.3b and e) and 1C (Fig. 3c and f) evidence excellent performance. Both tests show an activation occurring upon

the initial 10 – 15 cycles which leads to a progressive improvement of the voltage profile and a steady-state characterized by lower polarization (Fig. 2.4.3b and c). Furthermore, this ongoing process leads to a steep increase in the delivered capacity from about 800 mAh g_S^{-1} at C/3 and 600 mAh g_S^{-1} at 1C to values approaching 1200 and 1000 mAh g_S^{-1}, respectively (Fig. 2.4.3e and f). After 100 cycles, the battery retains 940 mAh g_S^{-1} at C/3 and 910 mAh g_S^{-1} at 1C, which corresponds to ca. 85% and 91% of the steady-state values. Notably, the data of Fig. 2.4.3 show a coulombic efficiency approaching 100% after the first cycle and suggest an effectual mitigation of possible parasitic reactions of the dissolved polysulfides due to the *in situ* protection of the lithium anode by using a suitable electrolyte solution.[43] It is worth mentioning that cell configuration in terms of composition and microstructure of the cathode, electrolyte formulation, and E/S ratio may significantly affect the electrochemical performance.[83] Accordingly, the Li|S:Au 97:3 w/w cell actually benefits from a cathode optimized by gold-doping, a porous support with suitable sulfur electrodeposition sites,[21,22] an electrolyte solution containing $LiNO_3$ to avoid the "shuttle effect" and massive formation of dendritic structures,[84] and an E/S ratio of 15 µL mg^{-1}.
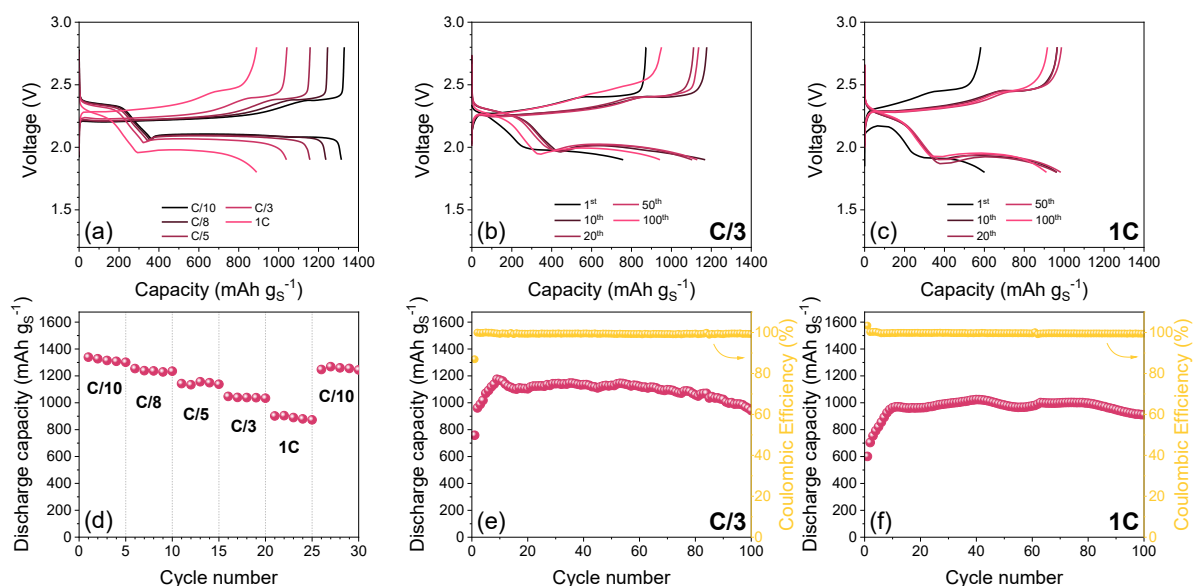
Figure 2.4.3. (a–c) Voltage profiles and **(d–f)** cycling trends in various testing conditions of the Li|S:Au 97:3 w/w cell with sulfur loading over the electrode of 1.9 – 2.2 mg cm^{-2} (electrode geometric area: 1.54 cm^2) and E/S ratio of 15 µL mg^{-1}. In detail: **(a, d)** rate capability of the cell within the range from C/10 to 1C, namely, at C/10, C/8, C/5, C/3 and 1C; **(b, c, e, f)** performance of the cell over 100 cycles at constant current rates of **(b, e)** C/3 and **(c, f)** 1C. Voltage ranges: 1.9 – 2.8 V from C/10 to C/3 rate and 1.8 – 2.8 V at 1C rate.

The effects of cycling on the cathode microstructure are subsequently investigated by performing X-ray CT scans in a field of view of about 330 µm (Fig. 2.4.4). These measurements provide a three-dimensional map of the various phases in the electrode which are identified by

differences in X-ray attenuation, thus enabling the detection of morphological features at the microscale with a voxel size smaller than 180 nm. Figure 2.4.4 shows the X-ray imaging of cathode samples before (panels a–c) and after 1 (panels d–f) and 100 cycles (panels g–i). The left-hand side panels (Fig. 2.4.4a, d and g) report sections of the electrodes represented in grayscale, where the brightness reflects the local density of the specimen.[14] Accordingly, the large Au aggregates already observed in detail by SEM-EDS, TEM, and X-ray CT at the nanoscale in Figure 2.4.1, can be detected as continuous bright spots in Fig. 2.4.4a, d and g, while sulfur appears as gray particles with moderate density. However, it is worth mentioning that smaller gold nanoparticles intimately mixed with sulfur cannot be detected by microscale CT. Besides, X-ray imaging reveals that the carbon-cloth support and the carbon-binder domain of the composite electrode film have lower density than sulfur, as suggested by the brightness scale of the images. Four domains are identified by analyzing the grayscale histogram of the CT reconstructions,[14] and image segmentation is performed by processing the 3D datasets as described in the Experimental section. Figure 2.4.4b, e and h show the segmented images of the electrode and depict *i)* highly attenuating gold in magenta, *ii)* moderately attenuating sulfur in yellow, *iii)* lowly attenuating carbon cloth and carbon-binder domain in gray, and *iv)* exterior/pores in black. Furthermore, Figure 2.4.4c, f and i display the volume rendering of the electrodes using the same color map. The tomographic datasets of Figure 2.4.4a–f suggest that the electrochemical activation of the cell is associated with a substantial reorganization of sulfur particles randomly distributed in the pristine cathode film, which dissolve during discharge and precipitate on suitable sites over the electrode surface during charge. Indeed, the multi-phase nature of the conversion process in the cell may enable favorable microstructural rearrangements in the electrode leading to an actual enhancement of the charge transfer kinetics at the interphase with the electrolyte solution as proposed in the previous sections. Therefore, improved performances may be achieved by tailoring preferred electrodeposition sites for sulfur and suitable hosts for Li_2S in the cathode, as well as by using a porous current collector which may accommodate the active material.[22] On the other hand, it was observed in section *2.1* that the pristine electrode morphology may affect the cell behavior possibly altering the nucleation rate of the solid species at the cathode side, the sulfur utilization, and the active material loss over long-term cycling. Figure 2.4.4g–i evidence a significant decrease in volume fraction of sulfur in the electrode after 100 cycles, which can be only in part related to the capacity fade observed in Figure 2.4.3. Indeed, the data of Figure 2.4.4 suggest a certain role played by the lithium polysulfides dissolved into the electrolyte as a catholyte in boosting the electrochemical process of the cell and ensuring a satisfactory performance.[85]
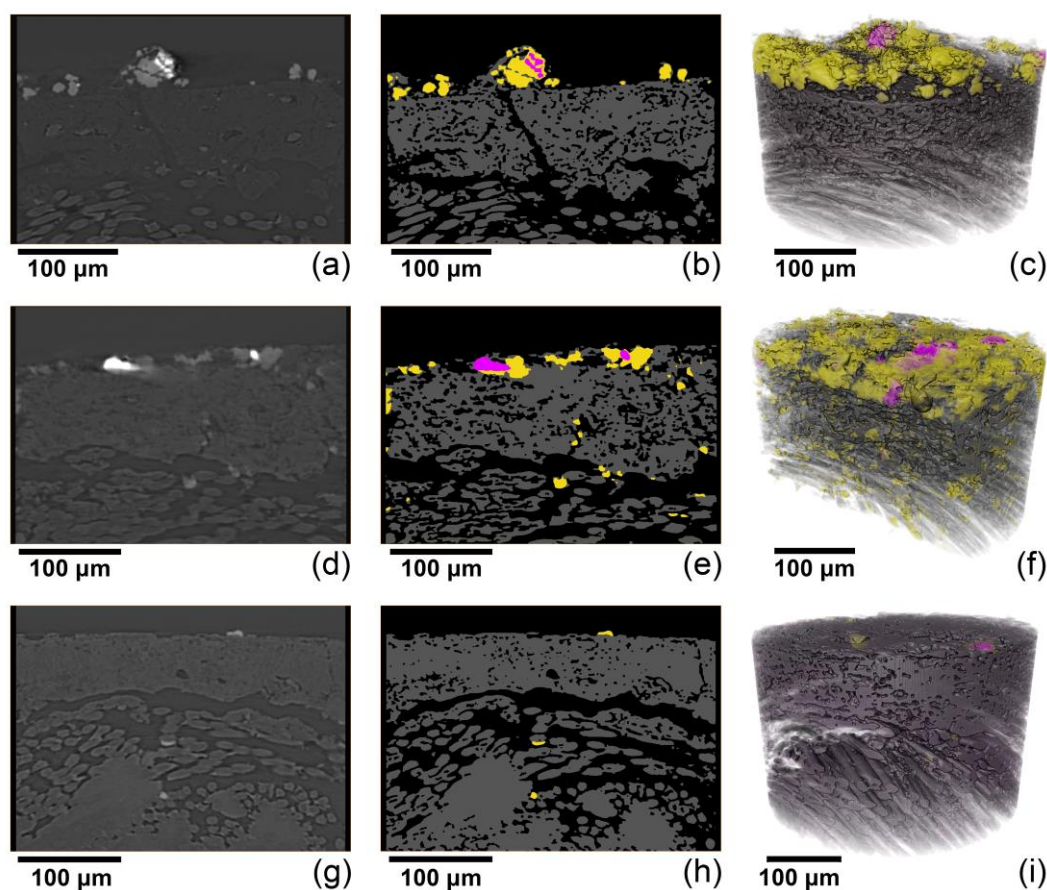
Figure 2.4.4. X-ray CT imaging at the microscale of S:Au 97:3 w/w electrodes with sulfur loading of 1.6 – 2.4 mg cm^{-2} (electrode geometric area: 1.54 cm^2) **(a–c)** before and after **(d–f)** 1 and **(g–i)** 100 cycles at a 1C rate. In detail: **(a, d, g)** cross-sectional slices extracted in a plane parallel to the rotation axis (Z axis) and orthogonal to the electrode plane (beam attenuation represented through a grayscale), **(b, e, h)** corresponding four-phase segmented slices (Au: magenta, S: yellow, C/PVDF/C-cloth: gray; exterior: black), and **(c, f** and **i)** four-phase segmented volume rendering (Au: magenta, S: yellow, C/PVDF/C-cloth: gray; exterior: not represented). See Figs. 2.4.3 and 2.4.5 showing the cycling performance of the cell and the distribution of the sulfur phase in the electrode samples, respectively.

Figure 2.4.5 reports a quantitative analysis of sulfur distribution within the instrumental field of view as determined by processing the tomographic data of the electrodes before (panels a and b) and after 1 (panels c and d) and 100 cycles (panels e and f) in Li-S cell. The volume renderings of the sulfur phase across a plane orthogonal to the electrode are represented in Figure 2.4.5a, c and e as orthographic projections without perspective distortion. These images evidence a significant rearrangement involving the active material upon the first cycle. Such a notable change can justify in part the significant decrease in electrode/electrolyte interphase resistance and the cell improvement already observed by electrochemical tests in Figures 2.4.2 and 2.4.3. In addition, the volume rendering after 100 cycles (Fig. 2.4.5e) reveals a substantial reduction of the overall sulfur phase into the electrode, which suggests either incomplete conversion of the long-chain polysulfides upon charging or electrodeposition at the interface between electrode and separator.[13] Further insight into

this reorganization is achieved by calculating for each dataset the sulfur phase fraction along the Z axis (Fig. 2.4.5b, d, and f) which may approximately indicate the electrochemically active electrode depth. The related graph before cycling (Fig. 2.4.5b) shows the sulfur mostly distributed on the top surface of the electrode with an estimated depth of about 70 μm. After the first cycle (Fig. 2.4.5d) a large fraction of sulfur remains hosted on the top surface, while a significant part migrates within the electrode bulk likely due to electrodeposition into the porous structure of the current collector. The analysis of the electrode after 100 cycles (Fig. 2.4.5f) reveals a further migration of sulfur to the inner side of the electrode, thus further suggesting a remarkable role of the cathode bulk and the current collector in driving the electrochemical reaction of the Li/S cell, particularly upon prolonged cycling.[13] Therefore, both the heterogeneous composite electrode film and the porous current collector are expected to have complex interactions with the various lithium polysulfides.[23]
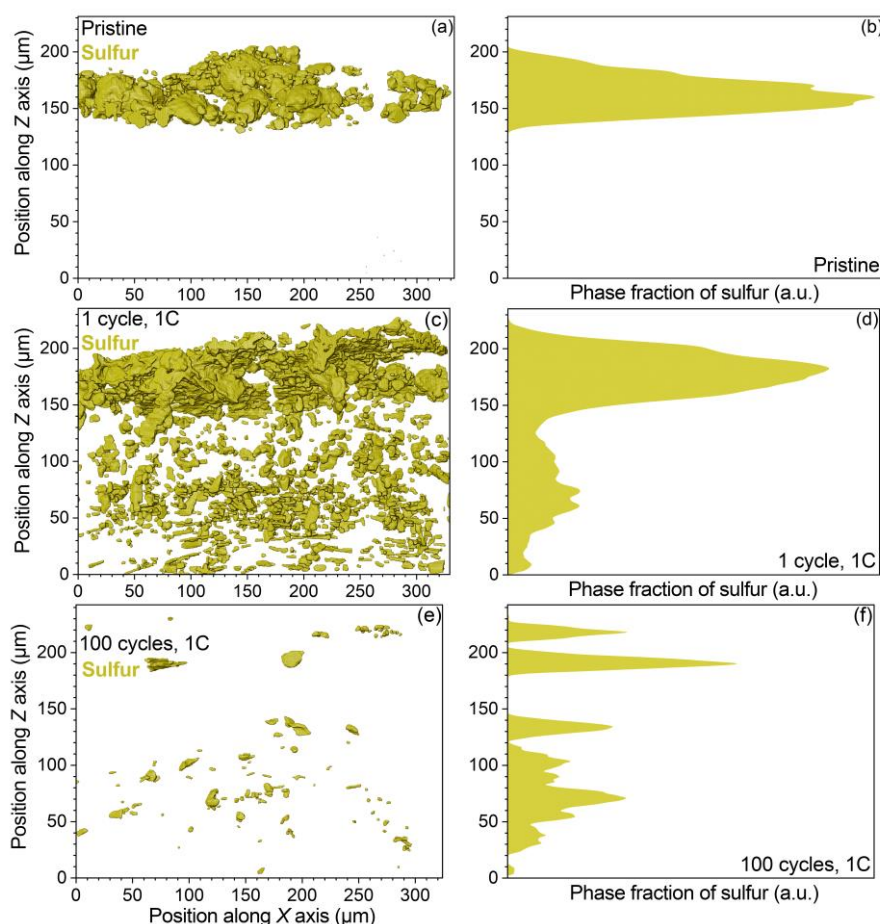
Figure 2.4.5. Distribution of the sulfur phase in the S:Au 97:3 w/w electrodes with sulfur loading of 1.6 – 2.4 mg cm^{-2} (electrode geometric area: 1.54 cm^2) **(a, b)** before and after **(c, d)** 1 and **(e, f)** 100 cycles at a 1C rate as determined by processing X-ray CT datasets. In detail: **(a, c, e)** volume rendering (orthographic projection) showing the distribution of the sulfur phase across the XZ plane, where X is the axis parallel to the electrode plane and Z is the sample rotation axis orthogonal to the electrode plane; **(b, d, f)** phase fraction of sulfur along the Z axis. See Figures 2.4.3 and 2.4.4 showing the cycling performance of the cell and the X-ray CT imaging of the electrode samples, respectively.

Further steps toward the achievement of practical Li-S batteries involve increasing the active material loading in the cathode and decreasing the E/S ratio in the cell.[76,83,86] Therefore, the S:Au 97:3 w/w material is further investigated in a more challenging experimental condition using a coin cell with sulfur loading of 5.7 mg cm^{-2} and E/S ratio of 5 µL mg^{-1}, still retaining a sulfur fraction of 78 wt% in the electrode film. It is worth mentioning that the sulfur loading was slightly lower with respect to the analogue measurements performed on the S:Sn 85:15 w/w and S:Ni 85:15 w/w electrodes in section *2.3* (Fig. 2.3.9c and d), that is, 6.8 and 6.3 mg cm^{-2}, respectively, in view of the lower amount of metal additive and E/S ratio (compare the experimental conditions in *2.3.2* and *2.42 Experimental* sections). Figure 2.4.6 shows the voltage profiles (Fig. 2.4.6a) and cycling trend over 40 cycles (Fig. 2.4.6b) of the above Li|S:Au 97:3 w/w cell at the constant current rate of C/20, which corresponds to about 0.5 mA cm^{-2}. Figure 2.4.6a reveals that the increased loading, the limited electrolyte amount, and the notable sulfur ratio into the cathode, raise the polarization of the cell compared to that using mild conditions (Fig. 2.4.3). On the other hand, the battery exhibits the typical voltage signature of the Li-S conversion process and displays a significant change of the curve after the 1st cycle (Fig. 2.4.6a). This above discussed process leads to an initial capacity increase from ca. 3.2 to 4.5 mAh cm^{-2} (referred to the electrode geometric area of 1.54 cm^2), subsequent fluctuations with a maximum value of 5.4 mAh cm^{-2} (i.e., about 950 mAh g$_S^{-1}$), and a final value of 4.2 mAh cm^{-2} (i.e., about 730 mAh g$_S^{-1}$) after 40 discharge/charge cycles (Fig. 2.4.6b).
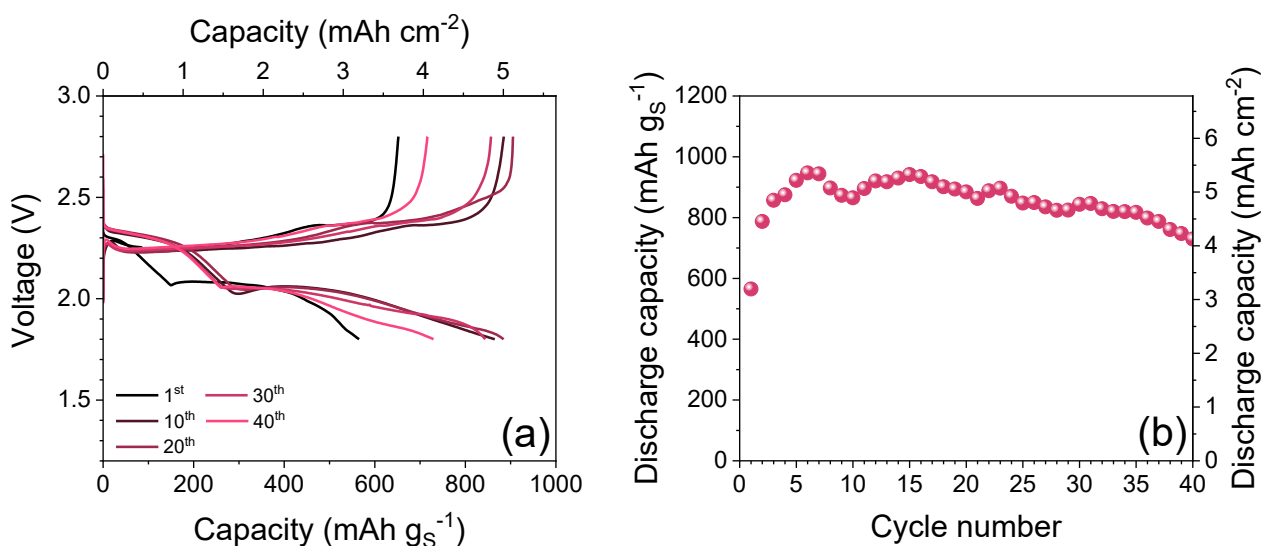

Figure 2.4.6. (a) Voltage profiles and **(b)** cycling trend at the constant current rate of C/20 of the Li|S:Au 97:3 w/w cell with sulfur loading over the electrode of 5.7 mg cm^{-2} and E/S ratio of 5 µL mg^{-1}. Voltage range: 1.8–2.8 V. Electrode geometric area: 1.54 cm^2.

X-ray CT imaging in Figure 2.4.7 demonstrates that increase in electrode loading and decrease in current rate only slightly affect the characteristic features of microstructural rearrangements associated with electrochemical activation of the cell upon a discharge/charge cycle. The figure shows cross-sectional slices visualized employing a grayscale (Fig. 2.4.7a and d) with corresponding segmentation (Fig. 2.4.7b and e) as well as segmented volume renderings of the samples in the field of view of the tomographic scan (Fig. 2.4.7c and f), referred to pristine and cycled electrodes.

As discussed above, gold aggregates exhibit significant attenuation of the beam, thereby forming bright spots in Figure 2.4.7a and b. Instead, sulfur, carbon-cloth, and carbon-binder domain are visualized as gray regions of different brightness due to the significantly higher X-ray transmittance. The comparison between Figures 2.4.7 and 2.4.4a–f, using the same color map for visualization, suggests similar depletion of sulfur along with its migration within the current collector pores by cycling. Furthermore, the low current rate and the increased loading likely boost the massive sulfur phase migration from the electrode surface to the bulk.
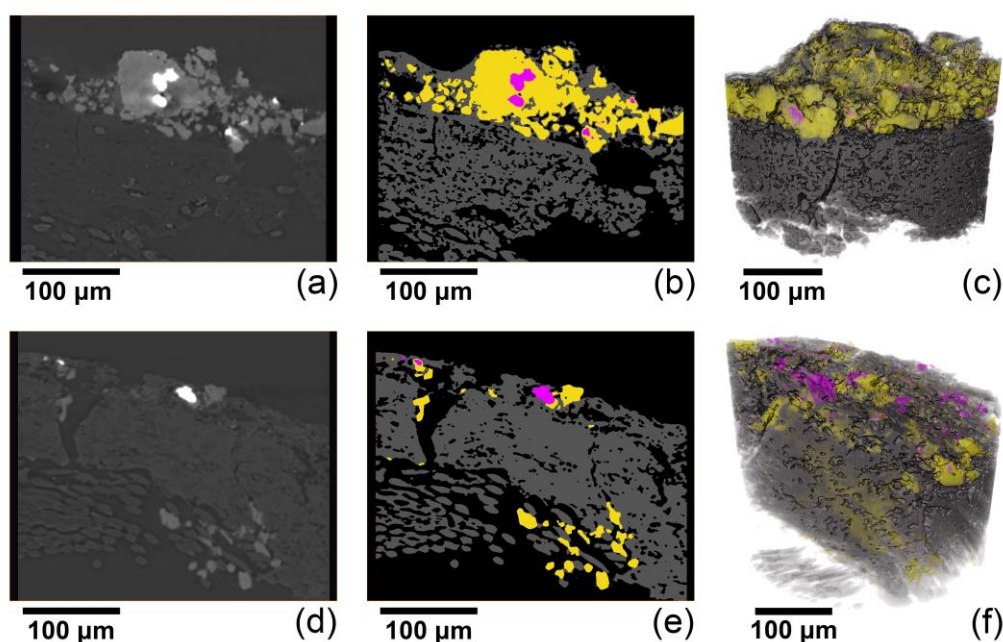
Figure 2.4.7. X-ray CT imaging at the microscale of S:Au 97:3 w/w electrodes with sulfur loading of 4.1 – 4.2 mg cm^{-2} (electrode geometric area: 1.54 cm^2) **(a–c)** before and **(d–f)** after 1 cycle at a C/10 rate. In detail: **(a, d)** cross-sectional slices extracted in a plane parallel to the rotation axis (Z axis) and orthogonal to the electrode plane (beam attenuation represented through a grayscale); **(b, e)** corresponding four-phase segmented slices (Au: magenta, S: yellow, C/PVDF/C-cloth: gray; exterior: black); **(c, f)** four-phase segmented volume rendering (Au: magenta, S: yellow, C/PVDF/C-cloth: gray; exterior: not represented. See Figures 2.4.6 and 2.4.8 showing the cycling performance of the cell and the distribution of the sulfur phase in the electrode samples, respectively.

A more quantitative description of this process is provided in Figure 2.4.8 which displays, in analogy to Figure 2.4.5, the sulfur distribution for pristine (Fig. 2.4.8a and b) and cycled electrodes (Fig. 2.4.8c and d) in the field of view of the X-ray CT scan. Indeed, volume renderings (Fig. 2.4.8a and c) and phase fraction of sulfur as a function of the position along the sample rotation axis Z (Fig. 2.4.8b and d) are studied upon cycling. The pristine cathode film, having approximate thickness of 110 µm (Fig. 2.4.8a and b), is significantly depleted after 1 cycle due to a substantial migration of the sulfur phase toward the current collector bulk (Fig. 2.4.8c and d). Furthermore, the comparison with the results of electrodes with lower loading studied at higher current rate (Fig. 2.4.5) suggests a significant effect of the cycling conditions on the extent of sulfur relocation. Relevantly, Figure 2.4.8c and d indicate a rather homogenous migration of the sulfur phase along the Z axis upon 1 cycle instead of the retention of large fraction on the electrode surface observed in Fig. 2.4.5c and d, thus suggesting that current rate, electrode loading, and E/S ratio can drive the local kinetics of electrodeposition on the current collector.
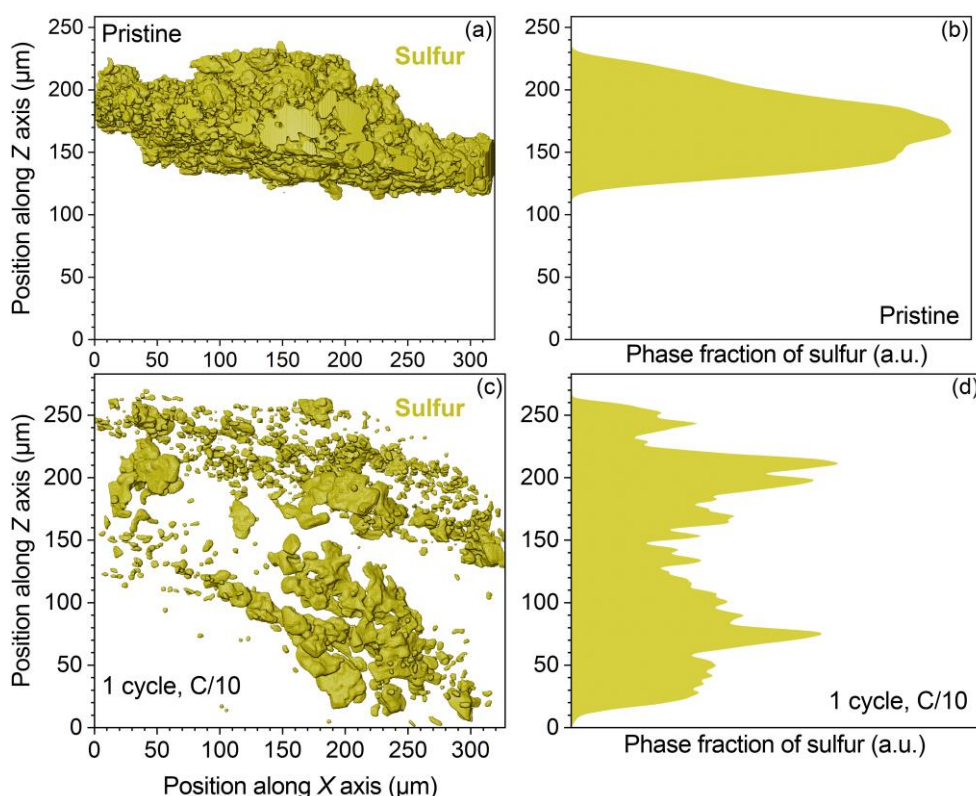

Figure 2.4.8. Distribution of the sulfur phase in the S:Au 97:3 w/w electrodes with sulfur loading of 4.1 – 4.2 mg cm^{-2} (electrode geometric area: 1.54 cm^2) **(a, b)** before and **(c, d)** after 1 cycle at a C/10 rate as determined by processing X-ray CT datasets. In detail: **(a, c)** volume rendering (orthographic projection) showing the distribution of the sulfur phase across the XZ plane, where X is the axis parallel to the electrode plane and Z is the sample rotation axis orthogonal to the electrode plane; **(b, d)** phase fraction of sulfur along the Z axis. See Figures 2.4.6 and 2.4.7 showing the cycling performance of the cell and the X-ray CT imaging of the electrode samples, respectively.

Therefore, it is important to remark that the porous carbon support plays herein a crucial role in improving the cell performance during repeated charge/discharge cycles by providing suitable reaction sites for the reversible conversion of sulfur.[22,87] However, the replacement of the Al foils commonly used in battery as electrode support with thicker 3D current collectors having high surface area and containing large amount of carbon may possibly decrease the energy density of the cell, thereby mitigating the effects of cathode film optimization. In this regard, both Figures 2.4.4 and 2.4.7 reveal that a considerable fraction of electrode support has a negligible contribution to the electrochemical reaction, thereby suggesting large room for improvement by technological engineering of suitable 3D carbon frameworks. Indeed, *ad hoc* designed carbon-coated thin supports with similar microstructure and surface chemistry to those employed herein are expected to ensure comparable cycling performances and remarkable energy density.

The results on sulfur migration within the positive electrode reported herein are in full agreement with previous sections and literature data[23] and reveal massive microstructural reorganizations in the cathode promoted by the reversible conversion of sulfur into soluble lithium polysulfides.[88] However, it has been discussed in section *2.1* that sulfur distribution in the pristine cathode affects the electrochemical performance of the cell, and supposed that the pristine morphology might influence the microstructure of the carbon-binder domain and the sulfur nucleation sites upon charging, thus driving the reaction kinetics. In this regard, the S:Au 97:3 w/w electrode herein optimized may achieve an outstanding performance in a suitable cell configuration, as demonstrated in Figure 2.4.9a. Indeed, this composite cathode has been tested upon 300 cycles at a 2C rate in a lithium cell with a sulfur loading over the electrode of 1.4 mg cm^{-2} and an E/S ratio of 15 µL mg^{-1}, revealing a maximum capacity approaching 1300 mAh gs^{-1} and a capacity retention at the end of the test of about 70%. These results further demonstrate the suitable characteristics of the S:Au 97:3 w/w electrode formulation for application in lithium-sulfur batteries. Figure 2.4.9b and c show the X-ray imaging of the anode before and after cycling, respectively, in terms of cross-sectional slices extracted in planes orthogonal to the electrode and volume rendering represented as an orthographic projection across the electrode plane. Notably, the observed capacity fading is in part ascribable to undesired reactions occurring over the negative electrode and leading to precipitation of micrometric particles that possibly hinder a smooth lithium electrodeposition, rather than to an actual degradation of the cathode material, as indeed confirmed by *ex situ* X-ray CT analyses (Fig. 2.4.9b and c). Large precipitates are observed over the anode both before (Fig. 2.4.9b) and after cycling (Fig. 2.4.9c). The X-ray CT data reveals the formation of a native passivation layer (Fig. 2.4.9b) over the anode along with a massive precipitation of particles with heterogenous morphology upon prolonged cycling (Fig. 2.4.9c). These precipitates have a higher density compared to lithium metal, which is

94

reflected as different attenuation of the X-ray beam in Fig. 2.4.9b and c. These results suggest additional improvements of the Li/S cell by developing *ad hoc* electrolyte formulations enabling in situ formation of a more stable SEI on the lithium-metal electrode and a smooth lithium electrodeposition, as well as by ex situ engineering of artificial passivation layers.
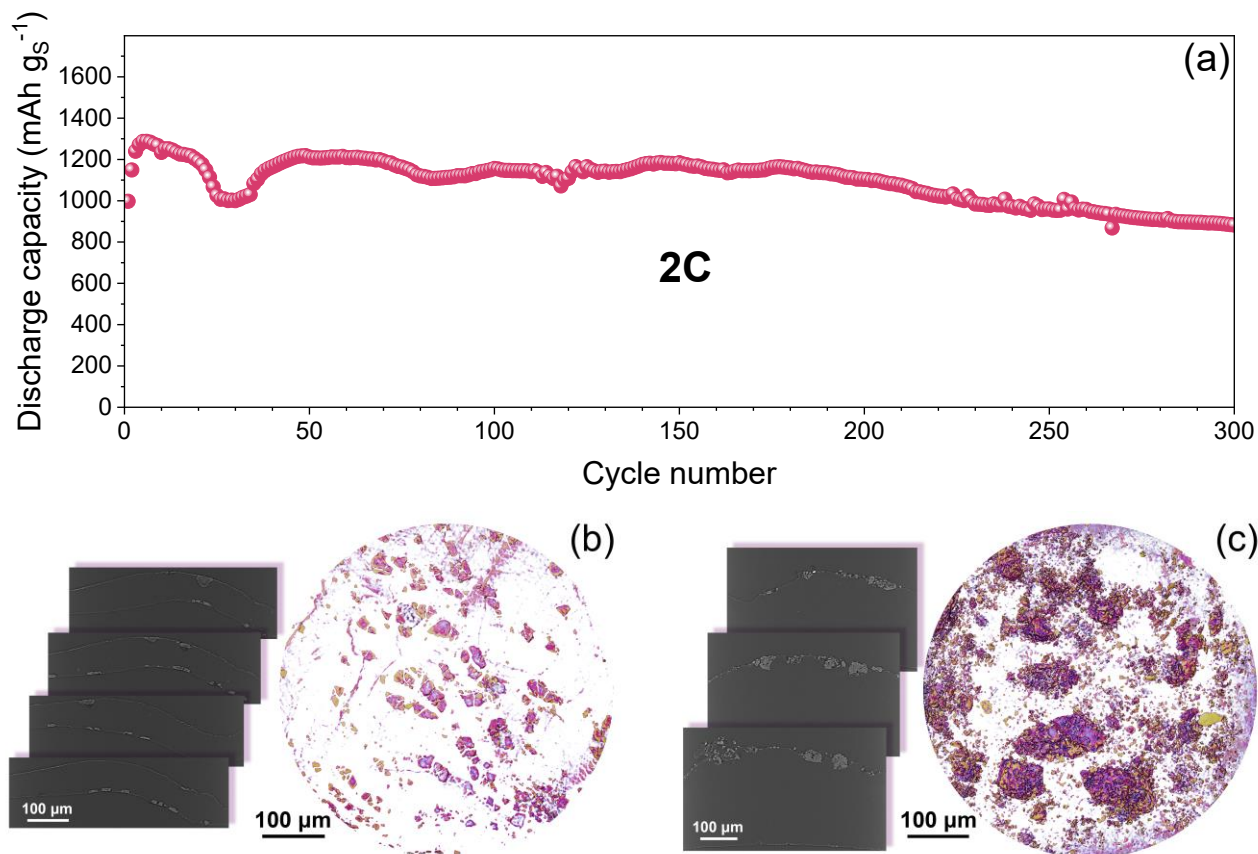
Figure 2.4.9. (a) Discharge capacity of the Li|S:Au 97:3 w/w cell over 300 cycles at the constant current rate of 2C. The sulfur loading over the electrode is 1.4 mg cm^{-2} (electrode geometric area: 1.54 cm^2) and the E/S ratio is 15 µL mg^{-1}. Voltage range: 1.8 – 2.8 V. **(b, c)** X-ray CT imaging at the microscale of the lithium-metal electrode **(b)** before and **(c)** after the cycling test, in terms of (left-hand side panels) cross-sectional slices extracted in planes orthogonal to the electrode and (right-hand side panels) volume rendering (orthographic projection) across the electrode plane; the sample of panel **(b)** was recovered from a Li|S:Au 97:3 w/w cell held at the OCV.

2.5 Summary

Straightforward preparation routes of S-C composites for lithium batteries are presented in section *2.1*, which involved mixing of commercial carbons, *i.e.*, super P carbon black (SPC) and multiwalled carbon nanotubes (MWCNTs), with sulfur (70wt%) by direct melting (MP) or by exploiting an alcohol dispersion route (SAP). Significant insights into the effects of the synthesis pathway and the carbon nature on the cathode microstructure, and of the latter on the electrochemical performances in lithium cell, were achieved by complementary combination of XRD, SEM, and X-ray CT at the nano- and microscale with galvanostatic cycling measurements across a wide current range. The composite cathodes consisted of heterogeneous dispersions of micrometric, crystalline sulfur particles surrounded by either SPC or MWCNTs and decreasing the average particle size with respect to the MWCNTs, while the SAP strongly mitigated the effect of the carbon nature on the morphology. On the other hand, SPC remarkably enhanced the sulfur conversion kinetics compared to MWCNTs, thus enabling a superior specific capacity. Remarkably, such an improvement was not affected by the sulfur particle size within the electrode, thereby suggesting a crucial role played by the SPC on the polysulfide conversion. Besides, the electrode prepared by SAP exploiting the MWCNTs (S@MWCNTs-SAP) benefited from a morphology consisting of large sulfur particles ensuring a capacity retention as high as 69% after 150 charge/discharge cycles.

The use of low amounts of metallic nanometric particles as conductive additive for sulfur cathodes was introduced in section *2.2*, where a sulfur–nanometric tin composite with a sulfur content as high as 80wt% was studied as the for application in Li/S batteries. The XRD measurements suggested a suitable physical mixing between sulfur and tin, while the electron microscopy (SEM, TEM, and EDS) indicated a uniform distribution of the nanometric tin into sulfur and a homogenous micrometric morphology of the composite. The electrochemical tests showed the expected sulfur-supporting role of the nanometric tin metal, which is electrochemically inactive within the exploited potential range, and the remarkable suitability for battery application of the resulting composite. Indeed, CV displayed a highly reversible electrochemical reaction with low polarization and material loss, whereas EIS suggested an activation process with the formation of a protective SEI layer and favorable structural modifications leading to an electrode/electrolyte interphase resistance limited to few ohms. The Li/S-Sn battery delivered a maximum capacity of about 1200 mAh gs^{-1} and a remarkable rate capability with a capacity approaching 800 mAh gs^{-1} at high C-rates (1C and 2C).

Upon showing in section *2.1* the suitability of X-ray CT technique for characterization of electrodes microstructure, sulfur-metal nanocomposites benefiting of either tin or nickel nanoparticles and an increased sulfur content as high as 85wt% were investigated in section *2.3* in

terms of structure, morphology and electrochemical behavior by combining X-ray imaging with the well-known techniques already employed in section *2.2*. This characterization has shown that pristine materials have microstructural characteristics depending on the metal additive, which directly affect the reaction kinetics. Notably, tin is effectually embedded into the sulfur particles forming nanocomposite clusters, thereby improving the electrode charge transfer; however, nickel easily segregates lowering the rate capability. *Ex situ* analyses supported by X-ray CT data revealed that the electrode undergoes substantial microstructural reorganization during the first discharge/charge cycle in the cell, entailing the gradual migration of sulfur *i)* toward the current collector bulk and close to the electron-conducting metal centers, which is in full agreement with the activation process proposed in section *2.2*. Thus, it is suggested that both conductive carbon-cloth electrode support and metal centers may act as preferred sites for sulfur electrodeposition upon charging. Such a process can lead to a massive loss of crystallinity of the sulfur phase along with a decrease in the average particle size. The observed electrode rearrangements are reflected as a shift in the potential and a remarkable drop in the electrode/electrolyte interphase resistance, probably attributable to the improved electric contact of newly electrodeposited sulfur. Meanwhile, Li–S cells using S–Sn and S–Ni electrodes exhibit cycling behavior at various currents in complete agreement with the microstructure. In detail, the former material exhibits higher rate capability probably due to the higher homogenous mixing between S and Sn particles, ensuring capacity of 560 mA h g$_S^{-1}$ at a 5C rate, while the latter delivers higher capacity at lower current rates, that is, from 1390 to 740 mA h g$_S^{-1}$ within the rates ranging from C/3 to 3C. Hence, reversible sulfur conversion at about 2.2 V *vs* Li$^+$/Li with coulombic efficiency close to 100% and capacity retention of about 70% have been demonstrated in discharge/charge measurements up to 300 cycles.

The content of active material in a sulfur-metal composite was further enhanced in section *2.4*, where sulfur was physically mixed with gold nanopowder in the ratio of 97:3 w/w and the novel composite was through by the multidisciplinary approach suggested in section *2.3*. X-ray CT reconstructions, electron microscopy images, and XRD patterns have revealed a crystalline material in which the noble metal forms micrometric and submicrometric aggregates of primary particles smaller 100 nm surrounded by sulfur clusters ranging from 5 to 50 μm. A cathode incorporating 78wt% of sulfur in the composite film was prepared by conventional casting on a carbon-cloth current collector. In according with sections *2.2* and *2.3*, electrochemical characterization of the cathode in a lithium cell *via* voltammetry, impedance spectroscopy, and galvanostatic cycling has identified a significant change in sulfur conversion kinetics after the first discharge/charge cycle, reflected as remarkable decrease in electrode/electrolyte interphase resistance and increase in reversible capacity. X-ray CT analyses at the microscale have evidenced the expected migration of sulfur upon cycling

throughout the porous electrode, from the surface to the inner side, and a gradual solubilization of the active material. Therefore, the electrochemical activation of the cell during the initial cycles has been causally related to the microstructural reorganizations observed in the positive electrode thank to the coherent data collected in sections *2.2*, *2.3* and *2.4*. The addition of gold in the cathode was observed to cause an increase in both electronic and Li^+ conductivities within the electrode, which triggers a raise in sulfur utilization and reversible capacity. Despite the low amount of additive in the cathode formulation, the lithium cell with sulfur loading of about 2 mg cm^{-2} and E/S ratio of 15 µL mg^{-1} has exhibited satisfactory rate capability, maximum capacity above 1300 mAh g_S^{-1} at C/10, capacities of about 1100 mAh g_S^{-1} at C/3 and 1000 mAh g_S^{-1} at 1C with retention in the 85% – 91% range after 100 cycles, and coulombic efficiency approaching 100%. Cycling tests have shown that the sulfur loading in the positive electrode may be increased up to almost 6 mg cm^{-2} simultaneously decreasing the E/S ratio to 5 µL mg^{-1}, thereby reaching areal capacity values between 5.4 and 4.2 mAh cm^{-2}, which correspond to about 950 and 730 mAh g_S^{-1}, respectively. Moreover, the Li/S-Au cell was able to achieve 300 cycles while retaining 70% of the maximum capacity. X-ray CT has enabled the clear visualization of large precipitates over the lithium-metal electrode, which possibly contribute to the partial degradation of the cell.

2.6 References

[1]   A. Manthiram, Y. Fu, S.-H. Chung, C. Zu, Y.-S. Su, *Chem. Rev.* **2014**, *114*, 11751.

[2]   P. Han, S.-H. Chung, C.-H. Chang, A. Manthiram, *ACS Appl. Mater. Interfaces* **2019**, *11*, 17393.

[3]   M. Shaibani, M. S. Mirshekarloo, R. Singh, C. D. Easton, M. C. D. Cooray, N. Eshraghi, T. Abendroth, S. Dörfler, H. Althues, S. Kaskel, A. F. Hollenkamp, M. R. Hill, M. Majumder, *Sci. Adv.* **2020**, *6*, eaay2757.

[4]   X. Ji, K. T. Lee, L. F. Nazar, *Nat. Mater.* **2009**, *8*, 500.

[5]   G. Zheng, Y. Yang, J. J. Cha, S. S. Hong, Y. Cui, *Nano Lett.* **2011**, *11*, 4462.

[6]   J. Zhang, H. Huang, J. Bae, S. Chung, W. Zhang, A. Manthiram, G. Yu, *Small Methods* **2018**, *2*, 1700279.

[7]   L. Carbone, T. Coneglian, M. Gobet, S. Munoz, M. Devany, S. Greenbaum, J. Hassoun, *J. Power Sources* **2018**, *377*, 26.

[8]   R. Xu, J. C. M. Li, J. Lu, K. Amine, I. Belharouak, *J. Mater. Chem. A* **2015**, *3*, 4170.

[9]   H. Tan, S. Wang, D. Tao, Z. Yang, *Energies* **2013**, *6*, 3466.

[10] Y.-T. Weng, H. Wang, R.-C. Lee, C.-Y. Huang, S.-S. Huang, M. Abdollahifar, L.-M. Kuo, B.-J. Hwang, C.-L. Kuo, Y. Cui, N.-L. Wu, *J. Power Sources* **2020**, *450*, 227676.

[11] L. Carbone, J. Peng, M. Agostini, M. Gobet, M. Devany, B. Scrosati, S. Greenbaum, J. Hassoun, *ChemElectroChem* **2017**, *4*, 209.

[12] H.-J. Peng, J.-Q. Huang, X.-B. Cheng, Q. Zhang, *Adv. Energy Mater.* **2017**, *7*, 1700260.

[13] C. Tan, T. M. M. Heenan, R. F. Ziesche, S. R. Daemi, J. Hack, M. Maier, S. Marathe, C. Rau, D. J. L. Brett, P. R. Shearing, *ACS Appl. Energy Mater.* **2018**, *1*, 5090.

[14] D. Di Lecce, S. Levchenko, F. Iacoviello, D. J. L. Brett, P. Shearing, J. Hassoun, *ChemSusChem* **2019**, 1.

[15] B. Meyer, *Chem. Rev.* **1976**, *76*, 367.

[16] O. O. Taiwo, D. P. Finegan, J. Gelb, C. Holzner, D. J. L. Brett, P. R. Shearing, *Chem. Eng. Sci.* **2016**, *154*, 27.

[17] T. M. M. Heenan, J. J. Bailey, X. Lu, J. B. Robinson, F. Iacoviello, D. P. Finegan, D. J. L. Brett, P. R. Shearing, *Fuel Cells* **2017**, *17*, 75.

[18] C. Tan, M. D. R. Kok, S. R. Daemi, D. J. L. Brett, P. R. Shearing, *Phys. Chem. Chem. Phys.* **2019**, *21*, 4145.

[19] B. Münch, L. Holzer, *J. Am. Ceram. Soc.* **2008**, *91*, 4059.

[20] X. Yu, H. Wu, J. H. Koo, A. Manthiram, *Adv. Energy Mater.* **2020**, *10*, 1902872.

[21] H.-J. Peng, W.-T. Xu, L. Zhu, D.-W. Wang, J.-Q. Huang, X.-B. Cheng, Z. Yuan, F. Wei, Q. Zhang, *Adv. Funct. Mater.* **2016**, *26*, 6351.

[22] A. Benítez, Á. Caballero, E. Rodríguez-Castellón, J. Morales, J. Hassoun, *ChemistrySelect* **2018**, *3*, 10371.

[23] L. Zielke, C. Barchasz, S. Waluś, F. Alloin, J.-C. Leprêtre, A. Spettl, V. Schmidt, A. Hilger, I. Manke, J. Banhart, R. Zengerle, S. Thiele, *Sci. Rep.* **2015**, *5*, 10921.

[24] J. Lee, A. S. Teja, *J. Supercrit. Fluids* **2005**, *35*, 83.

[25] L. Carbone, S. G. Greenbaum, J. Hassoun, *Sustain. Energy Fuels* **2017**, *1*, 228.

[26] S. Zhang, K. Ueno, K. Dokko, M. Watanabe, *Adv. Energy Mater.* **2015**, *5*, 1500117.

[27] G. Li, J. Sun, W. Hou, S. Jiang, Y. Huang, J. Geng, *Nat. Commun.* **2016**, *7*, 10601.

[28] A. Benítez, D. Di Lecce, G. A. Elia, Á. Caballero, J. Morales, J. Hassoun, *ChemSusChem* **2018**, *11*, 1512.

[29] H. Kim, J. T. Lee, A. Magasinski, K. Zhao, Y. Liu, G. Yushin, *Adv. Energy Mater.* **2015**, *5*, 1501306.

[30] Y.-S. Su, A. Manthiram, *Electrochim. Acta* **2012**, *77*, 272.

[31] M. Jeong, S. Ahn, T. Yokoshima, H. Nara, T. Momma, T. Osaka, *Nano Energy* **2016**, *28*, 51.

[32] H. Ren, X. Mu, Y. Huang, Z. Li, Y. Wang, P. Cai, Z. Peng, Y. Zhou, *Ionics (Kiel).* **2010**, *16*, 497.

[33] A. Sivashanmugam, T. P. Kumar, N. G. Renganathan, S. Gopukumar, M. Wohlfahrt-Mehrens, J. Garche, *J. Power Sources* **2005**, *144*, 197.

[34] S.-H. Chung, C.-H. Chang, A. Manthiram, *Energy Environ. Sci.* **2016**, *9*, 3188.

[35] D. Avellaneda, I. Sánchez-Orozco, J. A. A. Martínez, S. Shaji, B. Krishnan, *Mater. Res. Express* **2019**, *6*, 016409.

[36] D. H. Youn, S. K. Stauffer, P. Xiao, H. Park, Y. Nam, A. Dolocan, G. Henkelman, A. Heller, C. B. Mullins, *ACS Nano* **2016**, *10*, 10778.

[37] B. Scrosati, J. Hassoun, Y.-K. Sun, *Energy Environ. Sci.* **2011**, *4*, 3287.

[38] Q. Wang, D. A. Zhang, Q. Wang, J. Sun, L. L. Xing, X. Y. Xue, *Electrochim. Acta* **2015**, *173*, 476.

[39] J. Hassoun, G. Derrien, S. Panero, B. Scrosati, *Adv. Mater.* **2008**, *20*, 3169.

[40] A. Manthiram, S.-H. Chung, C. Zu, *Adv. Mater.* **2015**, *27*, 1980.

[41] Z. Zhao, D. Qin, S. Wang, G. H. Chen, Z. Li, *Electrochim. Acta* **2014**, *127*, 123.

[42] C. Barchasz, F. Molton, C. Duboc, J.-C. Leprêtre, S. Patoux, F. Alloin, *Anal. Chem.* **2012**, *84*, 3973.

[43] A. Rosenman, R. Elazari, G. Salitra, E. Markevich, D. Aurbach, A. Garsuch, *J. Electrochem.*

Soc. **2015**, *162*, A470.

[44] S. S. Zhang, *Electrochim. Acta* **2012**, *70*, 344.

[45] B. A. Boukamp, *Solid State Ionics* **1986**, *20*, 31.

[46] B. A. Boukamp, *Solid State Ionics* **1986**, *18–19*, 136.

[47] D. Aurbach, *J. Power Sources* **2000**, *89*, 206.

[48] C. fringant, A. Tranchant, R. Messina, *Electrochim. Acta* **1995**, *40*, 513.

[49] D. R. Franceschetti, J. R. Macdonald, R. P. Buck, *J. Electrochem. Soc.* **1991**, *138*, 1368.

[50] S. Drvarič Talian, J. Moškon, R. Dominko, M. Gaberšček, *ACS Appl. Mater. Interfaces* **2017**, *9*, 29760.

[51] S. Waluś, C. Barchasz, R. Bouchet, J.-C. Leprêtre, J.-F. Colin, J.-F. Martin, E. Elkaïm, C. Baehtz, F. Alloin, *Adv. Energy Mater.* **2015**, *5*, 1500165.

[52] G. Zhou, S. Pei, L. Li, D.-W. Wang, S. Wang, K. Huang, L.-C. Yin, F. Li, H.-M. Cheng, *Adv. Mater.* **2014**, *26*, 664.

[53] Y.-S. Su, A. Manthiram, *Nat. Commun.* **2012**, *3*, 1166.

[54] X. Tao, J. Wan, C. Liu, H. Wang, H. Yao, G. Zheng, Z. W. Seh, Q. Cai, W. Li, G. Zhou, C. Zu, Y. Cui, *Nat. Commun.* **2016**, *7*, 11203.

[55] G. Zhou, E. Paek, G. S. Hwang, A. Manthiram, *Adv. Energy Mater.* **2016**, *6*, 1501355.

[56] J. Hassoun, Y. K. Sun, B. Scrosati, *J. Power Sources* **2011**, *196*, 343.

[57] S. Xiong, K. Xie, Y. Diao, X. Hong, *Ionics (Kiel).* **2012**, *18*, 867.

[58] N. Moreno, A. Caballero, J. Morales, M. Agostini, J. Hassoun, *Mater. Chem. Phys.* **2016**, *180*, 82.

[59] H. Kim, H.-D. Lim, J. Kim, K. Kang, *J. Mater. Chem. A* **2014**, *2*, 33.

[60] A. Ševčík, *Collect. Czechoslov. Chem. Commun.* **1948**, *13*, 349.

[61] J. E. B. Randles, *Trans. Faraday Soc.* **1948**, *44*, 327.

[62] S. Yamada, M. Fujiwara, M. Kanda, *J. Power Sources* **1995**, *54*, 209.

[63] Y. Gao, L. Wang, W. Zhang, X. Yang, Y. Ma, J. Shao, Y. Li, *Electrochim. Acta* **2016**, *201*, 260.

[64] Y. Hou, H. Kondoh, T. Ohta, S. Gao, *Appl. Surf. Sci.* **2005**, *241*, 218.

[65] Q. Wang, J. Zheng, E. Walter, H. Pan, D. Lv, P. Zuo, H. Chen, Z. D. Deng, B. Y. Liaw, X. Yu, X. Yang, J.-G. Zhang, J. Liu, J. Xiao, *J. Electrochem. Soc.* **2015**, *162*, A474.

[66] H. Kim, J. Lee, H. Ahn, O. Kim, M. J. Park, *Nat. Commun.* **2015**, *6*, 7278.

[67] J. Zhu, E. Yildirim, K. Aly, J. Shen, C. Chen, Y. Lu, M. Jiang, D. Kim, A. E. Tonelli, M. A. Pasquinelli, P. D. Bradford, X. Zhang, *J. Mater. Chem. A* **2016**, *4*, 13572.

[68] A. Benítez, A. Caballero, J. Morales, J. Hassoun, E. Rodríguez-Castellón, J. Canales-

Vázquez, *Nano Res.* **2019**, *12*, 759.

[69]   H. D. Shin, M. Agostini, I. Belharouak, J. Hassoun, Y. K. Sun, *Carbon N. Y.* **2016**, *96*, 125.

[70]   C.-H. Liu, T.-H. Ko, W.-S. Kuo, H.-K. Chou, H.-W. Chang, Y.-K. Liao, *J. Power Sources* **2009**, *186*, 450.

[71]   G. Tonin, G. Vaughan, R. Bouchet, F. Alloin, M. Di Michiel, L. Boutafa, J.-F. Colin, C. Barchasz, *Sci. Rep.* **2017**, *7*, 2755.

[72]   F. Sun, M. Osenberg, K. Dong, D. Zhou, A. Hilger, C. J. Jafta, S. Risse, Y. Lu, H. Markötter, I. Manke, *ACS Energy Lett.* **2018**, *3*, 356.

[73]   H. Yuan, H.-J. Peng, B.-Q. Li, J. Xie, L. Kong, M. Zhao, X. Chen, J.-Q. Huang, Q. Zhang, *Adv. Energy Mater.* **2019**, *9*, 1802768.

[74]   S. Chung, A. Manthiram, *Adv. Mater.* **2019**, *31*, 1901125.

[75]   R. Fang, S. Zhao, Z. Sun, D.-W. Wang, H.-M. Cheng, F. Li, *Adv. Mater.* **2017**, *29*, 1606823.

[76]   D. Eroglu, K. R. Zavadil, K. G. Gallagher, **2015**, *162*, 982.

[77]   L. Carbone, M. Gobet, J. Peng, M. Devany, B. Scrosati, S. Greenbaum, J. Hassoun, *ACS Appl. Mater. Interfaces* **2015**, *7*, 13859.

[78]   H. Al Salem, G. Babu, C. V. Rao, L. M. R. Arava, *J. Am. Chem. Soc.* **2015**, *137*, 11542.

[79]   C.-Y. Fan, P. Xiao, H.-H. Li, H.-F. Wang, L.-L. Zhang, H.-Z. Sun, X.-L. Wu, H.-M. Xie, J.-P. Zhang, *ACS Appl. Mater. Interfaces* **2015**, *7*, 27959.

[80]   W. Zhang, C. Yang, B. Ding, J. Peng, F. Xu, M. Zheng, H. Hu, Y. Xiao, Y. Liu, Y. Liang, *Chem. Commun.* **2020**, *56*, 1215.

[81]   B. Hammer, J. K. Norskov, *Nature* **1995**, *376*, 238.

[82]   S.-H. Yu, X. Huang, K. Schwarz, R. Huang, T. A. Arias, J. D. Brock, H. D. Abruña, *Energy Environ. Sci.* **2018**, *11*, 202.

[83]   A. Bhargav, J. He, A. Gupta, A. Manthiram, *Joule* **2020**, *4*, 285.

[84]   W. Li, H. Yao, K. Yan, G. Zheng, Z. Liang, Y.-M. Chiang, Y. Cui, *Nat. Commun.* **2015**, *6*, 7436.

[85]   M. Agostini, S. Xiong, A. Matic, J. Hassoun, *Chem. Mater.* **2015**, *27*, 4604.

[86]   S. Dörfler, H. Althues, P. Härtel, T. Abendroth, B. Schumm, S. Kaskel, *Joule* **2020**, *4*, 539.

[87]   R. Fang, S. Zhao, P. Hou, M. Cheng, S. Wang, H.-M. Cheng, C. Liu, F. Li, *Adv. Mater.* **2016**, *28*, 3374.

[88]   J. B. Robinson, K. Xi, R. V. Kumar, A. C. Ferrari, H. Au, M.-M. Titirici, A. Parra-Puerto, A. Kucernak, S. D. S. Fitch, N. Garcia-Araez, Z. L. Brown, M. Pasta, L. Furness, A. J. Kibler, D. A. Walsh, L. R. Johnson, C. Holc, G. N. Newton, N. R. Champness, F. Markoulidis, C. Crean, R. C. T. Slade, E. I. Andritsos, Q. Cai, S. Babar, T. Zhang, C. Lekakou, N. Kulkarni,

A. J. E. Rettie, R. Jervis, M. Cornish, M. Marinescu, G. Offer, Z. Li, L. Bird, C. P. Grey, M. Chhowalla, D. Di Lecce, R. E. Owen, T. S. Miller, D. J. L. Brett, S. Liatard, D. Ainsworth, P. R. Shearing, *J. Phys. Energy* **2021**, *3*, 031501.

Chapter 3.

Promising glyme-based electrolytes

3.1 Highly-concentrated electrolyte solutions

3.1.1 Presentation

As reported in Chapter 1, metallic lithium is of great interest for the development of rechargeable batteries as it offers a high theoretical capacity (3860 mAh g^{-1}) and the lowest redox potential (−3.04 V vs SHE) among the various electrodes proposed as the battery anode.[1] Despite the various advantages, the application of lithium in a rechargeable battery has so far been hindered by the formation of dendritic structures due to heterogeneous deposition of lithium at the metal surface during charge that can lead to short circuits and hazards.[2] One of the most relevant solutions proposed to overcome this challenging issue and ensure efficient and safe discharge−charge cycling of the lithium battery is represented by the addition to the electrolyte of sacrificial agents such as lithium nitrate (LiNO$_3$), that can be reduced at the lithium surface to protect the metallic anode by the formation of a suitable solid electrolyte interphase (SEI) film.[3,4] A further relevant breakthrough was achieved by the replacement of carbonate-based solvents with more stable and less volatile end-capped glymes (CH$_3$O(CH$_2$CH$_2$O)$_n$CH$_3$).[5–7] Remarkable improvement of the safety content of the cell was furthermore obtained by increasing the salt concentration, in particular using the glyme-based electrolytes, in order to decrease the flammability and the volatility, holding at the same time long cycle life and high coulombic efficiency.[8–10] In this section, the chemical and electrochemical properties of highly concentrated di- and triglyme-based electrolytes employing the conductive salt lithium bis(trifluoromethanesulfonyl)imide (LiTFSI) and LiNO$_3$ in concentrations approaching the solvent saturation limit are characterized. In particular, X-ray photoelectron spectroscopy is used to analyze the composition of the SEI film formed at the lithium metal surface, thermogravimetric analyses are carried out to evaluate the thermal stability of the electrolytes, while electrochemical impedance spectroscopy, chronoamperometry, Li$^+$ stripping/deposition tests and voltammetry are exploited to investigate the Li$^+$ ions transport properties and measure the electrochemical stability window. Successively, the solutions are applied in Li-S batteries employing the sulfur-tin cathode characterized in Chapter 2, section *2.2*. The electrochemical behavior of the Li-S cells is evaluated by means of cycling voltammetry and galvanostatic cycling.

3.1.2 Experimental

Lithium bis(trifluoromethanesulfonyl)imide (LiTFSI, 99.95% trace metals basis, Sigma-Aldrich) and lithium nitrate (LiNO$_3$, 99.99% trace metals basis, Sigma-Aldrich) salts were dissolved by magnetic stirring overnight at room temperature in either diethylene glycol dimethyl ether (DEGDME, CH$_3$O(CH$_2$CH$_2$O)$_2$CH$_3$, anhydrous, 99.5 % Sigma-Aldrich) or triethylene glycol dimethyl ether (TREGDME, CH$_3$O(CH$_2$CH$_2$O)$_3$CH$_3$, anhydrous, 99.5 %, Sigma-Aldrich) solvents in a ratio of 1.5 mol of each salt in 1 kg of DEGDME (~1.4 M) and 2 mol of each salt in 1 kg of TREGDME (~2.1 M). The salts used for the electrolyte preparation were previously heated at 110 °C under vacuum for 24 h to remove traces of water, while the solvents were dried with molecular sieves (3 Å, Sigma-Aldrich) until a water content below 10 ppm was obtained, as verified by 899 Karl Fischer Coulometer, Metrohm. The obtained highly concentrated electrolytes will be subsequently indicated by the acronyms DEGDME_HCE and TREGDME_HCE, respectively. It is worth mentioning that the difference between the concentrations used in the two electrolytes is because of the different solubility of the salts in DEGDME and TREGDME, that is, higher in the latter than in the former.

X-ray photoelectron spectroscopy (XPS) measurements were carried out on lithium foils previously soaked in the electrolytes for 2 days inside an Ar-filled glovebox (MBraun, O$_2$ and H$_2$O content below 1 ppm) to allow SEI film formation and then dried under vacuum for 3 h in order to remove the electrolyte. The XPS response was obtained under vacuum (10^{-5} mbar) by using a PHOIBOS HSA3500 150 R6 spectrometer exploiting monochromatic Al-Kα radiation (250 W) and a multichannel detector. Depth-profile data of the lithium sample surface were obtained by Ar$^+$ etching (acceleration voltage of 2.7 kV) at various sputtering times, that is, 0, 60, 120, 300, and 600 s.

Thermogravimetric analysis (TGA) was performed on DEGDME_HCE, TREGDME_HCE, DEGDME, TREGDME, LiTFSI, and LiNO$_3$ samples by increasing temperature from 25 to 800 °C with a rate of 5 °C min^{-1} in nitrogen flow through a Mettler Toledo-TGA/DSC.

The electrochemical measurements reported below were carried out by using CR2032 coin-type cells (MTI Corp.) assembled in an Ar-filled glovebox (MBraun, O$_2$ and H$_2$O content below 1 ppm). The ionic conductivity of DEGDME_HCE and TREGDME_HCE was determined by electrochemical impedance spectroscopy (EIS) performed upon scan from room temperature to about 76 °C in symmetrical stainless-steel/electrolyte/stainless-steel cells employing an O-ring spacer (CS Hyde, 23-5FEP-2-50) with a 10 mm internal diameter and thickness of 127 µm to fix the cell constant

at 0.0162 cm^{-1}. The impedance spectra were recorded by applying an alternate voltage signal of 10 mV in a frequency range between 500 kHz and 100 Hz.

The properties and the performances of the electrolytes in lithium cells were investigated by employing lithium disks with a 14 mm diameter as electrodes and GF/A glass fiber (Whatman) 16 mm disks soaked with either DEGDME_HCE or TREGDME_HCE as separators.

The Li$^+$ transference number of DEGDME_HCE and TREGDME_HCE was determined through the Bruce−Vincent−Evans method.[11] A chronoamperometric test was performed on symmetrical Li/electrolyte/Li cells by applying a voltage of 30 mV for 90 min, and impedance spectra were recorded by EIS before and after polarization using a signal of 10 mV in the 500 kHz to 100 mHz frequency range. The Li$^+$ transference number values were then calculated through equation (3.1.1):[11]

$$t^+ = \frac{i_{ss}}{i_0} \frac{\Delta V - R_0 i_0}{\Delta V - R_{ss} i_{ss}} \qquad (3.1.1)$$

where i_0 and i_{ss} are the current values at the initial and steady state, respectively, ΔV is the applied voltage, R_0 and R_{ss} are the interphase resistance values before and after cell polarization, respectively, calculated from the impedance spectra. The chronoamperometric measurements were carried out by using a VersaSTAT MC Princeton Applied Research (PAR, AMETEK) instrument.

The electrochemical stability of the electrolytes was evaluated through a lithium stripping/deposition test by means of galvanostatic cycling, where a current of 0.1 mA cm^{-2} was applied to Li/electrolyte/Li symmetrical cells using a MACCOR Series 4000 battery test system.

The Li/electrolyte interphase resistance was analyzed by EIS upon aging of symmetrical Li/Li cells employing either DEGDME_HCE or TREGDME_HCE. The spectra were recorded by applying a 10 mV signal in the 500 kHz to 100 mHz frequency range.

The electrochemical stability window of the electrolytes was evaluated through cyclic voltammetry (CV) in the cathodic region in the $0.01 − 2$ V vs Li$^+$/Li potential range and through linear sweep voltammetry (LSV) in the anodic region from the open-circuit voltage (OCV) condition to 5 V vs Li$^+$/Li. The tests were carried out in cells employing a lithium anode, either DEGDME_HCE or TREGDME_HCE, and carbon as the working electrode, which was coated on copper or an aluminum current collector to perform the measurement in the cathodic or anodic region, respectively. The anodic region was further investigated by a chronoamperometry test in the $4.0 − 4.6$ V vs Li$^+$/Li potential range. Prior to the experiment, a LSV scan was performed from the OCV to 3.9 V vs Li$^+$/Li, then the cell was held at 4 V for 1 h, and the potential was subsequently increased by using steps of 0.1 V every hour until 4.6 V while the current was measured during each step of chronoamperometry.

The carbon working electrodes were prepared by doctor blade casting on the corresponding current collector of a slurry formed by Super P carbon (SPC, Timcal) and polyvinylidene fluoride (Solef ® 6020 PVDF) binder in a weight ratio of 90:10, dispersed in N-methyl-2-pyrrolidone (Sigma-Aldrich) solvent. The slurry was dried at 70 °C under air for 3 h and cut into 14 mm disks, and the resulting electrodes were subsequently dried at 110 °C under vacuum overnight to remove possible traces of water or solvent. The voltammetry tests were performed by employing a scan rate of 0.1 mV s^{-1}.

The synthesis of the sulfur-tin composite S:Sn 80:20 w/w through a physical mixing and melting process of elemental sulfur (80wt%, ≥99.5%, Riedel-de Haën) and nanometric tin powder (20wt%, <150 nm, ≥99% trace metal basis, Sigma-Aldrich) at 120 °C (see section *2.2* in Chapter 2).

The electrochemical tests were carried out in CR2032 coin-type cells assembled in an Ar-filled glovebox (MBraun, O_2 and H_2O content below 1 ppm) by employing a 14 mm diameter lithium disk as the anode. The S:Sn 80:20 w/w electrodes were obtained by NMP-solvent casting of the active material (80wt%), SPC (10wt%, Timcal) and polyvinilidene fluoride (10wt%, Solef ® 6020 PVDF) on a porous carbon-cloth foil (GDL, ELAT 1400, MTI Corp.) . The active material loading was of about 1.3 mg cm^{-2} as normalized to the electrode geometric area (1.54 cm^2). The cathode was separated from the lithium anode by a 16 mm Celgard (2400) foil soaked with the electrolyte solution (either DEGDME_HCE or TREGDME_HCE, see below for the related amounts).

Cyclic voltammetry (CV) was performed at a scan rate of 0.1 mV s^{-1} in the 1.8 − 2.8 V *vs* Li$^+$/Li potential range. Electrochemical impedance spectra were collected at the open circuit voltage (OCV) condition of the cell, as well as after 1, 5, and 10 CV cycles, and were analyzed through the nonlinear least-squares (NLLS) fitting method via the Boukamp software (χ^2 values of the order of 10−4 or lower).[12,13] EIS was performed by applying to the cells an alternate voltage signal with an amplitude of 10 mV within the frequency range from 500 kHz to 100 mHz. All of the CV and EIS measurements were performed by using a VersaSTAT MC Princeton Applied Research (PAR, AMETEK) instrument. All Nyquist plots recorded through EIS were analyzed through NLLS analyses.

The Li-S:Sn 80:20 cells were tested through galvanostatic cycling measurements carried out at the constant current rate of C/5 at 25 and 35 °C and of 1C at 35 °C (1C = 1675 mA g$_S^{-1}$). The cells cycled at the current of C/5 employed 60 μL of electrolyte solution and a voltage range of 1.9 − 2.8 V, while voltage limits of 1.6 and 2.8 V and an electrolyte/sulfur ratio of 20 μL mg^{-1} were adopted for the cells tested at 1C. The galvanostatic cycling measurements related to the Li-S batteries were performed by using a MACCOR series 4000 battery test system.

3.1.3 Results

As mentioned previously, the formation of a SEI layer at the lithium anode by partial reduction of the electrolyte and concomitant passivation of the metal surface is widely considered to be the key factor for ensuring the electrode stability in the battery and limiting the formation of dendritic structures that can lead to short circuits and cell failure.[14] On the other hand, the actual role of the SEI is still an open point which may be further clarified by the study of the chemical nature of the species formed at the electrode surface.[15] Therefore, Figure 3.1.1 investigates the SEI composition at an increasing depth of lithium metal foils soaked into DEGDME_HCE and TREGDME_HCE solutions by means of XPS performed upon Ar$^+$ sputtering at various times, that is, 0, 60, 120, 300, and 600 s, to etch the passivation layer (see the *3.1.2 Experimental* section for further details). Figure 3.1.1a and b shows the survey spectra recorded after 600 s for DEGDME_HCE and TREGDME_HCE, respectively. The binding energies of the curves reveal that the SEI layer is mainly composed by C, O, F, N, S, and Li (see the detailed identification in Figure 3.1.2), as indeed expected by the components of the electrolytes (see the *3.1.2 Experimental* section), namely, the poly-ether chains of the organic solvents, the LiTFSI, and the LiNO$_3$ salts. The analysis of the above XPS data, reported in Table 3.1.1 and plotted in Figure 3.1.1c and d, reveals that the percent of the various elements changes upon surface etching, that is, by increasing the Ar$^+$ sputtering time, and likely indicates a different composition of outer layers of the SEI over the lithium with respect to the inner ones for both DEGDME_HCE (Fig. 3.1.1c) and TREGDME_HCE (Fig. 3.1.1d).

Electrolyte	Sputtering time (s)	C (%)	O (%)	F (%)	N (%)	S (%)	Li (%)
DEGDME_HCE	0	11.27	37.87	6.14	0.82	2.36	41.54
	60	11.98	41.19	2.42	0.17	1.36	42.87
	120	11.76	40.61	2.73	0.13	1.43	43.33
	300	9.88	38.24	3.55	0.16	1.22	46.96
	600	9.95	37.49	3.94	0.14	1.03	47.46
TREGDME_HCE	0	14.5	37.83	5.76	1.02	2.62	38.27
	60	12.68	37.53	2.97	0.47	2.43	43.92
	120	12.22	40.2	2.57	0.19	1.88	42.95
	300	10.48	39.16	3.01	0.15	1.34	45.88
	600	9.11	36.71	3.99	0.16	1.32	48.72

Table 3.1.1. Percent elements content determined by fitting of the XPS spectra (non reported), recorded at various times of Ar$^+$ sputtering carried out on the surface of lithium foils soaked for 2 days with either DEGDME_HCE or TREGDME_HCE, respectively. The corresponding trends *vs* time are depicted in Figure 3.1.1c and d, respectively.

It is worth noting that Li has the most relevant contribution to the XPS signal because of its metallic nature, followed by O which is contained in all the species forming the electrolytes. Furthermore, SEI-film etching slightly increases the Li signal as expected by the progressive exposure of the metal surface, while only minor fluctuations are observed for oxygen. The decrease of the C content by etching (Fig. 3.1.1c and d, and Table 3.1.1 at increasing times) suggests for both electrolytes a higher content of side species such as lithium carbonate and lithium oxide in the inner side of the SEI compared to the outer side, possibly because of the remarkable reactivity of the fresh lithium surface.[16,17] On the other hand, the outer side of the SEI observed before etching (Fig. 3.1.1c and d, and Table 3.1.1 at t = 0 s) reveals the highest concentration of S, N, and F likely due to the preferential precipitation of $LiNO_3$ and LiTFSI salts. In spite of a continuous decrease of S and N contents by etching, the F content initially decreases and subsequently increases, thus suggesting the formation of fluorinated precipitates such as LiF in the inner side of the SEI in proximity of the metallic surface.[18]
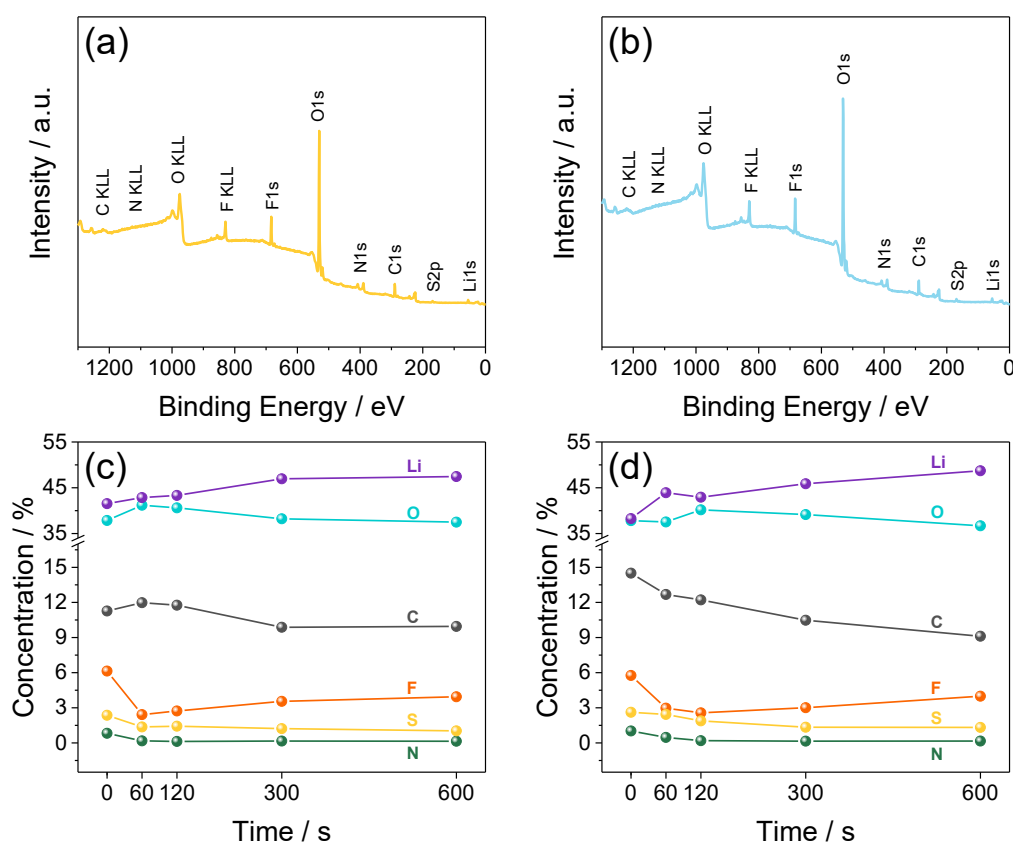
Figure 3.1.1. (a, b) X-ray photoelectron survey spectra recorded after 600 s of Ar^+ sputtering and **(c, d)** percent elements content detected upon Ar^+ etching of the surface of lithium foils soaked for 2 days with either **(a, c)** DEGDME_HCE or **(b, d)** TREGDME_HCE.

Further insights into the actual SEI composition are provided by the deconvoluted XPS responses referred to the various elements for DEGDME_HCE (Fig. 3.1.2a−f) and TREGDME_HCE (Fig. 3.1.2g−l). The C 1s signals (Fig. 3.1.2a and g) show a decreasing intensity upon etching of the peaks with binding energies of 284.6 and 286.7 eV, related to C−C and C−O−C or ROLi bonds,[19] respectively, and a concomitant increase of the intensity of the lithium carbonate Li_2CO_3 related peak at 289.6 eV.[20,21] A certain contribution to the carbon signal of LiTFSI salt cannot be completely excluded, however without significantly altering the qualitative evaluation of the results. This trend further suggests the predominant presence of Li_2CO_3 in the inner side of the SEI (t = 600 s), as already mentioned during discussion of Figure 3.1.1c and d, and indicates the precipitation in the outer SEI side of species characterized by organic C−C, C−O−C, and −CF3 bonds (t = 0 s).[22] In addition, a more intense signal at 286.7 eV (C−O−C, ROLi) for TREGDME_HCE (Fig. 3.1.2g) compared to DEGDME_HCE (Fig. 3.1.2a) suggests a bigger contribution to the SEI of the solvent with the longer ether chain. It is worth noting that the C 1s signal at 292.6 eV of the −CF3 groups because of LiTFSI salt[23] can be observed only at the initial stage before SEI etching for both electrolytes (Fig. 3.1.2a and g), thus suggesting possible lithium salt deposition at the outer SEI. This is likely confirmed by the F 1s signal (Fig. 3.1.2c and i) in which the peak between 687 and 688 eV, assigned to −CF3,[23] progressively vanishes by surface etching; concomitantly, the same panels reveal the increase of the peak at 683.6 eV and account for the formation of LiF due to salt decomposition on the lithium surface, particularly in the inner side of the SEI.[15] LiTFSI can also be associated to the broad S 2p signal (Fig. 3.1.2e and k) between 164 and 173 eV, which decreases by etching, and can be resolved in two peaks ascribable to the S $2p_{3/2}$ and S $2p_{1/2}$ doublet of the −SO2− group,[24] without excluding the possible formation of sulfur compounds with various oxidation states by reduction of the salt.[25] Moreover, the convoluted N 1s signals (Fig. 3.1.2d and j) between 394 and 401 eV, that merge into one after 120 s of etching, may likely account for the formation of negatively charged nitrogenous species, such as Li_3N (N^{3-}), and, more in general, LiN_xO_y[19] by the reduction of the $LiNO_3$ as well for the imide groups of LiTFSI salt.[23,25] On the other hand, the O 1s (Fig. 3.1.2b and h) and Li 1s (Fig. 3.1.2f and l) signals can actually identify the expected C−O bond and Li_2CO_3 at 531 eV, and ROLi species around 55 eV,[19,26] respectively, while the growth of the peaks at 527 eV by etching the samples (Fig. 3.1.2b and h) suggests the presence of Li_2O at the inner side of the SEI,[19,27] which is expected by the unavoidable partial oxidation of the lithium metal surface.

A further signal for TREGDME_HCE at 54.2 eV (Fig. 3.1.2l) may account for the presence of Li−C bonds[19,27] while possible contribution of LiF around 56.5 eV[23] and Li_2CO_3 at about 55.5 eV[28] to the broad Li 1s signal cannot be excluded. Overall, the XPS evidences the formation of a complex SEI on the lithium surface which is mainly composed of inorganic species, such as LiF,

Li$_2$CO$_3$, Li$_3$N, LiN$_x$O$_y$, and Li$_2$O, in the inner side near by the reactive metal, and organic solvent reduction products, such as ROLi and ROR as well as precipitated salts (e.g., LiTFSI), in the outer side. Indeed, the features of the SEI formed by DEGDME_HCE and TREGDME_HCE at the lithium surface can actually indicate possible applications of the electrolyte in efficient and stable batteries.
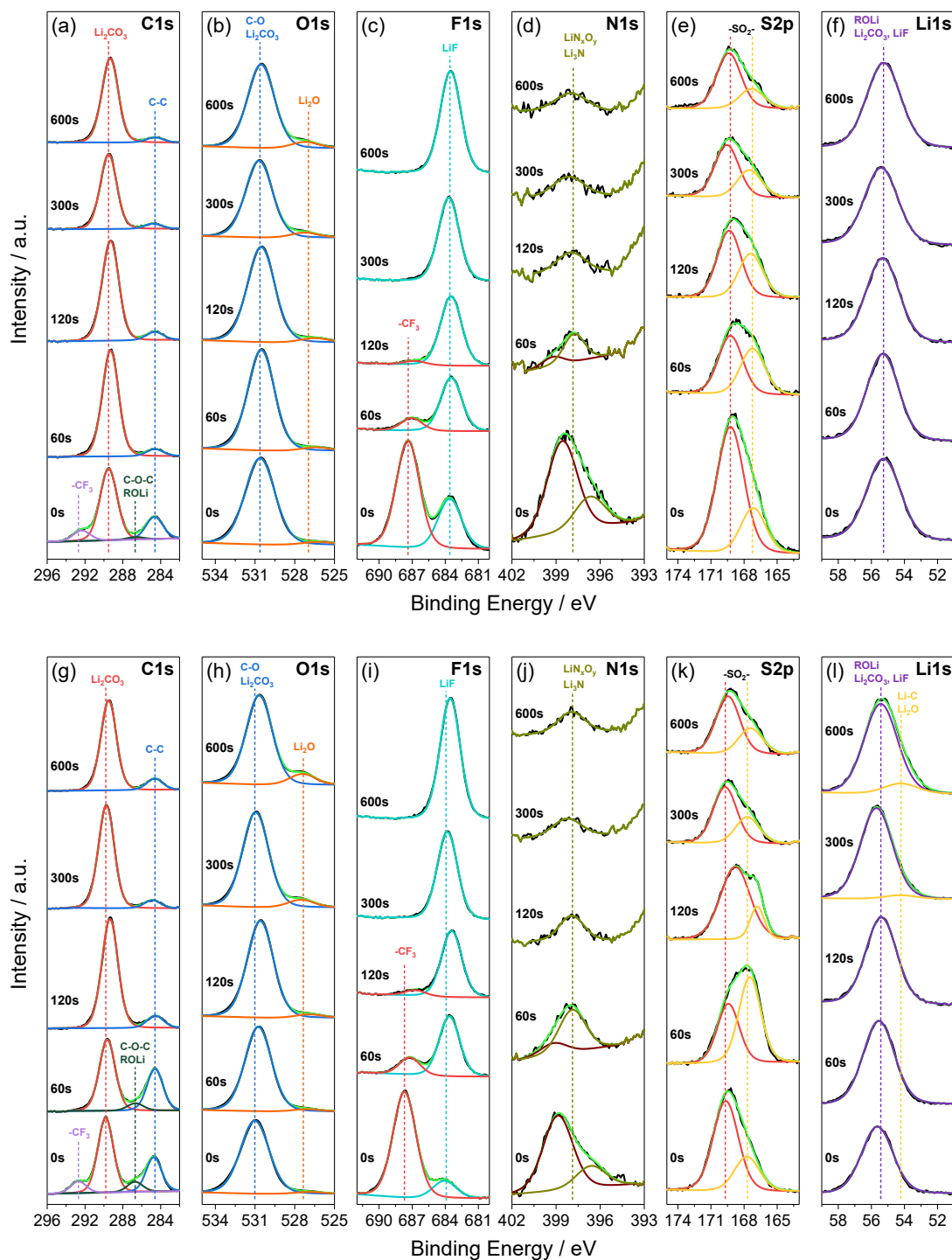
Figure 3.1.2. Deconvoluted XPS spectra of C 1s, O 1s, F 1s, N 1s, S 2p, and Li 1s for **(a−f)** DEGDME_HCE and **(g−l)** TREGDME_HCE at various times of Ar$^+$ sputtering on lithium foil surfaces aged in contact with the electrolytes for 2 days.

111

The thermal stability of electrolytes and solution components is investigated by TGA in view of possible applications in the Li-S battery. Figure 3.1.3 compares the responses of the two electrolytes with those of DEGDME and TREGDME solvents as well as LiTFSI and LiNO$_3$ salts, both in terms of weight loss (TGA, top panel) and corresponding differential curves (DTG, bottom panel). It is worth noting that the weight loss due to evaporation observed for DEGDME (green) and TREGDME (violet) begins at around 50 and 100 °C, respectively, while the one associated to the corresponding electrolytes occurs at 80 °C for DEGDME_HCE (orange) and 130 °C for TREGDME_HCE (blue). The remarkable boiling point elevation observed above may be likely ascribed to the relevant presence of lithium salts into the electrolyte formulation.[29] Furthermore, the longer glyme chain in TREGDME solvent compared with DEGDME is actually reflected into a lower volatility for TREGDME_HCE electrolyte compared to DEGDME_HCE and consequently into a higher safety content.[7] The multiple weight loss observed between 200 and 400 °C for the two electrolytes can be ascribed to the removal of the glyme from crystallized salt−solvent complexes which are principally promoted by the strong interaction between the oxygen atoms in the ether chains and the Li$^+$ ions rather than the anions.[30]
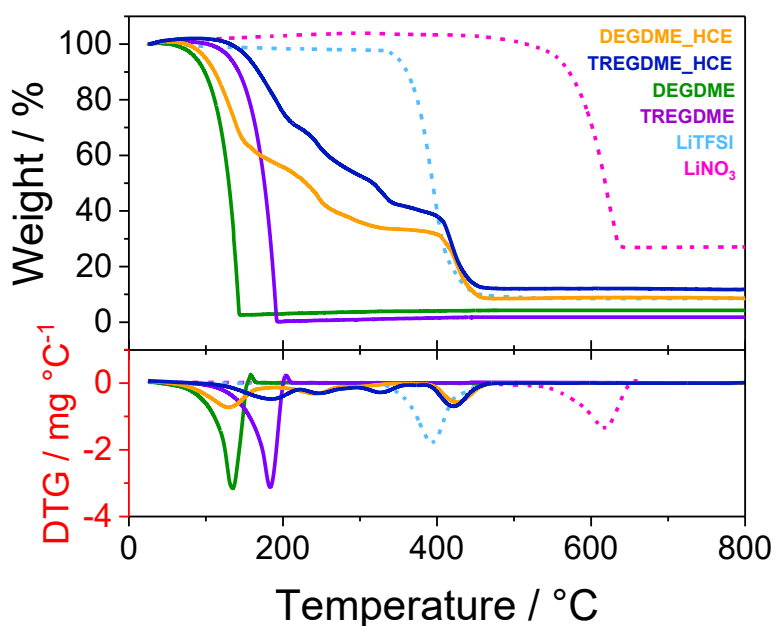
Figure 3.1.3. TGAs (black left-y axis) and corresponding differential curves (DTG, red left-axis) of DEGDME_HCE (orange), TREGDME_HCE (blue), DEGDME solvent (green), TREGDME solvent (violet), LiTFSI (light blue, dashed), and LiNO$_3$ (pink, dashed). Temperature range: 25 − 800 °C; heating rate: 5 °C min^{-1}.

Therefore, the degradation of the glyme−salt complexes by solvent evaporation occurs throughout a multiple-step dry-recrystallization mechanism leading to the bare lithium salts, that is, LiTFSI and LiNO₃.[31] Further weight loss above 400 °C indicates LiTFSI salt degradation (compare plain blue and orange TGA curves with the light blue dashed-curve related to the above salt shown in Fig. 3.1.3), while LiNO₃ degradation expected around 600 °C (the pink dashed-curve shown in Fig. 3.1.3) is not observed or kinetically slowed down. The missing degradation of LiNO₃ until 800 °C is also confirmed by TGA residues of about 9 % for DEGDME_HCE and 11% for TREGDME_HCE which can be obtained only by taking into account the presence of the above salt.

The ionic conductivity, that is, a key factor for the electrolyte applicability, is determined by means of EIS measurements performed during the scan from room temperature to around 76 °C, while the corresponding Arrhenius plots are displayed in Figure 3.1.4a (see the related Nyquist plots in Fig. 3.1.5a and b). The data of Figure 3.1.4a reveal that TREGDME_HCE (blue) has lower conductivity with respect to DEGDME_HCE (orange), with values ranging from 8.9×10^{-4} S cm^{-1} at room temperature to 2.5×10^{-3} S cm^{-1} at 76 °C for the former and from 3.3×10^{-3} to 7.8×10^{-3} S cm^{-1} for the latter. This experimental response may be partially justified by an easier mobility of the ions in DEGDME_HCE compared to TREGDME_HCE which has in turn a more relevant concentration of the lithium salts and a longer polyether chain of the glyme solvent, thus a higher viscosity.
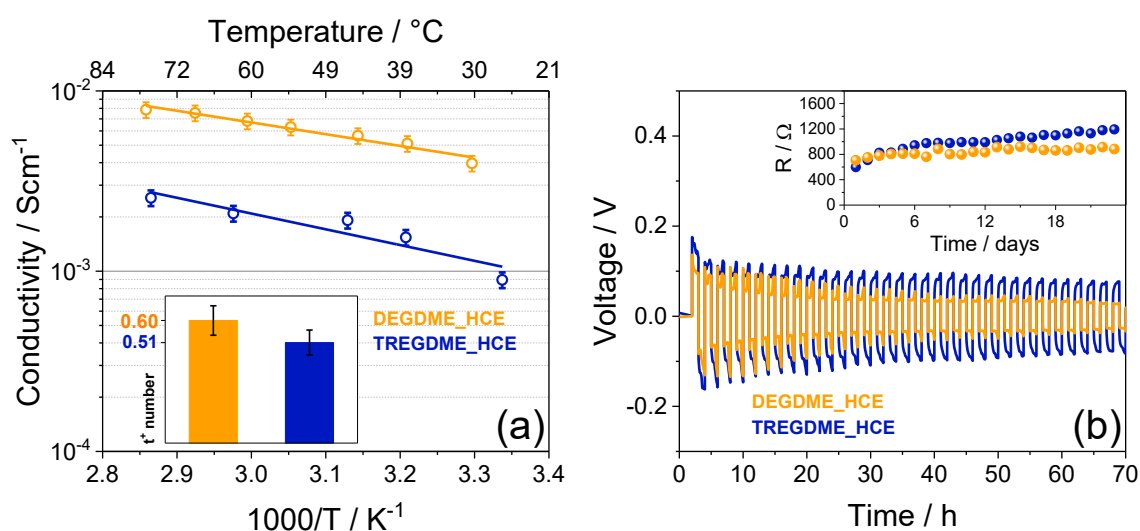
Figure 3.1.4. (a) Arrhenius conductivity plots and Li$^+$ transference number values (inset) of DEGDME_HCE (orange) and TREGDME_HCE (blue). **(b)** Lithium stripping/deposition tests performed on Li/electrolyte/Li symmetrical cells employing either DEGDME_HCE (orange) or TREGDME_HCE (blue) by applying a current of 0.1 mA cm^{-2}; inset shows the interphase resistance trends recorded upon Li/electrolyte/Li symmetrical cells aging employing DEGDME_HCE (orange) or TREGDME_HCE (blue) through EIS in the 500 kHz to 100 mHz frequency range by applying a signal of 10 mV (see the corresponding Nyquist plots in Figure 3.1.6, NLLS analyses are not reported).

On the other hand, both electrolytes exhibit conductivity values approaching or even higher than 10^{-3} S cm^{-1}, thereby matching the requirement for electrochemical applications. Subsequently, the electrolytes were investigated in the symmetrical Li/Li cell to determine the Li$^+$ transference number (t$^+$) according to the Bruce−Vincent−Evans method (see the *3.1.2 Experimental* section).[11] Table 3.1.2 reports the parameters used in equation (3.1.1) while the chronoamperometric curves and the Nyquist plots related to the EIS measurements are reported in Figure 3.1.5c and d. The t$^+$ values reported in Table 3.1.2 and depicted in Figure 3.1.4a (inset) imply that the higher viscosity and salt concentration of TREGDME_HCE compared to DEGDME_HCE reflect into a lower Li$^+$ ion transport and transference number (i.e., 0.51 for the former and 0.60 for the latter). On the other hand, the obtained t$^+$ values appear adequate for applications in lithium cells and comparable with those usually ascribed to glyme electrolytes.[32]
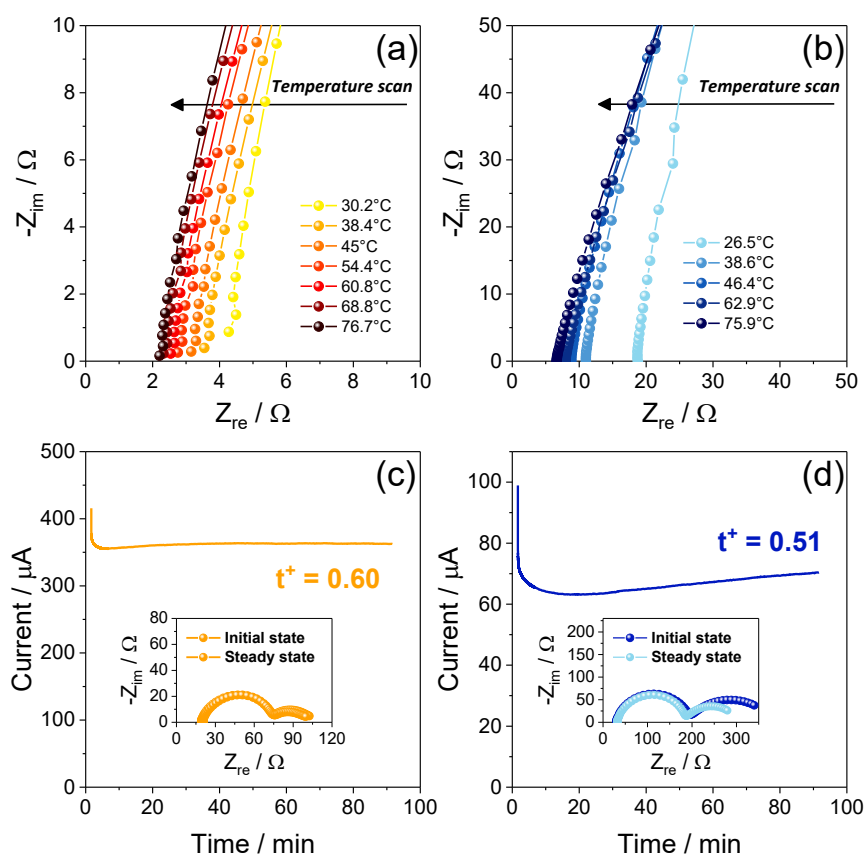
Figure 3.1.5. (a,b) Nyquist plots recorded at various temperatures by EIS on symmetrical Li/Li cells employing either **(a)** DEGDME_HCE or **(b)** TREGDME_HCE to determine the ionic conductivity of the electrolytes; frequency range: 500 kHz – 100 Hz, signal amplitude: 10 mV. NLLS analyses are not reported. **(c,d)** Chronoamperometric curves and Nyquist plots recorded by EIS before and after polarization (insets) used to determine the Li$^+$ transference number of **(c)** DEGDME_HCE and **(d)** TREGDME_HCE in Li/Li symmetrical cells by employing the Bruce-Vincent-Evans equation (see equation (3.1.1) in the *3.1.2 Experimental* section); the actual values of the parameters used in the equation are reported in Table 3.1.2. Chronoamperometry polarization voltage: 30 mV, EIS frequency range: 500 kHz – 100 mHz, signal amplitude: 10 mV.

The electrochemical stability of the two electrolytes is investigated by prolonged lithium stripping/deposition throughout galvanostatic cycling in the symmetrical Li/Li cell reported in Figure 3.1.4b. Initially, DEGDME_HCE (orange) and TREGDME_HCE (blue) exhibit overvoltage values of 135 and 175 mV that decrease to 30 and 75 mV, respectively, after 70 h of measurement and subsequently stabilize around the latter values. The observed decrease of the overvoltage is likely due to a partial dissolution of the SEI film which is formed at the lithium surface after cell assembly, while the final stabilization indicates the consolidation of the abovementioned SEI which may actually allow the prolonged cycling of the lithium cells without any further side reaction.[33] The chemical stability of the electrolytes is instead investigated by EIS measurements (inset in Fig. 3.1.4b), carried out upon prolonged aging of Li/Li symmetrical cells. It is worth noting that all the recorded Nyquist plots, reported in Figure 3.1.6, can be suitably represented by the $R_e(R_1Q_1)(R_2Q_2)$ equivalent circuit, where R_e is the electrolyte resistance, (R_1Q_1) element accounts for the charge transfer at the electrode/electrolyte interphase and the SEI layer (high-middle frequency semicircle), and (R_2Q_2) represents a Warburg-type Li^+ ion diffusion (low-frequency semicircle).[14]
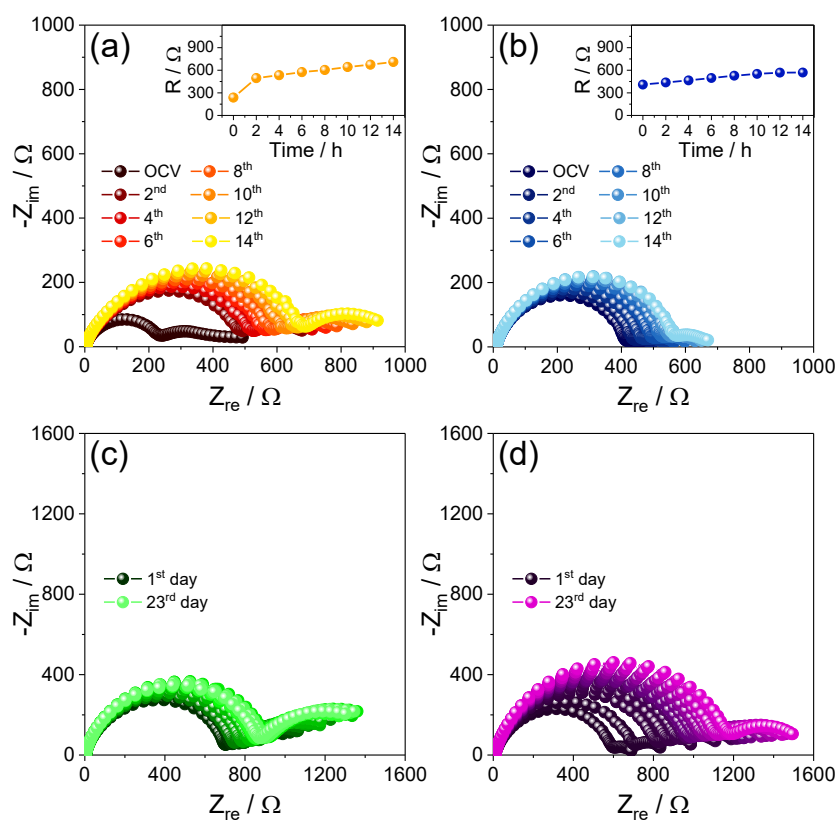
Figure 3.1.6. (a, b) Nyquist plots and corresponding interphase resistance trends (insets) recorded by EIS upon aging for 14 hours of symmetrical Li/Li cells using either **(a)** DEGDME_HCE or **(b)** TREGDME_HCE. **(c, d)** Nyquist plots recorded by EIS upon prolonged aging for 23 days of symmetrical Li/Li cells employing either **(c)** DEGDME_HCE or **(d)** TREGDME_HCE (see the corresponding interphase resistance trends in inset of Fig. 3.1.4b); frequency range: 500 kHz – 100 mHz, signal amplitude: 10 mV. NLLS analyses are not reported.

Interestingly, during the initial 14 h upon cell assembly the DEGDME_HCE (Fig. 3.1.6a) exhibits slightly higher values of the interphase resistance with respect to TREGDME_HCE (Fig. 3.1.6b). Furthermore, the resistance trends related to the subsequent EIS measurements reported in the inset of Figure 3.1.4b reveal a less significant growth for DEGDME_HCE with respect to TREGDME_HCE, with steady-state values between 800 and 900 Ω after 10 days for the former, while a slight continuous increase over the whole test to the final value of 1194 Ω for the latter (see related Nyquist plots in Fig. 3.1.6c and d, respectively). The different electrode/electrolyte interphase resistance trending observed for the two solutions likely suggests diverse stabilization kinetics of the SEI at the lithium surface because of their different composition in terms of solvent nature and salt contents, as actually indicated by the literature.[2]

Afterward, the electrochemical stability window of the electrolytes is determined in lithium cells by means of LSV and CV to investigate the anodic and the cathodic regions, respectively, employing carbon as the working electrode. The obtained current versus potential curves displayed in Figure 3.1.7a and b for DEGDME_HCE and TREGDME_HCE, respectively, show similar trends. Indeed, the first CV cycle of the cells reveals in the cathodic region an irreversible peak centered at about 1.5 V vs Li$^+$/Li related to the LiNO$_3$ salt reduction[3] and a convoluted response extended down to 0.01 V vs Li$^+$/Li accounting for multiple processes such as the electrolyte decomposition with SEI formation, the insertion of Li$^+$ ions into the amorphous SPC, and their possible electrodeposition at the carbon electrode surface.[34] The subsequent well-overlapped profiles exhibit reversible broad peaks at about 1 V and 0.01 V vs Li$^+$/Li accounting for Li$^+$ (de)-insertion and electrodeposition processes, respectively.[34] On the other hand, the LSV scan performed in the anodic region reveals for both electrolytes the absence of significant reactions from the OCV condition until a potential of about 4.4 V vs Li$^+$/Li which instead runs the oxidative decomposition of the solutions, as effectually indicated by a relevant increase of the current value. Therefore, the electrochemical stability of the two electrolytes can be estimated to range from 0 to around 4.4 V vs Li$^+$/Li, that is, an appropriate range for applications in the lithium battery.[7] A more accurate evaluation of the anodic limit of the two solutions can be obtained by chronoamperometry at gradually raising potentials, that is, by steps of 0.1 V every hour from 4.0 to 4.6 V vs Li$^+$/Li. The responses of the cells using DEGDME_HCE and TREGDME_HCE, depicted in the insets of Figure 3.1.7a and b, respectively, reveal significant electrolyte oxidation at 4.4 V vs Li$^+$/Li for the former with a current of 90 μA and at 4.5 V vs Li$^+$/Li for the latter with a current of 130 μA. Further increase of the potential leads to more relevant electrolyte decomposition with currents of 350 and 960 μA at 4.5 and 4.6 V vs Li$^+$/Li, respectively, for the cell using DEGDME_HCE and of 330 μA at 4.6 V for the one using TREGDME_HCE. These results confirm for TREGDME_HCE an anodic stability of 4.4 V vs Li$^+$/Li and restrict the one of

DEGDME_HCE to 4.3 V *vs* Li⁺/Li. It is worth mentioning that both electrolytes reveal a sufficient anodic stability for operation in the lithium battery, in particular TREGDME_HCE which has lower degradation current and improved electrochemical stability.
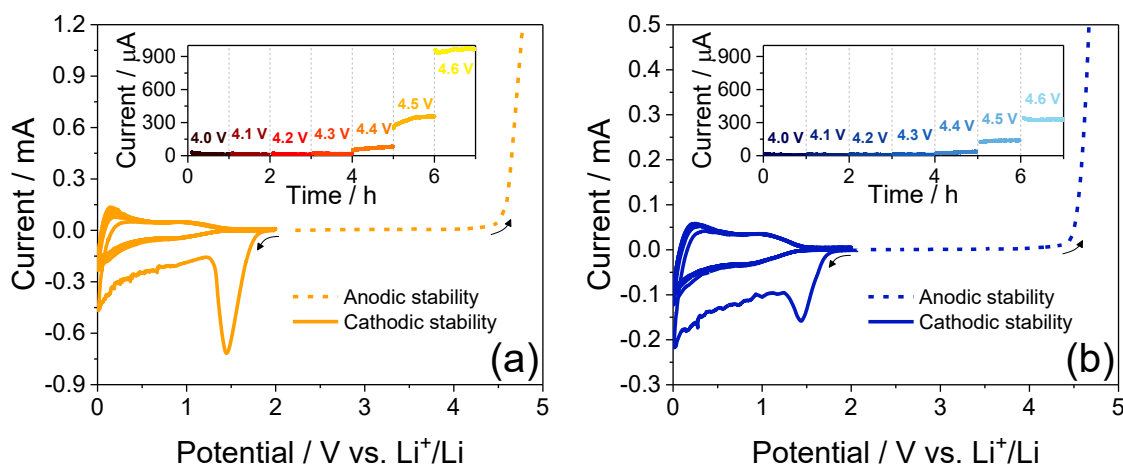
Figure 3.1.7. (a, b) Electrochemical stability window determined by means of CV in the cathodic region (solid line) and LSV in the anodic one (dashed line) performed on lithium cells employing either **(a)** DEGDME_HCE or **(b)** TREGDME_HCE, and SPC as the working electrode; scan rate: 0.1 mV s⁻¹, CV potential range: 0.01−2 V *vs* Li⁺/Li; insets show the chronoamperometry test carried out in the 4.0−4.6 V *vs* Li⁺/Li potential range through voltage increase by steps of 0.1 V every hour.

Thus, DEGDME_HCE and TREGDME_HCE are exploited in Li-S cell using the S:Sn 80:20 w/w cathode by means of CV coupled with EIS as reported in Figure 3.1.8. The corresponding voltammograms (Fig. 3.1.87a and c) show the typical profiles expected for the reversible multiple-step Li-S electrochemical process consisting of a first cycle with a different shape compared to the subsequent ones, which are well overlapped into various peaks centered at about 2.4 and below 2.0 V *vs* Li⁺/Li during cathodic scan and merged between 2.3 and 2.5 V *vs* Li⁺/Li during the anodic one.[35] The above peaks correspond to the reduction of sulfur with formation of soluble polysulfides (Li_2S_x with $x \geq 6$ at 2.4 V, and Li_2S_x with $2 < x < 6$ below 2.0 V) during discharge, and to the oxidation back to sulfur during the charge process.[35] Furthermore, the difference between the first and subsequent cycles is well justified by the EIS performed at the OCV and after 1, 5, and 10 voltammetry cycles for the cells using DEGDME_HCE (Fig. 3.1.8b) and TREGDME_HCE (Fig. 3.1.8d). The corresponding Nyquist plots suggest the activation process typical of Li-S cells using a suitable electrolyte associated with the consolidation of a favorable electrode/electrolyte interphase by the ongoing electrochemical process, as revealed in Chapter 2. In particular, This Li-S activation process has been attributed to microstructural modifications of the electrode that allow an enhanced

electric contact between sulfur and the conductive carbon support, and lead to an improved conductivity of the electrode/electrolyte interphase. Indeed, the EIS data evidence a remarkable decrease of the cell impedance from values between 100 and 200 Ω at the OCV (see insets of Fig. 3.1.8b and d) to values of the order of 10 Ω for DEGDME_HCE (Fig. 3.1.8b) and 20 Ω for TREGDME_HCE (Fig. 3.1.8d). An exhaustive summary of the results of the NLLS analyses performed on the Nyquist plots of Figure 3.1.8b and Figure 3.1.8d is reported in Table 3.1.3.[12,13] Notably, both CV and EIS results indicate differences between the Li-S cells using DEGDME_HCE and TREGDME_HCE; the former shows smoother less-polarized peaks and a slightly lower steady-state impedance with respect to the latter (compare Fig. 3.1.8a and the inset of Figure 3.1.8b with Figure 3.1.8c and the inset of Figure 3.1.8d, respectively). These differences may be likely associated with favorable effects on the Li-S electrochemical process promoted by the lower solvent viscosity (0.94 g mL^{-1})[36] and higher conductivity (3.3 × 10^{-3} S cm^{-1}) of DEGDME_HCE compared to the TREGDME_HCE (0.98 g mL^{-1} and 8.9 × 10^{-4} S cm^{-1}, respectively)[36] at room temperature.
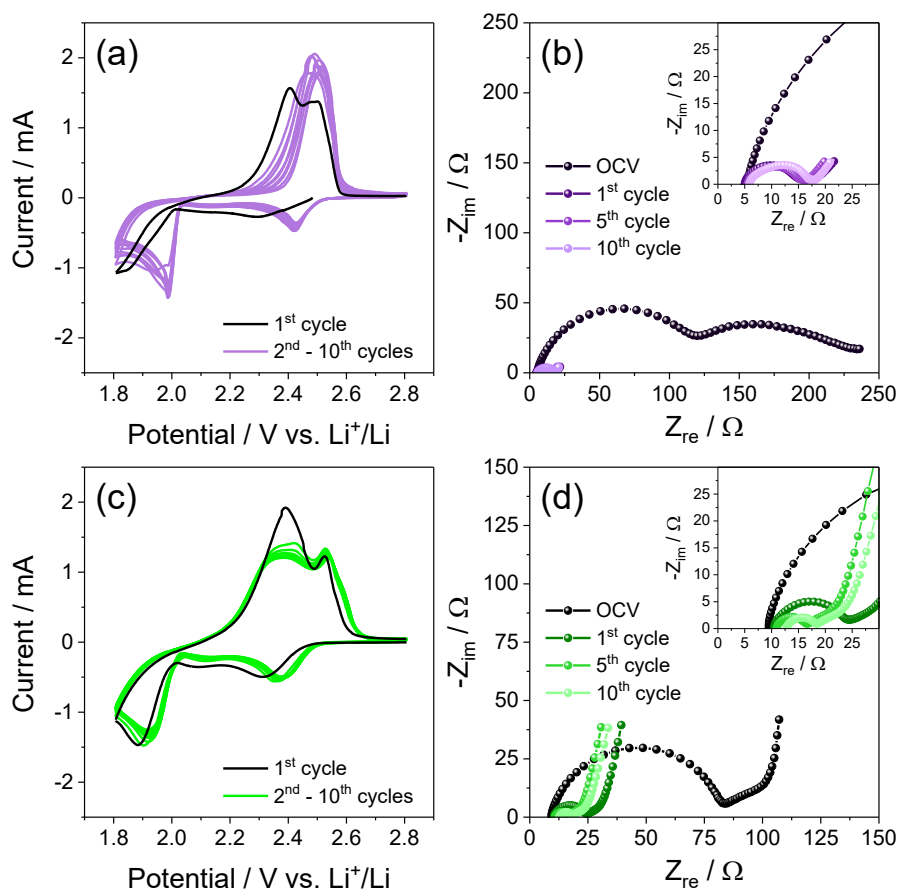
Figure 3.1.8. (a, c) CV and **(b, d)** EIS measurements performed on Li-S cells employing either **(a, b)** DEGDME_HCE or **(c, d)** TREGDME_HCE. CV potential range, 1.8 − 2.8 V *vs* Li$^+$/Li; scan rate, 0.1 mV s^{-1}. EIS carried out at the OCV of the cells and after 1, 5, and 10 voltammetry cycles (inset reports magnification); frequency range, 500 kHz − 100 mHz; alternate voltage signal amplitude, 10 mV.

Electrolyte	Cell condition	Circuit	R_1 [Ω]	R_2 [Ω]	$R_1 + R_2$ [Ω]	χ^2
DEGDME_HCE	OCV	$R_e(R_1Q_1)(R_2Q_2)$	103 ± 2	129 ± 3	232 ± 4	1×10⁻⁴
	1 cycle	$R_e(R_1Q_1)(R_2Q_2)Q_3$	9.9 ± 0.1	3.4 ± 0.2	13.3 ± 0.2	2×10⁻⁵
	5 cycles	$R_e(R_1Q_1)(R_2Q_2)Q_3$	10.1 ± 0.1	0.8 ± 0.1	10.9 ± 0.1	3×10⁻⁵
	10 cycles	$R_e(R_1Q_1)(R_2Q_2)Q_3$	9.8 ± 0.5	1.5 ± 0.5	11.3 ± 0.7	6×10⁻⁵
TREGDME_HCE	OCV	$R_e(R_1Q_1)(R_2Q_2)Q_3$	73.3 ± 0.4	27 ± 3	101 ± 3	5×10⁻⁵
	1 cycle	$R_e(R_1Q_1)(R_2Q_2)Q_3$	13.1 ± 0.3	9.0 ± 1.5	22.1 ± 1.5	4×10⁻⁵
	5 cycles	$R_e(R_1Q_1)(R_2Q_2)Q_3$	5.3 ± 0.1	7.2 ± 0.3	12.5 ± 0.3	2×10⁻⁵
	10 cycles	$R_e(R_1Q_1)(R_2Q_2)Q_3$	5.4 ± 0.1	6.8 ± 0.3	12.2 ± 0.3	2×10⁻⁵

Table 3.1.3. NLLS analyses performed on the Nyquist plots reported in Figure 3.1.7b and d recorded upon CV measurements of Li-S cells employing either DEGDME_HCE (Fig. 3.1.7b) or TREGDME_HCE (Fig. 3.1.7d).[12,13]

Figure 3.1.9 displays the performance of DEGDME_HCE (Fig. 3.1.9a and b) and TREGDME_HCE (Fig. 3.1.9c and d) in a Li-S cell, cycled at the constant rate of C/5 (1C = 1675 mA g$_S^{-1}$) at 25 and 35 °C. The selected voltage profiles related to the steady state of the cells (Fig. 3.1.9a and c) reveal the characteristic response of a Li-S battery, in agreement with CVs of Figure 3.1.8, where the two distinct discharge plateaus around 2.4 and 2.0 V ascribed to the formation of long chain lithium polysulfides (Li$_2$S$_x$ with x ≥ 6) and short chain ones (Li$_2$S$_x$ with 2 < x < 6), respectively, are reversed into two charge plateaus above 2.3 V.[37] Furthermore, the figure shows for both DEGDME_HCE (Fig. 3.1.9a) and TREGDME_HCE (Fig. 3.1.9c) a relatively high polarization at room temperature (25 °C), in particular for the latter electrolyte, leading to steady-state specific capacities of about 800 mAh g$_S^{-1}$ and 340 mAh g$_S^{-1}$, respectively. The poor response at room temperature of the Li-S cells is most likely due to the hindering of the insulating sulfur kinetics by the high viscosity of the concentrated electrolytes, which is particularly relevant in the case of the TREGDME_HCE due to its longer ether chain, higher lithium salts concentration (see *3.1.2 Experimental* section), and consequently higher viscosity compared to DEGDME_HCE.[38] In order to favor the electrochemical kinetics and achieve better performances, subsequent galvanostatic cycling tests were performed on the Li-S cells at a higher temperature, that is, 35 °C, by employing the same Crate of C/5. Advantageously, the increase of temperature leads to higher capacity values and to lower polarization for both DEGDME_HCE (Fig. 3.1.9a) and TREGDME_HCE (Fig. 3.1.9c), as expected by the decrease of the electrolytes viscosity and the concomitant rise of their Li+ ions conductivity in accordance with Figure 3.1.4.

In particular, the cycling trends reported in Figure 3.1.9b and d reveal that the cell using DEGDME_HCE delivers at 35 °C a maximum specific capacity of about 1320 mAh g_S^{-1} (Fig. 3.1.9b), while the one exploiting TREGDME_HCE exhibits a value approaching 890 mAh g_S^{-1} (Fig. 3.1.9d). Furthermore, the cell using DEGDME_HCE shows over the 50 cycles of the tests an excellent retention of the maximum capacity with values ranging from 92% at room temperature to 90% at 35 °C (Fig. 3.1.9b), while lower but still satisfactory values of 88% at room temperature and 77% at 35 °C are observed for the cell using the more-viscous TREGDME_HCE (Fig. 3.1.9d).
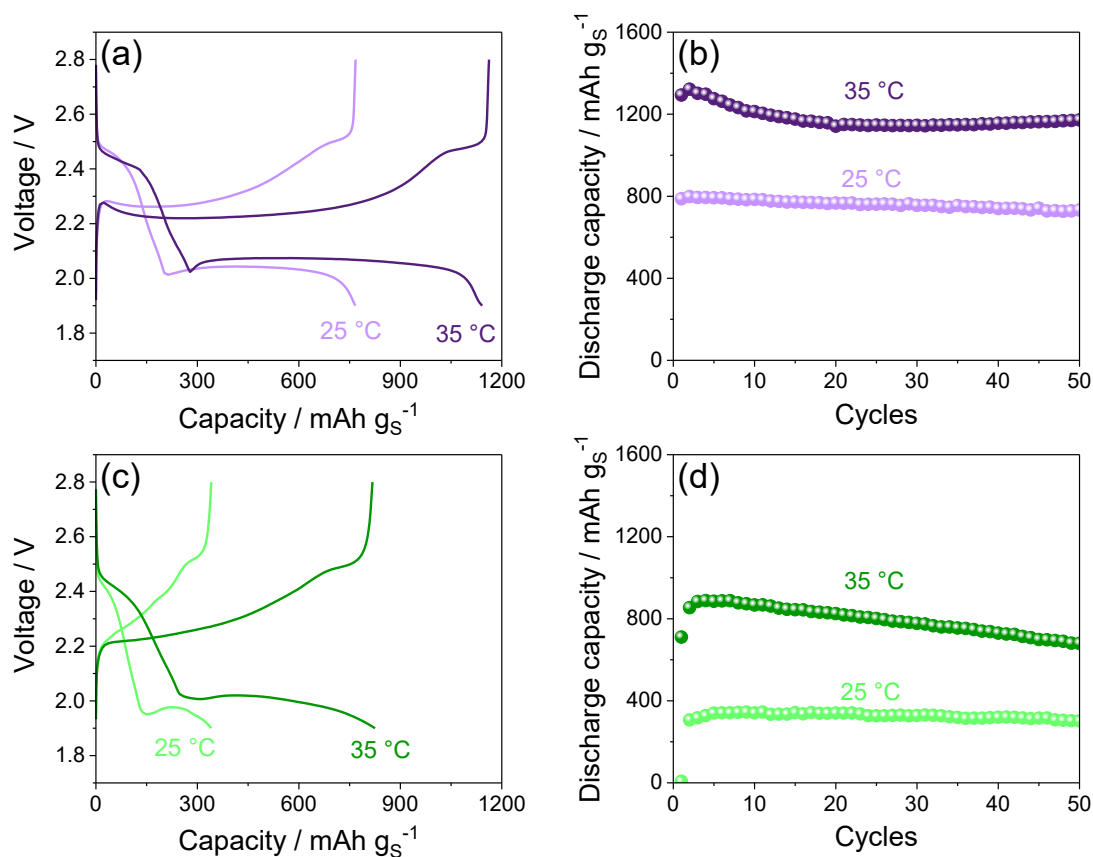
Figure 3.1.9. (a, c) Selected voltage profiles and **(b and d)** corresponding cycling trends at 25 and 35 °C of Li-S cells employing either **(a and b)** DEGDME_HCE or **(c and d)** TREGDME_HCE. The cells are galvanostatically cycled using a voltage range between 1.9 and 2.8 V at the constant current rate of C/5.

In order to extend the cycle life, additional galvanostatic cycling tests were performed on Li-S cells by adopting the most suitable operative conditions according to the data reported in this section. Indeed, Figure 3.1.10 reports the cycling trend of a Li|DEGDME_HCE|S:Sn 80:20 w/w cell operating at 35 °C. It is worth mentioning that the Li-S cell adopted an electrolyte/sulfur ratio limited to 20 µL mg^{-1} in order to reduce the excess of electrolyte and, thus, to increase the practical energy density of the device. As observed in Figure 3.1.10, the cell exhibits notable performances, long cycle

life, and coulombic efficiency around 100% even by cycling at higher current rates, that is, at 1C (1675 mA g_S^{-1}). In particular, the cell delivers 140 cycles with an initial capacity upon activation of almost 750 mAh g_S^{-1} retained at the 70% at the end of the test (Fig. 3.1.10). Despite the lower delivered capacity values with respect to the tests performed at C/5 (see Figure 3.1.9), as expected by the employment of higher currents, these tests further evidence that the optimal tuning of the working conditions can lead to the extension of the cycle life and to a notable as well as steady delivered capacity values of Li-S cells with lowly flammable concentrated glyme-based electrolytes. Moreover, the Li|DEGDME_HCE|S:Sn 80:20 w/w cell shows a comparable specific capacity with respect to that achieved by employing the highly-flammable state-of-the-art Li-S electrolyte, that is, the DOL:DME-LiTFSI-LiNO₃ solution (see Figure 2.2.5 in section *2.2* of Chapter 2). Indeed, both the cells deliver maximum capacity values between 750 and 800 mAh g_S^{-1}, demonstrating the suitability of the DEGDME_HCE as possible next generation electrolyte.
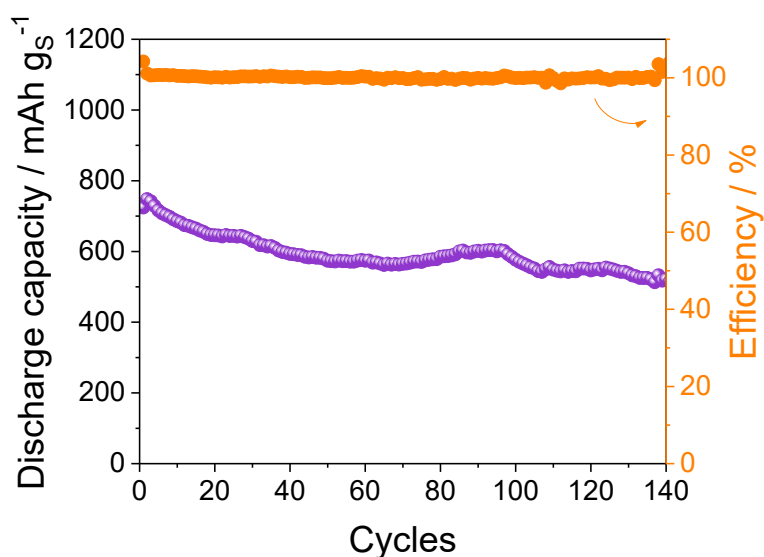
Figure 3.1.10. Cycling trends with Coulombic efficiency (right y-axis) related to a Li-S cell employing the DEGDME_HCE galvanostatically cycled at 1C. The cell was cycled at 35 °C by exploiting an electrolyte/sulfur ratio of 20 μL mg⁻¹ and a 1.6 − 2.8 V voltage range.

3.2 A novel composite polymer electrolyte

3.2.1 Presentation

Electrolyte solutions exploiting high concentrations of lithium salts may confer a notable safety content to Li-S batteries maintaining at the same time suitable Li^+ transport properties, as suggested in section *3.1*. On the other hand, solid composite polymer electrolytes benefit from high mechanical stability, as well as negligible volatility and flammability. Polyethylene oxide (PEO) is commonly employed as solid solvent thank to its high chemical, thermal, and mechanical stability and compatibility with lithium salts,[39] however, suitable ionic conductivity ($>10^{-4}$ S cm^{-1}) and adequate Li^+ transport properties are typically achieved at the predominantly amorphous state of the PEO above 65°C,[39] which allows battery application employing insertion[40–42] or sulfur-based conversion cathodes.[43–45] In this regard, polyethylene glycol dimethyl ether ($CH_3(OCH_2CH_2)_nOCH_3$, PEGDME) is solid at room temperature for molecular weights higher than 1000 g mol^{-1} and has mechanical and chemical stability compatible with lithium cell application, as well as a melting point allowing operation at lower temperature compared to PEO.[46] Moreover, the combination with sacrificial additives, such as $LiNO_3$ which forms a protective layer at the lithium surface and avoids parasitic reactions,[17,19,47] and the use of ceramic fillers such as SiO_2 that promotes the amorphous phase of the polymer,[48] may actually allow the efficient use of high molecular weight PEGDME-based solid electrolytes in Li-S cell. Therefore, the next session proposes an alternative composite polymer electrolyte (CPE) exploiting PEGDME with an average molecular weight of 2000 g mol^{-1}, LiTFSI salt, $LiNO_3$ film-forming additive, and fumed SiO_2 ceramic filler, for application in lithium battery operating at temperatures lower than the ones ascribed to the common solid polymers (e.g., at 50 °C). The solid electrolyte is fully characterized in terms of Li^+ transport properties, Li/electrolyte interphase stability and thermal behavior, as seen in section *3.1*, including the study of structure and morphology through X-ray diffraction and electron microscopy, respectively. The applicability of the polymer electrolyte in lithium battery is firstly demonstrated by exploiting a $LiFePO_4$ cathode and then tested in a challenging system such as the Li-S one. In particular, the interphase formed between the sulfur electrode and the solid electrolyte is thoroughly studied through photographic images, thermogravimetric analyses and electron microscopy, while cyclic voltammetry, impedance spectroscopy and galvanostatic cycling measurements are used to investigate the electrochemical behavior of the novel Li-S polymer battery.

3.2.2 Experimental

Lithium bis(trifluoromethanesulfonyl)imide (LiTFSI, 99.95% trace metals basis, Sigma-Aldrich) and lithium nitrate (LiNO$_3$, 99.99% trace metals basis, Sigma-Aldrich) salts were mixed with polyethylene-glycol dimethyl-ether solid powder (CH$_3$O(CH$_2$CH$_2$O)$_n$CH$_3$, average molecular weight 2000 g mol^{-1}, Sigma-Aldrich) by a ratio of 1 mol of each salt in 1 kg of polymer. Fumed silica (SiO$_2$, fumed, average particle size: 0.007 μm, Sigma-Aldrich) was then added to the above polymer/salts mixture by a 10% weight ratio. The components were subsequently dissolved in acetonitrile (ACN, Sigma-Aldrich) to obtain a viscous slurry. Upon two days of magnetic stirring at the room temperature (Fig. 3.2.1a), the slurry was cast onto plastic foil (Mylar) using a doctor blade with a thickness of 1.5 mm (Figs. 3.2.1b and c). The slurry was dried at about 45 °C overnight, transferred into a Büchi oven and heated under vacuum for 5 days at 45 °C and for 2 days at 60 °C (Fig. 3.2.1d). The slurry was finally introduced into an Ar-filled glove box (MBraun, O$_2$ and H$_2$O content below 1 ppm) where it was left for about 20 days at 25 °C until complete crystallization (Fig. 3.2.1e–i). The composite solid polymer electrolyte will be subsequently indicated by the acronym PEGDME_CPE, while the PEGDME polymer with average molecular weight 2000 g mol^{-1} by the acronym PEGDME2000. A membrane with the same composition except for LiNO$_3$ additive, indicated as blank, was prepared for comparison.
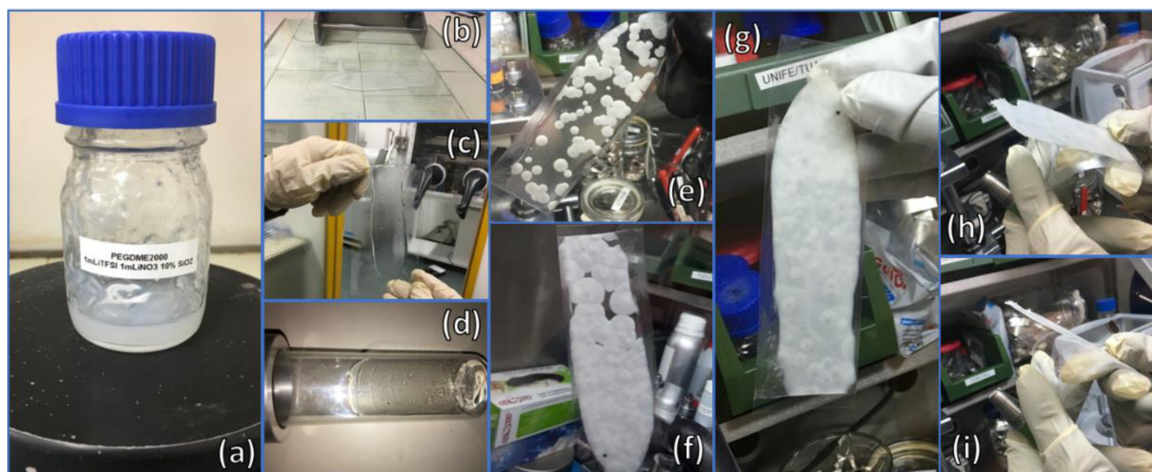
Figure 3.2.1. Photographic images of the PEGDME_CPE during solvent casting procedure: **(a)** magnetic stirring after the addition of acetonitrile to the component powders, i.e., PEGDME2000, LiTFSI, LiNO$_3$ and fumed SiO$_2$; **(b)** doctor blade casting; **(c)** membrane upon one night of heating at 45 °C under air and **(d)** 5 days at 45 °C and 2 days at 60 °C under vacuum in Büchi oven; **(e)** after 1 hour, **(f)** 3 hour, **(g)** 4 days, and **(h** and **i)** 19 days of aging in glove box at 25° C.

The PEGDME_CPE structure was investigated by XRD at the room temperature (25 °C) by using a Bruker D8 Advance diffractometer equipped with a Cu-Kα source, performing a scan in the 2θ range between 10° and 40° at a rate of 10 s per step with angle increments of 0.02°. The patterns of the single components of the PEGDME_CPE, that is, PEGDME2000, LiTFSI, $LiNO_3$ and fumed SiO_2, were recorded using the same conditions.

A Zeiss EVO 40 microscope equipped with a LaB_6 thermoionic beam was used to study the morphology of the samples through SEM technique, while energy dispersion X-ray analyses (EDS) were performed using a X-ACT Cambridge Instruments analyzer.

The solid configuration of the PEGDME_CPE membrane was investigated at various temperatures by a heating-cooling treatment consisting of 3 steps, that is, heating at 50 °C for 3 h, heating at 70 °C for 3 h and, finally, cooling back to the room temperature.

TGA was carried out under a N2 atmosphere and employing a heating rate of 5°C min^{-1} in the 25–800°C temperature range, through a Mettler-Toledo TGA 2 instrument. Several samples were investigated by TGA: *i)* PEGDME2000 powder, *ii)* PEGDME_CPE membrane and (*iii*, *iv*) PEGDME_CPE on a S:SPC 70:30 w/w electrode (see preparation below) in pristine condition and after CV.

All the electrochemical measurements reported below were performed using CR2032 coin-type cells (MTI Corp.) assembled in an Ar-filled glove box (MBraun, O_2 and H_2O content below 1 ppm). The ionic conductivity of the PEGDME_CPE was evaluated by performing EIS measurements in a blocking electrode SS|PEGDME_CPE|SS cell, using an O-ring (Mylar) with an internal diameter of 10 mm and thickness of 120 μm to fix the cell constant at 0.0153 cm^{-1}. The impedance spectra were recorded by applying a signal of 10 mV in the 500 kHz – 100 Hz frequency range.

The Bruce-Vincent-Evans method[11] was applied to determine the Li$^+$ transference number (t$^+$) of the electrolyte in symmetrical Li|PEGDME_CPE|Li cell at 45, 50 and 70 °C. The cells were assembled by using three O-rings (CS Hyde, 23-5FEP-2-50) with an internal diameter of 10 mm and thickness of 127 μm holding the polymer electrolyte and 2 lithium disks. The chronoamperometric tests were performed by using a voltage of 30 mV for 90 min, and the impedance spectra were recorded before (initial state) and after (steady state) cell polarization with the same instrument applying a signal of 10 mV in the 500 kHz – 100 mHz frequency range. The values of the Li$^+$ transference number were calculated using equation (3.2.1):[11]

$$t^+ = \frac{i_{ss}}{i_0} \frac{\Delta V - R_0 i_0}{\Delta V - R_{ss} i_{ss}} \qquad (3.2.1)$$

where i_0 and i_{ss} are the current values at the initial and steady state, respectively, ΔV is the applied voltage, R_0 and R_{ss} are the interphase resistance values before and after cell polarization, respectively, calculated from the impedance spectra.

The electrochemical stability of the PEGDME_CPE was investigated by performing lithium stripping-deposition tests on Li/Li cells. A constant current of 0.1 mA cm^{-2} was applied at the temperature of 45, 50 and 70 °C. Afterwards, a constant temperature of 50 °C was selected for the subsequent measurements, which were carried out by cooling back the cells at the above temperature after a first heating treatment at 70 °C for one day. The PEGDME_CPE/Li interphase resistance was evaluated by EIS measurements upon symmetrical Li/Li cell aging. The impedance spectra were recorded by applying a signal of 10 mV in the 500 kHz – 100 mHz frequency range. The electrochemical stability window of the electrolyte was determined in Li/PEGDME_CPE/SPC cells through linear sweep voltammetry (LSV) from the open circuit voltage (OCV) to 5 V *vs* Li$^+$/Li in the anodic region, and cyclic voltammetry (CV) within the 0.01 – 2.0 V *vs* Li$^+$/Li range in the cathodic region. The anodic region was further investigated through a chronoamperometry test at 50 °C in the potential windows ranging from 4.0 to 4.7 V *vs* Li$^+$/Li. The cell potential was initially increased from OCV to 3.9 V *vs* Li$^+$/Li by linear scan voltammetry. The cell was held at 4 V *vs* Li$^+$/Li and the current flow measured for 1 h, then the potential was increased by steps of 0.1 V every 1 h from 4 V until 4.7 V *vs* Li$^+$/Li and the current flow measured at the corresponding potentials by subsequent chronoamperometry.

The working electrodes of the above cells (SPC) were formed by doctor blade casting of a slurry, containing Super P carbon (SPC, Timcal) and polyvinilidene fluoride (Solef ® 6020 PVDF) dissolved by a weight ratio of 90:10 in *N*-methyl pyrrolidone (NMP, Sigma–Aldrich), on an Al foil for anodic scan, and Cu foil for cathodic scan. The slurry was then dried at 70 °C for 3 h under air, cut into electrode disks with a diameter of 10 mm, and heated at 110 °C under vacuum for 3 h to remove traces of water and solvent. The first step at 70 °C is typically used in order to allow uniform drying by slow solvent evaporation, thus avoiding the formation of bubbles or undesired cracks on the wet electrode surface, while the second one at 110 °C is performed to ensure proper performances of the electrode in lithium battery and avoid side reactions. The cells were assembled by using two O-rings (CS Hyde, 23-5FEP-2-50) with an internal diameter of 10 mm and thickness of 127 μm holding the polymer electrolyte, a lithium disk, and the selected SPC carbon working electrode. LSV and CV measurements were both performed with a scan rate of 0.1 mV s^{-1}.

LiFePO$_4$ (LFP) was selected as the cathode material to evaluate the electrochemical performances of PEGDME_CPE in lithium battery.[49] The LFP electrode was formed by doctor blade casting on aluminum foil of a slurry containing the active material (LiFePO$_4$), SPC, and PVDF

dissolved by a weight ratio of 80:10:10 in NMP. The slurry was then dried at 70 °C for 3 h under air, cut into electrode disks with a diameter of 10 mm, and heated at 110 °C under vacuum for 3 h to remove traces of water and solvent. The lithium cells were assembled by using two O-rings (CS Hyde, 23-5FEP-2-50) with an internal diameter of 10 mm and thickness of 127 μm holding the polymer electrolyte, a lithium disk, and the LFP working electrode. EIS tests were performed from the room temperature to 70 °C at the open circuit voltage (OCV) of the polymer cell, recording the impedance spectra by applying a signal of 10 mV in the 500 kHz – 100 mHz frequency range. Galvanostatic cycling measurements were carried out at 50 °C and 70 °C at various C-rates (1C = 170 mA g^{-1}, referring to LFP mass).

The sulfur-carbon composite was prepared as described in section *2.1* of Chapter 2, by mixing elemental sulfur (S, ≥99.5 %, Riedel de Haën) and SPC by the weight ratio of 70:30 under magnetic stirring in a silicone oil bath at about 125°C. The resulting composite was subsequently cooled down to room temperature and ground in an agate mortar to obtain a fine powder. This composite is herein referred as S:SPC 70:30 w/w. Sulfur electrode disks were obtained through doctor blade casting (MTI Corp.) of a slurry formed by 80wt% sulfur-carbon composite (*i.e.*, S:SPC 70:30 w/w), 10wt% SPC, and 10wt% PVDF) homogeneously dispersed in NMP. The slurry was cast on a porous carbon-cloth foil (GDL ELAT 1400, MTI Corp.), which was then heated on a hot plate at 50°C for about 3 h under a fume hood. Afterwards, electrode disks with diameter of 14 mm and 10 mm were cut out from the coated carbon-cloth and dried overnight at 35°C under vacuum before being transferred in argon-filled glovebox (MBraun, H$_2$O and O$_2$ content below 1 ppm). The obtained sulfur loading on the electrodes was about 1 mg cm^{-2}.

Li|PEGDME_CPE|S:SPC 70:30 w/w cells were assembled by stacking a lithium disk with a diameter of 14 mm, with PEGDME_CPE membrane and S:SPC 70:30 w/w electrode having diameters of 10 mm housed into 4 polymeric O-rings (CS Hyde, 23-5FEP-2-50) with internal diameter of 10 mm, and thickness of 127 μm each. Prior to the tests, all the Li|PEGDME_CPE|S:SPC 70:30 w/w cells were exposed to 4 heating-cooling cycles between 25 and 70°C to decrease the crystallinity and enhance the ionic conductivity of the PEGDME_CPE; each cycle had a duration of 24 h (*i.e.*, 12 h for each heating and cooling step). CV measurements were carried out on a Li|PEGDME_CPE|S:SPC 70:30 w/w cell at 50, 60, 70, and 80°C by employing a scan rate of 0.1 mV s^{-1} in the 1.8–2.8 V *vs* Li$^+$/Li potential range. EIS measurements were performed at the OCV condition as well as upon the voltammetry cycles at the above-mentioned temperature conditions, by applying an alternate voltage signal with amplitude of 10 mV within the 500 kHz–100 mHz frequency range. Galvanostatic cycling tests were performed on Li|PEGDME_CPE|S:SPC 70:30 w/w cells at the constant current rate of C/10 (1 C = 1675 mAgs^{-1}) in the 1.7–2.8 V voltage range at 50°C.

All CV, EIS and chronoamperometry data were collected using a VersaSTAT MC Princeton Applied Research (PAR, AMETEK) instrument, while the galvanostatic cycling measurements were performed by a MACCOR Series 4000 battery test system. All the impedance spectra were analyzed with the Boukamp software using the non-linear least squares (NLLS) method (the χ^2 was in the order of 10^{-4} or lower).[12,13]

3.2.3 Results

Figure 3.2.1 in *3.2.2 Experimental* section reports the photographic images of the various steps adopted for the solvent casting procedure of the PEGDME_CPE. The figure reveals that the membrane becomes self-standing upon 20 days of aging in glove box at the room temperature, which represents a key configuration suitable for adopting the electrolyte in a solid-polymer lithium battery. Structure and morphology of the aged solid electrolyte are detected by XRD, SEM and EDS in Figure 3.2.2 in order to investigate the dispersion of the various components into the solid polymer matrix, which is generally promoted by the solvent casting pathway.[50] Indeed, homogeneous dispersions of the components may actually lead to the formation of salt/polymer/ceramic complexes with a structure differing by the one of the single components, thus improving both the mechanical and electrochemical characteristics of the electrolyte.[39,51] The patterns of Figure 3.2.2a show that the PEGDME_CPE (blue) exhibits various peaks, particularly within the $17° - 28.5°$ 2θ range, and aside broad signal in pattern baseline. The latter may be likely attributed to the SiO_2 ceramic filler (see the SiO_2 cyan pattern in Fig. 3.2.2a for comparison), however the complex pattern of PEGDME_CPE appears only partially ascribed to the single species forming the electrolyte. Indeed, only few peaks for each component of the electrolyte, i.e., PEGDME2000 (orange pattern), LiTFSI (yellow pattern) and $LiNO_3$ (purple pattern), may be identified, thus suggesting the formation of a new crystalline structure by the rearrangement of the various components into a complex during the synthesis procedure.[39,51] Several studies, in particular those focusing on PEO-based solid polymer electrolytes, have indicated the role of the polymer/salt complexes for enhancing the ion transport, and the multiple effect of efficiently dispersed nanometric ceramics for favoring both the mechanical stability and the electrochemical characteristics of the electrolyte.[39,51–54] The uniform dispersion of the various components into the PEGDME_CPE membrane is further evidenced by EDS (Fig. 3.2.2c) performed on a SEM image of a micrometric fractured portion of the surface, which appears uniform without signs of grains or discontinuities (Fig. 3.2.2b). Moreover, the absence of impurities into the membrane is suggested by the weight ratio of the elements reported in Figure 3.2.2d, which shows weak signals

of fluorine, silicon, sulfur and nitrogen, attributed only to salts and ceramic filler, beside the expected 87.6% of carbon and oxygen mainly related to the polymeric chains of the PEGDME2000.
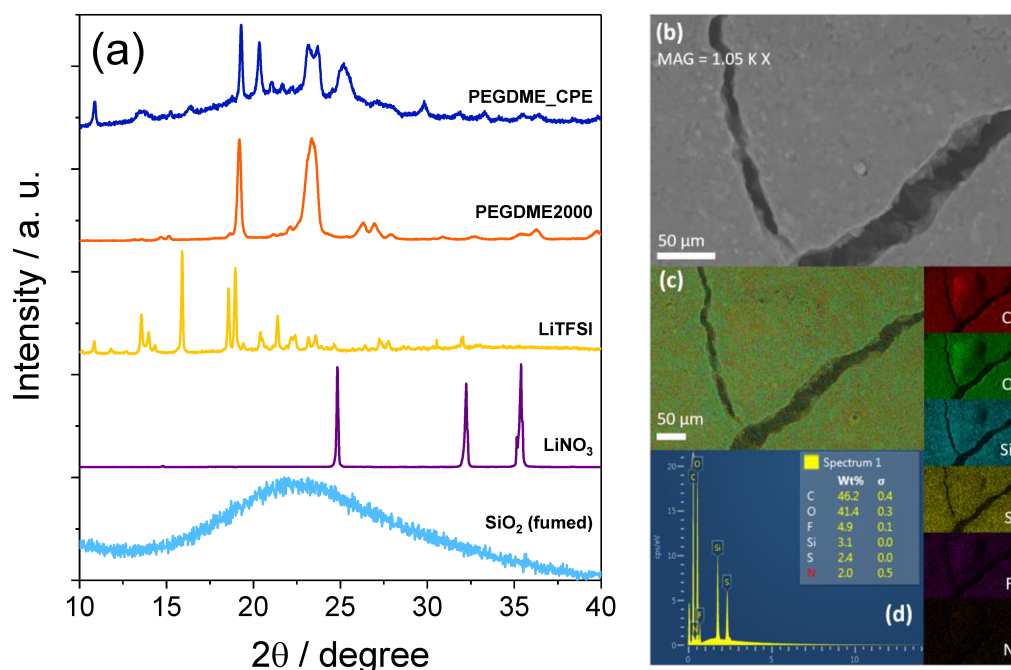
Figure 3.2.2. (a) X-ray diffraction patterns of the PEGDME_CPE membrane (blue), PEGDME2000 (orange), LiTFSI (yellow) and LiNO$_3$ (purple) salts, and of the fumed SiO$_2$ ceramic filler (cyan); **(b)** SEM image of the PEGDME_CPE membrane; **(c)** EDS map of the PEGDME_CPE membrane (insets on the right show the single EDS elemental maps) and **(d)** its elemental composition. All measurements collected at the room temperature, where membrane and components are solid.

It is worth mentioning that the absence of contaminants and impurities, promoted by the synthesis conditions adopted herein, may be actually reflected into high efficiency of the PEGDME_CPE membrane in lithium cell. The electrolyte behavior in terms of conductivity change by repeated cooling and heating, that is, the *thermal history*, plays a key role in determining its applicability in lithium cell, and for setting up proper operating protocols for achieving suitable performances and low polarization.[55]

Figure 3.2.3 reports the conductivity Arrhenius plots of the PEGDME_CPE membrane upon six subsequent cooling/heating scans from about 70 °C to room temperature. Relevantly, the plots of Figure 3.2.3a show a conductivity of the order or higher than 10^{-4} S cm^{-1} above 45 °C, that is, a temperature much lower than the one ascribed to other solid polymer electrolytes used in lithium battery such as PEO-based ones that favors instead efficient and suitable ion conduction only at temperatures higher than 60 °C.[56] Furthermore, the figure reveals a very interesting and progressive change of the crystallization/melting temperature by the ongoing of cycles. Indeed, the single thermal

cycle of Figure 3.2.3b reveals a drop of the ionic conductivity during the first cooling scan (orange) below 32 °C due to membrane crystallization, while the subsequent heating scan shows the two slope regions typically observed in the Arrhenius plots of solid polymer electrolytes.[53] The above heating trend may be reasonably represented by two different lines, where the first, from room temperature to 45 °C, represents the conductivity of an electrolyte mainly formed by crystalline part, instead the second from 45 °C to higher temperatures indicates the conductivity of the electrolyte in its amorphous state.[46,57] The subsequent scans evidence a continuous increase of the room temperature ionic conductivity from about 4×10^{-6} S cm^{-1} during the first scan to 4×10^{-5} S cm^{-1} during the last one, i.e., by a factor of 10, and at the same time a progressive overlapping of heating and cooling trends into a Vogel-Tammann-Fulcher (VTF) profile.[58] This behavior may be attributed to initial kinetic limits avoiding fast crystallization and subsequent melting during cooling and heating scans, respectively, thus leading to the *hysteresis* loop observed in Figure 3.2.3.

The mitigation and progressive vanishing of the above mentioned loop may be most likely ascribed to the rearrangement of the polymer chains into a thermally stable complex.[59] This favorable condition may be promoted both by heating/cooling cycles and by a plasticizing effect of the nanometric SiO_2 particles dispersed into the electrolyte which can actually prevent the segregation of the polymer from the electrolyte complexes, avoid excessive crystallization during cooling[39,56] and enhance the ion transport.[59] Remarkably, the last scan in Figure 3.2.3 (pink) shows that the PEGDME_CPE has an ionic conductivity ranging from about 4×10^{-5} S cm^{-1} at the room temperature to about 4×10^{-4} S cm^{-1} at 73 °C, which are considered values well suitable for application of a solid polymer electrolyte in lithium battery.

The effect of the thermal treatment on the electrolyte is further investigated by performing XRD and SEM measurements on PEGDME_CPE upon heating at 70 °C and subsequent cooling down to room temperature. The XRD pattern (Fig. 3.2.3c) reveals only a broad signal between 17° and 25° and the absence of defined diffraction, thus suggesting membrane amorphization in line with the conductivity trends observed in Fig. 3.2.3a and b which indicate the gradual increase of the conductivity at the lower temperatures by the thermal cycles. Furthermore, the SEM image (Fig. 3.2.3d) after the above heating/cooling protocol displays a very flat, uniform electrolyte surface without significant signs of cracks, therefore suggesting an actual improvement of the mechanical and interfacial properties of the membrane which can efficiently compensate the contact resistance between electrodes and the polymer electrolyte in the cell.
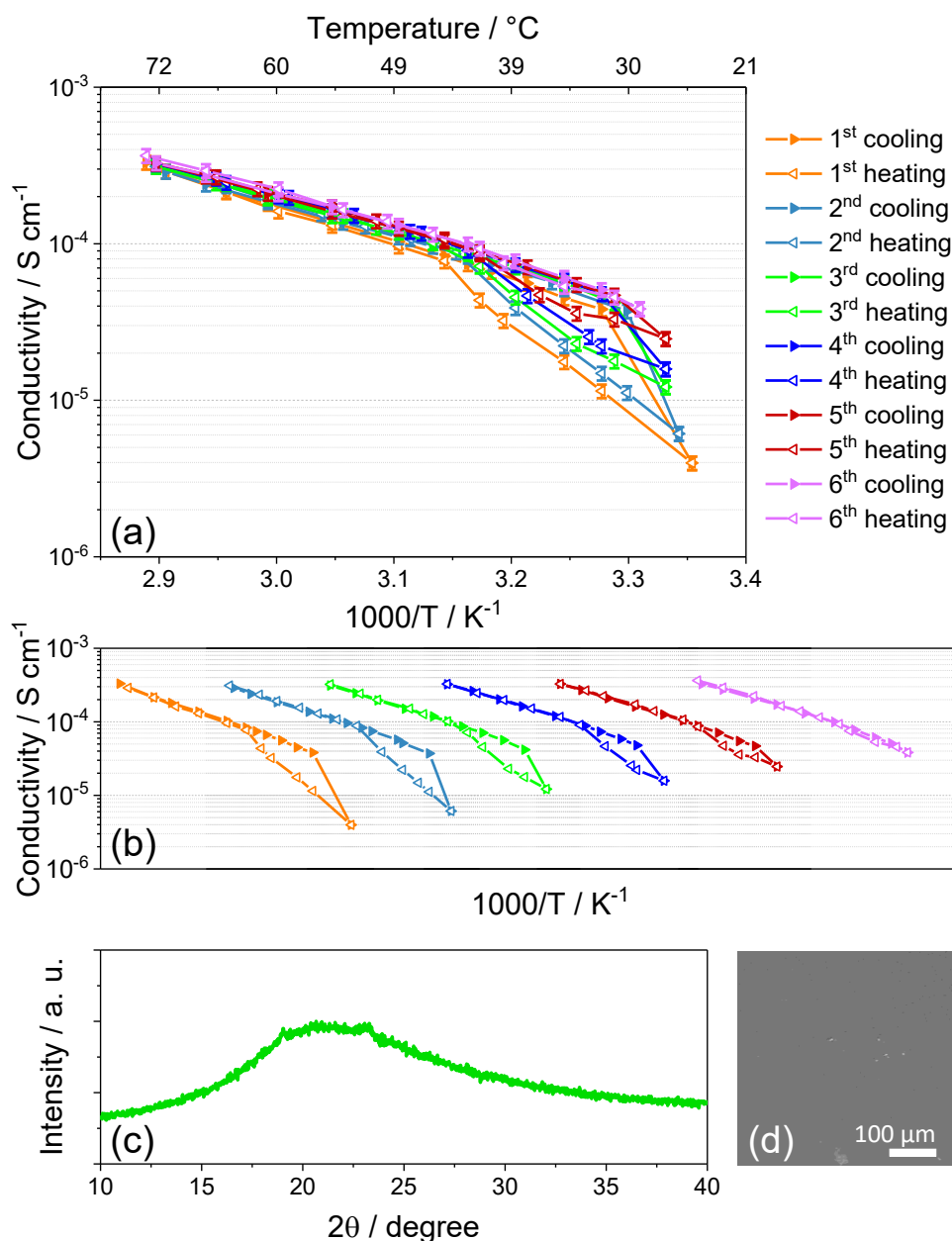
Figure 3.2.3. (a) Arrhenius conductivity plots during subsequent thermal cycles of cooling and heating of the PEGDME_CPE from about 75 °C to room temperature (25 °C), and **(b)** corresponding individual cooling/heating cycles. Conductivity determined by EIS using frequency ranging from 500 kHz to 100 Hz, with signal amplitude of 10 mV (corresponding Nyquist plots are not reported). **(c)** XRD pattern of the PEGDME_CPE membrane after heating at 70 °C and subsequent cooling to room temperature (25 °C), and **(d)** corresponding SEM image.

In order to study the retention of the solid configuration of PEGDME_CPE, a heating-cooling treatment was carried out on the membrane and the results are depicted in Figure 3.2.4. The figure shows that the membrane is characterized by a solid configuration at room temperature (Fig. 3.2.4a, in agreement with Figs. 3.2.1h and i) and during all the steps of the heating treatment, that is, after heating for 3 h at 50 °C (Fig. 3.2.4b) and, subsequently, for 3 h at 70 °C (Fig. 3.2.4c). It is worth

noting that after being heated at 70 °C, PEGDME_CPE presents a slight transparency, most likely due to amorphization processes discussed above. When cooled back to the room temperature (Fig. 3.2.4d), the membrane recovers the initial self-standing condition. Therefore, Figure 3.2.4 demonstrates that the solid nature of PEGDME_CPE is retained from room temperature to 70°C. However, partial membrane softening at the higher temperature values is not excluded.
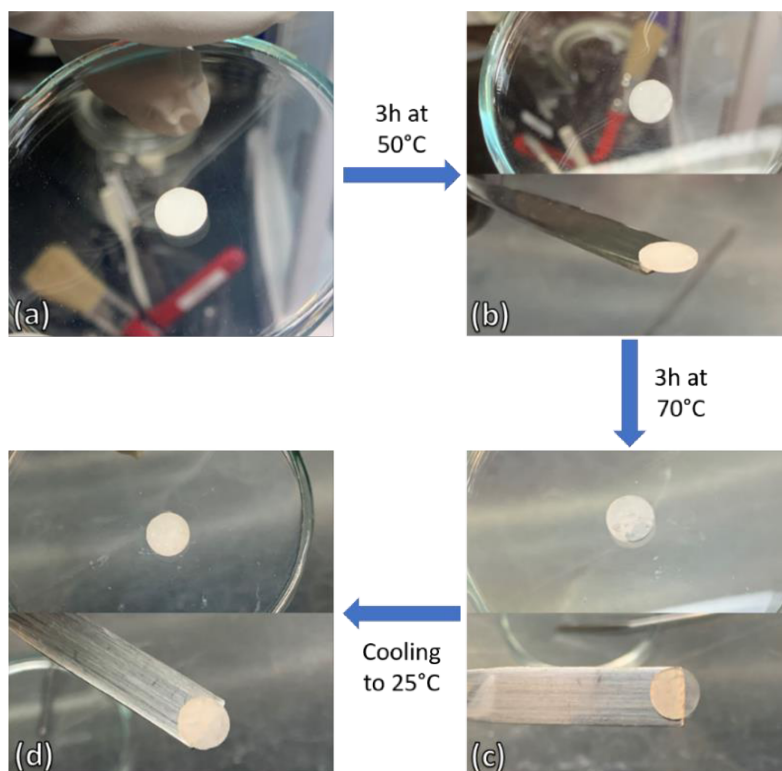
Figure 3.2.4. Photographic images of the PEGDME_CPE membrane **(a)** at room temperature (i.e., 25°C), **(b)** after 3 hours at 50°C, **(c)** after 3 hours at 70°C and **(d)** after cooling back to 25°C.

In addition, PEGDME_CPE shows high thermal stability, as confirmed by thermogravimetric analysis (TGA) under inert atmosphere of Figure 3.2.5a (see Figure 3.2.5b showing the corresponding DTG). The thermal analysis of the solid PEGDME2000 polymer, reported in the same figure for comparison, reveals a single weight loss starting at about 280 °C and centered slightly above 380 °C, which suggests a large application temperature range. On the other hand, the PEGDME_CPE exhibits three weight-loss steps: the first one is centered at 340 °C and might be ascribed to removal of the fraction of PEGDME2000 chains that interact with the SiO_2 particles;[60] the second one occurs at 400°C and is likely related to complexes formed between PEGDME2000 and the lithium salts, which are characterized by higher decomposition temperature;[61] the third one is observed in the temperature range from 420 °C to 470°C and is mainly attributed to the decomposition of LiTFSI

(see Fig. 3.1.3 in section *3.1*). Notably, 15wt% sample residues after the measurement mostly consist of SiO$_2$ along with chemical compounds formed by the decomposition of the lithium salts (LiTFSI and LiNO3). Therefore, the composite polymer electrolyte ensures a a remarkable thermal stability (up to 280 °C).
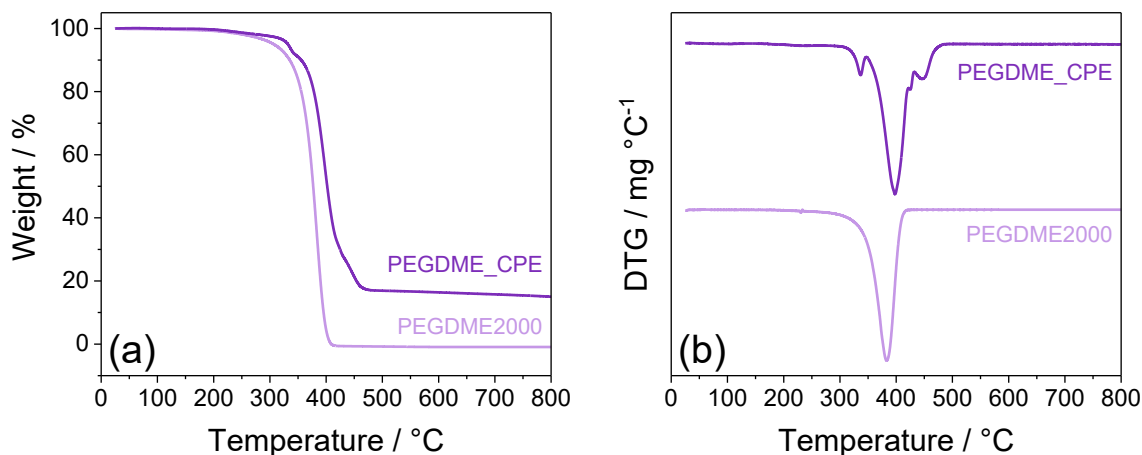
Figure 3.2.5. (a) TGA and **(b)** corresponding DTG curves of the PEGDME_CPE and PEGDME2000 powder recorded under N$_2$ in a temperature range between 25 °C and 800 °C at a heating rate of 5 °C min^{-1}.

The ion transport characteristics of the PEGDME_CPE at various temperatures are further investigated in Figure 3.2.6 by determining the Li$^+$ transference number (t$^+$) by the Bruce-Vincent-Evans method[11] at 45, 50 and 70 °C (see the *3.2.2 Experimental* section for details). Figure 3.2.6a reports the chronoamperometric curves for each temperature, while inset shows the Nyquist plots recorded through EIS before and after cells polarization (see Table 3.2.1 for the parameter values).

The t$^+$ values of PEGDME_CPE (Table 3.2.1) calculated by equation (3.2.1) and the data of Figure 3.2.6 range from 0.22 at 45 °C, to 0.23 at 50 °C, and to 0.27 at 70 °C, with a slight increase possibly due to a more efficient anion solvation by polymer chains at the higher temperature which favors the lithium ion motion.[53] The t$^+$ values of PEGDME_CPE are comparable to those of solid polymer electrolytes such as PEO-based ones at similar temperatures,[62,63] however they are lower than the ones ascribed to the liquid electrolytes, such as glyme-based solutions, which generally approach and exceed 0.5.[7] The relatively low t$^+$ expected by the polymer electrolyte design can actually limit the rate capability of the PEGDME_CPE compared to liquid electrolytes, however the solid state of the membrane likely ensures good safety content and thermal stability, which represent key factors for allowing the use of the high energy lithium metal in efficient and scalable battery. It is worth noting that the Nyquist plots of Figure 3.2.6a are characterized by a low-frequency linear

132

Warburg element due to the Li$^+$ ions diffusion, a middle-frequency semicircle ascribed to the interphase, and by a high-frequency element (only at temperatures lower than 70 °C) most likely due to grain boundary or heterogeneity into the electrolyte with resistances gradually decreasing by increasing the temperature. Grain boundary and heterogeneity may be associated to the coexistence of crystalline and amorphous phases into the electrolyte structure, in particular at the lower temperatures, as well as to possible agglomeration of the ceramic filler.[56] The electrolyte heterogeneity may be strongly mitigated by adequate heat thermal cycles, performed in order to achieve the optimal characteristics of the membrane, as indeed demonstrated by the conductivity measurements discussed in Figure 3.2.3.

Temperature [°C]	Initial current (i_0) [A]	Steady state current (i_{ss}) [A]	Initial resistance (R_0) [Ω]	Steady state resistance (R_{ss}) [Ω]	Li$^+$ transference number (t^+)
45	6.8×10^{-5}	2.5×10^{-5}	231	235	0.22
50	9.5×10^{-5}	3.5×10^{-5}	153	158	0.23
70	1.5×10^{-4}	5.6×10^{-5}	78	75	0.27

Table 3.2.1. Parameters used to determine lithium transference number of PEGDME_CPE at different temperatures using the Bruce-Vincent-Evans equation (3.2.1). Resistance values were obtained by NLLS analyses of the Nyquist plots displayed in Fig. 3.2.6a, recorded using a frequency ranging from 500 kHz to 100 mHz with signal amplitude of 10 mV, upon chronoamperometry performed for 90 min by applying a voltage of 30 mV to a Li|PEGDME_CPE|Li symmetrical cell.

Figure 3.2.6b reports the voltage profiles of the lithium stripping/deposition tests performed at 45, 50 and 70 °C in a Li|PEGDME_CPE|Li cell in order to evaluate the electrochemical stability of the electrolyte. The low and constant overvoltage exhibited by the cell at each temperature, that is 45 mV at 70 °C, 90 mV at 50 °C and 120 mV at 45 °C, and the absence of lithium dendrite formation reflect a relevant stability of the Li/electrolyte interphase which may promote the safety content of the polymer cell. Furthermore, inset of Figure 3.2.6b reports the voltage profiles of lithium stripping/deposition test prolonged to over 350 h at 50 °C, which is considered a suitable temperature for achieving good electrochemical performance of the electrolyte and, at the same time, a sufficiently moderate operating value, adequate for a wide range of application, including electric vehicles (EVs).[64] The figure reveals a pronounced stability, and an overvoltage limited to about 100 mV during charge and discharge, thus suggesting a well reversible lithium stripping/deposition upon cycling.
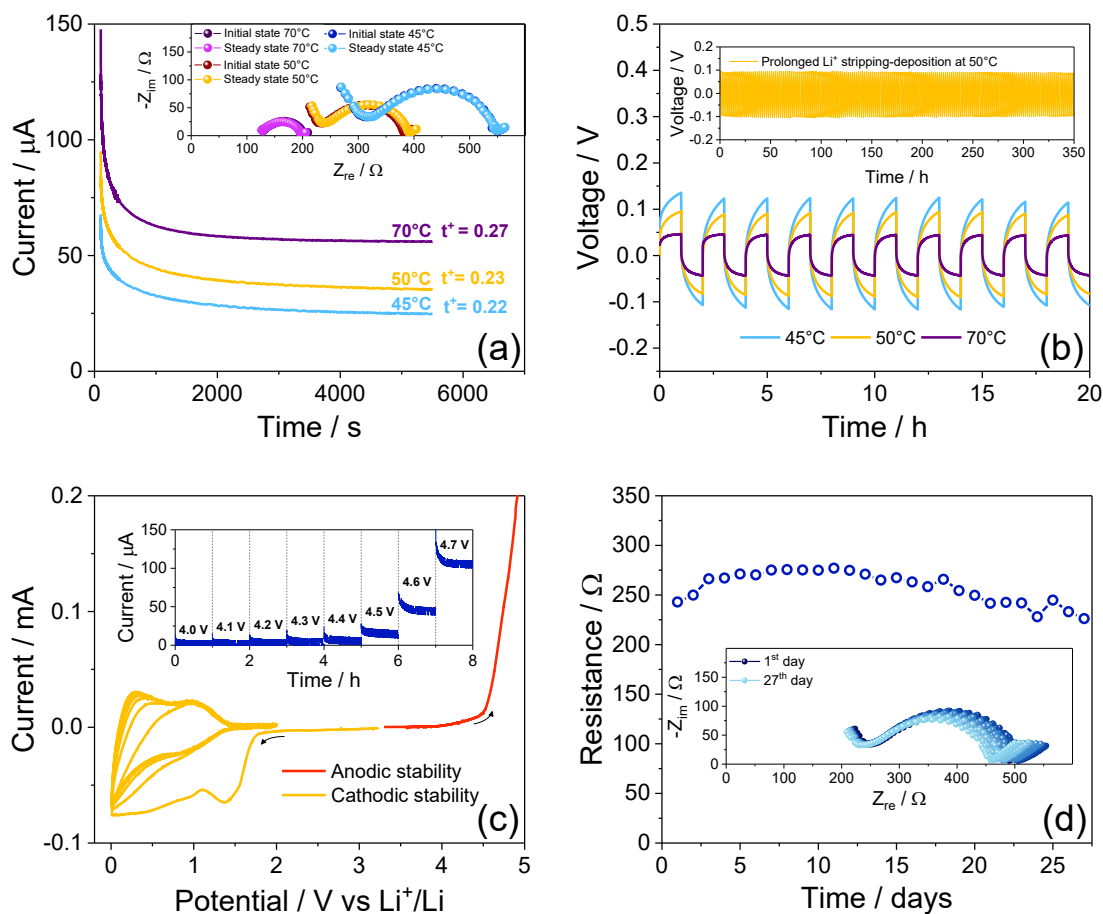
Figure 3.2.6. **(a)** Chronoamperometric profiles of a symmetrical Li/PEGDME_CPE/Li cell used for determining the Li^+ transference number of PEGDME_CPE at 45 °C (cyan), 50 °C (yellow) and 70 °C (purple). Chronoamperometric polarization voltage: 30 mV, inset shows the corresponding Nyquist Plots obtained by EIS at the initial and steady state for each temperature. Frequency range: 500 kHz – 100 mHz. Signal amplitude: 10 mV. **(b)** Lithium stripping-deposition galvanostatic test performed in symmetrical Li/PEGDME_CPE/Li cell at 45 °C (cyan), 50 °C (yellow) and 70 °C (purple), inset shows a prolonged lithium stripping-deposition test performed at 50 °C. Applied Current: 0.1 mA cm^{-2}. **(c)** CV in the cathodic region (yellow) and LSV in the anodic region (red) performed at 50 °C with a scan rate of 0.1 mV s^{-1} in lithium cell using the PEGDME_CPE. Cyclic voltammetry range: 0.01 – 2 V *vs* Li$^+$/Li. Inset shows the chronoamperometry test at potentials from 4.0 V to 4.7 V *vs* Li$^+$/Li with increment of 0.1 V every 1 h at 50 °C. **(d)** Trend of interphase resistance upon Li/PEGDME_CPE/Li cell aging at 50 °C determined by NLLS fit of the corresponding EIS Nyquist plots, reported in figure inset. Frequency range: 500 kHz–100 mHz. Signal amplitude: 10 mV.

The electrochemical stability window of the PEGDME_CPE is evaluated by the voltammograms displayed in Figure 3.2.6c in the anodic (red) and cathodic (yellow) regions. The LSV anodic curve shows a flat profile without significant current flow extending from the OCV of the cell until 4.5 V *vs* Li$^+$/Li, where a further increment of the voltage causes a raise of the current over 10 μA due to the beginning of oxidative electrolyte decomposition. The anodic stability was further investigated by measuring the current by chronoamperometry from 4.0 to 4.7 V *vs* Li$^+$/Li (see

134

3.2.2 Experimental section for details). The results reported in inset of Figure 3.2.6c reveal a significant current flow only at 4.5 V *vs* Li$^+$/Li where a value of 15 μA is observed, as well as at higher potentials. Therefore, the chronoamperometry and voltammetry agree in indicating a remarkable anodic stability slightly below 4.5 V *vs* Li$^+$/Li. The cathodic CV scans show irreversible peaks at about 1.4 V *vs* Li$^+$/Li and below 1.0 V *vs* Li$^+$/Li during the first cycle, attributed to the reduction of the LiNO$_3$ and of the PEGDME2000, respectively, with concomitant formation of a SEI layer which passivates the electrodes surface.[65] Indeed, the subsequent CV cycles, performed in the cathodic region within 0.01 V *vs* Li$^+$/Li and 2.0 V *vs* Li$^+$/Li, are characterized by overlapping curves suggesting a reversible and kinetically favorable Li$^+$ ion insertion into the carbon electrode and possibly lithium stripping/deposition around 0 V *vs* Li$^+$/Li. Thus, the electrochemical stability window of PEGDME_CPE extends from 0.01 V *vs* Li$^+$/Li to about 4.4 – 4.5 V *vs* Li$^+$/Li at 50 °C that is well suitable for application in lithium battery.[66] The chemical stability of Li/electrolyte interphase is investigated through EIS measurements upon aging of a symmetrical Li/PEGDME_CPE/Li cell and reported in Figure 3.2.6d along with the related Nyquist plots in inset. As already mentioned during discussion of Figure 3.2.3, the Nyquist plots exhibit a high-frequency grain boundary element, a middle-frequency semicircle ascribed to the interphase and a low-frequency Warburg element. Furthermore, Figure 3.2.6d shows a raise of the electrode/electrolyte interphase resistance from 242 Ω up to 277 Ω by the initial 11 days of test due to SEI growth, a decrease to about 225 Ω, and a stabilization during the subsequent days, thus suggesting a partial dissolution and final consolidation of the passivation layer with appropriate suitability for battery application[67] in view of the limited resistance fluctuations (about 50 Ω).

The PEGDME_CPE is subsequently tested in lithium metal battery, exploiting a LiFePO$_4$ (LFP) cathode.[49] Prior to cycling, the cell is held at 70 °C for 14 h and then cooled down at the operating temperature of 50 °C, which was found to be the most adequate value for the application of the PEGDME_CPE in lithium battery (see Fig. 3.2.6 discussion). Figure 3.2.7 shows the EIS Nyquist plots recorded upon the above mentioned heat treatment. During the initial stages at 70 °C (Fig. 3.2.6a) all the Nyquist plots may be reasonably represented by the equivalent circuit R$_e$(R$_1$Q$_1$)(R$_2$Q$_2$)Q$_3$ where the electrolyte resistance (R$_e$) is in series with a middle-high frequency element (R$_1$Q$_1$) due to the electrode/electrolyte interphase, including SEI film at the electrodes surface and charge transfer, and a low-frequency element (R$_w$Q$_w$) due to a Warburg-type Li$^+$ ion diffusion, and an almost vertically tilted line (Q$_g$) due to the cell geometrical capacity possibly accounting for a blocking electrode configuration at the OCV of the cell (see Table 3.2.2 for EIS data analysis).[14] The interphase resistance (R$_1$) trend reported in inset of Figure 3.2.7a shows an initial value of about 40 Ω, slightly increasing to about 45 Ω by 6 h of test and subsequently decreasing to about 33 Ω.

Cell condition	Equivalent circuit	R_1 [Ω]	χ^2
2h at 70°C	$R_e(R_1Q_1)(R_wQ_w)Q_g$	40.6 ± 2.1	1.0×10^{-4}
4h at 70°C	$R_e(R_1Q_1)(R_wQ_w)Q_g$	41.4 ± 1.2	6.5×10^{-5}
6h at 70°C	$R_e(R_1Q_1)(R_wQ_w)Q_g$	45.4 ± 0.91	3.6×10^{-5}
8h at 70°C	$R_e(R_1Q_1)(R_wQ_w)Q_g$	45.4 ± 0.9	3.0×10^{-5}
10h at 70°C	$R_e(R_1Q_1)(R_wQ_w)Q_g$	43.7 ± 0.7	1.3×10^{-5}
12h at 70°C	$R_e(R_1Q_1)(R_wQ_w)Q_g$	37.6 ± 0.9	1.3×10^{-5}
14h at 70°C	$R_e(R_1Q_1)(R_wQ_w)Q_g$	33.9 ± 1.0	2.0×10^{-5}
Steady state at 50°C	$R_e(R_1Q_1)Q_w$	374 ± 14	1.0×10^{-4}

Table 3.2.2. NLLS analyses performed on the impedance Nyquist plots of Figure 3.2.7 related to the open circuit voltage (OCV) of the Li/PEGDME_CPE/LFP cell at 70 °C by various time intervals and at 50 °C upon the steady state condition. Frequency range: 500 kHz – 100 mHz
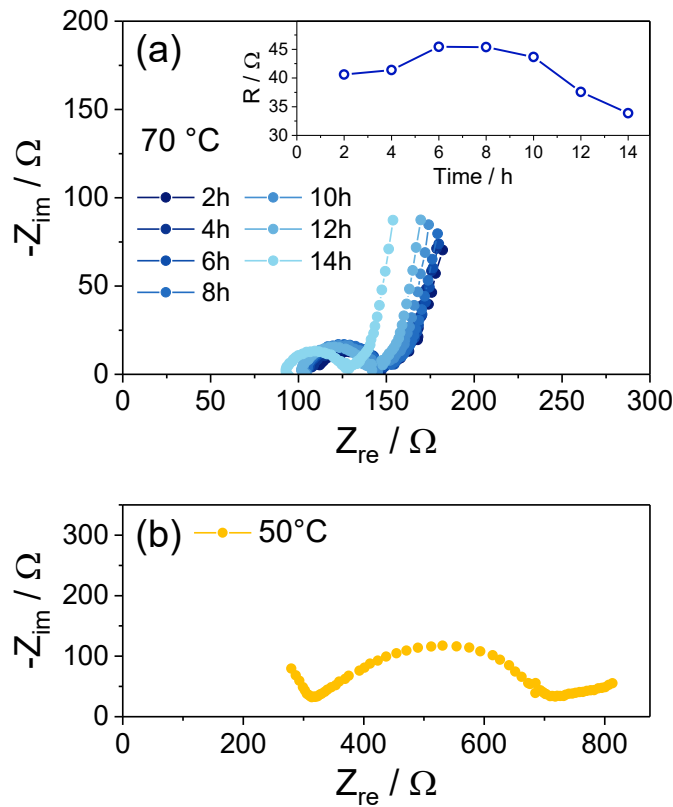
Figure 3.2.7. Nyquist plots recorded by EIS measurements at the open circuit voltage (OCV) of the Li|PEGDME_CPE|LFP cell **(a)** performed every 2 h after cell assembly during heating from room temperature (25 °C) to 70 °C; **(b)** at the steady state upon lowering the temperature back to 50 °C. Frequency range: 500 kHz – 100 mHz. Signal amplitude: 10 mV.

Upon cell cooling to 50 °C, the Nyquist plot reported in Figure 3.2.7b reveals the additional element at high frequency due to possible grain boundary or heterogeneity, already observed previously in Li/Li symmetrical cell, due to partial crystallization of the electrolyte (not considered by NLLS in Table 3.2.2).[53] Furthermore, the figure shows an increase of the interphase resistance to about 374 Ω, while the final vertically tilted line is not detected most likely due to the higher impedance value at 50 °C compared to 70 °C.[14] Despite the increase of the interphase resistance at 50 °C, which is however considered still within the applicability range of the polymer membrane in efficient lithium cell, the lower operating temperature is considered herein more suitable for a practical use.

Therefore, the electrolyte is subsequently studied in a Li|PEGDME_CPE|LFP cell by using an operating temperature of 50 °C indicated above. Figure 3.2.8 reports the voltage profiles (a) and the cycling trend of the galvanostatic test performed at various current rates, i.e., C/10, C/8, C/5, C/3, and 1C (1C = 170 mA g^{-1}) at 50 °C within 2.7 V and 3.9 V which is considered the most suitable range for allowing proper cell operation without possible occurrence of side reactions.[49,68] The figure evidences that the cell performs at C/10 by a voltage profile reflecting the electrochemical process expected by the olivine cathode, i.e., $LiFePO_4 \rightleftarrows Li + FePO_4$, centered at about 3.5 V with a flat profile typical of a two phases process,[68] with very limited polarization, and a specific capacity approaching 150 mAh g^{-1}, i.e., about 88% of the theoretical capacity associated with the adopted cathode.[49,68] Furthermore, the cell shows at 50 °C only a limited change of polarization and capacity at C/8 rate.
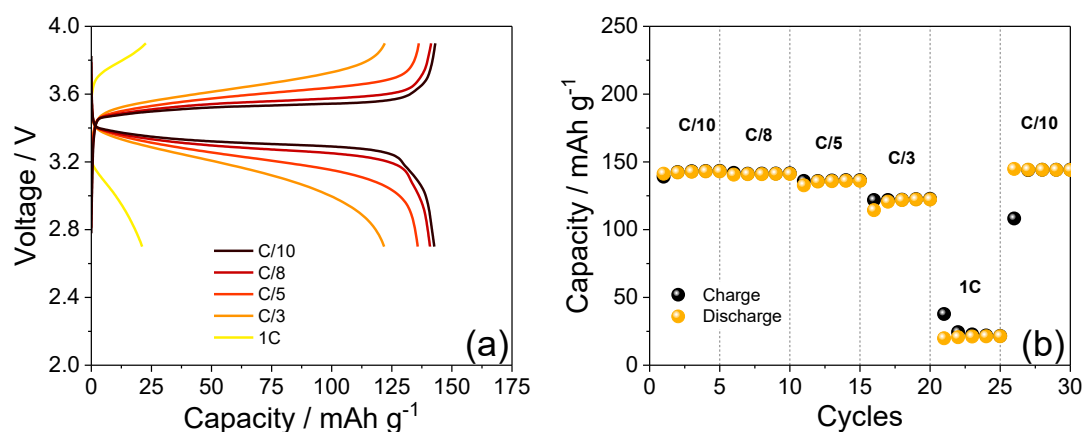
Figure 3.2.8. (a) Voltage profiles and **(b)** corresponding charge/discharge cycling trend of the galvanostatic test performed on a Li|PEGDME_CPE|LFP cell using various current rates, i.e., C/10, C/8, C/5, C/3, and 1C at a temperature of 50 °C. Voltage limits 2.7–3.9 V.

The voltage shape appears more affected by the current raise to C/5 and C/3 (Fig. 3.2.8a), while the capacity holds a satisfactory value at both C-rates, i.e., of about 140 and 125 mAh g^{-1}, respectively (Fig. 3.2.8b). However, a further raise of the current to 1C notably increases the cell polarization and limits its capacity to negligible value, as indeed expected by the solid configuration of the cell and the relatively low lithium transference number of the polymer electrolyte which hinders the charge transfer at high currents. The cell stability is evidenced by the recovery of the initial capacity by lowering back the current to the pristine value of C/10 (Figure 3.2.8b), which is considered an optimal characteristic of the PEGDME_CPE studied herein.

The stability of the PEGDME_CPE in lithium cell is further demonstrated by the prolonged galvanostatic cycling test reported in Figure 3.2.9. The voltage profiles of the measurement performed at a current rate of C/5 (Fig. 3.2.9a) well overlap upon the first cycle during which a passivating SEI layer is formed over the electrodes,[14] and the lithium polymer cell reveals constantly low polarization, a working voltage centered at about 3.5 V, and a steady state capacity of about 150 mAh g^{-1}. Remarkably, the cell shows a coulombic efficiency exceeding 99% after the first cycle which is reflected into a very stable cycling trend (Fig. 3.2.9c) and a capacity retention as high as 99% with respect to the first cycle upon 140 cycles. In order to further analyze the cycling life of the Li|PEGDME_CPE|LFP cell, a galvanostatic test at a higher current (i.e., C/3 rather than C/5) prolonged over 300 cycles was performed. The corresponding voltage profiles (Fig. 3.2.9b) exhibit a remarkable overlapping upon the first cycle, and higher polarization compared the test at C/5 (Fig. 3.2.9a), fully in line with the rate capability test (compare with Fig. 3.2.8a), which decreases during cycles likely due to gradual improvement of the electrode/electrolyte interphase. Furthermore, the cell delivers a capacity exceeding 120 mAh g^{-1} (Fig. 3.2.9d), coulombic efficiency higher than 99% and a remarkable stability over 300 cycles with a capacity retention of about 99%. It is worth noting that the voltage shape of the battery does not modify upon repeated charge and discharge which occur without any sign of increasing polarization, thus accounting for the absence of side reactions both during oxidation and during reduction, in full agreement with the electrochemical stability windows observed for the PEGDME_CPE in Figure 3.2.6. This behavior is notable, in particular considering the relatively low temperature compared to the common solid polymer cells, and suitable for application in high performance battery safely operating using the high-energy lithium metal.
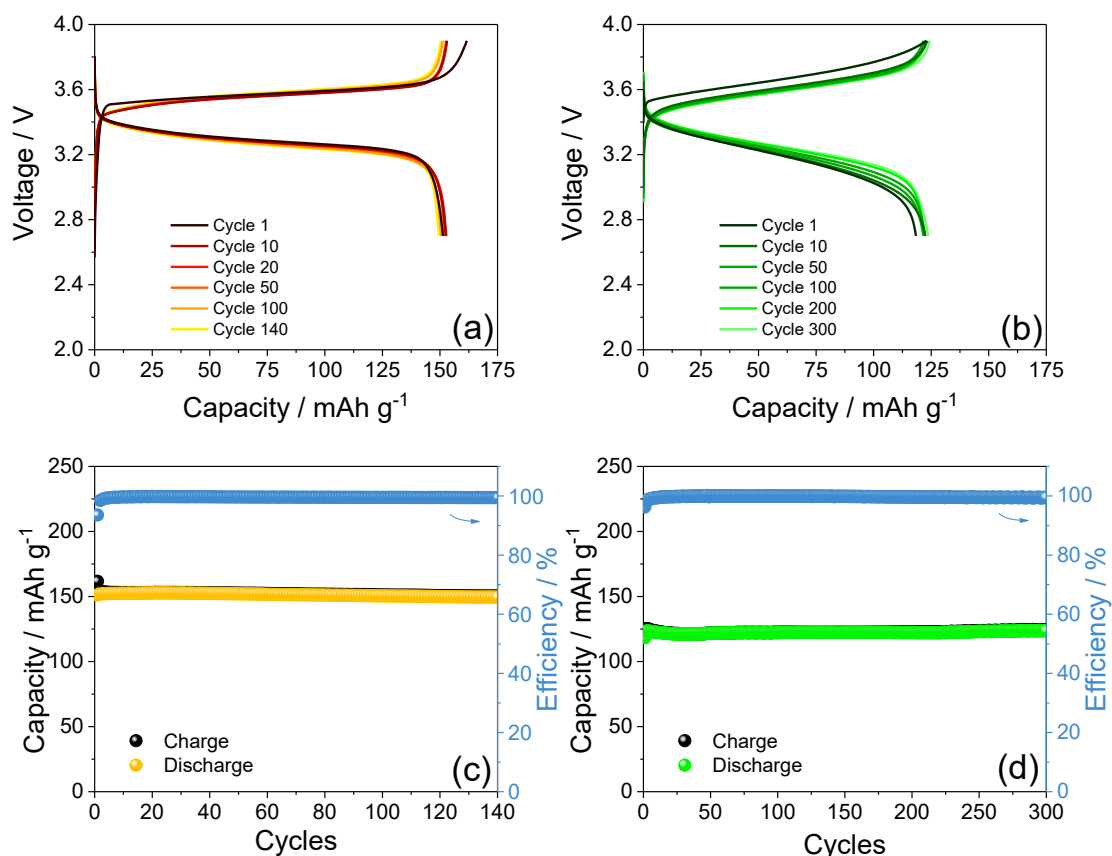
Figure 3.2.9. (a, b) Voltage profiles and **(c, d)** corresponding charge/discharge cycling trend in terms of delivered capacity (left y-axis) and coulombic efficiency (right y-axis) of the galvanostatic tests performed on Li|PEGDME_CPE|LFP cells using current rates of **(a, c)** C/5 and **(b, d)** C/3 at 50 °C. Voltage limits 2.7 – 3.9 V.

In spite, a different behavior is shown by cycling a lithium cell within the same current and temperature conditions above reported using the membrane without $LiNO_3$ (i.e., the blank electrolyte). Figure 3.2.10 shows the comparison of cycling responses of Li|blank|LFP and Li|PEGDME_CPE|LFP cells using a current rate of C/5 at 50 °C. The voltage profile (Fig. 3.2.10a) related to the Li/blank/LFP cell (black color) reveals a higher polarization with respect to Li|PEGDME_CPE|LFP cell (orange color), a lower and a less stable capacity characterized by an initial increase, followed by a more remarkable decrease evidenced by the cycling trend comparison reported in Fig. 3.2.10a inset. Furthermore, the voltage profile of Li|blank|LFP cell evidences the presence of irregular spikes, likely ascribed to formation and dissolution of dendritic structures on the lithium surface.[69,70] The higher polarization of the cell using the blank membrane with respect to PEGDME_CPE is reflected into a lower energy efficiency, which is further lowered together with the coulombic efficiency by dendrite growth and dissolution as evidenced by the trends of Fig. 3.2.10b. It can be supposed that the decrease of the cell efficiency and the evolution of the dendritic

structures typical of the lithium metal anode is remarkably mitigated by the use of the $LiNO_3$ additive in the polymer electrolyte, which is fundamental for application in Li-S battery.[47]
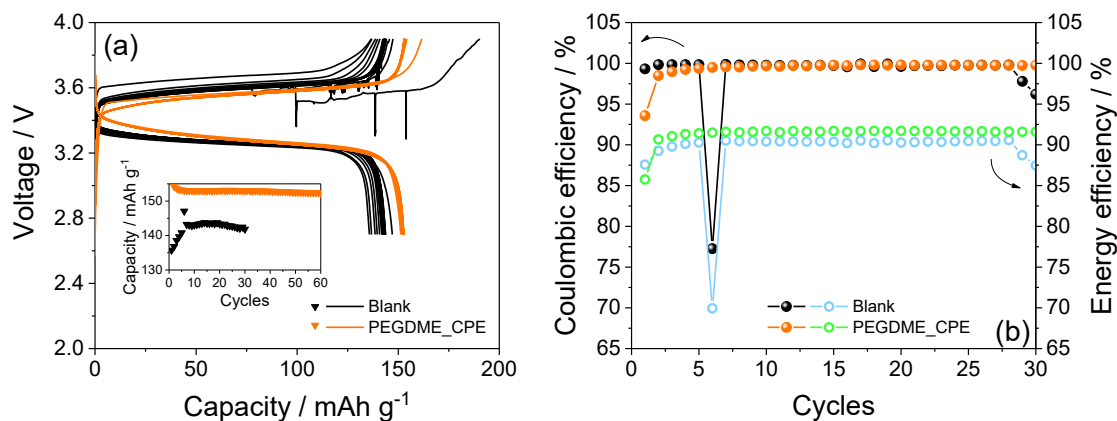
Figure 3.2.10. (a) Voltage profiles related to the first 30 cycles of the galvanostatic cycling measurements performed on Li|PEGDME_CPE|LFP (orange) and Li|blank|LFP (black) cells by applying a current rate of C/5 at 50°C. Inset shows the related discharge cycling trend; **(b)** corresponding coulombic efficiency (left y-axis) and energy efficiency (right y-axis). Voltage limits: 2.7 – 3.9 V.

Following this trend, the PEGDME_CPE is subsequently applied in a Li-S battery employing a scalable sulfur cathode (S:SPC 70:30 w/w, see *3.2.2 Experimental* section for details). The electrochemical response of the Li-S polymer battery is investigated by CV and EIS from 50 to 80°C, to demonstrate the actual applicability and stability of this cell configuration in a wide temperature range. Figure 3.2.11a, b, c and d reports the voltammograms of the cell tested consecutively at 50, 60, 70, and 80 °C, respectively. Figure 3.2.11a reveals for the polymer battery a discharge process at 50 °C with current peaks at 1.94 and 2.33 V *vs* Li^+/Li upon the first cycle, which are reflected as two charge signals at 2.28 and 2.60 V *vs* Li^+/Li. This response is in part consistent with that of conventional Li-S batteries using liquid electrolyte solutions typically characterized by two discharge peaks at about 2.3 and 2.0 V *vs* Li^+/Li, reflecting the reversible conversion of lithium and sulfur to soluble lithium polysulfides with various chain lengths (Li_2S_x with $4 \leq x \leq 8$) along with solid Li_2S_2 and Li_2S, and two overlapped charge signals around 2.3 V *vs* Li^+/Li.[71] The subsequent CV profiles of the polymer battery at 50 °C (Figure 3.2.11a) exhibit a shift of the discharge peaks to higher potentials likely due to improved reaction kinetics, and a raise of the charge peak at 2.28 V *vs* Li^+/Li suggesting an enhancement of the polysulfide oxidation rate. According to the results presented in Chapter 2, this activation upon cycling can be associated with micro-structural rearrangements in cathode which increase the sulfur utilization and enhance the electrode/electrolyte interphase. Further improvements in electrochemical activity can be achieved by rising the operating temperature, as

shown in Figure 3.2.11b, c and d. Indeed, an increase in temperature up to 60 (Fig. 3.2.11b), 70 (Fig. 3.2.11c) and 80 °C (Fig. 3.2.11d) leads to a higher peak current upon charge and to a better overlap of the CV profiles (in particular at 60 and 70 °C), thus suggesting a very stable and reversible electrochemical process. Furthermore, a discharge peak appears slightly above 2 V *vs* Li^{+}/Li when the temperature ranges from 60 to 80 °C, thereby indicating that the segmental motion of the polymer chains may assist the ionic transport through the electrolyte and at the electrode/electrolyte interphase during the conversion process.[72] Furthermore, the presence of an additional reduction peak between 2.0 and 2.1 V *vs* Li^{+}/Li observed in the CV measurements performed at 60, 70 and 80 °C, as well as the absence of a zero-current response at the end of cathodic scan, is likely ascribed to relatively slow kinetics for the formation of the various polysulfides in the PEGDME_CPE matrix, and actually indicates a partially reversible reaction.
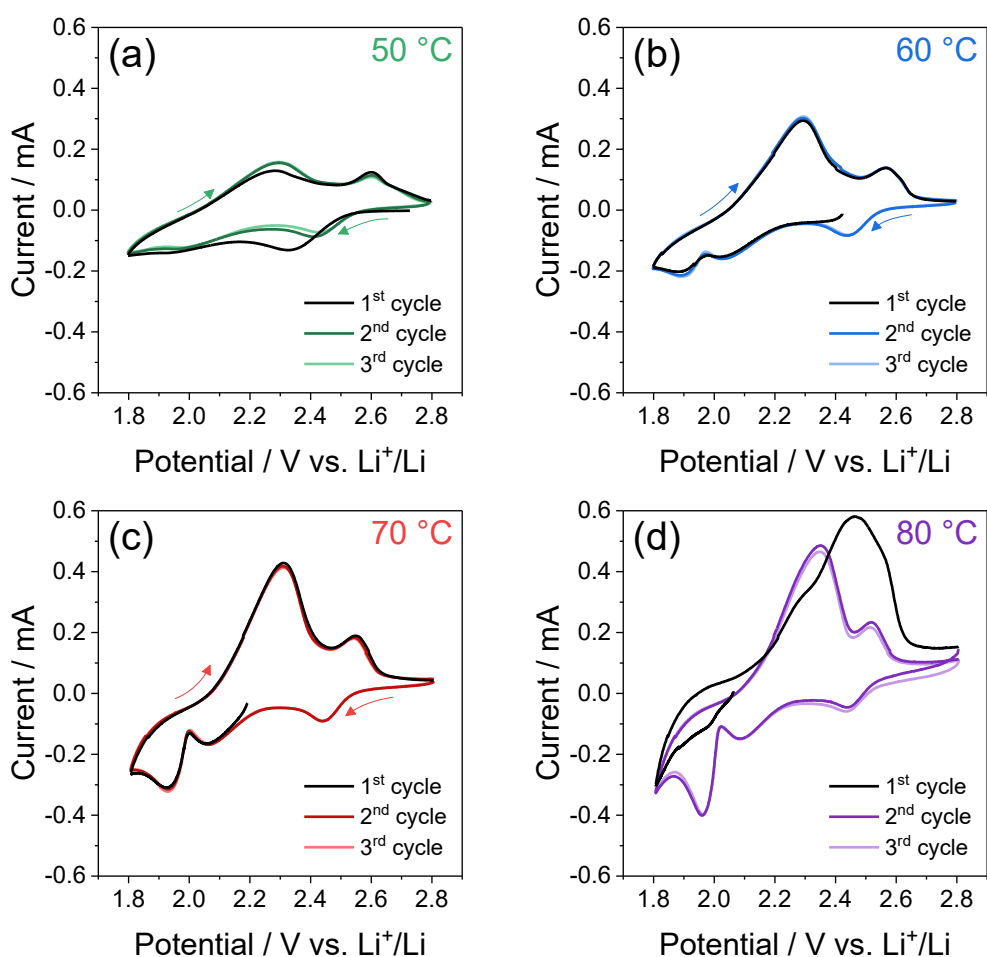
Figure 3.2.11. CV curves and of the Li|PEGDME_CPE|S:SPC 70:30 w/w cell at increasing temperatures, that is, **(a)** 50 °C, **(b)** 60 °C, **(c)** 70 °C and **(d)** 80 °C. CV performed between 1.8 and 2.8 V *vs* Li^{+}/Li at 0.1 mV s^{-1}.

On the other hand, the reduction of S_8 to polysulfides in the lithium cell occurs through various reaction steps and leads to Li_2S_x species with different chain length within the full range of the

discharge potential. These steps may be partially detected by voltammetry depending on the operating temperature, as indeed shown in Figure 3.2.11. In particular, the additional peaks at the lower potential during reduction may be reasonably ascribed to the kinetically hindered formation of low-chain polysulfides (such as Li_2S_4 and Li_2S_2). Notably, the significant polarization of the polymer cell upon charging at 50°C leads to two distinct charge peaks in the CV (Figure 3.2.11a), while those employing common DOL:DME solutions display broad, convoluted peaks during oxidation.[73] Therefore, the different electrochemical response of the Li-S polymer cell compared to the Li-S conventional ones using a liquid solution may be in part ascribed to the mobility of Li^+ ions within the electrolyte medium and at the interphase between electrolyte and sulfur electrode. Accordingly, the polymer battery exhibits an electrochemical response approaching the *liquid-like* behavior as the temperature is gradually increased up to 80°C.

In this regard, further insight is given by Figure 3.2.12 and Table 3.2.3, which show that the above discussed charge voltammetry peaks shift toward each other at elevated temperature, whilst the discharge peaks attributed to the short polysulfides shift at higher potential. In particular, Figure 3.2.12a identifies the charge and discharge signals in the voltammetry curve taken in consideration, while the corresponding trends of potential as a function of temperature are reported in Figure 3.2.12b-f. Notably, the 1st charge peak moves from 2.29 V *vs* Li^+/Li at 50 °C to 2.35 V *vs* Li^+/Li at 80 °C (Figure 3.2.12b), while the 2nd charge signal from 2.60 to 2.52 V *vs* Li^+/Li (Figure 3.2.12c), thereby leading to a gradual merging of these peaks promoted by the increase in PEGDME chains mobility and Li^+ ions conductivity, as discussed in Figure 3.2.3. On the other hand, the 1st discharge signal (Fig. 3.2.12d) maintains a constant potential value around 2.44 V *vs* Li^+/Li throughout the entire test, while the 2nd one (Fig. 3.2.12e) and the 3rd one (Fig. 3.2.12f) increase from 1.98 to 2.09 *vs* Li^+/Li and from 1.89 to 1.96 *vs* Li^+/Li, respectively. It is worth noting that the polymer cell at 80°C exhibits in CV a *liquid-like* performance (Fig. 3.2.11d) similar to that of Li-S batteries employing low-molecular-weight glymes, typically characterized by a higher viscosity than that of conventional DOL:DME mixtures.[74] Remarkably, the tests reported in Figure 3.2.11a-d refer to 12 consecutive CV runs at various temperatures, thus suggesting a notable stability of the electrochemical process.
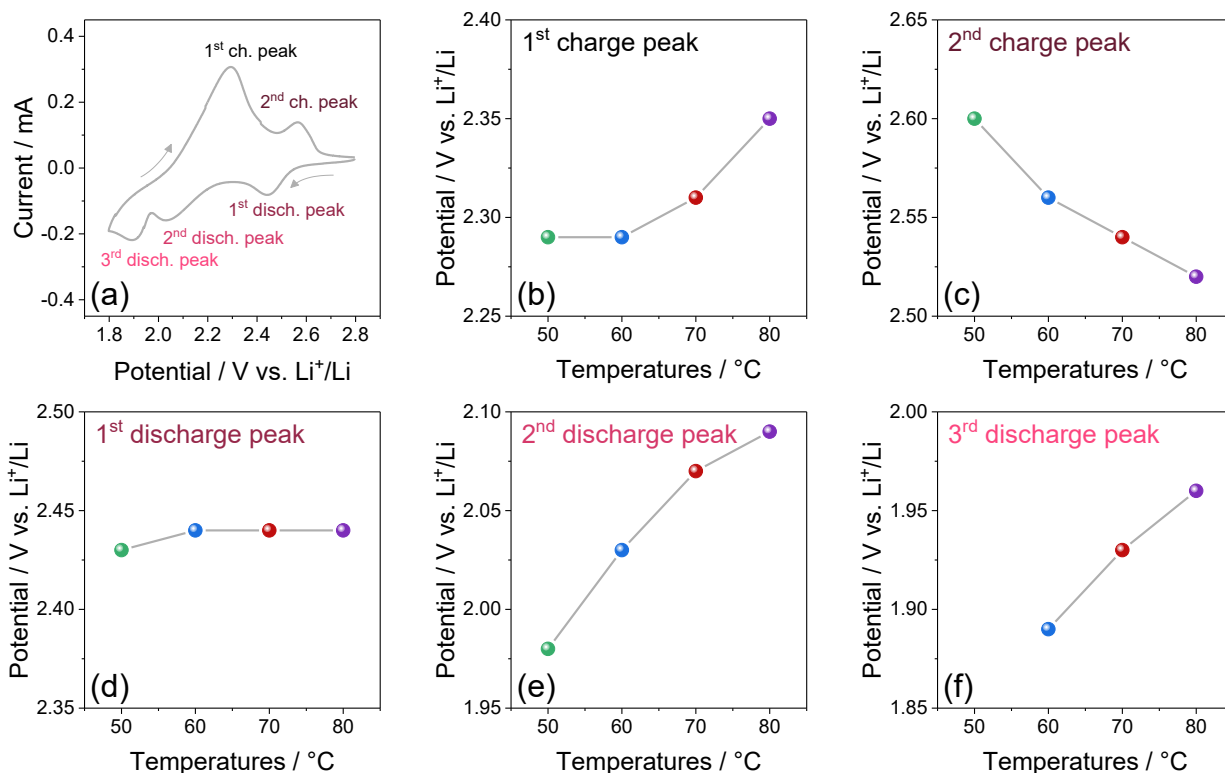
Figure 3.2.12. Trends of electrochemical potential of the Li|PEGDME_CPE|S:SPC 70:30 w/w cell at various temperatures from 50 to 80 °C. In detail: **(a)** CV profile of the cell with indication of the potential of the main current peaks, *i.e.*, during charge **(b)** around 2.3 V *vs* Li$^+$/Li (1st charge peak) and **(c)** between 2.5 and 2.6 V *vs* Li$^+$/Li (2nd charge peak), and during discharge **(d)** at 2.45 V *vs* Li$^+$/Li (1st discharge peak), **(e)** around 2.00 V *vs* Li$^+$/Li (2nd discharge peak) and **(f)** at about 1.90 V *vs* Li$^+$/Li (3rd discharge peak). See the related CV profiles in Figure 3.2.11, as well as the peak potential values in Table 3.2.3. All the potential values were measured during the 3rd cycle at each temperature.

Temperature [°C]	1st charge peak [V *vs* Li$^+$/Li]	2nd charge peak [V *vs* Li$^+$/Li]	1st discharge peak [V *vs* Li$^+$/Li]	2nd discharge peak [V *vs* Li$^+$/Li]	3rd discharge peak [V *vs* Li$^+$/Li]
50	2.29	2.60	2.43	1.98	/
60	2.29	2.56	2.44	2.03	1.89
70	2.31	2.54	2.44	2.07	1.93
80	2.35	2.52	2.44	2.09	1.96

Table 3.2.3. Electrochemical potential of the Li|PEGDME_CPE|S:SPC 70:30 w/w cell at various temperatures from 50 to 80 °C as measured by CV. See the related voltammetry curves in Figure 3.2.11. All the potential values were measured during the 3rd cycle at each temperature.

EIS measurements performed upon CV (see the Nyquist plots in Fig. 3.2.13) reveal modifications at the electrode/electrolyte interphase in the Li-S polymer cell during cycling. Table

3.2.4 reports the results of NLLS analyses of the corresponding spectra, in terms of equivalent circuits (*i.e.*, $R_e(R_iQ_i)Q_w$), resistance values (*i.e.*, R_e and R_i), and χ^2 parameter. In particular, the impedance response of the Li|PEGDME_CPE|S:SPC 70:30 w/w cell was modelled by using equivalent circuits which incorporate the high-frequency electrolyte resistance (R_e), high-to-middle frequency resistive and constant phase elements (R_iQ_i) arranged in parallel and ascribed to the electrode/electrolyte interphase, as well as low frequency elements accounting for the Warburg-type, Li+ diffusion (R_w and Q_w).[12,13] The overall electrode/electrolyte interphase resistance (R_1+R_2) of the polymer cell at 50 °C is represented by the width of the high-middle frequency semicircles of the Nyquist plot (Figure 3.2.13a), and incorporates contributes by SEI film, electrode charge transfer, and possible grain boundaries.[53] The above resistance drops from 83 Ω at the open circuit voltage (OCV) condition at 50 °C to stable values around 42 Ω after 3 voltammetry cycles at the same temperatures (Table 3.2.4).
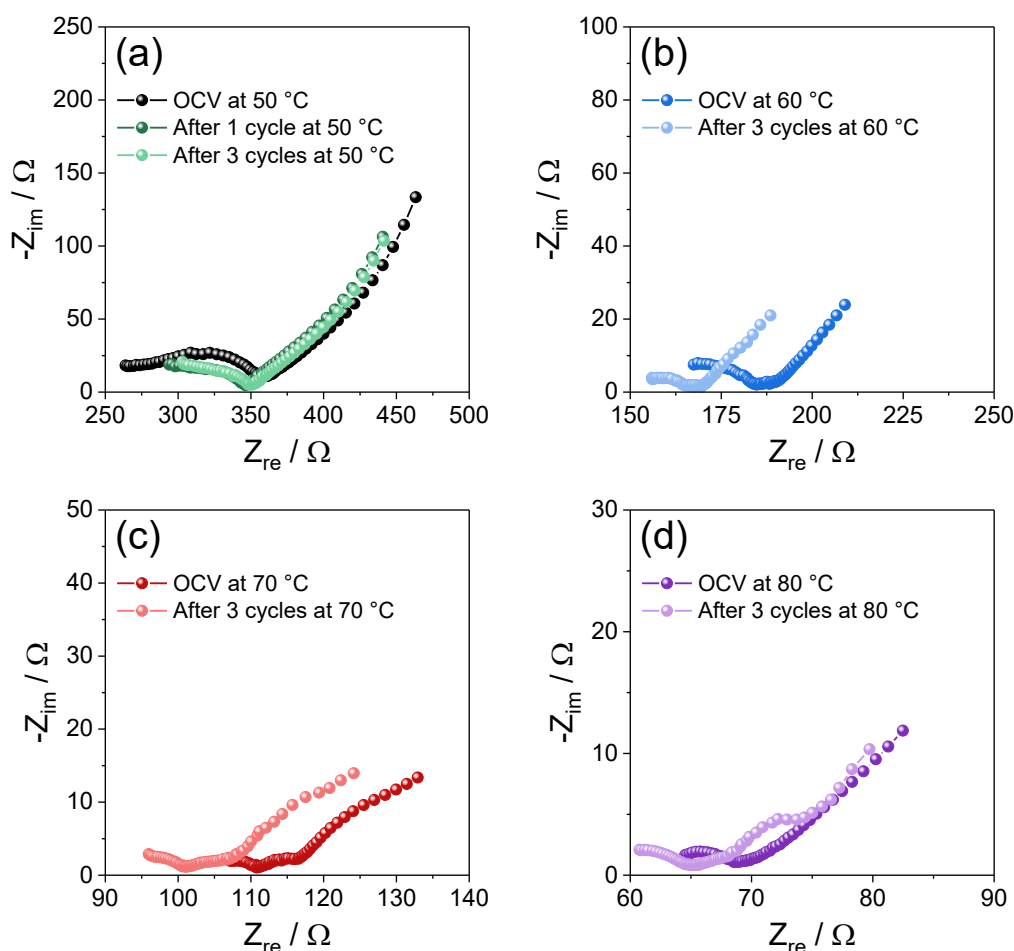
Figure 3.2.13. EIS Nyquist plots of the Li|PEGDME_CPE|S:SPC 70:30 w/w cell at various temperatures, that is, **(a)** 50 °C, **(b)** 60 °C, **(c)** 70 °C and **(d)** 80 °C. EIS carried out at the OCV condition of the cell as well as upon the voltammetry cycles (Fig. 3.2.11), by applying an alternate voltage signal of 10 mV within the 500 kHz–100 mHz frequency range.

This behavior indicates the occurrence of the above mentioned activation processes and consequent enhancement of the electrode/electrolyte interphase by favorable microstructural modifications upon cycling. Accordingly, the rise in operative temperature leads to a further decrease in the overall electrode/electrolyte resistance, thus reflecting the improvements in conversion kinetics observed in Figure 3.2.11, with final values of 17, 14 and 12 Ω at 60, 70, and 80 °C (Table 3.2.4). In this regard, Table 3.2.4 shows that the charge transport through both the interphase and the electrolyte are thermally activated processes. Indeed, the electrolyte interphase resistance measured after subsequent voltammetry cycles decreases from 304 Ω at 50 °C to 150 Ω at 60 °C, 90 Ω at 70 °C, and 55 Ω at 80 °C. The thermal activation of the charge transfer process is also observed by the increase of the (R_iQ_i) elements number in the equivalent circuit (Table 3.2.4). Indeed, the difference between the circuits at 50 °C (Fig. 3.2.13a) and at higher temperatures (Fig. 3.2.13b-d) reflects the modifications of the electrode/electrolyte interphase achieved through temperature rise, which cause the deconvolution of the high-middle frequency semicircle into various contributes (SEI film, electrode charge transfer, and possible grain boundaries) represented by additional (R_iQ_i) elements. Relevantly, these changes are in line with the modification of the CV characteristics of the corresponding Li-S cell (Fig. 3.2.11). Therefore, both the CV and the EIS data reveal that the electrochemical activity of the Li-S polymer battery is adequate at 50°C, and enhanced by thermal activation within the wide operative temperature range extending from 50 to 80 °C.

Temperature (°C)	Cell condition	Circuit	R_e [Ω]	R_1 [Ω]	R_2 [Ω]	$R_1 + R_2$ [Ω]	χ^2
50 °C	OCV	$R_e(R_1Q_1)Q_w$	272 ± 1	83 ± 2	/	83 ± 2	5×10^{-6}
	1 CV cycle	$R_e(R_1Q_1)Q_w$	298 ± 2	44 ± 2	/	44 ± 2	4×10^{-6}
	3 CV cycles	$R_e(R_1Q_1)Q_w$	304 ± 3	42 ± 3	/	42 ± 3	3×10^{-6}
60 °C	OCV	$R_e(R_1Q_1)(R_2Q_2)Q_w$	150 ± 2	36 ± 2	3.4 ± 0.5	39 ± 2	2×10^{-6}
	3 CV cycles	$R_e(R_1Q_1)(R_2Q_2)Q_w$	151 ± 2	15 ± 3	2.3 ± 0.9	17 ± 3	1×10^{-5}
70 °C	OCV	$R_e(R_1Q_1)(R_2Q_2)Q_w$	102 ± 1	9 ± 1	3.9 ± 0.4	13 ± 1	8×10^{-7}
	3 CV cycles	$R_e(R_1Q_1)(R_2Q_2)Q_w$	90 ± 4	11 ± 4	3 ± 1	14 ± 4	9×10^{-6}
80 °C	OCV	$R_e(R_1Q_1)Q_w$	61.0 ± 0.4	7.2 ± 0.4	/	7.2 ± 0.4	1×10^{-6}
	3 CV cycles	$R_e(R_1Q_1)(R_2Q_2)(R_wQ_w)$	55 ± 1	10 ± 1	3 ± 2	12 ± 2	2×10^{-6}

Table 3.2.4. PEGDME_CPE bulk resistance (R_e) and S:SPC 70 :30 w/w/PEGDME_CPE interphase resistances (R_1, R_2) obtained by NLLS analysis of the EIS data (Fig. 3.2.13) via the Boukamp software.[12,13] The EIS data have been collected at various temperatures during CV measurements (Fig. 3.2.11) on the Li|PEGDME_CPE|S:SPC 70 :30 w/w cell.

Figure 3.2.14 illustrates the characteristics of the electrode/polymer electrolyte assembly by showing photographic images of a sample before and after cycling (panel a and b), along with TGA data (panel c and d), respectively, and SEM images (panel e; see the *3.2.2 Experimental* section for details on sample preparation). A direct comparison between the PEGDME_CPE hosted on the positive electrode in the pristine condition and after consecutive CV cycles performed at 50, 60, 70, and 80 °C reveals a change in color of the polymer membrane from white (Figure 3.2.14a) to a dark red (Figure 3.2.14b), which demonstrates the expected dissolution of the lithium polysulfides into the electrolyte upon the electrochemical process.[75] It is worth mentioning that the dissolution of lithium polysulfides into the electrolyte, which is common process and not fully avoidable, does not necessarily lead to a compromising shuttle effect. In fact, the shuttle process that usually leads to an unlimited anodic reaction without charge accumulation and efficiency decrease is not observed in these tests, as indeed expected by the inclusion of the $LiNO_3$ additive into the PEGDME_CPE formulation, which promotes the formation of a protective SEI layer on the lithium surface.[7] TGA of the pristine and cycled PEGDME_CPE/electrode samples (Figure 3.2.14c, and 3.2.14d for corresponding DTG) indicates various weight losses, which are attributed to the components of the assembly. Thus, the pristine sample (black curves in Figure 3.2.14c and 3.2.14d) shows a weight loss between 230 and 300 °C due to sulfur evaporation from the positive electrode,[76,77] along with two subsequent processes at 340 and 400 °C ascribed to the PEGDME2000, which are in agreement with the TGA of Figure 3.2.5. Furthermore, weight variations ascribable to LiTFSI are observed between 420 and 445 °C, and partial degradation of the electrode support likely occurs at about 560 °C.[31] A residue of 27 % of the initial weight after the heating scan accounts for $LiNO_3$, SiO_2 particles, and electrode support. The cycled sample exhibits rather different thermal behavior (orange curves in Figure 3.2.14c and 3.2.14d) characterized by an increase in weight at about 130 °C, which likely reflects reactions between N_2 and the lithium polysulfides during the thermogravimetric experiment, followed by a slight decrease due to sulfur evaporation up to 300°C.[76,77] In addition, the loss of PEGDME2000 and LiTFSI appears as a single process centered at 390°C, rather than the multiple losses between 340 and 445°C observed for the pristine sample, thus suggesting changes in electrolyte composition by cycling in line with the macroscopic modifications displayed in Figure 3.2.14a and 3.2.14b. A residual mass of 43% is measured after complete degradation of the electrode support at 560 °C, accounting perhaps for possible crystalline Li_2S (melting point = 940 °C). The modifications of the cathode/polymer interface during cycling in the cell are further investigated by SEM in Figure 3.2.14e, which shows at the left-hand side a cross section image of a sample recovered after consecutive CV between 50 and 80 °C and on the right-hand side panel a graphic representation of the cathode/polymer-electrolyte stack with indication of the investigated area.
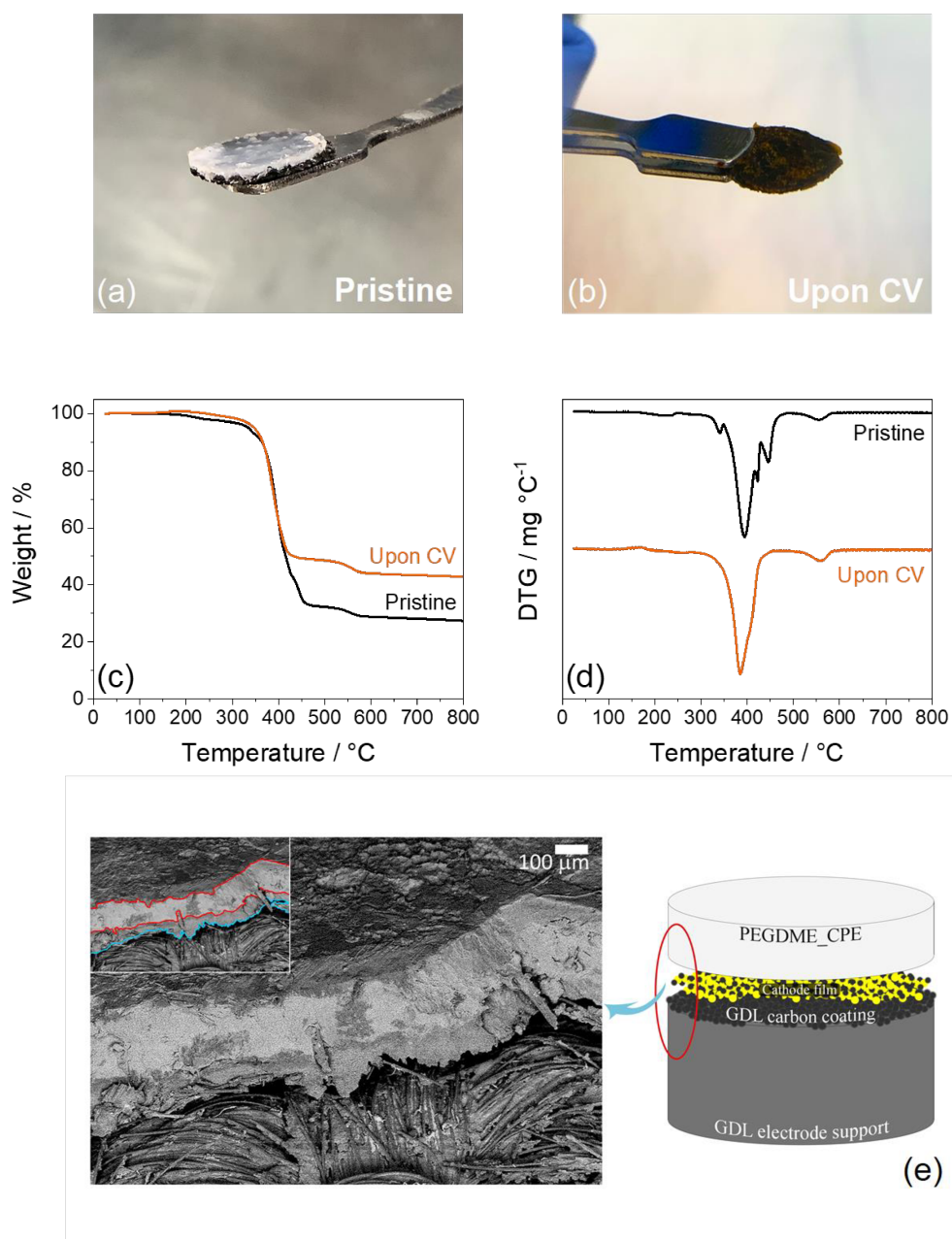
Figure 3.2.14. (a, b) Photographic images and **(c)** TGA curves with **(d)** corresponding DTG profiles of a PEGDME_CPE membrane on a S:SPC 70:30 w/w electrode (*i.e.*, the PEGDME_CPE|S:SPC 70:30 w/w electrode assembly) **(a)** in the pristine condition (before assembling the cell) and **(b)** after CV in lithium cell at various temperatures (see Figure 3.2.11); TGA carried out under N_2 in the 25–800 °C temperature range by employing a heating rate of 5 °C min^{-1}. **(e)** SEM image (left-hand side) showing the PEGDME_CPE|S:SPC 70:30 w/w electrode assembly after CV in lithium cell at various temperatures (see Figure 3.2.11), with related graphic scheme (right-hand side); SEM inset highlights the presence of the assembly layers, *i.e.*, *i)* the PEGDME_CPE membrane (between red lines) and *ii)* the carbon-sulfur electrode film (between bottom-red line and cyan line).

In agreement with X-ray CT data discussed in Chapter 2, the SEM image of the composite clearly shows various layers, which are attributed to *i)* the fibrous carbon-cloth electrode support (below the cyan mark in Figure 3.2.14e inset), *ii)* the carbon coating of the electrode support along with the sulfur-carbon cathode film (gray layer between the cyan and the red marks in Figure 3.2.14e inset), and *iii)* a portion of the PEGDME_CPE membrane (light gray layer between red marks in Figure 3.2.14e inset). Notably, the electron microscopy data suggest improved contact between the PEGDME_CPE and the sulfur-carbon electrode, which may favor the charge transfer at the interphase, as well contact regions in the electrolyte layer (colored by dark gray) which might be associated with the dissolution of lithium polysulfides during the electrochemical process. It is worth mentioning that PEGDME_CPE was not involved in the electrode formulation and the only polymeric species included in the cathode is poly(vinylidene fluoride) (PVDF), which acts as binding agent (see *3.2.2 Experimental* section), although the addition of a polymer electrolyte to the cathode composition is a well-known technique to achieve the formation of an enhanced electrode/electrolyte interphase.[78] Therefore, the formation of a suitable electrode/electrolyte interphase may be promoted by the relevant mobility of the PEGDME polymer chains at 50 °C, which is sufficient for allowing a proper cathode wetting and Li$^+$ ions exchange. Furthermore, a contribution to the Li$^+$ ions conductivity given by blending between PEGDME and PVDF cannot be excluded. On the other hand, the formation of a stable electrode/electrolyte assembly is suggested by the SEM image in panel e, which displays an adequate contact between the electrolyte and the cathode film.

The galvanostatic-cycling performance of the Li-S polymer battery at 50 °C is herein evaluated at the current rate of C/10 (1C = 1675 mAgs^{-1}). These testing conditions represent an optimal choice, which might match the typical requirements of the stationary storage market. It is worth mentioning that the polymer configuration would ensure enhanced thermal stability, possibly allowing a safe use in large battery packs, whilst low current rate and moderately high temperature are well compatible with load-balancing applications in smart grids.[72] Figure 3.2.15 shows the voltage profiles (panel a) and cycling behavior (panel b) of the above Li-S polymer cell, which steadily delivers a satisfactory capacity with high coulombic efficiency. In more detail, Figure 3.2.15a reveals the partial merging of the two characteristic plateaus at about 2.4 and 1.8 V upon the first discharge, accounting for the conversion of lithium and sulfur to lithium polysulfides (see CV in Figure 3.2.11a),[79] as well as two definite charge plateaus at about 2.3 and 2.6 V. The sloping shape of the discharge plateau may suggest moderate Li$^+$ diffusion hindering within the PEGDME_CPE as well as slow stabilization of the electrode/electrolyte interphase,[80] which is gradually improved upon the subsequent cycles. Indeed, microstructural reorganizations due to polysulfide dissolution upon cycling favor a gradual change in cell response, as seen in Chapter 2, leading to well-defined

discharge plateaus at 2.4 and 1.9 V (Figure 3.2.15a). Furthermore, subsequent overlapping voltage curves characterized by moderate polarization between charge and discharge indicate a stable and efficient electrochemical process. In this regard, Figure 3.2.15b reveals a maximum capacity of 770 mAh g$_S^{-1}$, with a steady-state value ranging between 700 and 600 mAh g$_S^{-1}$, and a retention of 71% for over 90 cycles. Interestingly, the cell shows after the initial activation cycles a coulombic efficiency approaching 99%, except for few intermediate cycles particularly occurring at the final stages of the test, characterized by values decreasing down to about 90%, and raising again to the steady state (Figure 3.2.15b, light-green curve and right-side y-axis). This decrease in efficiency likely suggests the occurrence of micro-dendrites which are efficiently suppressed by the polymer electrolyte with the ongoing of the cycling to achieve the pristine efficiency value. This important aspect represents an additional bonus, in particular concerning the high safety content, of the PEGDME_CPE proposed in this section for Li-S battery application.
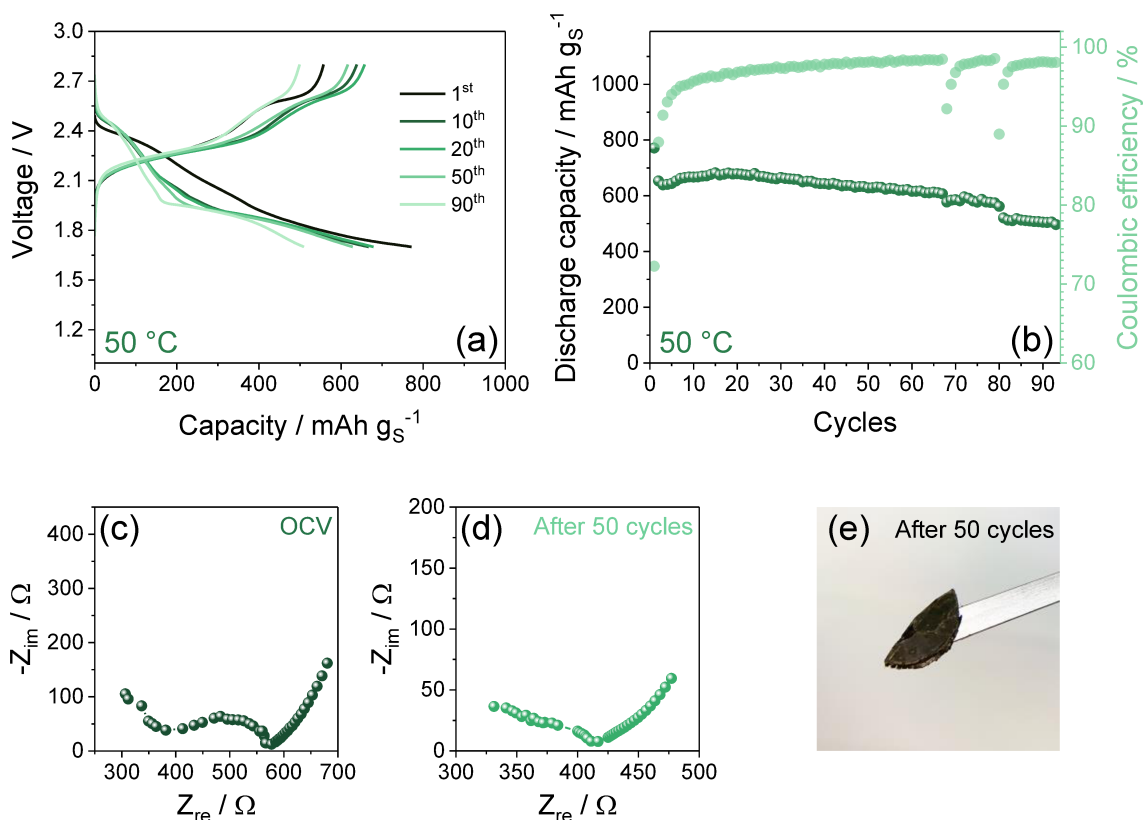
Figure 3.2.15. Electrochemical performance of a Li|PEGDME_CPE|S:SPC 70:30 w/w cell at 50 °C in terms of **(a)** voltage profiles and **(b)** cycling trend (coulombic efficiency reported in right-hand side y-axis) at the constant current rate of C/10; voltage range: 1.7 – 2.8 V. **(c, d)** EIS measurements performed on a Li|PEGDME_CPE|S:SPC 70:30 w/w cell at 50 °C at various states, that is, **(c)** at the OCV condition and **(d)** after 50 discharge/charge cycles performed at C/10 between 1.7 and 2.8 V. EIS frequency range: 500 kHz–100 mHz; alternate voltage signal: 10 mV. **(e)** Photographic image of a PEGDME_CPE membrane on a S:SPC 70 :30 w/w electrode recovered after the cycling test.

149

The stability of the electrode/electrolyte interphase is further demonstrated in Figure 3.2.15c and 3.2.15d, which reports the Nyquist plots at 50 °C of a Li-S cell employing the PEGDME_CPE at the OCV condition and after 50 cycles at C/10, respectively, while the related results of the NLLS analysis are displayed in Table 3.2.5. These Nyquist plots reveal a drop of the interphase resistance (R_1) upon cycling from about 180 Ω to 110 Ω (high-frequencies grain boundaries due to partial crystalline phase were not considered), denoting enhancements of the electrochemical activity at the electrode/electrolyte interphase by cycling in agreement with the EIS data reported in Figure 3.2.13. In addition, the portion of cycled PEGDME_CPE/electrode sample recovered from the cell after 50 cycles is shown in Figure 3.2.15e, which reveals the formation of a blend between the electrolyte and the electrode evidencing suitable contact, while the dark red color of the cycled PEGDME_CPE membrane confirms the uniform dissolution of the lithium polysulfides during cell activity without any shuttle process, as also observed in Figure 3.2.14. These data clearly demonstrate the suitability of the Li-S system and display the stability of the electrode/electrolyte interphase upon cycling. Thus, considering an average capacity of 600 mAh gs^{-1} and an electrochemical process centered at 2.2 V, the Li-S polymer cell has a theoretical energy density of about 1300 Wh kg^{-1}, which might lead to a suitable practical energy density and high efficiency for applications that require thermal stability.[72] On the other hand, challenging operative conditions including high temperature may hinder the application of typical Li-S battery configurations based on volatile liquid electrolytes. Indeed, common DOL and DME solvents suffer from marked volatility which may be promoted by the challenging temperature value, whilst the target performance of this liquid electrolyte is achieved at 25°C.[81–83] These data suggest the poor applicability of the DOL:DME solutions at high temperature, which, on the other hand, improves the performance of the PEGDME_CPE electrolyte.

Cell condition	Circuit	R_1 [Ω]	χ^2
OCV	$R_e(R_1Q_1)Q_w$	179 ± 10	8×10^{-5}
After 50 cycles	$R_e(R_1Q_1)Q_w$	108 ± 17	3×10^{-5}

Table 3.2.5. S :SPC 70:30 w/w/PEGDME_CPE interphase resistance (R1) obtained by nonlinear least squares (NLLS) analysis of the EIS data (Fig. 3.4.15) via the Boukamp software.[12,13] The EIS data have been collected at 50 °C during a galvanostatic cycling measurement on the Li|PEGDME_CPE|S:SPC 70:30 w/w cell.

3.3 Semi-liquid Li-S batteries

3.3.1 Presentation

As mentioned in the Introduction, the concept of *catholyte* consists in the dissolution of lithium polysulfides into the electrolyte solution. The employing of a catholyte in a semi-liquid Li-S battery may lead to various benefits, that is, the formation of a stable SEI, the buffering of sulfur dissolution from the sulfur cathode, mitigation of volume changes due to the conversion process between sulfur and lithium, and Li-S batteries employing dissolved polysulfides as active material demonstrated remarkable electrochemical performances and stable cycle life.[33,47,84–87] Thus, this section explores the application of glyme-based catholytes dissolving a modest amount of Li_2S_8, a conductive lithium salt and the protective agent $LiNO_3$, in a semi-liquid Li-S battery exploiting a carbon-based electrode at the cathode side with no presence of solid sulfur. In particular, two catholyte solutions dissolving either LiTFSI or $LiCF_3SO_3$ salts are investigated in terms of chemical composition through X-ray photoelectron spectroscopy, thermal stability, Li^+ transport properties, electrochemical stability window, as well as electrochemical performances evaluated through galvanostatic cycling tests. The catholyte dissolving LiTFSI is successively selected and combined with a porous carbon-Cr_2O_3 composite derived from metal organic framework (MOF). Indeed, the use of carbon-metal oxide composites obtained from MOFs is an effective strategy to enhance the electrode conductivity and promoting at the same time the interaction of the electrode host matrix with the polysulfides produced by the Li-S reaction.[88–90] Furthermore, composites including Cr_2O_3 and carbon, obtained by different procedures, have been principally used in Li-ion batteries, and Cr_2O_3/C electrodes have been efficiently used as anode with enhanced cycling and rate performance compared with pure Cr_2O_3 due to the important role played by the carbon in improving the electrical conductivity of Cr_2O_3, inhibiting the aggregation and acting as a favorable buffer to the volume change during the electrochemical process.[91,92] Therefore, structure, morphology, composition, thermal behavior and porosity of the carbon-Cr_2O_3 composite are evaluated and the combination with a safe and efficient glyme-based catholyte is proposed for application in lithium cell. Beside the electrochemical response, *ex situ* analyses are performed to study morphology and structure of the carbon-Cr_2O_3 electrode upon cycling in the semi-liquid Li-S battery.

3.3.2 Experimental

Diethylene glycol dimethyl ether (DEGDME, $CH_3O(CH_2CH_2O)_2CH_3$, anhydrous, 99.5%, Sigma-Aldrich) was dried under molecular sieves (5 Å, Sigma-Aldrich) until the water content was below 10 ppm, as tested through 899 Karl Fischer Coulometer (Metrohm). Two liquid catholytes were prepared as reported in a previous work:[93] elemental sulfur powder (≥99.5%, Riedel-de Haën) and lithium pieces (Rockwood Lithium), respectively in the 4:1 molar ratio, were mixed in DEGDME to get a yellow suspension, which was stirred for 12 h at 80 °C and for two days at room temperature to obtain a dark red catholyte precursor. Either lithium bis(trifluoromethanesulfonyl)imide (LiTFSI, 99.95% trace metals basis, Sigma-Aldrich) or lithium trifluoromethanesulfonate (LiCF$_3$SO$_3$, 99.995% trace metals basis, Sigma-Aldrich), and lithium nitrate (LiNO$_3$, 99.99% trace metals basis, Sigma-Aldrich) were dissolved in the precursor by stirring for 12 h at room temperature to get a concentration of 1 mol of each salt in 1 kg of DEGDME solvent. The catholyte solutions, shown in Figure 3.3.1 and subsequently indicated by the acronyms DEGDME–Li$_2$S$_8$–1m LiNO$_3$–1m LiTFSI and DEGDME–Li$_2$S$_8$–1m LiNO$_3$–1m LiCF$_3$SO$_3$, respectively, had dark red color and nominal Li$_2$S$_8$ content of 5 wt.%. The catholytes preparation was performed inside an Ar-filled glovebox (MBraun, O$_2$ and H$_2$O content below 1 ppm).

Figure 3.3.1. Photographic images of DEGDME–Li$_2$S$_8$–1m LiNiO$_3$–1m LiTFSI and DEGDME–Li$_2$S$_8$–1m LiNiO$_3$–1m LiCF$_3$SO$_3$ catholytes

Samples for X-ray photoelectron spectroscopy (XPS) were prepared by depositing few drops of catholyte solution onto Al foil inside an Ar filled glovebox (MBraun, O$_2$ and H$_2$O content below 1 ppm), and transferring to a Büchi glass oven for overnight drying. Then, the samples were collected in Eppendorf vessels, sealed, and moved to the XPS instrument. This operation was carried out

through a home-made glovebox with a specific vacuum transference vessel, thus avoiding the contact of the substrates with air. XPS studies were performed through a Physical Electronics spectrometer (PHI Versa Probe II Scanning XPS Microprobe) with monochromatic X-ray Al-Kα radiation (100 μm, 100 W, 20 kV, 1486.6 eV) as the excitation source. High-resolution spectra were recorded at a given takeoff angle of 45° by a concentric hemispherical analyzer operating in the constant pass energy mode at 23.5 eV using a 1400 μm line (with a 100 μm diameter of the X-ray highly focused beam) analysis area. The spectrometer energy scale was calibrated using Cu $2p_{3/2}$, Ag $3d_{5/2}$, and Au $4f_{7/2}$ photoelectron lines at 932.7, 368.2, and 84.0 eV, respectively. Under these conditions, the Au $4f_{7/2}$ line was recorded with 0.73 eV FWHM at a binding energy (BE) of 84.0 eV. A PHI Smart Soft-VP 2.6.3.4 software package was used for acquisition and data analysis. Recorded spectra were always fitted using Gauss−Lorentz curves. Atomic concentration percentages of the characteristic elements of the surfaces were determined taking into account the corresponding area sensitivity factor for the different measured spectral regions.

Coupled thermogravimetric analysis (TGA) and differential scanning calorimetry (DSC) measurements were performed on the DEGDME–Li_2S_8–1m $LiNO_3$–1m LiTFSI and DEGDME–Li_2S_8–1m $LiNO_3$–1m $LiCF_3SO_3$ catholyte solutions through a Metter Toledo-TGA/DSC, by heating the samples at 5 °C min^{-1} in a nitrogen flow.

The ionic conductivity of the catholyte solutions was evaluated by electrochemical impedance spectroscopy (EIS) on symmetrical blocking CR2032 coin-cells (MTI Corp.) using stainless steel (SS) current collectors and a Teflon O-ring spacer to fix the cell constant to 4.0×10^{-2} cm^{-1}. Impedance spectra were recorded by applying an alternate voltage signal of 10 mV amplitude in the 500 kHz – 1 Hz frequency range.

Carbon electrodes were prepared by doctor blade coating of a slurry formed by Super P carbon (90 wt.%, SPC, Timcal) and polyvinylidene fluoride (10 wt.%, Solef ® 6020 PVDF) in *N*-methyl pyrrolidone (NMP, Sigma-Aldrich) over a gas diffusion layer foil (GDL ELAT LT1400, MTI Corp.). The wet coated foil was dried for about 3 h on a hot plate at 70 °C, cut into the form of either 10 or 14 mm diameter disks, and then dried overnight at 110 °C under vacuum.

All the cells were assembled inside an Ar-filled glovebox (MBraun, O_2 and H_2O content below 1 ppm). CR2032 coin-cells (MTI Corp.) were assembled by properly stacking two electrodes (either lithium disks or coated GDL) and one Celgard separator soaked by 80 μl of catholyte solution, corresponding to a sulfur loading of 4.4 and 4.2 mg for DEGDME–Li_2S_8–1m $LiNO_3$–1m LiTFSI and DEGDME–Li_2S_8–1m $LiNO_3$–1m $LiCF_3SO_3$, respectively, and to superficial sulfur contents of 2.9 and 2.7 mg cm^{-2} on the carbon electrode by considering the geometric area of 1.54 cm^2. Further Li|catholyte|SPC cells were prepared by using 160 μl of catholyte solution, corresponding to a sulfur

loading of 8.8 and 8.4 mg for DEGDME–Li$_2$S$_8$–1m LiNO$_3$–1m LiTFSI and DEGDME–Li$_2$S$_8$–1m LiNO$_3$–1m LiCF$_3$SO$_3$, respectively. Taking into account the electrode geometric area (1.54 cm^2) the sulfur surface loading was around 3 and 6 mg cm^{-2} for 80 and 160 μl volumes, respectively.

The lithium transference numbers (t$^+$) of DEGDME–Li$_2$S$_8$–1m LiNO$_3$–1m LiTFSI and DEGDME–Li$_2$S$_8$–1m LiNO$_3$–1m LiCF$_3$SO$_3$ were determined by employing the Bruce-Vincent-Evans method.[11] Chronoamperometry and EIS were performed on symmetrical Li|catholyte|Li T-type cells using several Whatman® GF/D glass fiber separators soaked by the catholyte solution. EIS was carried out before and after chronoamperometry by applying an alternate voltage signal of 10 mV amplitude in the 500 kHz – 100 mHz frequency range. Chronoamperometry was performed by using a voltage of 30 mV for 90 minutes. The lithium transference number was calculated through the equation (3.3.1):[11]

$$t^+ = \frac{i_{ss}}{i_0} \frac{\Delta V - R_0 i_0}{\Delta V - R_{ss} i_{ss}} \tag{3.3.1}$$

where i$_0$ and i$_{ss}$ are the initial and steady-state current values of the chronoamperometry measurement, respectively, ΔV is the chronoamperometry voltage, R$_0$ and R$_{ss}$ are the initial and steady-state interphase resistances as determined by EIS.

Lithium stripping-deposition tests were performed on symmetrical Li|catholyte|Li coin-cells at 100 μA cm^{-2} and 1 h of step time. The lithium/catholyte interphase resistance was measured by EIS on symmetrical Li|catholyte|Li coin-cells throughout 30 days, by applying an alternate voltage signal of 10 mV amplitude in the 500 kHz – 100 mHz frequency range.

The electrochemical stability window of the catholyte solutions was determined by linear sweep voltammetry (LSV) and cyclic voltammetry (CV) at a scan rate of 0.1 mV s^{-1} in the anodic and cathodic regions, respectively, on Li|80 μl catholyte|SPC coin-cells. Fresh cells were cycled at 1 mV s^{-1} within the voltage range from 1.8 to 2.8 V vs Li$^+$/Li, and then used for either LSV or CV. A first cathodic CV scan was performed at 0.1 mV s^{-1} down to 0.01 V vs Li$^+$/Li, followed by several cycles between 0.01 and 1.2 V vs Li$^+$/Li. Further CV measurements at 0.1 mV s^{-1} were carried out on Li|80 μl catholyte|SPC coin-cells within the voltage ranges from 1.8 to 2.8 V vs Li$^+$/Li in order to characterize the electrochemical process of the catholytes. EIS measurements were performed upon the CV measurements by applying an alternate voltage signal of 10 mV amplitude in the 500 kHz – 100 mHz frequency range.

Rate capability tests were performed on Li|80 μl catholyte|SPC coin-cells at current rates of C/10, C/8, C/5, C/3, C/2, 1C and 2C increasing after 10 cycles and then decreasing back to C/10, within the 1.9 – 2.8 V range from C/10 to C/3 and within the 1.7 – 2.8 V range from C/2 to 2C (1C =

154

1675 mA g_S^{-1}). Li|80 µl catholyte|SPC coin-cells were studied by galvanostatic tests upon 120 cycles at a current rate of C/3 within the 1.8 – 2.8 V range. Further cycling tests at C/20 within the 1.8 – 2.8 V range were performed on Li|160 µl catholyte|SPC coin-cells. Both specific capacity and specific current values were referred to the nominal sulfur mass in the catholyte solution.

The MIL-101(Cr) MOFs were prepared by a previously reported method.[94,95] Specifically, 2.0 g (5.0 mmol) of chromium (III) nitrate nonahydrate (Cr(NO$_3$)$_3$·9H$_2$O, Panreac) and 0.55 g (3.3 mmol) of 1,4-benzene dicarboxylic acid (H$_2$BDC, Sigma-Aldrich) were dissolved in 50 mL of deionized water under vigorous stirring for 30 min to completely dissolve the dicarboxylic acid. The dark green suspension obtained was transferred to a 100 mL Teflon-lined autoclave. The mixture was sealed, held at 180 °C for 10 h and naturally cooled down to room temperature. Subsequently, MIL-101(Cr) was filtered, dipped into distilled water for one day, filtered again, washed several times with ethanol, and dried at 80 °C overnight. Then, as-synthesized MIL-101(Cr) was calcined in nitrogen atmosphere at 600 °C for 3 h in a tubular oven with heating rate of 10 °C min^{-1} using a constant gas flow of 50 mL min^{-1} (preliminary purge was performed at room temperature for 30 min using N$_2$ flow of 100 mL min^{-1}). The final sample is subsequently indicated by the acronym Cr$_2$O$_3$@C.

The electrode was prepared by mixing 80wt% of Cr$_2$O$_3$@C, 10wt% of conductive agent (SPC) and 10wt% of PVDF polymer binder in NMP to form a slurry. Then, a carbon paper (GDL, ELAT LT1400W, MTI Corp.) was used as substrate and coated with the slurry by doctor blade (MTI Corp.). The electrodes were dried in air for 3 h at 70 °C by using a hot-plate to remove the solvent, cut into disks with a diameter of 14 mm, and vacuum dried overnight at 100 °C to remove residual traces of water and solvent before inserting in Ar-filled glovebox (MBraun, O$_2$ and H$_2$O content below 1 ppm).

X-ray diffraction (XRD) patterns were obtained with a Bruker D8 Advance diffractometer using monochromatic Cu Kα radiation. The patterns were recorded in the 2θ range between 5° and 90° at a rate of 10 s per step with step size of 0.02°. TGA was performed using a Mettler Toledo-TGA/DSC under nitrogen or oxygen atmosphere by heating the sample from 30 to 800 °C at 10 °C min^{-1}. XPS measurements were carried out using a SPECS mod. PHOBIOS 150 MCD spectrometer with a Mg-Kα radiation and a chamber able to reach a pressure of 4×10^{-9} mbar. The textural properties were determined by a Micromeritics ASAP 2020 system using nitrogen as adsorbent. Pore size distribution was calculated by the Barret-Joyner-Halenda (BJH) method applied to the adsorption branch of the isotherms. Sample morphologies were investigated by transmission electron microscopy (TEM), employing a Zeiss EM 910 microscope equipped with a tungsten thermoionic electron gun operating at 100 kV, and through scanning electron microscopy (SEM) by means of a JEOL JSM-7800F for the Cr$_2$O$_3$@C and precursor powders, and a Zeiss EVO 40 microscope

equipped with a LaB$_6$ thermoionic electron gun for the Cr$_2$O$_3$@C electrode. The SEM was coupled to a microanalysis system for obtaining the energy dispersive X-ray spectra (EDS). SEM images of the Cr$_2$O$_3$@C electrode were obtained at the pristine state and *ex-situ* after a galvanostatic cycling test performed at a constant current rate of C/5 (1C = 1675 mA gs^{-1}) in lithium cell (see below for further details on the galvanostatic cycling conditions). Prior to the *ex-situ* SEM analyses, the electrode was washed with 1,2-dimethoxyethane (DME, anhydrous, inhibitor-free, 99.5%, Sigma-Aldrich) to remove possible traces of lithium salts, and subsequently dried under vacuum at room temperature for 20 min.

Electrochemical experiments were performed on CR2032 coin-type cells assembled inside an Ar-filled glove box (MBraun, H$_2$O and O$_2$ content below 1 ppm). The cells were prepared by using the disk with 14 mm diameter coated by Cr$_2$O$_3$@C as the working electrode, a lithium metal disk as the counter/reference electrode and a polyethylene membrane (PE, Celgard) as the separator soaked with 80 µL of the catholyte solution (corresponding to a sulfur surface loading of 2.9 mg cm^{-2}). The electrochemical process was studied by CV and electrochemical impedance spectroscopy EIS tests. CV measurements were performed at a constant scan rate of 0.1 mV s^{-1} within the 1.8 – 2.8 V *vs* Li$^+$/Li range over ten cycles, as well as at scan rates increasing from 0.05 mV s^{-1}, to 0.1, 0.15, 0.2 and 0.25 mV s^{-1} in order to determinate the lithium-ion diffusion coefficients (D). EIS measurements were taken at the OCV, after the first, fifth, and tenth CV cycles in the 500 kHz – 100 mHz frequency range using a 10 mV amplitude signal. All the Nyquist plots recorded by the EIS were studied by nonlinear least-squared (NLLS) fitting through a Boukamp tool.[12,13] It is worth mentioning that only fits with a χ^2 of the order of 10^{-4} or lower were considered suitable (NLLS analyses for Li|80 µl catholyte|SPC are not reported) . Galvanostatic cycling tests were carried out within the 1.9 – 2.8 V range by using C-rates of C/10, C/8, C/5, and C/3 (1C = 1675 mA gs^{-1}). Both specific capacity and current rate were referred to the sulfur mass in the catholyte (4.4 mg in the coin cell).

The voltammetry and EIS measurements were performed by a VersaSTAT MC Princeton Applied Research (PAR) analyzer, while the galvanostatic tests were carried out through a MACCOR series 4000 battery test system.

3.3.3 Results

The chemical composition of the two catholyte solutions is investigated by means of XPS and reported in Figure 3.3.2. The survey spectra of panels a and b reveal similar response for the DEGDME–Li$_2$S$_8$–1m LiNO$_3$–1m LiTFSI and DEGDME–Li$_2$S$_8$–1m LiNO$_3$–1m LiCF$_3$SO$_3$ catholytes, respectively, however with different relative intensity of the signals due to the different

salts used. Panels c and d of Figure 3.3.2, respectively, report the analyses of the S 2p core level spectra of DEGDME–Li_2S_8–1m $LiNO_3$–1m LiTFSI and DEGDME–Li_2S_8–1m $LiNO_3$–1m $LiCF_3SO_3$ catholytes, which represent important evidence for the Li_xS_y active material identification. Besides the different relative intensities ascribed to LiTFSI and $LiCF_3SO_3$ salts, the S 2p peaks are fitted by three main S $2p_{3/2}$ and S $2p_{1/2}$ doublets. The first doublet with main peaks at binding energy (BE) of 167.5 and 168.7 eV in DEGDME–Li_2S_8–1m $LiNO_3$–1m LiTFSI, and 168.7 and 169.9 eV in DEGDME–Li_2S_8–1m $LiNO_3$–1m $LiCF_3SO_3$ is attributed to S bound to O (i.e., $LiN(SO_2CF_3)_2$, $LiCF_3SO_3$, and possibly Li_2SO_3 of the electrolyte salts).[24] The second doublet at S $p_{3/2}$ binding energy values of 165.4 eV in DEGDME–Li_2S_8–1m $LiNO_3$–1m LiTFSI and 166.1 eV in DEGDME–Li_2S_8–1m $LiNO_3$–1m $LiCF_3SO_3$ is attributed to the Li_2S_8 polysulfide which has nominal concentration in the solution of 5 wt.%.[96]
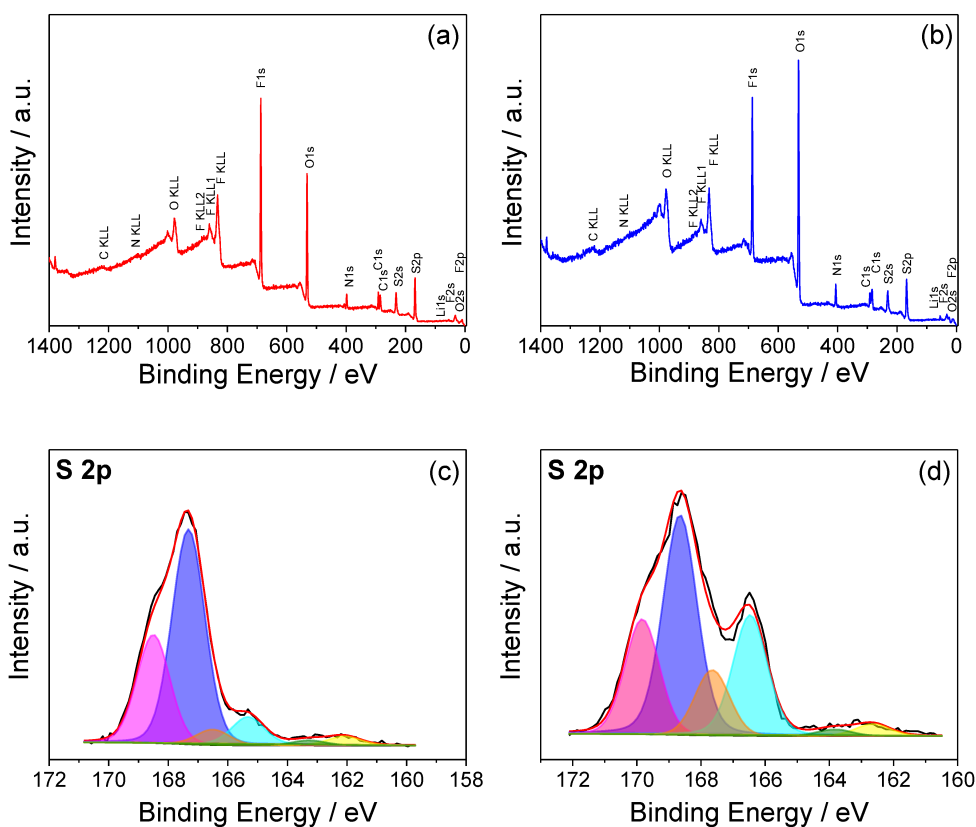
Figure 3.3.2. X-ray photoelectron spectra of **(a, c)** DEGDME–Li_2S_8–1m $LiNO_3$–1m LiTFSI and **(b, d)** DEGDME–Li_2S_8–1m $LiNO_3$–1m $LiCF_3SO_3$ catholytes. **(a, b)** Survey spectra and **(c, d)** deconvoluted S 2p core level spectra.

However, the presence of minor peaks at BE of 163 and 162 eV does not exclude completely possible presence of small amount of Li_2S_6 and Li_2S_4 into the two catholyte solutions.[96] Hence, Figure 3.3.2c and d confirms that the active material in the two catholytes is mainly dominated by the Li_2S_8 species, with possible presence of a minor amount of Li_2S_6 and Li_2S_4.

Figures 3.3.3a and 3.3.4a show the deconvoluted C 1s core level spectra of both catholytes. These spectra can be decomposed in several contributions, being those at around 284 eV assigned to adventitious carbon and bonds C–C, C–H related to DEGDME. The contribution between 286 and 287 eV is mainly due to the etheric moieties (C–O–C) from DEGDME, presenting a much higher relative intensity in the catholyte with $LiCF_3SO_3$. As expected, a strong contribution at high binding energy (BE > 292 eV) is observed for both catholytes and assigned C–F bonds. Figures 3.3.3b and 3.3.4b show the F 1s core level spectra, where two contributions are observed. The main contribution at high binding energy (687.5–688.5 eV) corresponds to CF_n of the fluorinated salts in the catholytes, i.e., LiTFSI, and $LiCF_3SO_3$, respectively.[22,23,97]
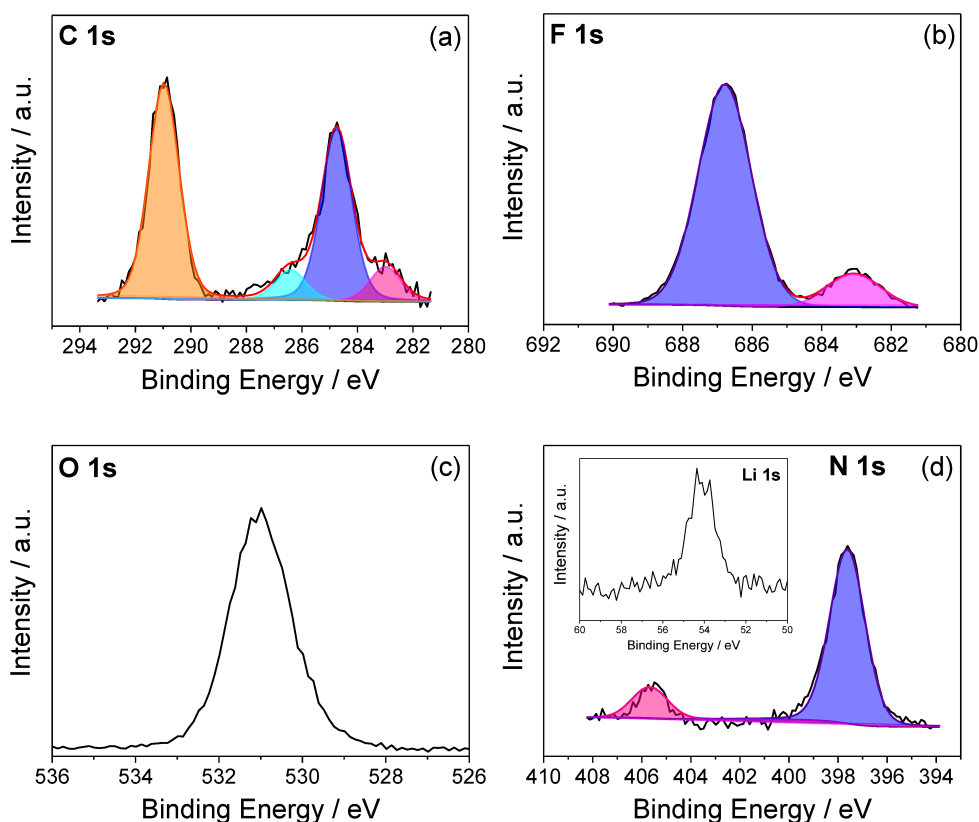
Figure 3.3.3. XPS of the DEGDME–Li_2S_8–1m $LiNO_3$–1m LiTFSI catholyte. Analyses of the **(a)** C 1s, **(b)** F 1s, **(c)** O 1s, **(d)** N 1s, and **(d inset)** Li 1s signals.

The low intensity contributions at low binding energy (683–684 eV) can be assigned to impurities of ionic fluorides, probably LiF.[18] Furthermore, Figures 3.3.3c and 3.3.4c show the O 1s signal, which is dominated by the component at 532.4 eV assigned to O bound to S in the solutions ($-SO_3$). The observed contribution at low binding energy in the case of the catholyte with $LiCF_3SO_3$ is due to the oxygen of DEGDME in agreement with that observed in the C 1s spectrum. The N 1s spectra (Figs. 3.3.3d and 3.3.4d) show one contribution around 406–407 eV assigned to the film forming additive (i.e., NO_3^- in $LiNO_3$). [22,23,98] In the case of the catholyte with LiTFSI, a strong contribution is also observed at about 398 eV due to the imide group.[23] The insets of Figures 3.3.3d and 3.3.4d show the Li 1s core level spectra with binding energy values typical of Li^+. The observation of these clear Li 1s signals is relevant if the low sensitivity of this photoemission is considered.
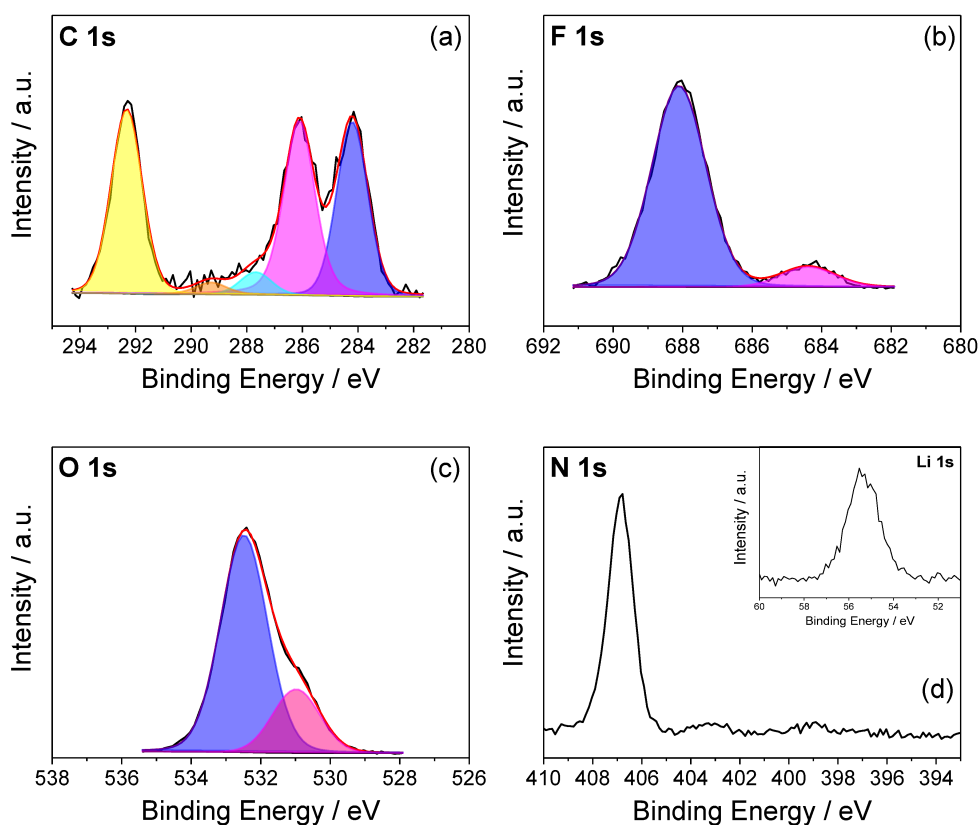
Figure 3.3.4. XPS of the DEGDME–Li_2S_8–1m $LiNO_3$–1m $LiCF_3SO_3$ catholyte. Analyses of the **(a)** C 1s, **(b)** F 1s, **(c)** O 1s, **(d)** N 1s, and **(d inset)** Li 1s signal.

For further sample identification, Table 3.3.1 reports the atomic composition of the two samples. The more relevant feature is the high concentration of O in the case of the catholyte with $LiCF_3SO_3$. The different XPS response of the two catholyte samples might indicate a different amount of DEGDME adsorbed over the sample holder following the vacuum drying process required to

remove the solvent (see the *3.3.2 Experimental* section for further details about sample preparation for XPS). However, possible significant effect of the sample preparation on the surface composition of the sample may reasonably affect quantitative analysis of the solvent traces. Therefore, this study provides only qualitative information about the chemical species deposited over the sample surface, thereby further confirming the suitability of the already reported Li_2S_8 synthesis herein employed, while effective quantification of the compound forming the solutions requires ad hoc analyses suitable for liquid solutions and able to identify polysulfides with different chain length.

Samples	C 1s	N 1s	O 1s	F 1s	S 2p	Li 1s
LiTFSI	17.46	5.97	26.99	29.08	9.63	10.86
$LiCF_3SO_3$	12.16	5.03	40.72	16.47	8.01	17.44

Table 3.3.1. Percent atomic composition of the catholytes using LiTFSI and $LiCF_3SO_3$ salts as determined by XPS.

The thermal behavior of the solutions is detected in panels a and b of Figure 3.3.5 which show the TGA, differential thermogravimetry (DTG), and DSC traces of the $DEGDME–Li_2S_8–1m\ LiNO_3–1m\ LiTFSI$ and $DEGDME–Li_2S_8–1m\ LiNO_3–1m\ LiCF_3SO_3$ catholytes, respectively. Figure 3.3.5a reveals for the $DEGDME–Li_2S_8–1m\ LiNO_3–1m\ LiTFSI$ solution a weight loss starting above 70 °C attributed to the evaporation of the solution through two main processes, centered at 157 and 210 °C as indicated by TGA and corresponding DTG.[7] The DSC curve (red trace) indicates heat absorption upon the whole investigated temperature range due to evaporation as well as an exothermic peak corresponding to the weight loss at 210 °C observed by TGA/DTG, which may be reasonably attributed to a solid-state phase transition in LiTFSI (recrystallization) possibly associated with the evaporation of the solvent linked to the salt (i.e., crystallization solvent). The $DEGDME–Li_2S_8–1m$ $LiNO_3–1m\ LiCF_3SO_3$ sample (Fig. 3.3.5b) exhibits similar thermal behavior upon heating, however with evaporation centered at a slightly lower temperature, i.e., 150 °C, with respect to DEGDME–Li2S8–1m LiNO3–1m LiTFSI. Furthermore, a less pronounced DTG peak at 200 °C suggests lower content of the crystallization solvent in $LiCF_3SO_3$ than in LiTFSI (compare panels a and b of Fig. 3.3.5). Therefore, both catholyte solutions are stable up to about 70 – 80 °C without showing any significant thermal transition at moderately high temperatures, thereby matching the conventional application requirements.[99] It is worth mentioning that the thermal stability range herein observed is wider than that of common electrolyte solutions both for lithium-ion batteries, based on carbonates–$LiPF_6$ mixtures,[100] and for lithium-sulfur batteries, typically containing volatile DOL and DME solvents.[7]

160
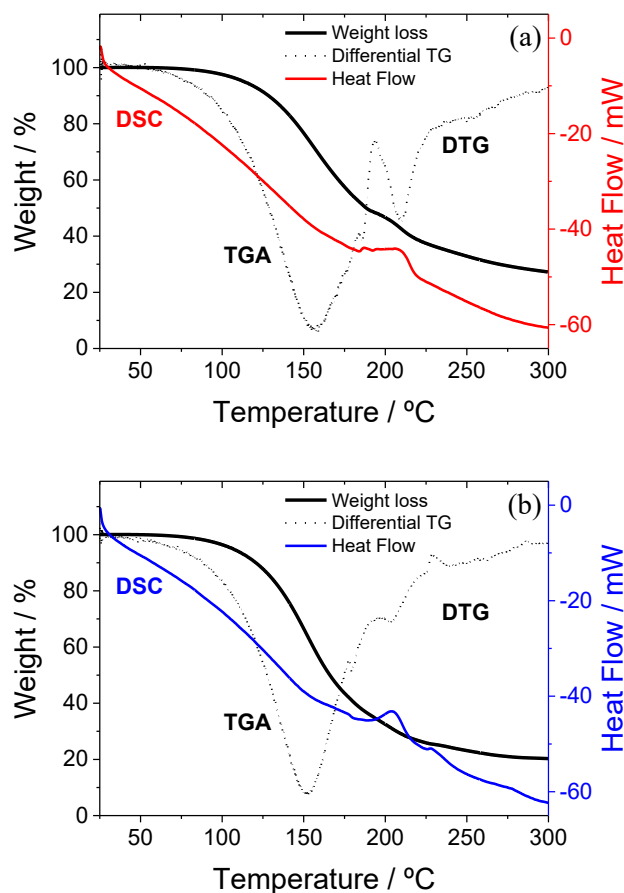
Figure 3.3.5. TGA, corresponding differential curve (DTG), and DSC curves of **(a)** DEGDME–Li$_2$S$_8$–1m LiNO$_3$–1m LiTFSI and **(b)** DEGDME–Li$_2$S$_8$–1m LiNO$_3$–1m LiCF$_3$SO$_3$ samples.

The lithium-ion transport properties of the catholyte solutions are crucial parameters for determining the cell performance. Accordingly, fast and efficient Li$^+$ motion within the electrolyte medium can ensure low cell polarization at high current, thus leading to relevant power capability, while hindered mobility usually affects the cell behavior in terms of energy efficiency and rate capability.[101] Thus, the charge transport characteristics of DEGDME–Li$_2$S$_8$–1m LiNO$_3$–1m LiTFSI and DEGDME–Li$_2$S$_8$–1m LiNO$_3$–1m LiCF$_3$SO$_3$ are evaluated by combining lithium transference number measurements and ionic conductivity, as shown in Figure 3.3.6 and Figure 3.3.7a and b, respectively. The Li$^+$ transference number, has been determined through the method reported by Bruce−Vincent−Evans (see the *3.3.2 Experimental* section for further details).[11] Panels a and b of Figure 3.3.6 show the related chronoamperometry and EIS Nyquist plots (inset) for DEGDME–Li$_2$S$_8$–1m LiNO$_3$–1m LiTFSI and DEGDME–Li$_2$S$_8$–1m LiNO$_3$–1m LiCF$_3$SO$_3$, respectively. A shift of the high-frequency *x*-axis intercept is observed after the chronoamperometry measurement in the

Nyquist plots of Figure 3.3.6. This evidence reveals an increase of electrolyte resistance, which is possibly attributed to a change of the catholyte composition owing to current flow during the test.
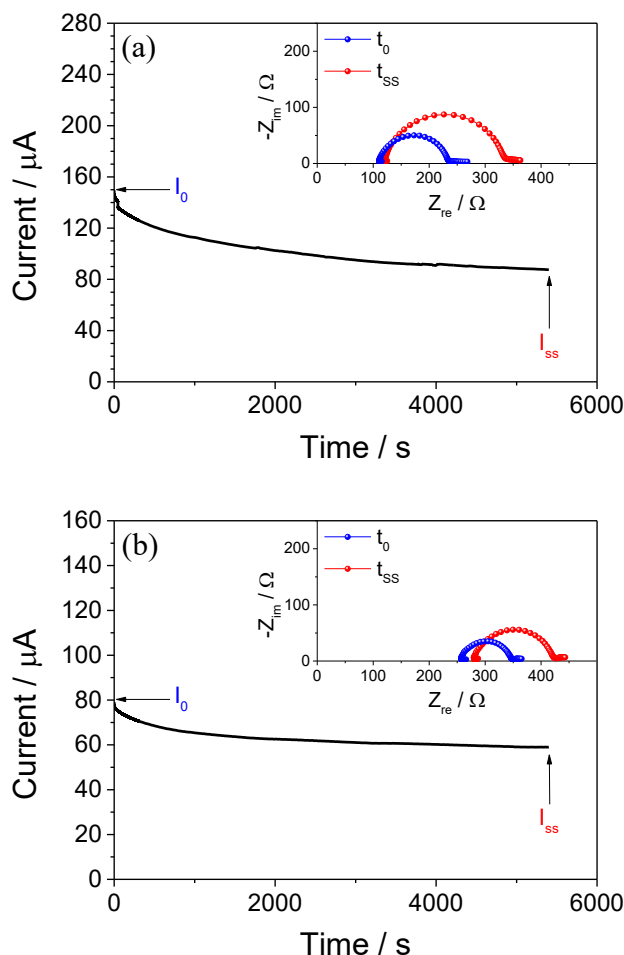
Figure 3.3.6. Chronoamperometric curves and in inset EIS Nyquist plots before and after cell polarization used for the determination of the lithium transference number of **(a)** DEGDME–Li_2S_8–1m $LiNO_3$–1m LiTFSI and **(b)** DEGDME–Li_2S_8–1m $LiNO_3$–1m $LiCF_3SO_3$ catholytes. Chronoamperometric polarization voltage: 30 mV. Impedance spectroscopy within 500 kHz – 100 mHz frequency range using a signal amplitude of 10 mV.

Furthermore, electrolyte decomposition over the lithium metal surface during the SEI formation and consolidation, and possible parasitic reactions with partial consumption of the catholyte species may lead to an increase of the cell resistance upon current flow.[102] As for the lithium transference number, both solutions are characterized by high values suitable for lithium cell application, i.e., 0.60 for DEGDME–Li_2S_8–1m $LiNO_3$–1m LiTFSI and 0.79 for DEGDME–Li_2S_8–1m $LiNO_3$–1m $LiCF_3SO_3$, thereby indicating higher Li^+ mobility in the latter than in the former. This result suggests that large fraction of charge upon cell polarization is carried by Li^+ ions, while the mobility of the relatively

large NO_3^-, $CF_3SO_3^-$, and $TFSI^-$ is hindered. Furthermore, the latter catholyte is expected to ensure better performance at high current.

Both DEGDME–Li_2S_8–1m LiNO$_3$–1m LiTFSI and DEGDME–Li_2S_8–1m LiNO$_3$–1m LiCF$_3$SO$_3$ catholytes exhibit an Arrhenius trend of the ionic conductivity, reported in panels a and b of Figure 3.3.7, with high values within the investigated temperature range. On the other hand, the DEGDME–Li_2S_8–1m LiNO$_3$–1m LiTFSI solution shows slightly higher conductivity than the DEGDME–Li_2S_8–1m LiNO$_3$–1m LiCF$_3$SO$_3$ one (compare panel a and b of Fig. 3.3.7), that is, 3×10^{-3} S cm^{-1} with respect to 2×10^{-3} S cm^{-1} at room temperature, increasing to 7×10^{-3} S cm^{-1} with respect to 4×10^{-3} S cm^{-1} by rising the temperature to about 70 °C. The activation energy for the ion transport is 12 and 10 kJ mol^{-1} for DEGDME–Li_2S_8–1m LiNO$_3$–1m LiTFSI and DEGDME–Li_2S_8–1m LiNO$_3$–1m LiCF$_3$SO$_3$, respectively, as calculated by conductivity linear trends. Thus, EIS reveals charge transport characteristics approaching those observed in conventional carbonate-based electrolytes for lithium-ion batteries, thereby suggesting the suitability of both solutions for practical applications.[103,104]

The stability of the lithium-metal anode in polysulfide-containing electrolytes for Li-S batteries is a key requirement to avoid shuttle reactions, and ensure small cell polarization and long cycle life.[105] The electrochemical characteristics of the lithium/catholyte solution interphase have been investigated under dynamic and static conditions by performing on Li/Li symmetrical cells lithium plating/stripping tests and EIS measurements during cell aging at room temperature, respectively (Fig. 3.3.7c–f). Panels c and d of Figure 3.3.7 show the voltage profiles for DEGDME–Li_2S_8–1m LiNO$_3$–1m LiTFSI and DEGDME–Li_2S_8–1m LiNO$_3$–1m LiCF$_3$SO$_3$, respectively, with magnifications in inset revealing the steady-state curves. The catholyte solution based on the LiTFSI salt (Fig. 3.3.7c) exhibits an overvoltage rise during the first day, possibly attributed to gradual formation of a stable SEI on lithium,[74] followed by a significant polarization decrease upon the subsequent 15 days indicating partial dissolution and consolidation of the Li$^+$-conductive passivation layer.[33] Then, the cell shows a constant polarization as low as 7 mV, which suggests remarkable electrochemical stability and low resistance of the SEI upon dynamic condition. As for the catholyte based on LiCF$_3$SO$_3$ salt, Figure 3.3.7d reveals a different polarization trend, characterized by an initial voltage approaching 100 mV and a significant polarization decrease down to 10 mV throughout the test owing to the cell operation. In particular, the cell shows a steady cycling behavior after 15 days.
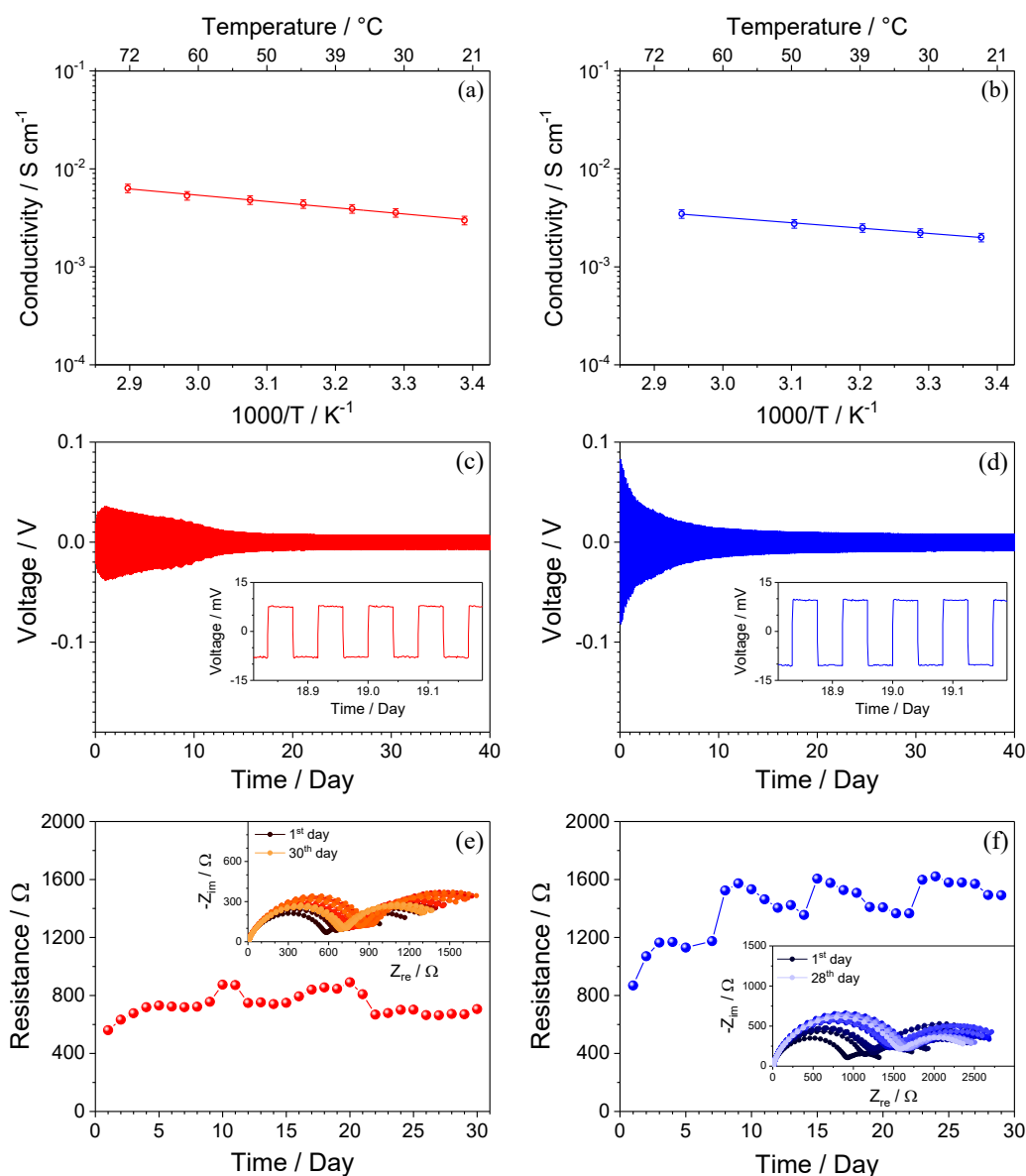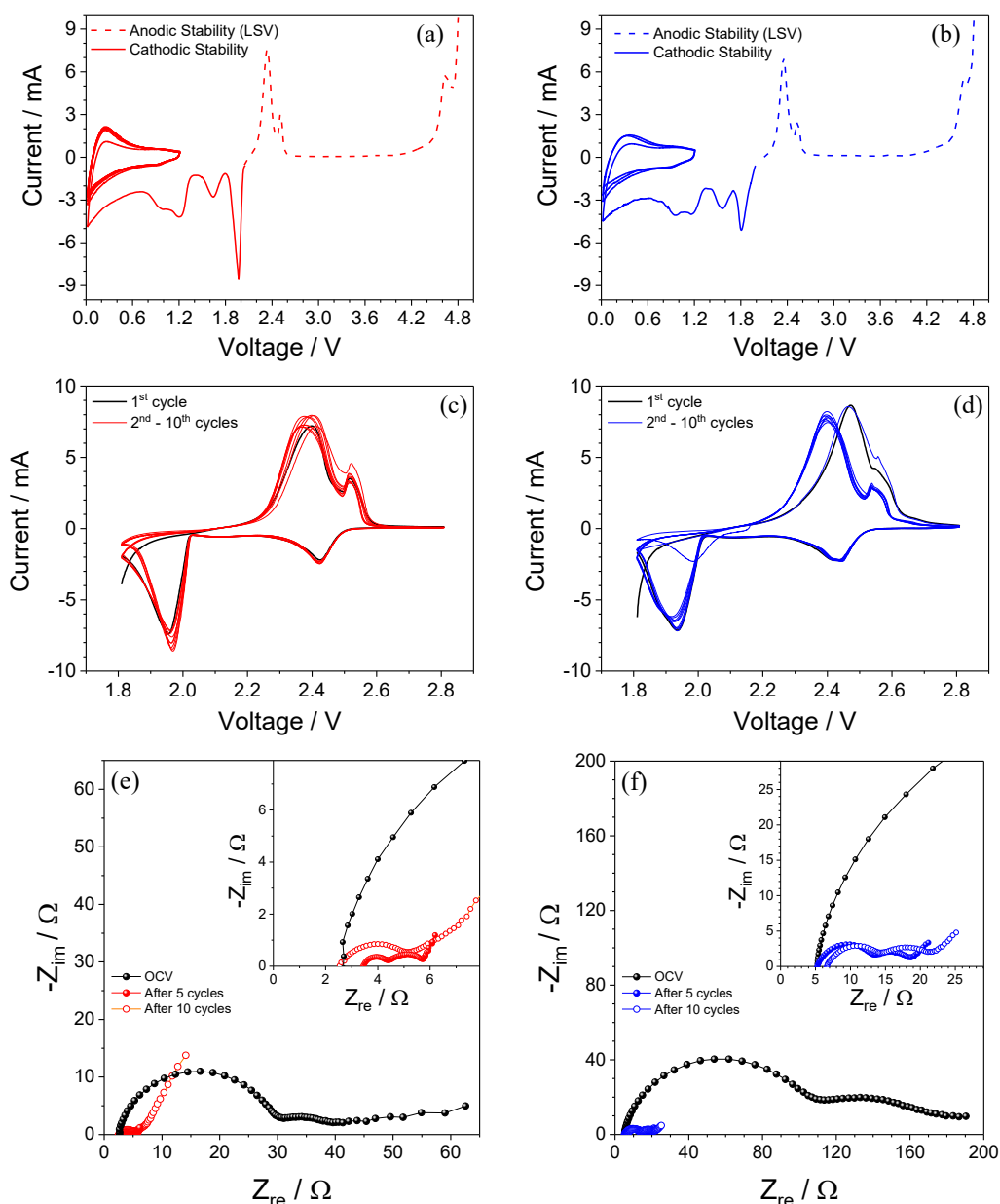
Figure 3.3.7. (a,b) Ionic conductivity versus temperature of **(a)** DEGDME–Li$_2$S$_8$–1m LiNO$_3$–1m LiTFSI and **(b)** DEGDME–Li$_2$S$_8$–1m LiNO$_3$–1m LiCF$_3$SO$_3$ catholytes. **(c,d)** Lithium stripping-deposition galvanostatic test performed at 0.1 mA cm^{-2} and 1 h step-time of **(c)** DEGDME–Li$_2$S$_8$–1m LiNO$_3$–1m LiTFSI and **(d)** DEGDME–Li$_2$S$_8$–1m LiNO$_3$–1m LiCF$_3$SO$_3$ catholytes, with magnifications in panel insets showing steady-state cycles. **(e,f)** Time evolution of the lithium/catholyte interphase resistance of symmetrical Li/Li cells using **(e)** DEGDME–Li$_2$S$_8$–1m LiNO$_3$–1m LiTFSI and **(f)** DEGDME–Li$_2$S$_8$–1m LiNO$_3$–1m LiCF$_3$SO$_3$ catholytes, and corresponding EIS Nyquist plots in panel insets. Frequency range: 500 kHz – 100 mHz. Signal amplitude: 10 mV.

Therefore, both the DEGDME–Li$_2$S$_8$–1m LiNO$_3$–1m LiTFSI and the DEGDME–Li$_2$S$_8$–1m LiNO$_3$–1m LiCF$_3$SO$_3$ catholyte solutions form a remarkably stable SEI over the lithium-metal anode suitable for prolonged Li$^+$ dissolution and deposition, and able to mitigate the dendrite formation.[106] According to the high lithium transference numbers, both Li/Li cells exhibit flat voltage profile with

polarization lower than 10 mV at the steady state, thus suggesting the Li^+ diffusion through the SEI as the limiting step of the electrochemical process at a current of 100 µA cm^{-2}.

Panels e and f of Figure 3.3.7 report the lithium/catholyte solution interphase resistance trend upon aging of symmetrical Li/Li cells, with the related Nyquist plot in inset, for DEGDME–Li$_2$S$_8$–1m LiNO$_3$–1m LiTFSI and DEGDME–Li$_2$S$_8$–1m LiNO$_3$–1m LiCF$_3$SO$_3$, respectively. The Nyquist plots generally reveal an impedance response characterized by high-middle frequency semicircles due to the interphase resistance and a low frequency finite-length Warburg element accounting for Li^+ diffusion phenomena related to non-blocking interphases.[107,108] Figure 3.3.7e shows that the Li/DEGDME–Li$_2$S$_8$–1m LiNO$_3$–1m LiTFSI resistance varies within the 600 – 900 Ω range due to recurring SEI dissolution and formation,[109] thus reaching a steady state. On the other hand, the Li/DEGDME–Li$_2$S$_8$–1m LiNO$_3$–1m LiCF$_3$SO$_3$ interphase has a resistance of about 800 Ω after 1 day of aging, which increases to about 1200 Ω after 3 days and to about 1600 Ω after 8 days (Fig. 3.3.7f). Subsequently, the interphase resistance fluctuates between 1400 and 1600 Ω, in agreement with the periodic SEI dissolution and formation as observed also for the DEGDME–Li$_2$S$_8$–1m LiNO$_3$–1m LiTFSI solution (compare panels f and e of Fig. 3.3.7).[109]

Voltammetry and EIS measurements have been carried out to investigate the electrochemical stability window of the solutions, the redox processes occurring in lithium cell as well as the cell impedance evolution upon cycling (Fig. 3.3.8). The voltage stability window has been determined by LSV and CV experiments on Li|catholyte|SPC cells in the anodic and cathodic regions, respectively. The LSV of DEGDME–Li$_2$S$_8$–1m LiNO$_3$–1m LiTFSI (dashed curve in Fig. 3.3.8a), shows two anodic peaks at 2.4 and 2.5 V *vs* Li$^+$/Li related to the reversible catholyte oxidation,[37] and the electrolyte decomposition starting at about 4.2 V *vs* Li$^+$/Li. The first cathodic CV scan (solid curve in Fig. 3.3.8a) reveals the catholyte reduction at about 1.9 and 1.8 V *vs* Li$^+$/Li,[37] as well as the cathodic electrolyte decomposition at about 1.2 V *vs* Li$^+$/Li leading to the SEI formation over the electrodes, while the subsequent cycles within 0.01 and 1.2 V *vs* Li$^+$/Li are characterized by overlapped curves indicating steady and reversible Li^+ insertion into the carbon working electrode.[66] The DEGDME–Li$_2$S$_8$–1m–LiNO$_3$–1m LiCF$_3$SO$_3$ solution exhibits a similar voltammetry response, as shown in Figure 3.3.8b. Thus, the anodic LSV (dashed curve in Fig. 3.3.8b) indicates decompositions reactions starting at about 4.2 V *vs* Li$^+$/Li, besides reversible catholyte oxidation at 2.4 and 2.5 V *vs* Li$^+$/Li, while the CV (solid curve in Fig. 3.3.8b) reveals catholyte reduction at 1.9 and 1.6 V *vs* Li$^+$/Li,[37] SEI formation at 1.2 V *vs* Li$^+$/Li, and reversible Li^+ insertion into the carbon working electrode between 0.01 and 1.2 V *vs* Li$^+$/Li.[66] Therefore, both the DEGDME–Li$_2$S$_8$–1m LiNO$_3$–1m LiTFSI and the DEGDME–Li$_2$S$_8$–1m LiNO$_3$–1m LiCF$_3$SO$_3$ catholyte solutions have an electrochemical stability window from 1.2 to 4.2 V *vs* Li$^+$/Li.

Figure 3.3.8. (a, b) CV profiles in the cathodic region and LSV profiles in the anodic region of lithium cells using SPC working electrode with **(a)** DEGDME–Li₂S₈–1m LiNO₃–1m LiTFSI and **(b)** DEGDME–Li2S8–1m LiNO₃–1m LiCF₃SO₃ catholytes. **(c, d)** CV profiles of **(c)** Li/DEGDME–Li₂S₈–1m LiNO₃–1m LiTFSI/SPC and **(d)** Li/DEGDME–Li₂S₈–1m LiNO₃–1m LiCF₃SO₃/SPC cells within 2.8 V and 1.8 V range. **(e, f)** Nyquist plots of EIS during CV tests of **(e)** Li/DEGDME–Li₂S₈–1m LiNO₃–1m LiTFSI/SPC and **(f)** Li/DEGDME–Li₂S₈–1m LiNO₃–1m LiCF₃SO₃/SPC cells within the 1.8 V – 2.8 V range at the OCV, after 5 and 10 cycles with magnification in insets. Scan rate: 0.1 mV s⁻¹. Frequency range: 500 kHz – 100 mHz. Signal amplitude: 10 mV.

However, the formation of a stable SEI below 1.2 V *vs* Li⁺/Li leads to a practical voltage window extended down to 0 V *vs* Li⁺/Li, considered suitable for the semi-liquid Li-S cell operation at about 2 V *vs* Li⁺/Li. Panels c and d of Figure 3.3.8 show the CV curves within 1.8 and 2.8 V *vs* Li⁺/Li for

the two solutions. Figure 3.3.8c reveals reversible electrochemical processes which are stable upon cycling, as suggested by overlapping profiles typical of the Li-S conversion reaction. In particular, DEGDME–Li_2S_8–1m $LiNO_3$–1m LiTFSI exhibits two reduction peaks at about 2.4 and 2 V *vs* Li^+/Li corresponding to the long-chain (Li_2S_6, Li_2S_8) and the short-chain (Li_2Sx, $2 \leq x \leq 4$) sulfide species, which are reversed into two oxidation peaks at 2.3 and 2.5 V *vs* Li^+/Li related to the stepwise catholyte conversion with Li deposition at the anode side and concomitant S_8 formation.[37] Furthermore, possible formation of insoluble Li_2S upon reduction scan below 2 V cannot be excluded.[37] EIS measurements performed during the CV experiment (Fig. 3.3.8e) reveal a favorable activation process occurring upon cell operation, which leads to a remarkable cell impedance decrease. Indeed, the Nyquist plot of Figure 3.3.8e indicates an electrode/electrolyte interphase resistance at the open circuit voltage (OCV) of about 30 Ω, as revealed by the width of the high-middle frequency semicircle, and a low-frequency Li^+ diffusion response.[107,108] The interphase resistance drops to values as low as about 3 Ω after 5 and 10 cycles, as displayed by magnification in Figure 3.3.8e inset, most likely due to a gradual wetting as well as to progressive surface modification of the carbon electrode by the catholyte solution, leading to improved reaction kinetics by cycling as observed in Chapter 2 (NLLS analysis not reported). DEGDME–Li_2S_8–1m $LiNO_3$–1m $LiCF_3SO_3$ shows a CV, reported in Figure 3.3.8d, revealing the reversible Li-S conversion between 1.8 and 2.8 V *vs* Li^+/Li mostly occurring through overlapping profiles, except for the 1st and 6th cycles which show a different trend with respect to the other cycles likely due the above mentioned activation phenomena. Thus, the long-chain (Li_2S_6, Li_2S_8) and short-chain (Li_2S_x, $2 \leq x \leq 4$) polysulfide formation reactions occur at 2.4 and 1.9 V *vs* Li^+/Li upon discharge, along with possible Li_2S precipitation at about 1.8 V *vs* Li^+/Li, while the reversed oxidation leads to CV peaks at 2.4 and 2.5 V *vs* Li^+/Li.[37] This activation process is further shown in Figure 3.3.8f, which reports the Nyquist plot of the Li|DEGDME–Li_2S_8–1m $LiNO_3$–1m $LiCF_3SO_3$|SPC cell throughout the CV measurement. Accordingly, the cell has initial electrode/electrolyte interphase resistance of about 100 Ω, decreasing to about 15 Ω after 5 and 10 cycles (NLLS analysis not reported). Despite the DEGDME–Li_2S_8–1m $LiNO_3$–1m $LiCF_3SO_3$ catholyte exhibits higher interphase resistance than the DEGDME–Li_2S_8–1m $LiNO_3$–1m LiTFSI one, the observed values indicate fast electrode kinetics for both solutions.

The results shown in Figure 3.3.7c–f suggest that LiTFSI ensures an enhanced SEI layer over the lithium metal with respect to $LiCF_3SO_3$, under both static and dynamic conditions. Accordingly, the Li/Li cells using DEGDME–Li_2S_8–1m $LiNO_3$–1m LiTFSI exhibit lower, more stable SEI resistance (see panels e and f of Fig. 3.3.7), reflected into a lower polarization upon prolonged cycling (see panels c and d of Fig. 3.3.7) than the ones using DEGDME–Li_2S_8–1m $LiNO_3$–1m $LiCF_3SO_3$. Furthermore, Figure 3.3.8e and f indicates larger resistance at the electrode/electrolyte interphase for

the Li|catholyte|SPC cell employing LiCF₃SO₃ as the electrolyte salt. Based on the above mentioned results for the lithium symmetrical cells, it is expected that the higher SEI resistance at the lithium side due to the presence of $LiCF_3SO_3$ may contribute to the larger electrode/electrolyte interphase resistance values in Li-SPC cell compared to LiTFSI. This speculation is in agreement with previous literature works demonstrating the significant effect of the anion nature on the evolution and transformation of the SEI over lithium metal in polysulfide-containing electrolytes for lithium-sulfur batteries.[110,111] However, a further effect on the electrode/electrolyte interphase resistance at the cathode side cannot be excluded, since the anion nature might influence the electrolyte decomposition products at high voltage. Furthermore, it is worth mentioning that both Li|catholyte|SPC cells of Figure 3.3.8e and f exhibit after cycling low interphase resistance values with same order of magnitude, which may be slightly affected by cell assembling, electrode morphology, and cycling conditions.

In summary, CV and EIS reveal a steady electrochemical Li-S conversion processes centered at about 2.4 and 2 V *vs* Li⁺/Li upon reduction, and at about 2.4 V *vs* Li⁺/Li upon oxidation, which occur through fast charge transfer at SPC electrode/catholyte solution interphase. The results indicate highly reversible catholyte operation promoted by a cell activation, which remarkably compares the data obtained in Chapter 2. Moreover, the cell configuration studied in this section does not require any fine engineering of cathode and separator. Therefore, the semi-liquid cell might be an advantageous strategy to develop Li-S cell without relevant drawbacks in terms of electrochemical behavior with respect to conventional configuration.

The cycling responses of the two Li|catholyte|SPC cells have been further evaluated by performing galvanostatic measurements at several current rates. Figure 3.3.9 shows the results of a rate capability test of the cells in terms of voltage profiles (panels a, b) and cycling behavior (panels c, d). Both Li|DEGDME–Li₂S₈–1m LiNO₃–1m LiTFSI|SPC and Li|DEGDME–Li₂S₈–1m LiNO₃–1m LiCF₃SO₃|SPC cells show the typical voltage curves centered at about 2.2 V, associated with the reversible Li-S conversion[37] with the expected increasing polarization as the C-rate raises. In agreement with CV, the cells exhibit two discharge plateaus at about 2.4 and 2.1 V, reflected upon charge into plateaus at 2.2 and 2.5 V. The Li|DEGDME–Li₂S₈–1m LiNO₃–1m LiCF₃SO₃|SPC cell shows higher rate performances than the Li|DEGDME–Li₂S₈–1m LiNO₃–1m LiTFSI|SPC one in terms of both reversible capacity and polarization at high current (compare panels a and c with panels b and d in Fig. 3.3.9). In particular, the Li|DEGDME–Li₂S₈–1m LiNO₃–1m LiCF₃SO₃|SPC cell delivers higher reversible capacity than the Li|DEGDME–Li₂S₈–1m LiNO₃–1m LiTFSI|SPC one in the current range from C/10 to C/5, *i.e.*, 1160, 1125, and 1050 mAh g$_S^{-1}$ for the former and 1050, 1030, and 1000 mAh g$_S^{-1}$ for the latter, while both catholytes ensure reversible capacity of about 900

mAh g$_S^{-1}$ at C/3 and C/2 (1C = 1675 mA g$_S^{-1}$). Furthermore, the performance of the Li|DEGDME–Li$_2$S$_8$–1m LiNO$_3$–1m LiCF$_3$SO$_3$|SPC cell exceeds the one of Li|DEGDME–Li$_2$S$_8$–1m LiNO$_3$–1m LiTFSI|SPC cell at current rates as high as 1C and 2C. Thus, the reversible capacity at 1C and 2C decreases to 740 and 300 mAh g$_S^{-1}$ for the Li|DEGDME–Li$_2$S$_8$–1m LiNO$_3$–1m LiCF$_3$SO$_3$|SPC cell, and to 115 and 80 mAh g$_S^{-1}$ for the Li|DEGDME–Li$_2$S$_8$–1m LiNO$_3$–1m LiTFSI|SPC one, respectively, while both cells remarkably recover the initial capacity as the current is decreased to C/10 at the 71st cycle.
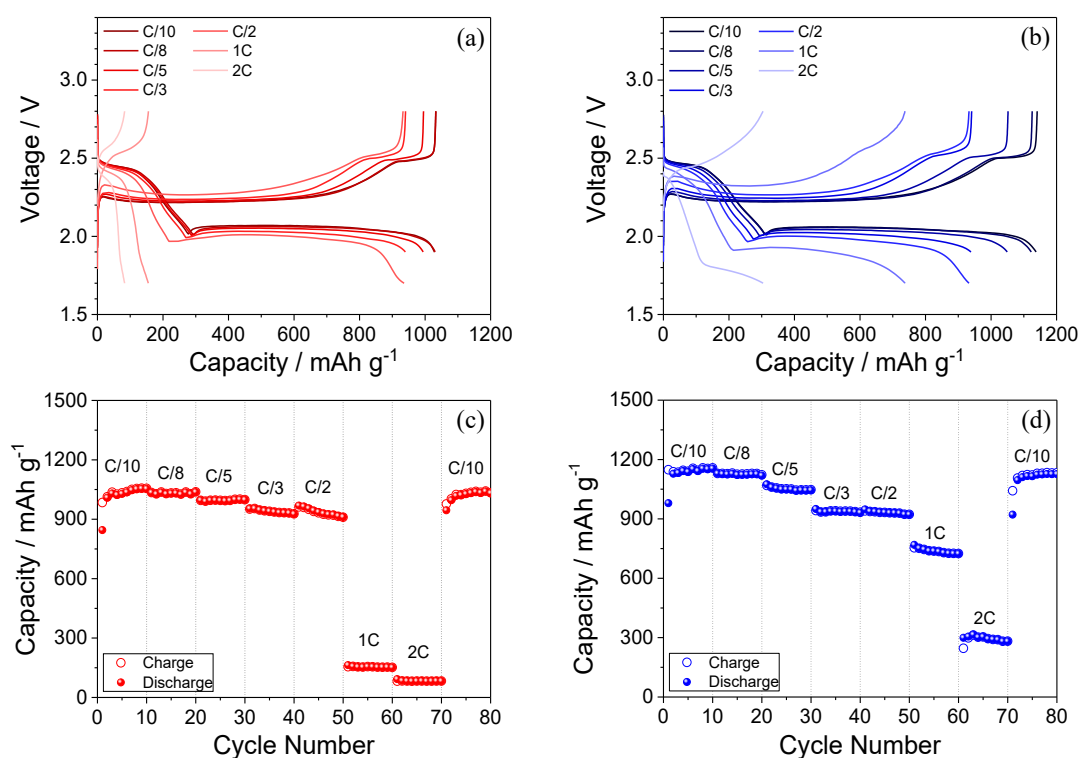
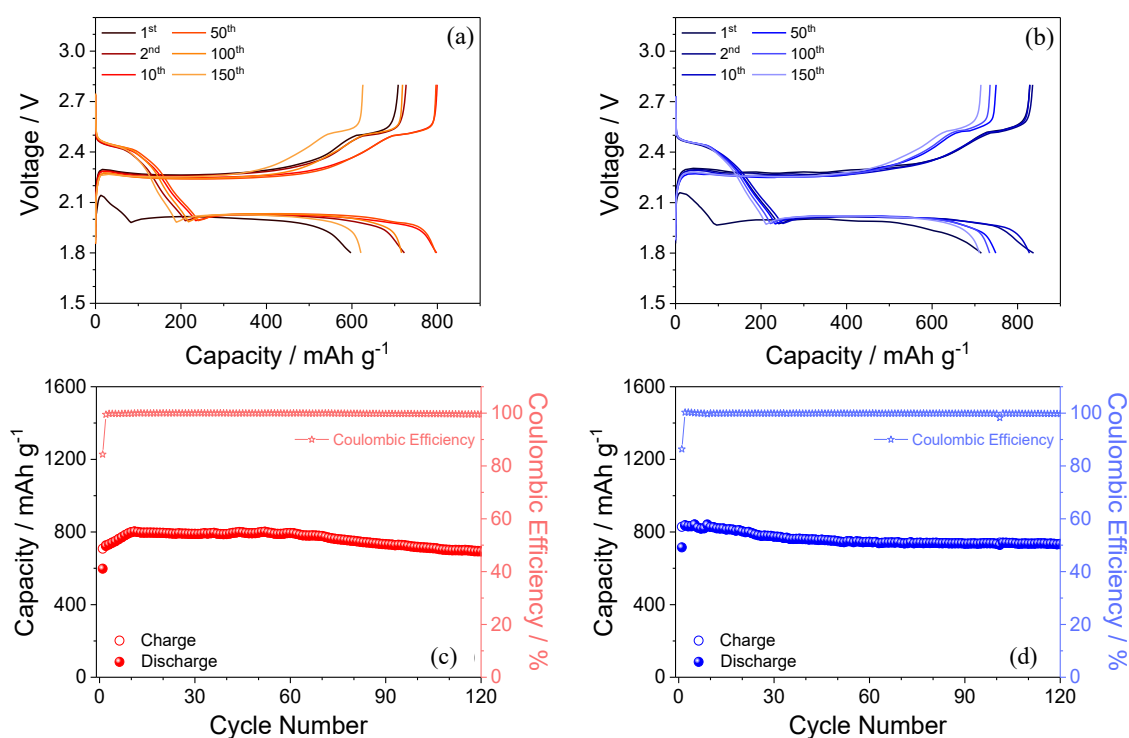**Figure 3.3.9. (a, b)** Galvanostatic voltage profiles at C/10, C/8, C/5, C/3, C/2, 1C and 2C rates of **(a)** Li|DEGDME–Li$_2$S$_8$–1m LiNO$_3$–1m LiTFSI|SPC and **(b)** Li|DEGDME–Li$_2$S$_8$–1m LiNO$_3$–1m LiCF$_3$SO$_3$|SPC cells, and **(c, d)** corresponding cycling trends, respectively. Voltage range of 1.9 V – 2.8 V from C/10 to C/3, and of 1.7 V – 2.8 V from C/2 to 2C.

However, EIS of Figure 3.3.8e and f suggests minor difference in terms of electrode/electrolyte interphase resistance between the two cell configurations studied, as well as fast electrode charge transfer, after an electrochemical activation likely attributed to already observed gradual wetting and progressive surface modification of the carbon electrode by the catholyte solution. Despite the initial interphase resistance is significantly lower when using LiTFSI rather than LiCF$_3$SO$_3$, *i.e.*, 30 compared to 100 Ω, respectively, both resistances drop down to values as low as 3 and 15 Ω after 10 voltammetry cycles (see Fig. 3.3.8e and f). The poor performance above 1C of the Li|DEGDME–

Li_2S_8–1m $LiNO_3$–1m LiTFSI|SPC cell can be reasonably attributed to high overvoltage of the processes occurring at the second plateau.

The cells have been also galvanostatically cycled at rate fixed to C/3 for 120 cycles. Figure 3.3.10 reports the related cycling behavior and voltage profiles, respectively. The two cells deliver a maximum specific capacity above 800 mAh g_S^{-1}, which is reflected into areal capacity of about 2.3 mAh cm^{-2}, referred to the geometric surface of the carbon electrode, with slightly higher value for the cell using the DEGDME–Li_2S_8–1m $LiNO_3$–1m $LiCF_3SO_3$ catholyte, likely due to the above mentioned effect of the higher lithium transference number with respect to the cell using the DEGDME–Li_2S_8–1m $LiNO_3$–1m LiTFSI catholyte. The cells exhibit very stable cycling behavior, a Coulombic efficiency above 99.5 % after the first cycle (Fig. 3.3.10c, d), and relatively low polarization (Fig. 3.3.10a, b). Moreover, the Li/DEGDME–Li_2S_8–1m $LiNO_3$–1m LiTFSI/SPC cell undergoes the above discussed activation process upon the first 10 cycles, in agreement with the EIS results of Figure 3.3.8.

Figure 3.3.10. (a, b) Galvanostatic cycling voltage profile and **(c, d)** corresponding cycling trend with Coulombic efficiency (right x-axis) of **(a, c)** Li|DEGDME–Li_2S_8–1m $LiNO_3$–1m LiTFSI|SPC and **(b, d)** Li|DEGDME–Li_2S_8–1m $LiNO_3$–1m $LiCF_3SO_3$|SPC cells at C/3 rate within the 1.8 V – 2.8 V range.

Although the observed capacity values may be lower than those reported for Li-S cells using a solid configuration sulfur electrode, the semi-liquid configuration benefits from various advantages including easy cell assembling, simple electrode and separator engineering to ensure suitable cycling behavior, and high stability of the electrode/catholyte interphase.[112]

In order to further highlight the practical interest of the battery configuration proposed, the areal capacity was enhanced by doubling the catholyte volume to increase the sulfur loading in the cells from 4.4 and 4.2 mg to 8.8 and 8.4 mg for DEGDME–Li₂S₈–1m LiNO₃–1m LiTFSI and DEGDME–Li₂S₈–1m LiNO₃–1m LiCF₃SO₃, respectively. Preliminary cycling, performed at a current rate of C/20 using 2032-coin cells and shown in Figure 3.3.11, reveals areal-capacity approaching 4 mAh cm⁻² referred to the geometric surface of the carbon electrode, *i.e.*, a value even higher than that of high-performance Li-ion batteries,[113] with negligible cell polarization increase.
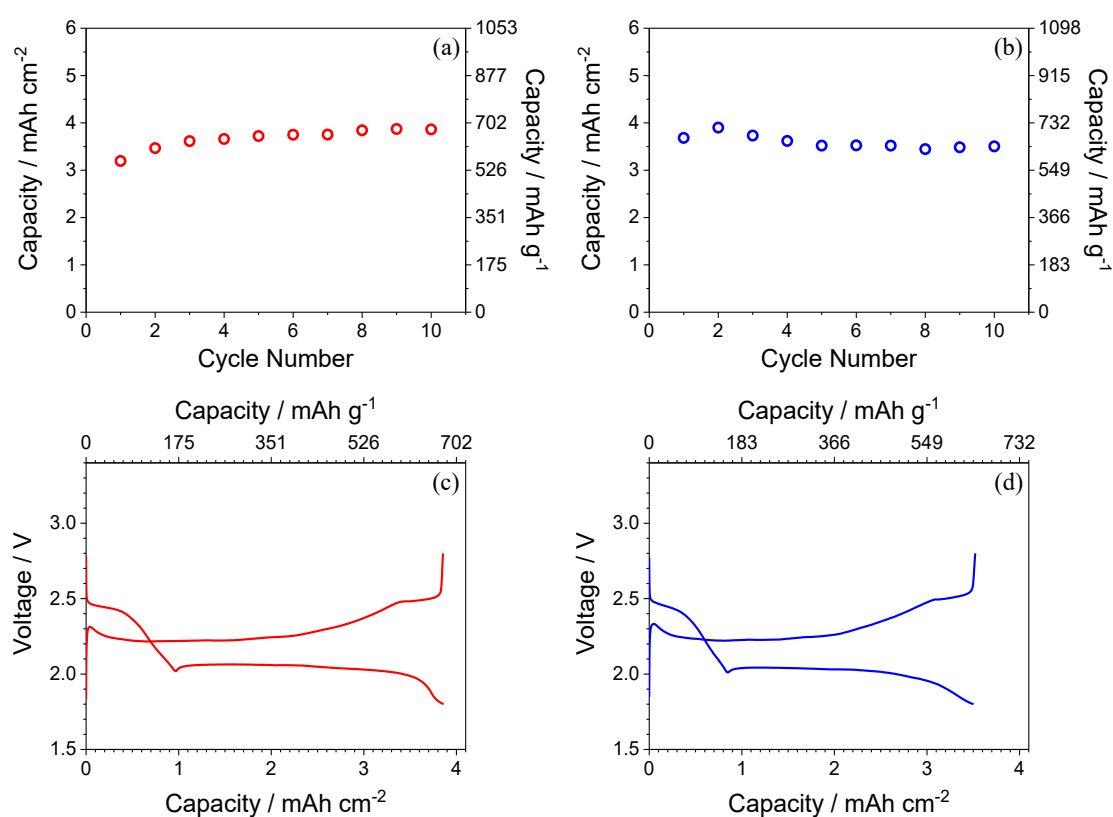
Figure 3.3.11. (a,b) Galvanostatic cycling trend and **(c,d)** voltage profiles of a steady-state galvanostatic cycle of **(a,c)** Li/DEGDME–Li₂S₈–1m LiNO₃–1m LiTFSI/SPC and **(b,d)** Li/DEGDME–Li₂S₈–1m LiNO₃–1m LiCF₃SO₃/SPC cells at C/20 rate within the 1.8 V – 2.8 V range. The areal capacity (mAh cm⁻²) is referred to the electrode geometric area of the cell (1.54 cm²).

Afterwards, the DEGDME–Li₂S₈–1m LiNO₃–1m LiTFSI was selected and combined in lithium cell with the Cr₂O₃@C electrode, obtained by the MIL-101(Cr) precursor (see *3.3.2 Experimental* section for further details), to explore the compatibility of the catholyte concept with an alternative and sustainable MOF-derived electrode. Firstly, the novel electrode was characterized by investigation of its physical-chemical properties. The changes upon annealing of MIL-101(Cr)

171

precursor to obtain the Cr_2O_3@C composite are detected by XRD and TGA in Figure 3.3.12. The XRD pattern of MIL-101(Cr) shown in Figure 3.3.12a reveals the characteristic peaks below 25° of 2θ.[114,115] Above this value, intense peaks not assigned to the MIL-101(Cr) compound are also detected and ascribed to the α-CrOOH phase, thus suggesting the presence in the pristine MOF of a Cr oxy-hydroxide impurity.[115] After heating at 600 °C under N_2 only peaks belonging to the α-Cr_2O_3 phase are detected, while the typical peak of C assigned to (002) planes is not observed at 26.5° of 2θ, thus indicating its amorphous nature ascribed to a mild calcination temperature.[116] The TGA curves of the pristine MOF recorded under N_2 and O_2 atmosphere, respectively, as well as the curve of the Cr_2O_3@C recorded under O_2 atmosphere, are shown in Figure 3.3.12b. The TGA curves of MOF under N_2 and O_2 reveal similar weight loss of about 20% below 100 °C, which may be likely ascribed to the loss of physically adsorbed water. The observed weight loss is of about $8H_2O$ (molecules per formula unit) higher than that reported by literature for MOFs with the same chemical composition, that is, $Cr_3O(OH)(H_2O)_2(BDC)_3$.[117] On the other hand, an amount of adsorbed water as high as 40 % have been already reported in literature.[118] At temperatures higher than 100 °C the weight loss becomes greater in the O_2 atmosphere, being very pronounced around 300 °C where the expected oxidation of the organic matrix occurs. The total weight loss for the MOF precursor is therefore detected at 600 °C to be of about 70 %.[118] Considering the theoretical MOF composition, including absorbed water, the theoretical weight loss should be 68.3 %:[117] the difference with respect to the results reported herein (70 %) may be reasonably attributed to the presence of the above mentioned α-CrOOH impurity. The TGA curve recorded under N_2 reveals different kinetics and a lower overall weight loss, that is, of about 57%, as expected by the missing oxidation of the organic matrix. On the other hand, the TGA curve recorded under O_2 of the Cr_2O_3@C is characterized by weight loss only ascribed to CO_2 evolution, thus indicating a carbon content of about 13% into the composite. The carbon content observed for the composite is lower than that expected by annealing the MIL-101 (Cr) MOF,[118] most likely due to a partial volatilization of the organic component during the thermal treatment and to the presence of α-CrOOH impurity in the pristine MOF.
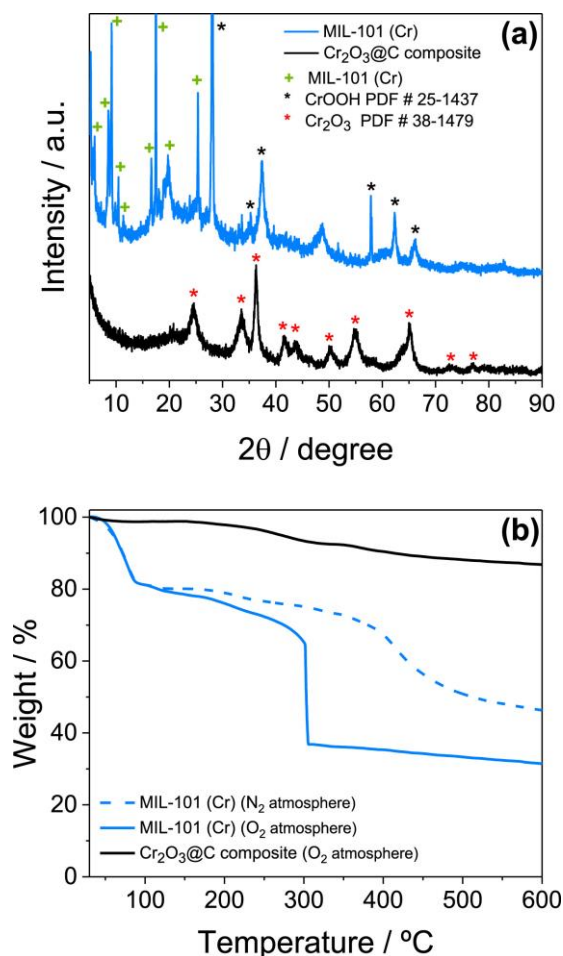
Figure 3.3.12. (a) XRD patterns of MIL-101 (Cr) MOF (cyan) and $Cr_2O_3@C$ (black) composites; reference data of CrOOH (black stars, PDF # 25- 1437) and Cr_2O_3 (red stars, PDF # 38-1479) are also reported for comparison. **(b)** TGA curves of MIL-101 (Cr) MOF in N_2 and O_2 atmosphere (cyan) and $Cr_2O_3@C$ in O_2 atmosphere (black).

The surface composition of the $Cr_2O_3@C$ composite is analyzed by XPS (Fig. 3.3.13). The survey spectrum (Fig. 3.3.13a) clearly indicates the presence of Cr, C and O elements, along with Al used as the support for measurement. The spectrum of Cr 2p (Fig. 3.3.13b) may be resolved into peaks with binding energy values around 576.7 and 686.3 eV assigned to Cr $2p_{3/2}$ and Cr $2p_{1/2}$, respectively, which suggests Cr^{3+} bound to O.[119] Furthermore, the C 1s spectrum (Fig. 3.3.13c) can be fitted according to three components located at 284.55 (70.7%), 286.7 (11.5%) and 288.9 (17.8%) eV, assigned to C−C/C=C, C−O epoxy and C−O carboxyl environments, respectively.[71] Finally, the O 1s signal is fitted according to two components at 529.8 and 531.9 eV (Fig. 3.3.13d), where the first one is assigned to O^{2-} ions, while the second peak is more complex since it can be assigned to OH⁻ ions or to O⁻ ions, which can compensate deficiencies in the sub-surface of the transition metal oxide,[120] and even to adsorbed H_2O.[121] The atomic concentrations calculated by XPS are 23.0, 62.4 and 15.6% for C, O and Cr, respectively. The XPS data indicate relevantly higher amount of O

compared to the value estimated by the TGA curves of Cr$_2$O$_3$@C, thus suggesting a different surface composition for the sample with respect to the bulk as the XPS mainly focuses at the material surface.
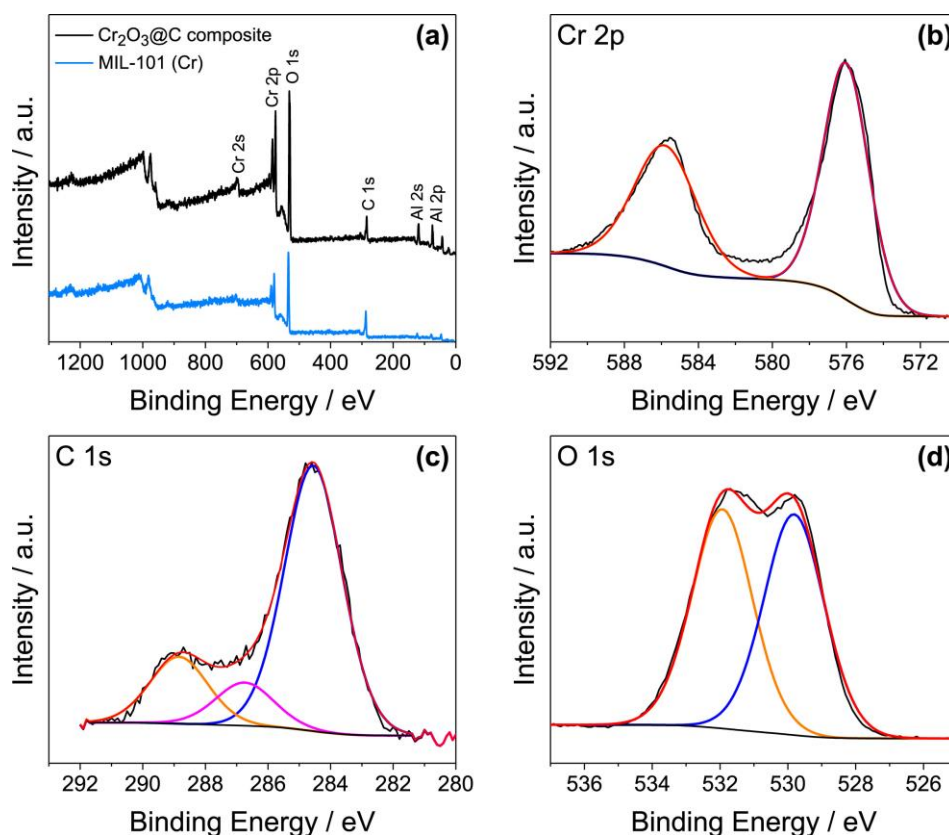

Figure 3.3.13. (a) XPS survey spectra of MIL-101 (Cr) MOF (cyan) and Cr$_2$O$_3$@C (black) composites, and **(b)** Cr 2p, **(c)** C 1s and **(d)** O 1s deconvoluted XPS spectra of Cr$_2$O$_3$@C composite.

Figure 3.3.14 reports the morphology of the composite as detected by SEM, EDS and TEM, as well as its textural properties determined by N$_2$ adsorption/desorption isotherms. The SEM image of the MOF precursor, reported for comparison in Figure 3.3.14a, reveals particles having the typical pseudo-octahedral morphology of MIL-101(Cr) with size ranging between 100 nm and 200 nm, in addition to other particles characterized by a more irregular morphology most likely ascribed to the α-CrOOH.[115] In spite, the SEM of the Cr$_2$O$_3$@C composite (Fig. 3.3.14b) shows morphology changes after calcination: the pseudo-octahedral shape almost vanishes by pyrolysis of the organic ligand, being replaced by nanometric particles forming agglomerates (>100 nm) with remarkably higher surface roughness compared to the pristine MOF. In addition, the EDS elemental mapping reveals homogeneous C, O, and Cr elements distribution over the Cr$_2$O$_3$@C sample (Fig. 3.3.14c, d and e, respectively). The TEM images of the Cr$_2$O$_3$@C composite (Fig. 3.3.14f and g) well support the SEM data (compare with Fig. 3.3.14a and b), and show a wide size distribution of primary

particles into the agglomerates ranging from few nanometers (Fig. 3.3.14f) to values approaching 100 nm (Fig. 3.3.14g). It is worth mentioning that particle interconnection may be actually promoted by carbon, which is detected by TGA in Figure 3.3.12b to reach 13% in weight and most likely represented by light grey particles with an irregular shape, such that circled in the TEM image of Figure 3.3.14f. The surface area and pore volume of the Cr_2O_3@C composite are determined by N_2 adsorption measurements (Fig. 3.3.14h and i). The adsorption/desorption isotherm reported in Figure 3.3.14h shows a hysteresis loop at high relative pressure indicating a narrow pore size distribution into the composite, and allows to calculate a BET surface area of 170 m^2 g^{-1} and a pore volume of 0.5 cm^3 g^{-1}. The pore size distribution (Fig. 3.3.14i) mainly indicates a mesoporous structure and an average pore size of 12 nm. It is worth noting that the shape of the isotherms and the specific surface values are in line with those reported for Cr_2O_3@C composites derived from MIL-101(Cr) MOF.[122,123] These values are expected to support an efficient reaction of the dissolved polysulfide in the semi-liquid Li-S cell. As mentioned previously, polysulfide-trapping ability of transition metal oxides included in the composition of the cathode support has been indicated in various papers to depend on the anchoring ability of the polar sites of the oxide, which attract the sulfur and lead to the absorption of dissolved polysulfides.[124–127] In particular, the absorption ability of Cr_2O_3 has been recently demonstrated using nanoparticle decorating carbon fibers derived from solid leather wastes adopted as coating for separator and aimed to achieve high performance lithium-sulfur battery.[128] The absorbent properties of acetylene black (AB) and Cr_2O_3 were measured in the above work using a Li_2S_6 polysulfide solution. Accordingly, polysulfide solutions exposed to AB upgraded by Cr_2O_3 powders turned nearly colorless and transparent, while the bare AB powders had a negligible impact on the color of the solution, thus qualitatively suggesting the polysulfide-trapping ability of the Cr_2O_3.

Figure 3.3.15 reveals the electrochemical features of the Cr_2O_3@C in a lithium cell employing the DEGDME–Li_2S_8–1m $LiNO_3$–1m LiTFSI catholyte. The CV profiles recorded within 1.8 – 2.8 V *vs* Li^+/Li at a constant scan rate of 0.1 mV s^{-1} (Fig. 3.3.15a) show during the first cathodic scan only one peak below 2 V ascribed to the reduction of Li_2S_8 to short chain polysulfides (e.g., Li_2S_4, Li_2S_2), while the subsequent anodic scan reveals two defined peaks above 2.4 V ascribed to the oxidation of the short chain polysulfides back to Li_2S_8 and finally to S.[35] The subsequent cycles evidence voltammetry profiles characterized by two reduction peaks around 2.4 V and 2 V during cathodic scan, and two corresponding oxidation peaks above 2.4 V during anodic scan, ascribed to the reversible redox process of S and Li with formation of long- and short-chain polysulfides.[35]
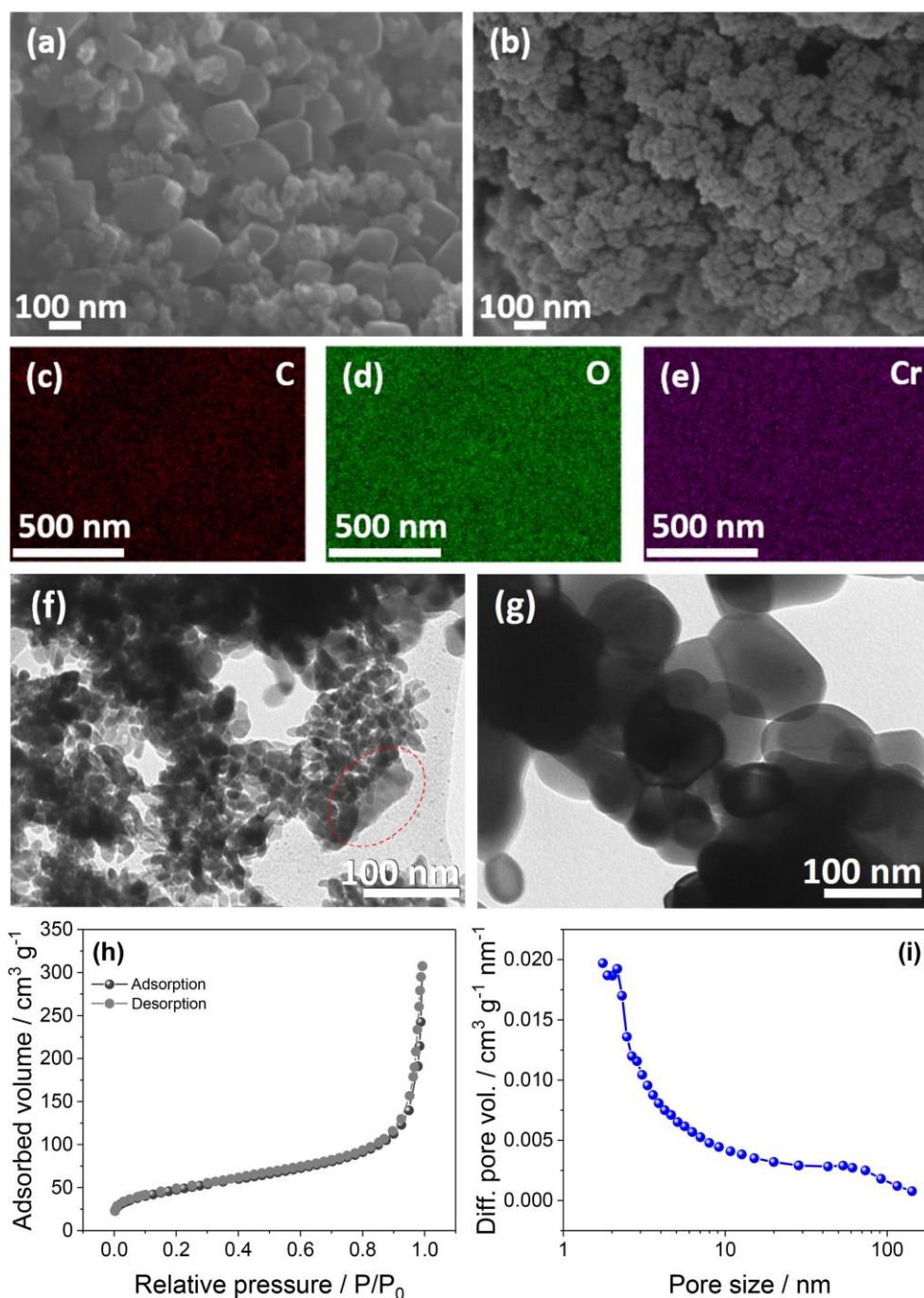
Figure 3.3.14. (a, b) SEM images of MIL-101 (Cr) MOF **(a)** before and **(b)** after heat treatment, and **(c–e)** EDS elemental maps of Cr_2O_3@C composite. **(f, g)** TEM images of the Cr_2O_3@C powder; red circle in panel **(f)** highlights a carbon particle. **(h)** N_2 adsorption/ desorption isotherms and **(i)** pore size distribution obtained through BJH method of Cr_2O_3@C composite.

Furthermore, the profiles well overlap and the polarization decreases, thus suggesting an optimized electrochemical process, the reversibility of which improves by the ongoing of cycles. The electrode/electrolyte interphase evolution of the $Li|DEGDME–Li_2S_8–1m$ $LiNO_3–1m$ $LiTFSI|Cr_2O_3$@C cell upon voltammetry is detected by EIS upon cycling (Fig. 3.3.15b), and the

recorded spectra are analyzed by NLLS fitting.[12,13] The Nyquist plot of the cell in its pristine condition at the OCV can be represented by the $R_e(R_1Q_1)(R_wQ_w)$ equivalent circuit consisting of an electrolyte resistance (R_e) at high frequency values, a well-defined semicircle in the medium-high frequency region accounting for both the SEI film formed at the electrodes surface and for the charge-transfer process (R_1Q_1), and a low-frequency depressed profile accounting for the lithium ion finite-length Warburg diffusion at the electrode/electrolyte interphase (R_wQ_w).[107] After subsequent CV cycles the Nyquist plot shrinks, the impedance remarkably decreases while the profile modifies, particularly in the low-frequency region, being now represented by the new equivalent circuit $R_e(R_1Q_1)Q_w$.[129] Hence, the depressed profile observed at the OCV at low-frequency modifies after CV cycles to form a tilted line associated with a semi-infinite Warburg element (Q_w).[129] These changes are likely ascribed to the electrochemical activation of the electrode/electrolyte interphase upon the first cycle, and by the ongoing of the redox process which progressively promotes the reversible formation of sulfur and the various polysulfides at the Cr_2O_3@C surface, as indeed observed for this catholyte using a SPC electrode. Accordingly, the electrode/electrolyte interphase resistance obtained from the semicircle width drops from about 60 Ω at the OCV to values as low as 4.7 Ω after 10 cycles (see Table 3.3.2), which is in line with the CV profiles that suggest progressive improvement of the reactions kinetics by cycling.

Cell condition	Circuit	R_1 [Ω]	χ^2
OCV	$R_e(R_1Q_1)(R_wQ_w)$	60 ± 2	2.7×10^{-4}
1 CV cycle	$R_e(R_1Q_1)$	10 ± 0.2	4.0×10^{-4}
5 CV cycles	$R_e(R_1Q_1)Q_w$	3.5 ± 0.1	1.5×10^{-4}
10 CV cycles	$R_e(R_1Q_1)Q_w$	4.7 ± 0.1	5.9×10^{-5}

Table 3.3.2. NLLS analyses performed on the Nyquist plots reported in Figure 3.3.15b. The impedance spectra were recorded by EIS upon CV, carried out on a Li|DEGDME-Li_2S_8-1m $LiNO_3$-1m LiTFSI|Cr_2O_3@C cell.

A further important characteristic of the electrode/electrolyte interphase is represented by the lithium-ion diffusion coefficient D, which may be obtained from CV measurements performed at increasing scan rates (Fig. 3.3.15c, top) and calculated at various states of charge (Fig. 3.3.15c bottom) using the Randles-Sevcik equation:[130,131]

$$I_p = 0.4463zFAC \left(\frac{zFvD}{RT}\right)^{1/2} \qquad (3.3.2)$$

where I_p is the peak current (A), z is the number of electrons transferred during the reaction, A is the electrode geometric area (cm^2), v the scanning rate (mV s^{-1}), and C the concentration of lithium ions in the catholyte (mol cm^{-3}).
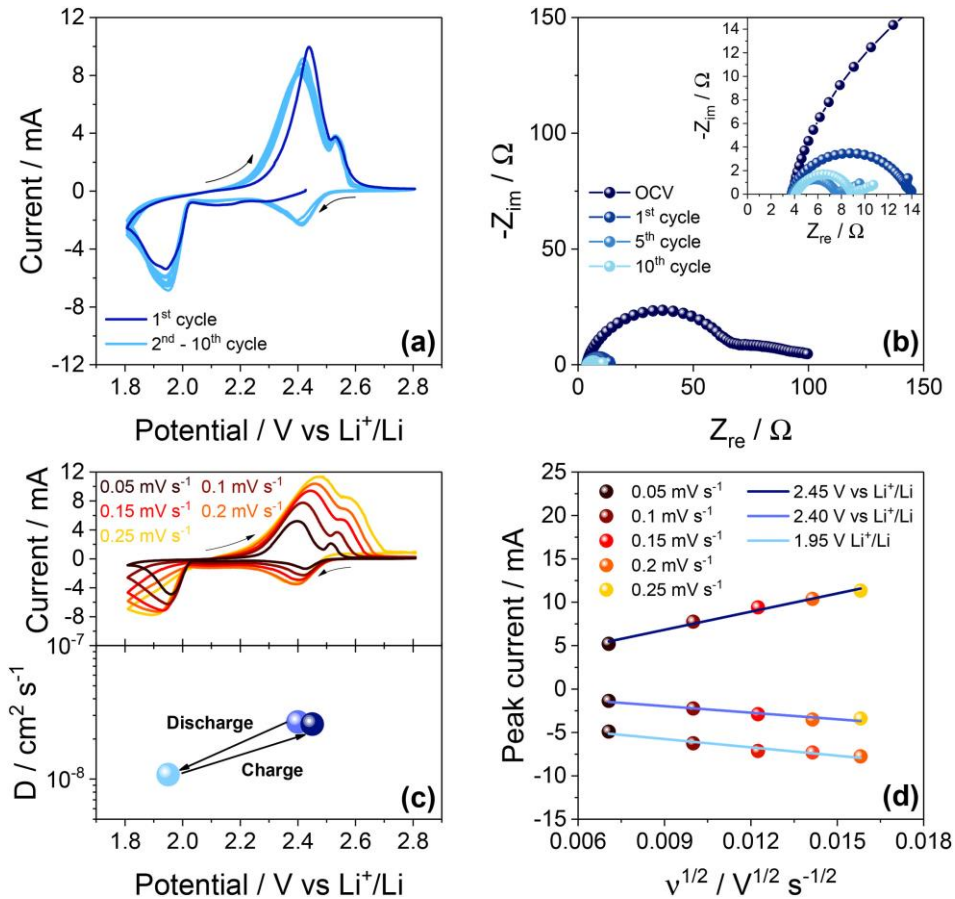
Figure 3.3.15. (a) CV measurement performed on a Li|DEGDME-Li$_2$S$_8$-1m LiNO$_3$-1m LiTFSI|Cr$_2$O$_3$@C cell at the constant scan rate of 0.1 mV s^{-1} and **(b)** Nyquist plots recorded by EIS at the OCV of the cell and after 1, 5 and 10 cycles (inset shows magnification). CV potential range: 1.8 – 2.8 V *vs* Li$^+$/Li; EIS frequency range: 500 kHz – 100 mHz; signal amplitude: 10 mV. **(c)** CV measurement performed on a Li|DEGDME-Li$_2$S$_8$-1m LiNO$_3$-1m LiTFSI|Cr$_2$O$_3$@C cell at various scan rates, that is, 0.05, 0.1, 0.15, 0.2 and 0.25 mV s^{-1} (top panel) and corresponding lithium diffusion coefficients (*D*) calculated through Randles-Sevcik equation (3.3.2) (bottom panel).[130,131] **(d)** Linear fitting of the peak currents obtained from the voltammograms reported in panel **(c)**. CV potential range: 1.8 – 2.8 V *vs* Li$^+$/Li.

According to equation (3.3.2), *D* may be determined by the slope of the linear plot of I_p *vs* $v^{1/2}$ during both cathodic and anodic scans (Fig. 3.3.15d). Two peaks, at about 2.4 and 2 V, are considered for *D* calculation during the cathodic scan (*z* = 1 for each peak), while only the major peak above 2.4 V is

taken into account during anodic scan ($z = 2$), since the subsequent minor peak can generally merge into the latter making problematic the evaluation.[74] Therefore, the values of D determined taking into account the above mentioned peaks are of 2.7×10^{-8}, 1.1×10^{-8}, and 2.6×10^{-8} cm^2 s^{-1}, respectively. These values are comparable with exceed the ones previously observed for the Li-S cell,[74] most likely due to the nature of the cell involving an enhanced carbon/metal oxide substrate and a catholyte instead of a solid electrode.

Galvanostatic discharge–charge experiments were carried out to evaluate the performance of the Cr_2O_3@C composite in the semi-liquid Li-S cell using the DEGDME–Li_2S_8–1m LiNO$_3$–1m LiTFSI catholyte at a current density of C/5 (1C = 1675 mA g^{-1}) and at various C-rates (Fig. 3.3.16). The voltage profiles of the cell at C/5 rate (Fig. 3.3.16a) show upon the first activation cycle (see discussion of CV in Fig. 3.3.15a) the two discharge plateaus at about 2.4 and 2 V, corresponding to the reversible reaction of sulfur to form long and short chain polysulfides, respectively, which are reversed during charge into two plateaus at about 2.3 and 2.5 V, in line with the CV curves. Furthermore, Figure 3.3.16a indicates that the cell at the steady state can deliver reversibly and with relatively low polarization a specific capacity exceeding 800 mAh g$_S^{-1}$. Insights on the cell performances at various currents is given by the cycling profiles of Fig. 3.3.16b which displays a steady state capacity approaching 900 mAh g$_S^{-1}$ at C/10 and C/8, exceeding 800 mAh g$_S^{-1}$ at C/5, and slightly below 800 mAh g$_S^{-1}$ at C/3 rate. The decrease of the capacity by increasing the C-rate may be ascribed to the increase of the cell polarization by raising currents. Therefore, it can be assumed that the Cr_2O_3@C composite enables efficient reaction of the semi-liquid lithium sulfur cell and a suitable polysulfides reversible conversion from C/10 to C/3 rate, with capacity ranging from 900 to 800 mAh g$_S^{-1}$, that is, a moderate range of operation in line with the data previously observed for the SPC electrode and similar cell configurations.[132] Remarkably, the cell cycled at C/5 holds almost its steady state capacity of about 800 mAh g$_S^{-1}$ with only limited signs of decay for 100 charge/discharge cycles, and retains a Coulombic efficiency approaching 100% over the whole cycling test (Fig. 3.3.16c).

The structural and morphological retention of the Cr_2O_3@C electrode is investigated in Figure 3.3.17 by *ex-situ* SEM/EDS and XRD analyses performed before and after cycling at C/5 rate. The SEM of the pristine electrode (Fig. 3.3.17a) shows that the heterogeneous morphology of the material remains almost unchanged upon cycling (Fig. 3.3.17b), while the brightness of the image intensifies as most likely due to the insulating character of traces of sulfur crystallized on the surface during the electrochemical process.
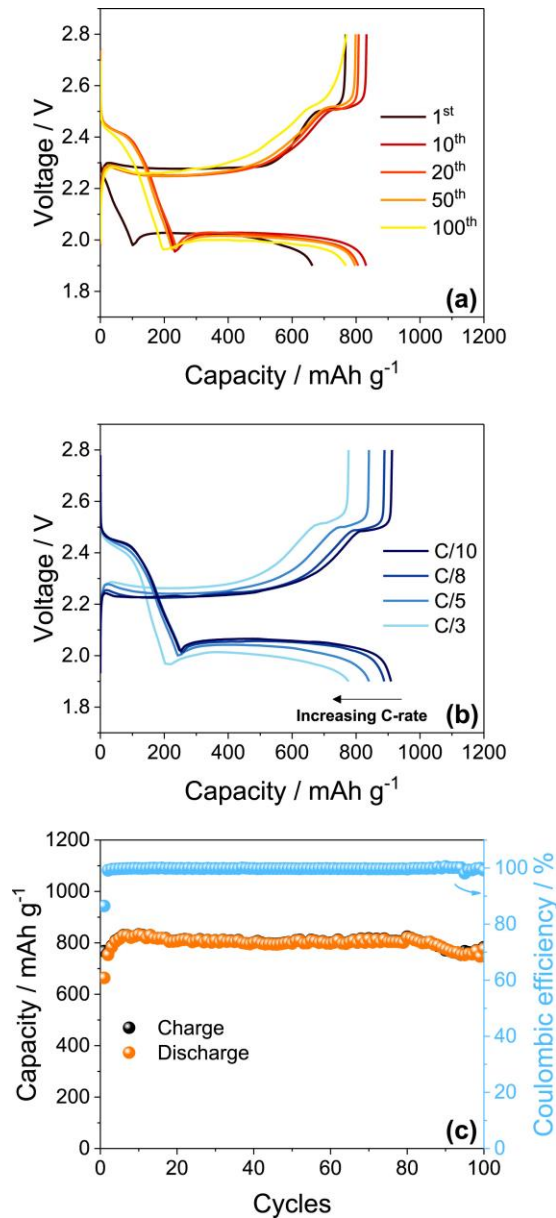
Figure 3.3.16. (a, b) Selected voltage profiles of the galvanostatic cycling measurement performed on a Li|DEGDME–Li$_2$S$_8$–1m LiNO$_3$–1m LiTFSI|Cr$_2$O$_3$@C cell **(a)** at the constant C-rate of C/5 (panel **(c)** shows the corresponding cycling trend and Coulombic efficiency) and **(b)** at increasing C-rates, that is, C/10, C/8, C/5 and C/3 (1C = 1675 mA g$_s^{-1}$). Voltage range: 1.9 – 2.8 V.

This speculation is fully supported by the EDS elemental map reported in inset in Figure 3.3.17b, which shows sulfur atoms uniformly distributed on the electrode surface after cycling. Furthermore, the structural stability of the material upon cycling is highlighted by the XRD patterns of Figure 3.3.17c which evidence the retention of the α-Cr$_2$O$_3$ phase upon operating in Li-S cell, and the absence of undesired by-products formation, thus suggesting the inert nature of the Cr$_2$O$_3$@C composite. Therefore, these remarkable features, as well as the promising electrochemical performances, suggest

the Cr_2O_3@C composite as a suitable electrode material for application in alternative Li-S cell configuration, such as the semi-liquid one investigated in this section.
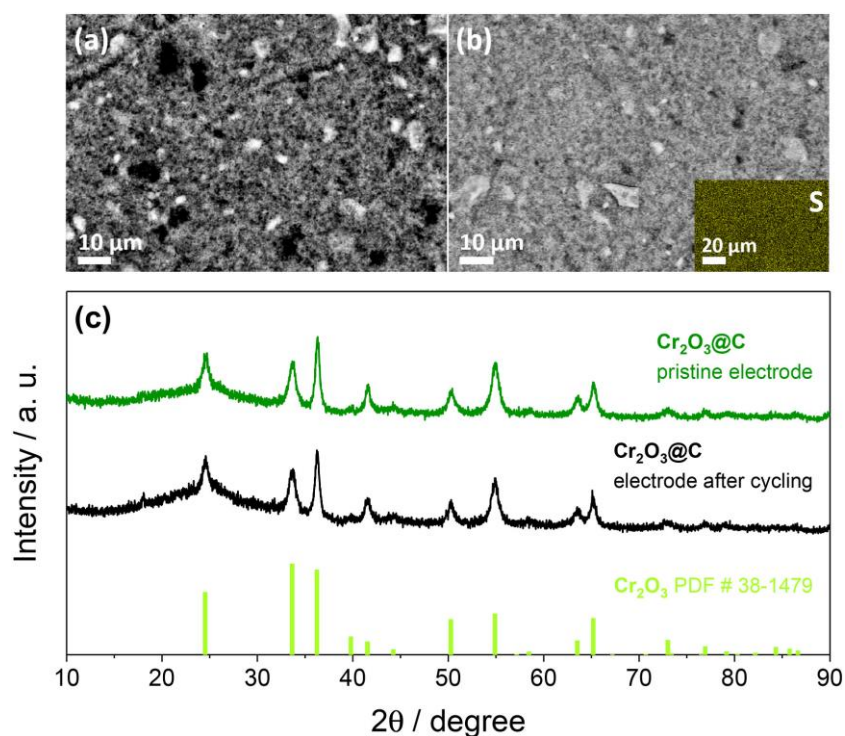
Figure 3.3.17. (a, b) SEM images of the Cr_2O_3@C electrode **(a)** at the pristine state and **(b)** after 7 cycles at C/5 in a cell exploiting the Li|DEGDME–Li_2S_8–1m $LiNO_3$–1m LiTFSI|Cr_2O_3@C configuration. Voltage range: 1.9 – 2.8 V. Inset in panel **(b)** displays the corresponding EDS elemental map for sulfur. **(c)** XRD patterns of the Cr_2O_3@C electrode at the pristine state (dark green) and after the galvanostatic cycling test (black); reference data of Cr_2O_3 (light green, PDF # 38-1479) are also reported for comparison.

3.4 Summary

New configurations of glyme-based electrolytes have been investigated in section *3.1* for improving the performances of Li-S batteries. Relevant concentrations of the conducting salt (LiTFSI) and the sacrificial agent (LiNO$_3$) were originally dissolved and the characteristics of the SEI layer were studied in first place. The outer/inner composition of the complex SEI on lithium samples was therefore analyzed by XPS measurements upon Ar$^+$ etching. The measurement revealed the mainly inorganic nature of the inner layer of the SEI formed by fast reactions on the metal to form LiF, Li$_2$CO$_3$, LiN$_x$O$_y$, and Li$_2$O and the organic character of the outer SEI accounting for minor electrolytes reduction to ROLi and ROR species with side precipitation of LiTFSI. These features hindered further deterioration of DEGDME_HCE and TREGDME_HCE at the lithium surface and suggested possible application of the electrolytes in an efficient and stable battery. Subsequently, TGA depicted a thermal stability of DEGDME_HCE extended up to 80 °C and a higher value for TREGDME_HCE, that is, above 130 °C, because of a more relevant salt concentration and longer glyme chain of the latter compared to the former, thus suggesting TREGDME_HCE as a more suitable candidate for application in a more challenging environment. On the other hand, the electrochemical investigation revealed for DEGDME_HCE an ionic conductivity ranging from 3 × 10^{-3} to 8 × 10^{-3} S cm^{-1}, a Li$^+$ transference number of about 0.60, and a stability window extending from about 0 up to 4.3 V *vs* Li$^+$/Li, whereas TREGDME_HCE has shown lower conductivity (from 9 × 10^{-4} to 2 × 10^{-3} S cm^{-1}) and Li$^+$ transference number (about 0.5), while a higher anodic stability with an oxidation potential of 4.4 V *vs* Li$^+$/Li. Both electrolytes revealed a limited lithium/electrolyte interphase resistance and the absence of dendritic structure formation upon prolonged galvanostatic cycling, thus confirming the consolidation of a stable SEI on the metal surface. The CV tests performed on the Li-S cells revealed for both electrolytes a reversible electrochemical process centered at about 2.1 and 2.4 V and an activation process leading to the decrease of the impedance from values of the order of 100 Ω to about 10 Ω upon cycling. Furthermore, galvanostatic measurements of the Li-S cells carried out using the constant current rate of C/5 at 25 and 35 °C indicated for DEGDME_HCE capacities of about 800 and 1300 mAh g$_S^{-1}$, respectively, while lower values of about 340 and 890 mAh g$_S^{-1}$ were obtained for TREGDME_HCE. The more relevant performances of the Li/S cells using DEGDME_HCE compared to TREGDME_HCE are in line with a faster charge transfer kinetics in the former electrolyte compared to the latter. Furthermore, the Li-S cell employing the DEGDME_HCE operating with the most adequate conditions have shown satisfactory performances at current rate increased to 1C, delivering 750 mAh g$_S^{-1}$ with capacity retention of 70% over 140 cycles at 35 °C.

Section *3.2* reports the investigation of a solid composite polymer electrolyte including a crystalline PEGDME substrate (PEGDME2000), LiTFSI, LiNO$_3$ and SiO$_2$, characterized at the same time by the versatility of linear EO-polymer and by a high conductivity at moderate temperature, with the additional bonuses of the relevant electrode/electrolyte interphase stability and the long cycling performance in lithium-metal battery. The electrolyte, indicated as PEGDME_CPE, revealed a complex structure and smooth surface with uniform distribution of the elements, as suggested by XRD and SEM-EDS measurements. Moreover, the electrolyte revealed an ionic conductivity higher than 10^{-4} S cm^{-1} above 45 °C, with a maximum value of about 4×10^{-4} S cm^{-1}, according to a trend suggesting a gradual change from Arrhenius-type to the VTF-type, promoted by subsequent cooling and heating cycles from about 70 °C to the room temperature. The above change relevantly increased the room temperature conductivity of the membrane by a factor of 10, *i.e.*, from about 4×10^{-6} S cm^{-1} to about 4×10^{-5} S cm^{-1}. TGA evidenced a thermal stability extended up to 300 °C, suggesting suitable characteristics for applications requiring high safety level. Study of the PEGDME_CPE in symmetrical Li/Li cell at various temperatures, ranging from 45 °C to about 70 °C, showed Li$^+$ transference number ranging from 0.22 at the lowest temperature to about 0.27 at the highest one, polarization always lower than 150 mV, and the absence of lithium dendrite formation upon prolonged lithium stripping/deposition tests. The PEGDME_CPE membrane also revealed an electrochemical stability extending from 0.01 to about 4.4 V at 50 °C, which was therefore selected as the preferred operating temperature for application in lithium metal battery. Aging tests in symmetrical lithium cell at the above temperature suggested a very stable Li/PEGDME_CPE interphase, with resistance values ranging from 226 to 277 Ω. The PEGDME_CPE applicability in Li cell has been studied in a solid polymer cell employing the LiFePO$_4$ cathode and operating at 50 °C, exhibiting low and stable interphase resistance, limited polarization, suitable rate capability, a maximum specific capacity approaching 90 % of the theoretical value ascribed to the cathode, and a cycle life of 300 cycles with coulombic efficiency approaching 100 % and a capacity retention of 99 %. The application of the PEGDME_CPE in Li-S battery revealed a stable conversion process with low charge transfer resistance within the temperature range from 50 to 80 °C. In this interval, the polymer battery operated by electrochemical processes mainly centered at 2.4 and 2.0 V *vs* Li$^+$/Li during discharge and at 2.3 and 2.6 V *vs* Li$^+$/Li during charge, as revealed by CV, although above 60 °C enhanced conversion kinetics were observed, leading to better overlapping of the potential profiles and more intense current signals. This promising cell response was attributed to the suitably low resistance of both electrode/electrolyte interphase (between 83 and 12 Ω) and electrolyte (between 304 and 55 Ω), which was measured by EIS in the 50 – 80 °C range. Furthermore, increase in temperature gave rise to a third discharge step at 2.3 V *vs.* Li+/Li along with a gradual shift of the

charge peaks up to formation of a broad double-signal similar to that observed in Li-S cells using a conventional liquid electrolyte. Indeed, the polymer system revealed a profile change from *solid-like* to *liquid-like* Li-S battery upon increasing the temperature from 50 °C to 80 °C. Accordingly, the data have provided evidence of lithium polysulfide dissolution into the electrolyte upon cell operation, which influenced the thermal and morphological characteristics of the cathode/electrolyte membrane array. The Li-S polymer battery operated at 50 °C with a working voltage of 2.2 V, delivering a capacity above 600 mAh g_S^{-1} at C/10 with a retention of 71 % for more than 90 discharge/charge cycles and a maximum coulombic efficiency of 98 %.

Catholyte-type Li-S batteries based on a dissolved polysulfide active material were investigated in section *3.3*. Li_2S_8 was chemically synthetized in DEGDME solvent and added by either LiTFSI or $LiCF_3SO_3$ salt, as well as by $LiNO_3$ film forming additive, leading to nominal polysulfide concentration of 5wt%. XPS revealed the chemical bonds characteristics of the catholyte species, and suggested Li_2S_8 as the main polysulfide component, along with possible minor amount of Li_2S_6 and Li_2S_4. The solutions were stable up to evaporation, which started at about 70–80 °C, as suggested by TGA. The electrochemical characterization, performed through electrochemical impedance spectroscopy, chronoamperometry, voltammetry and galvanostatic cycling, evidenced high conductivity, fast Li^+ transport, suitable lithium passivation properties, wide electrochemical stability window, and low cell polarization. Relevantly, the catholyte using LiTFSI revealed a higher conductivity while lower lithium transference number with respect to the one using the $LiCF_3SO_3$, that is, 3×10^{-3} S cm^{-1} and 0.6 with respect to 2×10^{-3} S cm^{-1} and 0.79 at room temperature, respectively. Reversible Li-S conversion occurred at about 2.4 and 2 V upon reduction, and at about 2.4 V upon oxidation, thereby leading to flat voltage profiles centered at about 2.2 V. Hence, the Li|DEGDME–Li_2S_8–1m $LiNO_3$–1m LiTFSI|SPC cell delivered a maximum reversible capacity of about 1050 mAh g_S^{-1} at C/10, while the Li|DEGDME–Li_2S_8–1m $LiNO_3$–1m $LiCF_3SO_3$|SPC one revealed a capacity approaching 1160 mAh g_S^{-1} at the same current, and a better performance at the elevated currents (1C and 2C), as ascribed the high lithium transference number. Both cells delivered nearly 800 mAh g_S^{-1} with Coulombic efficiency above 99 % during 120 galvanostatic cycles at C/3 rate, and exhibited a maximum areal capacity approaching 4 mAh cm^{-2}. Subsequently, a Cr_2O_3@C composite has been synthesized from MIL- 101(Cr) MOF, characterized by various chemical-physical techniques and successfully employed as the electrode support for the Li-S reaction in the semi-liquid cell employing a DEGDME-Li_2S_8-1m $LiNO_3$-1m LiTFSI catholyte. The composite revealed mesoporous agglomerates with primary particle size below 100 nm, homogeneous C, O, and Cr elements distribution, a BET surface area as high as 170 m^2 g^{-1} and a pore volume of 0.5 cm^3 g^{-1}. Furthermore, the tests indicated that the composite is predominantly formed by Cr_2O_3, and carbon

with a weight ratio of about 13 % due to the preparation technique which involved calcination in a nitrogen atmosphere at 600 °C and avoided oxidizing condition. The Cr_2O_3@C material enabled the reversible Li_2S_8 conversion to short chain polysulfides and back to sulfur with efficient kinetics and potentials ranging from about 2 V to above 2.4 V *vs* Li^+/Li. This performance was attributed to an enhanced electrode/electrolyte interphase characterized by resistance values below 5 Ω upon an electrochemical activation process, and a diffusion coefficient exceeding 10^{-8} cm^2 s^{-1} at the various states of the charge. The Li-S semi-liquid cell has operated between C/10 and C/3 current rates with a specific capacity ranging from about 900 mAh g^{-1} to values slightly below 800 mAh g^{-1}. Furthermore, the battery revealed remarkable stability and a Coulombic efficiency approaching 100 % at the steady state, while *ex-situ* SEM and XRD analyses evidenced the retention of both the electrode morphology and structure upon cycling.

The data obtained in this Chapter suggest that glyme-based electrolyte solutions exploiting either high salts concentration, a solid configuration or dissolved lithium polysulfides may allow the safe and efficient cyclability of Li-S batteries. On the other hand, the systems investigated herein are intended as proof-of-concept of promising strategies which certainly need *ad hoc* optimization in view of an actual application. In particular, the concentration of lithium salts and dissolved Li_2S_x species requires dedicated investigation in order to achieve relevant Li^+ ions conductivity and, at the same time, formation of a suitble SEI on the lithium surface, while the polymer/inorganic fillers ratio needs accurate tuning to concomitantly provide a stable solid structure of the electrolyte membrane and operative temperatures near to the room one. The strategies proposed in this Chapter do not necessarily exclude each other and, in this respect, a possible combination aiming to synthetize a solid glyme-based electrolyte membrane that operates at moderate temperatures and exploits a precisely balanced content of lithium salts, inorganic fillers, SEI-forming agents and polysulfides may represent a valid approach to boost the development of practical Li-S batteries.

3.5 References

[1] W. Xu, J. Wang, F. Ding, X. Chen, E. Nasybulin, Y. Zhang, J. G. Zhang, *Energy Environ. Sci.* **2014**, *7*, 513.

[2] J. B. Goodenough, Y. Kim, *Chem. Mater.* **2010**, *22*, 587.

[3] S. S. Zhang, *Electrochim. Acta* **2012**, *70*, 344.

[4] A. Jozwiuk, B. B. Berkes, T. Weiß, H. Sommer, J. Janek, T. Brezesinski, *Energy Environ. Sci.* **2016**, *9*, 2603.

[5] S. Tobishima, H. Morimoto, M. Aoki, Y. Saito, T. Inose, T. Fukumoto, T. Kuryu, *Electrochim. Acta* **2004**, *49*, 979.

[6] X. Liu, M. Zarrabeitia, B. Qin, G. A. Elia, S. Passerini, *ACS Appl. Mater. Interfaces* **2020**, *12*, 54782.

[7] L. Carbone, M. Gobet, J. Peng, M. Devany, B. Scrosati, S. Greenbaum, J. Hassoun, *ACS Appl. Mater. Interfaces* **2015**, *7*, 13859.

[8] J.-D. Xie, W.-J. Liu, C. Li, J. Patra, Y. A. Gandomi, Q.-F. Dong, J.-K. Chang, *Electrochim. Acta* **2019**, *319*, 625.

[9] B. D. Adams, E. V. Carino, J. G. Connell, K. S. Han, R. Cao, J. Chen, J. Zheng, Q. Li, K. T. Mueller, W. A. Henderson, J.-G. Zhang, *Nano Energy* **2017**, *40*, 607.

[10] Y. Yamada, A. Yamada, *J. Electrochem. Soc.* **2015**, *162*, A2406.

[11] J. Evans, C. A. Vincent, P. G. Bruce, *Polymer (Guildf).* **1987**, *28*, 2324.

[12] B. A. Boukamp, *Solid State Ionics* **1986**, *20*, 31.

[13] B. A. Boukamp, *Solid State Ionics* **1986**, *18–19*, 136.

[14] D. Aurbach, *J. Power Sources* **2000**, *89*, 206.

[15] Q. Liu, A. Cresce, M. Schroeder, K. Xu, D. Mu, B. Wu, L. Shi, F. Wu, *Energy Storage Mater.* **2019**, *17*, 366.

[16] M. Winter, *Zeitschrift für Phys. Chemie* **2009**, *223*, 1395.

[17] A. Rosenman, R. Elazari, G. Salitra, E. Markevich, D. Aurbach, A. Garsuch, *J. Electrochem. Soc.* **2015**, *162*, A470.

[18] R. Dedryvère, S. Leroy, H. Martinez, F. Blanchard, D. Lemordant, D. Gonbeau, *J. Phys. Chem. B* **2006**, *110*, 12986.

[19] S. Xiong, K. Xie, Y. Diao, X. Hong, *Electrochim. Acta* **2012**, *83*, 78.

[20] K. Kanamura, H. Tamura, S. Shiraishi, Z.-I. Takehara, *Electrochim. Acta* **1995**, *40*, 913.

[21] Ó. Vargas, Á. Caballero, J. Morales, E. Rodríguez-Castellón, *ACS Appl. Mater. Interfaces* **2014**, *6*, 3290.

[22] G. M. Veith, J. Nanda, L. H. Delmau, N. J. Dudney, *J. Phys. Chem. Lett.* **2012**, *3*, 1242.

[23] D. Ensling, M. Stjerndahl, A. Nytén, T. Gustafsson, J. O. Thomas, *J. Mater. Chem.* **2009**, *19*, 82.

[24] M. Agostini, S. Xiong, A. Matic, J. Hassoun, *Chem. Mater.* **2015**, *27*, 4604.

[25] M. Tułodziecki, J.-M. Tarascon, P.-L. Taberna, C. Guéry, *Electrochem. commun.* **2017**, *77*, 128.

[26] D. Aurbach, I. Weissman, A. Schechter, H. Cohen, *Langmuir* **1996**, *12*, 3991.

[27] A. Schechter, D. Aurbach, H. Cohen, *Langmuir* **1999**, *15*, 3334.

[28] K. P. C. Yao, D. G. Kwabi, R. A. Quinlan, A. N. Mansour, A. Grimaud, Y.-L. Lee, Y.-C. Lu, Y. Shao-Horn, *J. Electrochem. Soc.* **2013**, *160*, A824.

[29] G. A. Elia, R. Bernhard, J. Hassoun, *RSC Adv.* **2015**, *5*, 21360.

[30] K. Shimizu, A. A. Freitas, R. Atkin, G. G. Warr, P. A. FitzGerald, H. Doi, S. Saito, K. Ueno, Y. Umebayashi, M. Watanabe, J. N. Canongia Lopes, *Phys. Chem. Chem. Phys.* **2015**, *17*, 22321.

[31] K. Ueno, K. Yoshida, M. Tsuchiya, N. Tachikawa, K. Dokko, M. Watanabe, *J. Phys. Chem. B* **2012**, *116*, 11323.

[32] S. Wei, Z. Li, K. Kimura, S. Inoue, L. Pandini, D. Di Lecce, Y. Tominaga, J. Hassoun, *Electrochim. Acta* **2019**, *306*, 85.

[33] S. Phadke, E. Coadou, M. Anouti, *J. Phys. Chem. Lett.* **2017**, *8*, 5907.

[34] M. Winter, J. O. Besenhard, M. E. Spahr, P. Novák, *Adv. Mater.* **1998**, *10*, 725.

[35] S. Waluś, C. Barchasz, R. Bouchet, J.-C. Leprêtre, J.-F. Colin, J.-F. Martin, E. Elkaïm, C. Baehtz, F. Alloin, *Adv. Energy Mater.* **2015**, *5*, 1500165.

[36] C. F. Riadigos, R. Iglesias, M. A. Rivas, T. P. Iglesias, *J. Chem. Thermodyn.* **2011**, *43*, 275.

[37] C. Barchasz, F. Molton, C. Duboc, J.-C. Leprêtre, S. Patoux, F. Alloin, *Anal. Chem.* **2012**, *84*, 3973.

[38] K. Yoshida, M. Tsuchiya, N. Tachikawa, K. Dokko, M. Watanabe, *J. Phys. Chem. C* **2011**, *115*, 18384.

[39] F. Croce, G. B. Appetecchi, L. Persi, B. Scrosati, *Nature* **1998**, *394*, 456.

[40] W. Lyu, G. He, T. Liu, *ChemistryOpen* **2020**, *9*, 713.

[41] D. Lin, W. Liu, Y. Liu, H. R. Lee, P. C. Hsu, K. Liu, Y. Cui, *Nano Lett.* **2016**, *16*, 459.

[42] R. Lei, Y. Yang, C. Yu, Y. Xu, Y. Li, J. Li, *Sustain. Energy Fuels* **2021**, *5*, 1538.

[43] L. Zhong, S. Wang, M. Xiao, W. Liu, D. Han, Z. Li, J. Qin, Y. Li, S. Zhang, S. Huang, Y. Meng, *Energy Storage Mater.* **2021**, *41*, 563.

[44] X. Zhang, T. Zhang, Y. Shao, H. Cao, Z. Liu, S. Wang, X. Zhang, *ACS Sustain. Chem. Eng.*

2021, *9*, 5396.

[45] I. Gracia, H. Ben Youcef, X. Judez, U. Oteo, H. Zhang, C. Li, L. M. Rodriguez-Martinez, M. Armand, *J. Power Sources* **2018**, *390*, 148.

[46] J. Wang, Y. Wang, X. Zhu, X. Lu, *J. Phys. Chem. Lett.* **2013**, *4*, 1718.

[47] W. Li, H. Yao, K. Yan, G. Zheng, Z. Liang, Y.-M. Chiang, Y. Cui, *Nat. Commun.* **2015**, *6*, 7436.

[48] X.-L. Wang, A. Mei, X.-L. Li, Y.-H. Lin, C.-W. Nan, *J. Power Sources* **2007**, *171*, 913.

[49] S. Brutti, J. Hassoun, B. Scrosati, C.-Y. Lin, H. Wu, H.-W. Hsieh, *J. Power Sources* **2012**, *217*, 72.

[50] D. Di Girolamo, S. Panero, M. A. Navarra, J. Hassoun, *J. Electrochem. Soc.* **2016**, *163*, A1175.

[51] F. Croce, R. Curini, A. Martinelli, L. Persi, F. Ronci, B. Scrosati, R. Caminiti, *J. Phys. Chem. B* **1999**, *103*, 10632.

[52] S. Lascaud, M. Perrier, A. Vallée, S. Besner, J. Prud'homme, M. Armand, *Macromolecules* **1994**, *27*, 7469.

[53] G. . Appetecchi, F. Croce, J. Hassoun, B. Scrosati, M. Salomon, F. Cassel, *J. Power Sources* **2003**, *114*, 105.

[54] A. Manuel Stephan, K. S. Nahm, *Polymer (Guildf).* **2006**, *47*, 5952.

[55] E. Staunton, Y. G. Andreev, P. G. Bruce, *Faraday Discuss.* **2007**, *134*, 143.

[56] B. W. Zewde, S. Admassie, J. Zimmermann, C. S. Isfort, B. Scrosati, J. Hassoun, *ChemSusChem* **2013**, *6*, 1400.

[57] R. Frech, S. Chintapalli, P. G. Bruce, C. a Vincent, *Macromolecules* **1999**, *32*, 808.

[58] A. E. Visser, N. J. Bridges, R. D. Rogers, Eds. , *Ionic Liquids: Science and Applications*, American Chemical Society, Washington, DC, **2012**.

[59] D. Devaux, R. Bouchet, D. Glé, R. Denoyel, *Solid State Ionics* **2012**, *227*, 119.

[60] J. XIE, *Solid State Ionics* **2004**, *175*, 755.

[61] R. Frech, W. Huang, *Macromolecules* **1995**, *28*, 1246.

[62] M. M. Hiller, M. Joost, H. J. Gores, S. Passerini, H. D. Wiemhöfer, *Electrochim. Acta* **2013**, *114*, 21.

[63] J. Mindemark, B. Sun, E. Törmä, D. Brandell, *J. Power Sources* **2015**, *298*, 166.

[64] B. Scrosati, J. Garche, *J. Power Sources* **2010**, *195*, 2419.

[65] L. Carbone, M. Gobet, J. Peng, M. Devany, B. Scrosati, S. Greenbaum, J. Hassoun, *J. Power Sources* **2015**, *299*, 460.

[66] Z. Xue, D. He, X. Xie, *J. Mater. Chem. A* **2015**, *3*, 19218.

[67] G. T. Kim, G. B. Appetecchi, F. Alessandrini, S. Passerini, *J. Power Sources* **2007**, *171*, 861.

[68] F. Croce, A. D' Epifanio, J. Hassoun, A. Deptula, T. Olczac, B. Scrosati, *Electrochem. Solid-State Lett.* **2002**, *5*, A47.

[69] J.-M. Tarascon, M. Armand, *Nature* **2001**, *414*, 359.

[70] L. Gireaud, S. Grugeon, S. Laruelle, B. Yrieix, J. M. Tarascon, *Electrochem. commun.* **2006**, *8*, 1639.

[71] A. Benítez, A. Caballero, J. Morales, J. Hassoun, E. Rodríguez-Castellón, J. Canales-Vázquez, *Nano Res.* **2019**, *12*, 759.

[72] A. Varzi, K. Thanner, R. Scipioni, D. Di Lecce, J. Hassoun, S. Dörfler, H. Altheus, S. Kaskel, C. Prehal, S. A. Freunberger, *J. Power Sources* **2020**, *480*, 228803.

[73] Y. Chen, S. Lu, J. Zhou, W. Qin, X. Wu, *Adv. Funct. Mater.* **2017**, *27*, 1700987.

[74] L. Carbone, T. Coneglian, M. Gobet, S. Munoz, M. Devany, S. Greenbaum, J. Hassoun, *J. Power Sources* **2018**, *377*, 26.

[75] X. Judez, H. Zhang, C. Li, J. A. González-Marcos, Z. Zhou, M. Armand, L. M. Rodriguez-Martinez, *J. Phys. Chem. Lett.* **2017**, *8*, 1956.

[76] J. Guo, X. Du, X. Zhang, F. Zhang, J. Liu, *Adv. Mater.* **2017**, *29*, 1700273.

[77] J. Yao, T. Mei, Z. Cui, Z. Yu, K. Xu, X. Wang, *Chem. Eng. J.* **2017**, *330*, 644.

[78] D. Marmorstein, T. . Yu, K. . Striebel, F. . McLarnon, J. Hou, E. . Cairns, *J. Power Sources* **2000**, *89*, 219.

[79] F. Luna-Lama, C. Hernández-Rentero, A. Caballero, J. Morales, *Electrochim. Acta* **2018**, *292*, 522.

[80] G. B. Appetecchi, J. Hassoun, B. Scrosati, F. Croce, F. Cassel, M. Salomon, *J. Power Sources* **2003**, *124*, 246.

[81] J. Chang, J. Shang, Y. Sun, L. K. Ono, D. Wang, Z. Ma, Q. Huang, D. Chen, G. Liu, Y. Cui, Y. Qi, Z. Zheng, *Nat. Commun.* **2018**, *9*, 4480.

[82] Y. An, C. Luo, D. Yao, S. Wen, P. Zheng, S. Chi, Y. Yang, J. Chang, Y. Deng, C. Wang, *Nano-Micro Lett.* **2021**, *13*, 84.

[83] M. Rana, Q. He, B. Luo, T. Lin, L. Ran, M. Li, I. Gentle, R. Knibbe, *ACS Cent. Sci.* **2019**, *5*, 1946.

[84] S. S. Zhang, J. A. Read, *J. Power Sources* **2012**, *200*, 77.

[85] P. Chiochan, S. Kosasang, N. Ma, S. Duangdangchote, P. Suktha, M. Sawangphruk, *Carbon N. Y.* **2020**, *158*, 244.

[86] X. Pu, G. Yang, C. Yu, *Adv. Mater.* **2014**, *26*, 7456.

[87] X. Yu, Z. Bi, F. Zhao, A. Manthiram, *ACS Appl. Mater. Interfaces* **2015**, *7*, 16625.

[88]   S. Kuyuldar, D. T. Genna, C. Burda, *J. Mater. Chem. A* **2019**, *7*, 21545.

[89]   Y. Zheng, S. Zheng, H. Xue, H. Pang, *J. Mater. Chem. A* **2019**, *7*, 3469.

[90]   Q. Wu, X. Zhou, J. Xu, F. Cao, C. Li, *J. Energy Chem.* **2019**, *38*, 94.

[91]   Z. Cao, C. Zuo, *RSC Adv.* **2017**, *7*, 40243.

[92]   B. Guo, M. Chi, X.-G. Sun, S. Dai, *J. Power Sources* **2012**, *205*, 495.

[93]   M. Agostini, D. J. Lee, B. Scrosati, Y. K. Sun, J. Hassoun, *J. Power Sources* **2014**, *265*, 14.

[94]   W. Liu, J. Huang, Q. Yang, S. Wang, X. Sun, W. Zhang, J. Liu, F. Huo, *Angew. Chemie Int. Ed.* **2017**, *56*, 5512.

[95]   J. Gu, X. Yin, X. Bo, L. Guo, *ChemElectroChem* **2018**, *5*, 2893.

[96]   M. Agostini, J.-Y. Hwang, H. M. Kim, P. Bruni, S. Brutti, F. Croce, A. Matic, Y.-K. Sun, *Adv. Energy Mater.* **2018**, *8*, 1801560.

[97]   J. Mattsson, J. . Forrest, A. Krozer, U. Södervall, A. Wennerberg, L. . Torell, *Electrochim. Acta* **2000**, *45*, 1453.

[98]   D. Sharon, D. Hirsberg, M. Afri, F. Chesneau, R. Lavi, A. A. Frimer, Y.-K. Sun, D. Aurbach, *ACS Appl. Mater. Interfaces* **2015**, *7*, 16590.

[99]   J. Neubauer, E. Wood, *J. Power Sources* **2014**, *259*, 262.

[100] D. Di Lecce, C. Fasciani, B. Scrosati, J. Hassoun, *ACS Appl. Mater. Interfaces* **2015**, *7*, 21198.

[101] S. Zhang, K. Ueno, K. Dokko, M. Watanabe, *Adv. Energy Mater.* **2015**, *5*, 1500117.

[102] C. Zu, A. Manthiram, *J. Phys. Chem. Lett.* **2014**, *5*, 2522.

[103] M. S. Ding, *J. Chem. Eng. Data* **2003**, *48*, 519.

[104] A. Jarosik, S. R. Krajewski, A. Lewandowski, P. Radzimski, *J. Mol. Liq.* **2006**, *123*, 43.

[105] S. Xiong, K. Xie, Y. Diao, X. Hong, *J. Power Sources* **2013**, *236*, 181.

[106] S. Xiong, K. Xie, Y. Diao, X. Hong, *J. Power Sources* **2014**, *246*, 840.

[107] D. R. Franceschetti, J. R. Macdonald, R. P. Buck, *J. Electrochem. Soc.* **1991**, *138*, 1368.

[108] S. Drvarič Talian, J. Moškon, R. Dominko, M. Gaberšček, *ACS Appl. Mater. Interfaces* **2017**, *9*, 29760.

[109] D. J. Lee, M. Agostini, J. W. Park, Y. K. Sun, J. Hassoun, B. Scrosati, *ChemSusChem* **2013**, *6*, 2245.

[110] S.-Y. Lang, R.-J. Xiao, L. Gu, Y.-G. Guo, R. Wen, L.-J. Wan, *J. Am. Chem. Soc.* **2018**, *140*, 8147.

[111] R. Cao, J. Chen, K. S. Han, W. Xu, D. Mei, P. Bhattacharya, M. H. Engelhard, K. T. Mueller, J. Liu, J.-G. Zhang, *Adv. Funct. Mater.* **2016**, *26*, 3059.

[112] Q. Pang, X. Liang, C. Y. Kwok, L. F. Nazar, *Nat. Energy* **2016**, *1*, 16132.

[113] M. Li, J. Lu, Z. Chen, K. Amine, *Adv. Mater.* **2018**, *30*, 1800561.

[114] R. Demir-Cakan, M. Morcrette, F. Nouar, C. Davoisne, T. Devic, D. Gonbeau, R. Dominko, C. Serre, G. Férey, J.-M. Tarascon, *J. Am. Chem. Soc.* **2011**, *133*, 16154.

[115] H. M. Gobara, R. S. Mohamed, S. A. Hassan, F. H. Khalil, M. S. El-Sall, *Catal. Letters* **2016**, *146*, 1875.

[116] F. J. Soler-Piña, C. Hernández-Rentero, A. Caballero, J. Morales, E. Rodríguez-Castellón, J. Canales-Vázquez, *Nano Res.* **2020**, *13*, 86.

[117] S. Liu, F. Xu, L.-T. Liu, Y.-L. Zhou, W. Zhao, *J. Therm. Anal. Calorim.* **2017**, *129*, 509.

[118] M.-L. Chen, S.-Y. Zhou, Z. Xu, L. Ding, Y.-H. Cheng, *Molecules* **2019**, *24*, 3718.

[119] D. Briggs, *Surf. Interface Anal.* **1981**, *3*, v.

[120] J.-C. Dupin, D. Gonbeau, P. Vinatier, A. Levasseur, *Phys. Chem. Chem. Phys.* **2000**, *2*, 1319.

[121] J. R. Hoenigman, R. G. Keil, *Appl. Surf. Sci.* **1984**, *18*, 207.

[122] Z. Wang, M. Li, Y. Ye, Y. Yang, Y. Lu, X. Ma, Z. Zhang, S. Xiang, *J. Solid State Electrochem.* **2019**, *23*, 81.

[123] A. Farisabadi, M. Moradi, S. Hajati, M. A. Kiani, J. P. Espinos, *Appl. Surf. Sci.* **2019**, *469*, 192.

[124] X. Tao, J. Wan, C. Liu, H. Wang, H. Yao, G. Zheng, Z. W. Seh, Q. Cai, W. Li, G. Zhou, C. Zu, Y. Cui, *Nat. Commun.* **2016**, *7*, 11203.

[125] X. Tao, J. Wang, Z. Ying, Q. Cai, G. Zheng, Y. Gan, H. Huang, Y. Xia, C. Liang, W. Zhang, Y. Cui, *Nano Lett.* **2014**, *14*, 5288.

[126] X. Liu, J.-Q. Huang, Q. Zhang, L. Mai, *Adv. Mater.* **2017**, *29*, 1601759.

[127] X. Liang, C. Hart, Q. Pang, A. Garsuch, T. Weiss, L. F. Nazar, *Nat. Commun.* **2015**, *6*, 5682.

[128] Y. Guan, X. Liu, N. Akhtar, A. Wang, W. Wang, H. Zhang, J. Suntivich, Y. Huang, *J. Electrochem. Soc.* **2019**, *166*, A1671.

[129] T. Q. Nguyen, C. Breitkopf, *J. Electrochem. Soc.* **2018**, *165*, E826.

[130] J. E. B. Randles, *Trans. Faraday Soc.* **1948**, *44*, 327.

[131] A. Ševčík, *Collect. Czechoslov. Chem. Commun.* **1948**, *13*, 349.

[132] S. Kim, H. Song, Y. Jeong, *Carbon N. Y.* **2017**, *113*, 371.

Chapter 4.

Alternative and sustainable electrode materials

4.1 Biomass-derived carbon frames

4.1.1 Presentation

The insulant character of sulfur is a well-known issue affecting the kinetics of sulfur-based rechargeable batteries,[1] and the intensive work to allow suitable cycling of these devices led to the optimization of carbon materials with various structures which greatly enhance the conductivity of sulfur cathodes and provide efficient lithium polysulfides retention thank to their porous structure and polar functional groups.[2–7] On the other hand, an important point has been recently represented by the sustainability of the new energy storage devices, which focused the attention on the necessity of eco-friendly materials.[8,9] In this respect, outstanding studies have demonstrated that carbon-based electrodes obtained from the recycle of bio-waste products may represent a suitable alternative to enable sustainable and, at the same time, high-performance energy storage devices.[10–12] Following this trend, Li-S batteries relying on cathode materials derived from various sustainable carbon sources have been proposed as possible alternatives.[13] Nonetheless, despite the recent notable improvements of the Li-S technology[14] the use of a lithium metal anode may still represent a potential safety issue. Thus, the application of the Li-ion concept through the replacement of the metallic lithium with a stable and non-reactive anode based on Li-alloys with Sn,[15] Si[16] or their oxides[17–19] exploiting the nanostructured morphology may actually represent an attractive compromise to safely exploit the multi-electron Li-S conversion process.[20–22] This section explores the concept of a full lithium-ion-sulfur battery based on sustainable materials, that is, a biomass-derived sulfur-carbon cathode and a pre-lithiated silicon oxide-based anode characterized by suitable cell performances. The carbon frame exploited by the sulfur cathode is obtained from the ligno-cellulosic waste of cherry pits, which is considered a viable raw material since produced by a relevant amount.[23] This carbon substrate is selected between samples activated by using either H_3PO_4 acid or KOH, as well as and thermal steps to remove organic fractions and promoting carbon porosity as well as surface characteristics suitable for application in battery.[24–28] The applicability of the carbon materials for electrochemical purposes is firstly evaluated by employing it in lithium metal cell and full lithium-ion battery combined with a LiFePO$_4$ cathode. Afterwards, the H_3PO_4-activated carbon is considered a viable precursor to

synthetize the sulfur composite which, after thorough investigation, is applied in the above mentioned eco-friendly lithium-ion-sulfur cell.

4.1.2 Experimental

The two samples studied in this work were derived from biomass residues of cherry pits (CP), supplied by Asociación de Cooperativas del Valle del Jerte (Cáceres province, Spain). After being dried, and ground, the biomass residues of cherry pits (*i.e.*, a sample still not suitable for battery testing due to the organic residue) were sized and the fraction of particle between 1 and 2 mm was chosen. 50 g of residues were immersed in 250 mL of diluted H_2SO_4 solution (5 vol%) for 24 h, filtered, and washed with distilled water until pH reached a value of 6 in the residual liquid. The resulting powder (CP) was processed with two different activation agents, that is, potassium hydroxide (KOH)[29] (sample AC-K), and phosphoric acid (H_3PO_4)[30] (sample AC-H). 25 g of powder were dispersed in distilled water, and added by the specific amount of either H_3PO_4 (44 g, 85wt% in H_2O, 99.99 %, Sigma-Aldrich) or KOH (ACS reagent, ≥85 %, pellets, Sigma-Aldrich). Subsequently, the samples were dried for 24 h at 100 °C, annealed for 2 h at 800 °C under N_2 atmosphere with a flow of 100 mL/min and heating rate of 10 °C/min, washed with diluted HCl, with distilled water until a pH value above 6, and finally dried in oven at 120 °C overnight. The $LiFePO_4$ was purchased by Advanced Lithium Electrochemistry (Aleees Taiwan) and is characterized by a carbon content of about 5 % in weight.

The elemental chemical analysis of activated carbons was carried out using a LECO CHNS-932 micro-analyser coupled with a VTF900 furnace for oxygen. The system enables the analysis of carbon, hydrogen, nitrogen, and sulfur separately from oxygen.

The structural properties were examined using XRD, Raman and FT-IR spectroscopy. The XRD patterns were obtained with a Bruker D8 Discover X-ray diffractometer, using Cu-Kα radiation, and a Ge monochromator within a range of 2 – 80° (2θ) using a step size of 0.04° and 1.05 s per step.

Raman measurements were performed under ambient conditions through a Renishaw inVia Microscope equipped with a Renishaw CCD Camera (578 × 400) detector, and a 532 nm edge in line focus mode laser.

The FT-IR spectra were recorded in a Perkin-Elmer 1720 FT-IR spectrometer in the 4000 – 400 cm^{-1} wavenumber range, 40 scans being taken at 2 cm^{-1} resolution. Pellets were prepared by mixing powdered sample, and KBr (Merck, for spectroscopy) at a sample/KBr weight ratio of 1:500. Each mixture was compacted at 10 tons cm^{-1} for 3 min, using a Perkin-Elmer hydraulic press.

The textural properties were examined by nitrogen, and mercury porosimetry. Autosorb-1 semiautomatic apparatus (Quantachrome) using nitrogen as an adsorbent was used to obtain the micropore volume (V_{mi}), by applying the Dubinin–Radushkevich equation.[31] The pore size distribution of the carbons in the micropore and narrow mesopore ranges was obtained by applying the density functional theory (DFT) method. Macropore, and mesopore volumes were determined by a mercury porosimeter Autoscan-60 (Quantachrome). From the plots of cumulative pore volume (V_{cu}) versus pore radius (r), macropore volume, $V_{ma} = V_{cu}$ (at r = 250 Å), and mesopore volume, $V_{me} = V_{cu}$ (at r < 20 Å) – V_{ma}, of the samples were obtained. Finally, the total pore volume (VT) was estimated by using of the equation $V_T = V_{mi} + V_{me} + V_{ma}$.

Thermogravimetric analyses (TGA) were performed by using a Mettler Toledo TGA/DSC-1 at a heating rate of 10 °C min^{-1} from 30 to 800 °C, under either oxygen or nitrogen atmosphere. Before the measurements, the carbon samples were dried overnight at 120 °C to remove traces of moisture.

Samples morphology was studied by transmission electron microscopy (TEM), using a Zeiss EM 910 microscope equipped with a tungsten thermoionic electron gun operating at 100 kV, and scanning electron microscopy (SEM), using a Zeiss EVO 40 microscope equipped with a LaB$_6$ thermoionic electron gun. Energy-dispersive X-ray spectroscopy (EDS) was recorded on the SEM images through a X-ACT Cambridge Instruments analyzer to study the element distribution.

The electrodes were prepared by mixing the active material, either carbons or LiFePO$_4$, with carbon super P (Timcal, conducting agent) and polyvinylidene fluoride (Solef ® 6020 PVDF, binder) in a weight proportion of 80:10:10, and adding *N*-methyl-2-pyrrolidone (NMP, Sigma-Aldrich) to obtain a slurry for coating the materials on a Cu foil (MTI Corp., 18 μm) (carbons) or Al foil (LiFePO$_4$), using Doctor-Blade technique. The slurry was heated for 3 h at 70 °C by using a hot plate to remove the solvent, and cut into disks (either 10 or 14 mm-diameter), which were dried at 105 °C overnight under vacuum. The loading of the active material in the final electrode was about 3.5 mg cm^{-2} for carbons and 4 mg cm^{-2} for LiFePO$_4$.

The electrochemical process of the carbon materials was evaluated both in 2032 coin-type cells (MTI Corp.) and 3-electrode T-cell, prepared in an Ar-filled glove box (MBraun, O$_2$ and H$_2$O content below 1 ppm), with a Li|EC:DMC 1:1 w/w, 1 M LiPF$_6$|carbon configuration, using the selected carbon as the working electrode (14 mm-diameter in coin cell and 10 mm-diameter in T-cell), a Whatman disk soaked with the electrolyte as the separator, and a lithium metal disk as the counter and reference electrode.

Cyclic voltammetry (CV) and Electrochemical impedance spectroscopy (EIS) tests were performed by using 3-electrode T-cells. CV measurements consisted of ten cycles in the 0.01 – 2.8 V potential range with a scan rate of 0.1 mV s^{-1}, while EIS measurements were taken at the open circuit

voltage condition (OCV), after the first, fifth, and tenth CV cycle in the 500 kHz – 100 mHz frequency range using a 10 mV signal amplitude.

Galvanostatic cycling tests were performed in 2032 coin-type cells (MTI Corp.) within the voltage window 0.01 – 2.8 V. Rate Capability measurement was performed using current values of C/10, C/5, C/3, C/2, 1C, 2C and 5C (1C = 372 mA g^{-1}). Galvanostatic tests prolonged to 200 cycles were performed at constant rate of C/3. Both specific current and specific capacity were referred to the carbon mass, that is, the electrochemically active component in the electrode.

The stability of the two carbon materials in lithium cell upon prolonged galvanostatic cycling at C/3 was evaluated by performing EIS measurements at the OCV, and after the first, tenth, and hundredth discharge/charge cycle in the 500 kHz – 100 mHz frequency range using a 10 mV signal amplitude.

The lithium-ion full cells were assembled by coupling the selected carbon (either AC-K or AC-H) with a LiFePO$_4$ cathode in 2032 coin-type cells (MTI Corp.) using the configuration Carbon|EC:DMC 1:1 w/w, 1 M LiPF$_6$|LiFePO$_4$. Before use in Li-ion cell, the carbon electrodes were pre-activated by 30 galvanostatic cycles in lithium half-cell at a current rate of C/3 in a coin cell with the above mentioned configuration. After activation, the carbon electrodes were recovered from the corresponding cells upon disassembling, washed using DMC, dried under vacuum for 30 min, and employed in the above described Li-ion cell as the negative electrode.

Cycling tests of the Li-ion cells were performed within the voltage window 0.2 – 3.8 V. Rate capability measurements were performed using current values of C/5, C/3, 1C and 2C (1C = 170 mA g^{-1}). Galvanostatic tests prolonged over 200 cycles were performed at a current rate of C/3. Both specific current and specific capacity of the full-cell were referred to the LiFePO$_4$.

The sulfur-carbon composite was obtained by infiltrating sulfur in the AC-H carbon precursor via in-situ disproportionation of sodium thiosulfate pentahydrate (Na$_2$S$_2$O$_3$ · 5H$_2$O) in acidified aqueous solution. Accordingly, 3 g of Na$_2$S$_2$O$_3$ ·5H$_2$O (Sigma-Aldrich) was dissolved in a solution composed of 150 mL of H$_2$O and 4.5 mL of a Triton X-100 solution (1 vol %), that is, a polymer surfactant that avoids sulfur agglomerates and allows controlled sulfur particles size. Separately, 100 mg of carbon sample (AC-H) was dispersed in 100 mL of H$_2$O and sonicated for 1 h. Subsequently, the two solutions were mixed together and heated at 70 °C with the aid of a silicon oil bath, and 15 mL of HCl (12 M) was slowly added under vigorous magnetic stirring to achieve the following reaction (equation 4.1.1):

$$Na_2S_2O_3 \cdot 5H_2O \ (aq) + 2HCl \ (aq) \rightarrow 2NaCl \ (aq) + SO_2 \ (g) + S \ (s) + 6H_2O \qquad (4.1.1)$$
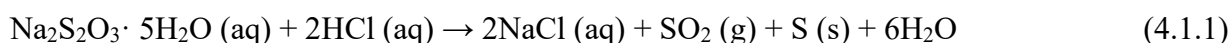
After 15 min, the silicon oil bath was removed and the mixture was left under mild magnetic stirring at room temperature for 24 h. Finally, the obtained sulfur-carbon composite was washed repeatedly with H_2O, ethanol, and acetone via centrifugation to remove HCl and Triton X-100, and then dried at 50 °C in an oven overnight. The final sample is indicated as AC-H@S.

The structural features of the AC-H@S powder were investigated through XRD and Raman spectroscopy. XRD pattern was obtained by a Bruker D8 Discover X-ray diffractometer exploiting monochromatic Cu-Kα radiation to scan the 2θ range between 10 and 80° by using a step size of 0.04° and a rate of 1.05 s step^{-1}.

Sample morphology was studied by SEM and TEM using a JEOL JSM-7800F and a JEOL 2010 electron microscope operating at 200 kV equipped with an Orius Gatan CCD camera, respectively. The elements distribution of the AC-H@S composite was evaluated via EDS, which was performed on the TEM images through a X-ACT Cambridge Instrument analyzer.

The synthesis of the SiO_x-C composite was achieved through solgel method.[32] 18 g of resorcinol was mixed with 58.5 g of formaldehyde at room temperature until a homogeneous mixture was obtained. Subsequently, 21 g of tetraethyl orthosilicate (TEOS) was added to the solution, which was then heated at 70 °C. The dropwise addition of 2 mL of HCl (1 M) to the heated solution catalyzed the formation of a semitrasparent pink gel, which was aged for 24 h at room temperature and then cut into pieces, washed with ethanol to remove residual HCl, and finally annealed at 1000 °C for 10 h under Ar-H_2 (5%) flow. The obtained black powder was ground in a mortar.

The electrodes slurries were prepared by dispersing 80wt% of the active material, either AC-H@S or SiO_x-C, 10wt% of Super P carbon (Timcal) as conductive agent, and 10 wt% of PVDF (Solef ® 6020 PVDF) as polymer binder, in NMP (Sigma-Aldrich). The slurries containing AC-H@S and SiO_x-C were coated on a carbon cloth foil (GDL, ELAT LT1400 W, MTI Corp.) and a Cu foil (MTI Corp.), respectively, by using a doctor blade (MTI Corp.). Then, the electrode films were heated at 50 °C for 5 h under air and subsequently cut into disks of 14 mm diameter, which were dried at 45 °C overnight under vacuum to remove residual traces of water and NMP. The active material loading on the final electrodes was of about 1.3 mg cm^{-2} for AC-H@S and 5.3 mg cm^{-2} for SiO_x-C.

The electrochemical processes of the AC-H@S and SiO_x-C composites were analyzed in 2032 coin-type cells (MTI Corp.) assembled in an Ar-filled glovebox (MBraun, O_2 and H_2O content below 1 ppm) by stacking either an AC-H@S or a SiO_x-C disk as the positive electrode, a 16 mm diameter Celgard foil soaked with the electrolyte as the separator, and a 14 mm diameter lithium metal disk as the negative electrode. The electrolyte solution exploited in this work was obtained by solvating bis(trifluoromethanesulfonyl)imide (LiTFSI, 99.95% trace metals basis, Sigma-Aldrich) conductive salt and lithium nitrate (LiNO$_3$, 99.99% trace metals basis, Sigma-Aldrich) sacrificial agent in a

solution of 1,3-dioxolane (DOL, anhydrous, contains ca. 75 ppm BHT as inhibitor, 99.8%, Sigma-Aldrich) and 1,2-dimethoxyethane (DME, anhydrous, 99.5%, inhibitor-free, Sigma-Aldrich) mixed in a 1:1 w/w ratio. LiTFSI and LiNO$_3$ were added to the DOL:DME (1:1 w/w) solution to obtain a final concentration of 1 mol kg^{-1} for each salt, as referred to the solvent mass. Prior to electrolyte preparation, LiTFSI and LiNO$_3$ were dried under vacuum to 110 and 80 °C, respectively, for 3 days to remove any trace of water, while DOL and DME were dried with the aid of molecular sieves (3 Å, rod, size 1/16 in., Honeywell Fluka) until a water content below 10 ppm was obtained, as measured by a Karl Fischer 899 Coulometer (Metrohm).

CV and EIS tests were performed on a Li|DOL:DME 1:1 w/w, 1 mol kg^{-1} LiTFSI, 1 mol kg^{-1} LiNO$_3$|AC-H@S cell. CV measurements were carried out in the 1.8 – 2.8 V vs Li$^+$/Li potential range by using a scan rate of 0.05 mVs^{-1}, while EIS measurements were performed at the OCV condition and after 1, 5, and 10 CV cycles in the 500 kHz to 100 mHz frequency range by using a 10 mV alternate voltage signal amplitude.

All the recorded impedance spectra were analyzed by NLLS method through a Boukamp tool and only fitting with a χ^2 value of the order of 10^{-4} or lower were considered suitable.[33,34]

The electrochemical performances of Li|DOL:DME 1:1 w/w, 1 mol kg^{-1} LiTFSI, 1 mol kg^{-1} LiNO$_3$|AC-H@S half-cells were evaluated through prolonged discharge/charge cycling at the constant current rate of C/3, and through rate capability measurements employing current values of C/10, C/8, C/5, C/3, C/2, 1C, and 2C by increasing the current rate every 5 cycles and lowering it to the initial value of C/10 after 35 cycles (1C = 1675 mA g$_S^{-1}$). The 1.9 – 2.8 V voltage range was employed from C/10 to C/2 rates, while tests at 1C and 2C were carried out between 1.8 and 2.8 V. Both specific current and specific capacity were referred to the sulfur mass.

The lithium-ion-sulfur cells were assembled by coupling the AC-H@S electrode as cathode with a pre-lithiated SiO$_x$-C anode (Li$_y$SiO$_x$-C) in 2032 coin-type cells (MTI Corp.) using the Li$_y$SiO$_x$-C|DOL:DME 1:1 w/w, 1 mol kg^{-1} LiTFSI, 1 mol kg^{-1} LiNO$_3$|AC-H@S configuration. SiO$_x$-C electrodes were pre-activated through 30 discharge-charge cycles by employing a constant current rate of 50 mA g^{-1} in the 0.01 – 2.0 V voltage range in Li|DOL:DME 1:1 w/w, 1 mol kg^{-1} LiTFSI, 1 mol kg^{-1} LiNO$_3$|SiO$_x$-C cells. The Li$_y$SiO$_x$-C electrodes were recovered from the above cell disassembled at 0.01 V, washed by using DME, and dried under vacuum for 30 min. Galvanostatic cycling tests were performed on the Li$_y$SiO$_x$-C|DOL:DME 1:1 w/w, 1 mol kg^{-1} LiTFSI, 1 mol kg^{-1} LiNO$_3$|AC-H@S full-cells within the 0.1 – 2.8 V voltage window at a current rate of C/5 (1C = 1675 mA g$_S^{-1}$). Both specific current and specific capacity of the full-cells were referred to sulfur mass.

Furthermore, chemical lithiation of the SiO$_x$-C electrode was performed to achieve a suitable condition for practical application of the Li$_y$SiO$_x$-C material in full-cell. The above lithiated anode

was achieved by direct contacting the SiO_x-C electrode with a lithium foil soaked with the DOL:DME 1:1 w/w, 1 mol kg^{-1} LiTFSI, 1 mol kg^{-1} $LiNO_3$ electrolyte under a pressure of 2 kg cm^{-2} for selected time regimes.[35] The electrode was then removed from the lithium foil, washed by DME, dried for 30 min under vacuum, and studied in lithium half-cell and full-cell using AC-H@S cathode. Galvanostatic cycling tests of chemically lithiated Li_ySiO_x-C preactivated for 30 min, 1, 2, and 14 h, as well as of a pristine SiO_x-C electrode, were performed in lithium half-cell using the DOL:DME 1:1 w/w, 1 mol kg^{-1} LiTFSI, 1 mol kg^{-1} $LiNO_3$ electrolyte at a current rate of 50 mA g^{-1} in the 0.01 – 2 V voltage range. Specific capacity and current were referred to the SiO_x-C mass.

A further lithium-ion sulfur cell with the Li_ySiO_x-C|DOL:DME 1:1 w/w, 1 mol kg^{-1} LiTFSI, 1 mol kg^{-1} $LiNO_3$|AC-H@S configuration was assembled by using a Li_ySiO_x-C anode achieved by the above described chemical pre-lithiation for 48 h and cycled within the 0.1 – 2.8 V voltage window at a current rate of C/5 (1C = 1675 mA gs^{-1}). SEM-EDS and XRD measurements were carried out on the AC-H@S and SiO_x-C electrodes employed for this cell at the pristine state, and *ex-situ* after 20 discharge/charge cycles. The SEM images were collected through a Zeiss EVO 40 microscope equipped with a LaB_6 thermoionic electron gun and the EDS analyses were performed by a X-ACT Cambridge Instruments analyzer. The XRD patterns were recorded through a Bruker D8 ADVANCE diffractometer employing a Cu-Kα source by performing scans between 10 and 90° in the 2θ range at a rate of 10 s $step^{-1}$ with a step size of 0.02°. Prior to perform SEM-EDS and XRD analyses the electrodes were washed with DME and dried under vacuum for 30 min.

All the CV and EIS tests were performed through a VersaSTAT MC Princeton Applied Research (PAR) analyzer, while the galvanostatic measurements were carried out by using a MACCOR series 4000 battery test system.

4.1.3 Results

Coals composition is detected by elemental analysis and reported in terms of weight % in Table 4.1.1. The carbon activated with KOH reveals higher content of C (about 89 %), less O (about 8 %) and H (about 1 %), compared to the sample activated by H_3PO_4 (about 81 %, 11 % and 2 %, respectively), while N and S contents appear almost negligible for both samples (*i.e.*, lower than 1%). Relevantly, AC-K evidences an overall element content higher than 99 %, instead AC-H shows an elemental content of about 94 %, thus suggesting the additional presence of different atoms in the latter carbon. X-ray energy dispersive spectroscopy (EDS) of the AC-H sample reported subsequently (see Fig. 4.1.3) indicates phosphorous (P) as the additional element (around 6 % weight).

Sample	C	H	N	S	O	Sum
AC-K	88.99	1.05	0.65	0.05	8.34	99.08
AC-H	80.57	2.0	0.18	0.06	11.40	94.21

Table 4.1.1. Elemental analysis of AC-K and AC-H samples: weight % of C, H, N, S and O, respectively.

The structural characteristics of the carbon samples investigated in this work are summarized in Figure 4.1.1. Indeed, Figure 4.1.1a shows the XRD patterns of AC-K (red line) and AC-H (green line) as well as the reference patterns of graphite (PDF # 41-1487). The figure evidences for both samples similar patterns characterized by the absence of defined peaks of ordered graphite, and the presence of two weak and broad signals around 26° and 44°, likely attributed to the (0 0 2) and (1 0 0) reflections of highly disordered carbons.[36,37] Furthermore, the Raman spectra of Figure 4.1.1b show the D and G bands of carbon at approximately $v = 1346$ and 1594 cm^{-1}, respectively, with an intensity ratio (I_D/I_G) of 0.96 in AC-K and 0.95 in AC-H. The relatively high I_D/I_G value likely indicates a pronounced defect content and a small average size of the sp^2 domains.[38] It is worth mentioning that the slightly lower intensity of the XRD reflections and higher I_D/I_G value of the AC-K sample may likely suggest a more effective activation of the carbon sample by using KOH rather than H_3PO_4.[29,30,39,40] The TGA curves performed under oxygen and reported in Figure 4.1.1c reveal a different trend for the studied carbons. The two samples begin losing weight from about 200 °C, most likely due to organic residues which are more relevant in AC-K (about 18 % of weight loss until 450 °C) compared to AC-H (about 7 % weight loss until 450 °C). Both samples reveal a fast decay of the weight around 500 °C due to the full oxidation of the carbon to CO_2. However, this pronounced weight loss represents more than 95 % in the sample activated with KOH and only 40 % when the activation is carried out with H_3PO_4. Therefore, the weight loss of the AC-H sample at temperatures higher than 500 °C may be likely ascribed to concomitant oxidative decomposition of impurities rather than the exclusive pyrolysis of C. The inset of Figure 4.1.1c, reporting the DTG curves, evidences at least two additional stages of weight loss for AC-H (green curve), that is, just above 500 °C and at about 650 °C, while only the main peak around 500 °C is observed for AC-K (red curve). Lignocellulosic materials react with H_3PO_4 according to a complex bond-breaking process involving CO, CO_2 and CH_4 gases evolution, even at low temperatures, with formation of phosphate esters by cellulose phosphorylation.[41] On the other hand, appreciable presence of P is actually suggested by EDS hereafter, while the presence of phosphorylated functional groups is confirmed by the FT-IR
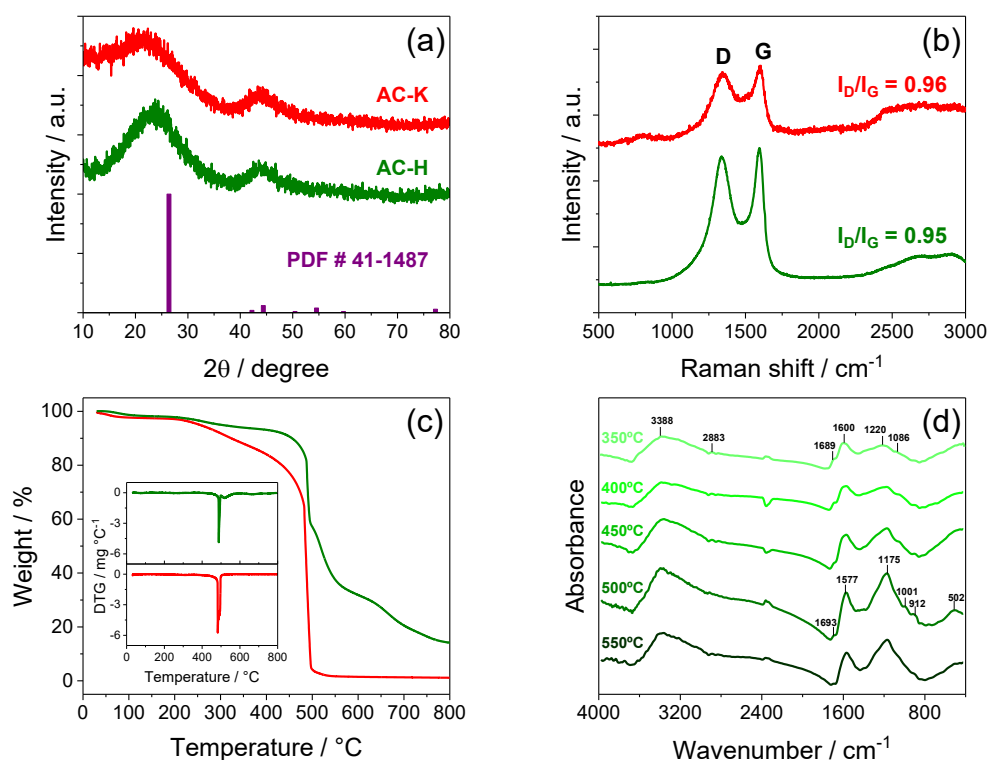
spectra of the AC-H sample reported in Figure 4.1.1d. The latter figure shows the absorption spectra of carbon samples activated using H_3PO_4 by heating at various temperatures between 350 and 550 °C, that is, temperature range corresponding to the change of TGA curve's slope observed in Figure 4.1.1c. The FT-IR spectra reveal a series of shoulders and absorption bands whose position and allocation are detailed in Table 4.1.2.[42]

As above mentioned, elemental analysis (see Table 4.1.1) and EDS suggest for the carbons surface groups involving both O and P, despite the repeated washing adopted to leach the phosphorus species. Interestingly, the relative intensity of the IR bands located between 1600 and 1200 cm^{-1} (Fig. 4.1.1d) tends to increase by raising the temperature from 350 and 500 °C, thus suggesting increased concentration of surface groups with C=C, C−O and/or P=O bonds, while a further temperature raise leads to the decrease of the functional groups content. Therefore, the weight loss at temperature higher than 500 °C observed by thermogravimetry (Fig. 4.1.1c) would mainly correspond to the gasification of carbon, while at higher temperatures additional phases related to the phosphorous groups would also be volatilized, thus accounting for the AC-H thermogram complexity observed in Figure 4.1.1c.

Wavenumber / cm^{-1}	Assignments	Group
3388	ν (O−H)	Intermolecular hydrogen bond: alcohols, phenols and carboxylic acids
1693	ν (C=O)	Esters: quinone and carboxylic acids
1577	ν (C=C)	Olefinic groups and aromatic rings
1175	ν (C−OH)	Phenols and carboxylic acids
	ν (C−O) in C−O−C	Ethers
	ν (P=O)	Phosphate esters and polyphosphate
1001	ν (P−OH)	Phosphate esters and polyphosphate
	ν (C−O) in P-O-C	Phosphate esters and polyphosphate
912	ν (P−O) in P-O-C	Phosphate esters and polyphosphate

Table 4.1.2. Assignment of absorption bands of the FT-IR spectra of AC-H sample (cm^{-1}) collected in Fig. 4.1.1d.

The high ash content in AC-H, around 15%, is also observed in other biomass-derived carbons activated with H_3PO_4[43] in a much higher ratio than samples activated by KOH such as AC-K. Therefore, the thermal measurements reveal substantial differences between the two sample, and likely suggest a more relevant organic fraction for AC-K while a more significant inorganic residue for AC-H.

Figure 4.1.1. (a-c) Structural study of the samples. **(a)** XRD (reference data for graphite are reported PDF # 41-1487), **(b)** Raman spectra, **(c)** TGA under oxygen atmosphere of AC-K (red line) and AC-H (green line); (insert: DTG curves); **(d)** FT-IR spectra of the AC-H sample heated at different temperatures.

The effects of the activation conditions on the surface area and the pore volume of the two samples are evaluated by N_2 and Hg adsorption-desorption measurements reported in Figure 4.1.2 and summarized in Table 4.1.3. The N_2 adsorption isotherms of the two activated carbons shown in Figure 4.1.2a reveal the expected trends, both belonging to a type I BDDT classification, typical of microporous solids with relatively small external surfaces. The higher adsorption values of the sample AC-H with respect to AC-K observed in Figure 4.1.2a indicate extended surface area of the former compared to the latter, that is, 1662 and 1171 m^2 g^{-1}, respectively, possibly suggesting a more efficient removal of the organic part by means of H_3PO_4 rather than KOH, in line with the TG measurements.[29,30] Although the two samples have the same micro-pore volume (V_{mi}), approaching 0.6 cm^3 g^{-1}, and an overall-pore volume (V_T) only slightly higher for AC-K compared to AC-H, with values of about 1.1 and 1.0 cm^3 g^{-1}, respectively, the DFT plots of Figure 4.1.2b show appreciable differences in pore size. Indeed, AC-K has pores with an average size below 0.8 nm, instead AC-H pores range around 1.5 nm. The analysis of the Hg porosimetry data reported in Figure 4.1.2c shows relevantly different distribution of macro- and meso-pores (see Table 4.1.3). AC-H has meso-pores with a volume (V_{me}) of about 0.4 cm^3 g^{-1}, and a much lower macro-pores volume (i.e., V_{ma} of about

0.08 cm^3 g^{-1}) compared to AC-K which contains predominantly macro-pores (V$_{ma}$ = 0.5 cm^3 g^{-1}). Furthermore, AC-K shows a slightly higher overall porosity compared to AC-H, that is, 1.13 and 0.97 cm^3 g^{-1}, respectively (V$_T$ in Table 4.1.3). These remarkable differences indicate an actual effect of the activation conditions on the samples characteristics, and suggest a careful selection of the operating conditions adopted during the synthesis for achieving the appropriate features.

| Sample	S$_{BET}$ (m^2 g^{-1})	V$_{mi}$ (N$_2$) (cm^3 g^{-1})	V$_{me}$ (Hg) (cm^3 g^{-1})	V$_{ma}$ (Hg) (cm^3 g^{-1})	V$_T$ (Hg) (cm^3 g^{-1})
AC-K	1171	0.57	0.08	0.48	1.13
AC-H	1662	0.57	0.40	0.08	0.97

Table 4.1.3. Surface area (S$_{BET}$), and micro-pores volume (V$_{mi}$) of AC-K, and AC-H as determined by N$_2$ adsorption-desorption BET isotherms. Volume of meso-pores (V$_{me}$), and macro-pores (V$_{ma}$) of AC-K, and AC-H as determined by Hg-porosimetry. V$_T$ represents the overall sample porosity.

Several literature papers have indicated the role of combination of the macro-, meso- and micro pores in enhancing the electrode performances in terms of *i)* electrolyte accessibility, and electrode wettability, which are particularly promoted by the macro and meso-pores,[44] *ii)* ion diffusion rate, and *iii)* charge transport kinetics at the electrode/electrolyte interphase which is mainly ascribed to micro pores.[45] Accordingly, a promoted electrolyte accessibility limits the cell polarization, thus favoring the energy efficiency, while low charge-transfer resistance, and fast ion diffusion at the electrode/electrolyte interphase increase the rate capability of the porous carbon materials.[10] Therefore, the simultaneous presence of various types of porosity into the hierarchical carbon actually allows enhanced performances of the electrode in energy storage devices.[45]
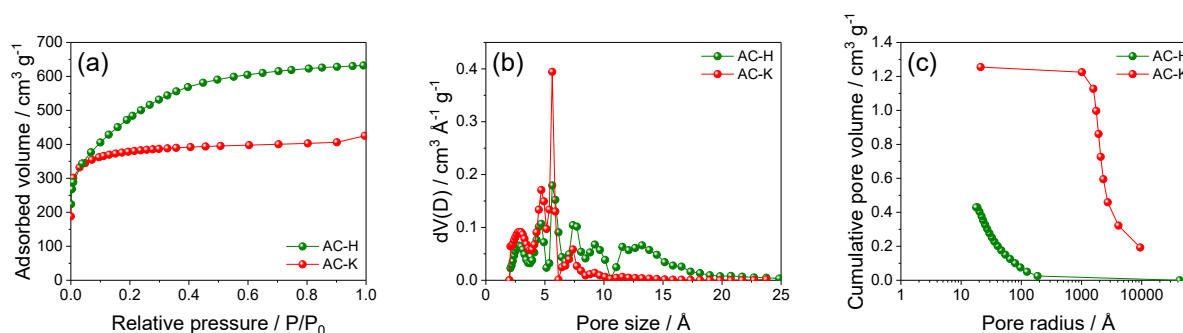
Figure 4.1.2. (a) N$_2$ adsorption BET isotherms recorded at 77 K, **(b)** pore size distribution obtained by density functional theory (DFT), and **(c)** cumulative pore volume trending determined by Hg porosimetry of AC-K (red) and AC-H (green) samples.

The morphological characteristics of the samples are delighted by SEM, and TEM as reported in Figure 4.1.3. The samples reveal primary micrometric particles with bigger size for AC-K (about 200 μm, SEM in Fig. 4.1.3b) compared to AC-H (about 60 μm, Fig. 4.1.3d), likely due to the different activation pathway, as well as secondary particles with a size of about 20 μm (SEM insets in Fig. 4.1.3b and Fig. 4.1.3d). Flakes having submicron dimensions are also observed by the TEM images (Fig. 4.1.3a, c), mostly due to exfoliation of the carbon during the synthesis. Furthermore, the uniform presence of P into the AC-H sample, not detected by elemental analysis in Table 4.1.1, is herein confirmed by EDS mapping as reported in inset of Figure 4.1.3d.
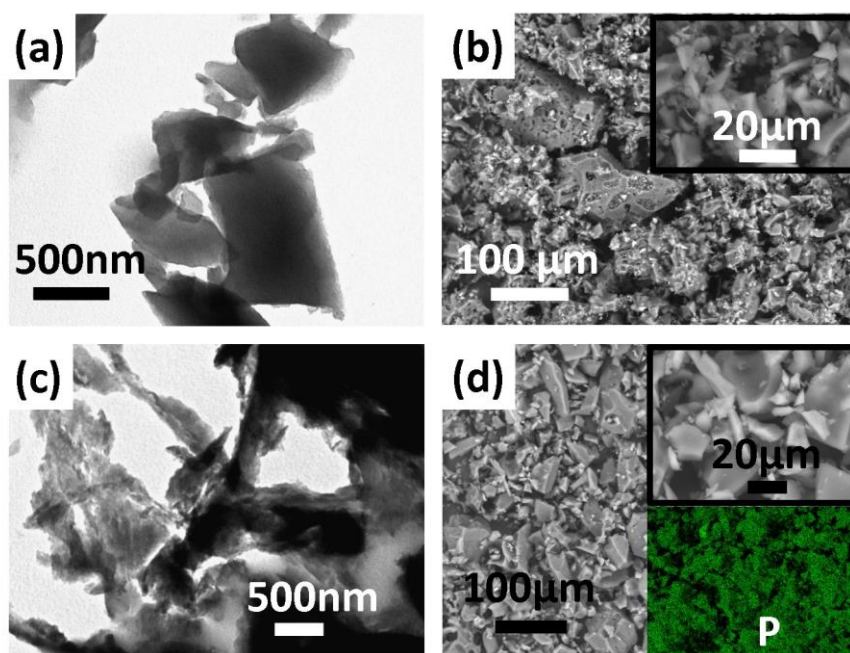
Figure 4.1.3. (a-d) Morphological study of the carbon samples. **(a, c)** TEM, and **(b, d)** SEM of AC-K and AC-H, respectively. EDS mapping of P in AC-H sample is shown in the inset of panel **(d)**.

The carbon electrodes are subsequently studied in lithium cell by combining voltammetry, impedance spectroscopy and galvanostatic measurements. Figure 4.1.4a, and Figure 4.1.4c show respectively the CV scans of AC-K, and AC-H electrodes in a three-electrode lithium cell between 0.01 and 2.8 V vs Li$^+$/Li at a rate of 0.1 mV s^{-1}. Both samples show during the first cathodic scan a voltammetry profile significantly differing from the subsequent, characterized by a substantial irreversibility. Indeed, AC-K evidences only a broad signal extending below 1.0 V vs Li$^+$/Li (inset of Fig. 4.1.4a), while AC-H shows a first reduction peak at about 1.2 V, a small signal at about 0.7 V followed by a tilted line extending to 0.01 vs Li$^+$/Li (inset of Fig. 4.1.4c). The differences between the curves related to AC-H and AC-K is particularly evidenced by the presence during the first cathodic scan of a peak at the higher potential value, $i.e.$, 1.2 V vs Li$^+$/Li, in the former and its absence

in the latter. This discrepancy may be likely ascribed to the different nature, and extent of the impurities in the two electrodes. The elemental analysis of Table 4.1.1 actually reveals that AC-H contains about 6 % of additional impurity compared to AC-K, which has been detected as P in the inset of Figure 4.1.3d. This impurity may possibly justify the side peak in the voltammetry curve related to AC-H. The irreversible trend of the first reduction is a typical characteristic of the electrochemical process of the carbons in lithium cell due to partial decomposition of the electrolyte, and the formation of a SEI layer at the electrode/electrolyte interphase.[46,47] The CV data also suggest additional irreversible processes ascribed to the specific impurities in the two carbon samples (revealed by TGA and EDS): hence, AC-K mostly has organic residues while AC-H contains mainly an inorganic fraction constituted by phosphates.[48] The subsequent CV cycles are characterized by reversible, progressively overlapping profiles, with broad signals around 1.0 V, 0.2 V and 0.01 V vs Li^+/Li due to the insertion/de-insertion of the lithium into the disordered carbon as well as to possible lithium plating/stripping into the pores of the active materials.[49] The achieved reversibility upon the first CV cycles likely indicates the stability of the SEI formed by the above mentioned irreversible reduction of the electrolyte,[46,47,49] and of the residues detected in the activated carbons.[25,50]

Additional insight on the electrode/electrolyte interphase characteristics are given by EIS analyses at the OCV and upon CV of the lithium cells using AC-K (Fig. 4.1.4b), and AC-H (Fig. 4.1.4d). Beside the electrolyte resistance, represented by the high-frequency intercept, the Nyquist plots show a middle-high frequency semicircle or deeply convoluted semicircles, accounting for both charge transfer and SEI film contributions in the electrode/electrolyte interphase, and a low-frequency tilted line with a slope approaching 45° likely related to the Warburg-type semi-infinite diffusion in the electrode or to cell geometric capacity.[51–53] Table 4.1.4 reports the values of the electrode/electrolyte interphase resistance, and the chi-square (χ^2) values obtained by non-linear least squares (NLLS) method using a Boukamp tool,[33,34] by adopting the equivalent circuits $R_e(R_iQ_i)Q_g$, where (R_iQ_i) are the resistances and the constant phase elements of the middle-high frequency semicircles ascribed to the interphase, R_e the electrolyte resistance, and Q_g the constant phase element related to the low-frequency line. The accuracy of the data obtained by the analysis, evidenced by χ^2 values of about 10^{-4} or below, is achieved by adopting either one or two RQ elements, that is, $R_e(R_1Q_1)Q_g$ or $R_e(R_1Q_1)(R_2Q_2)Q_g$ for the analysis of the middle-high frequency semicircle of the interphase for AC-K, and AC-H electrodes, respectively. This discrepancy may be partially justified by a SEI film, and charge transfer processes having significantly different time-constant in AC-K and AC-H electrode/electrolyte interphase, leading to elements overlapping in one only in the latter, and to two distinguishable elements in the former.[33,34,54] Interestingly, Table 4.1.4 evidences that the first

element vanishes by the ongoing of the voltammetry of the Li-cell using AC-K, with resistance value decreasing from about 7 Ω at the OCV to 1 Ω after 10 CV cycles.

AC-K					
Cell condition	Circuit	R_1 [Ω]	R_2 [Ω]	$R=R_1 + R_2$ [Ω]	χ^2
OCV	$R_e(R_1Q_1)(R_2Q_2)Q_g$	6.5 ± 1.4	26.6 ± 1.5	33.1± 2.9	4×10^{-5}
1 CV cycle	$R_e(R_1Q_1)(R_2Q_2)Q_g$	5.5 ± 0.7	15.8 ± 0.7	21.3 ± 1.4	2×10^{-5}
5 CV cycles	$R_e(R_1Q_1)(R_2Q_2)Q_g$	2.9 ± 0.7	39.6 ± 1.0	42.5 ± 1.7	4×10^{-5}
10 CV cycles	$R_e(R_1Q_1)(R_2Q_2)Q_g$	1.1 ± 0.3	76.5± 0.8	77.6 ± 1.1	4×10^{-5}
AC-H					
OCV	$R_e(R_1Q_1)Q_g$	2.9 ± 0.1	-	2.88 ± 0.1	2×10^{-4}
1 CV cycle	$R_e(R_1Q_1)Q_g$	23.5 ± 0.2	-	23.5 ± 0.2	8×10^{-5}
5 CV cycles	$R_e(R_1Q_1)Q_g$	32.3 ± 0.4	-	32.3 ± 0.4	7×10^{-5}
10 CV cycles	$R_e(R_1Q_1)Q_g$	39.5 ± 0.6	-	39.5 ± 0.6	5×10^{-5}

Table 4.1.4. Electrode/electrolyte interphase resistance and χ^2 values obtained by NLLS analyses using a Boukamp tool of the impedance spectra of AC-K (Fig. 4.1.4b), and AC-H (Fig. 4.1.4d) at the OCV, after 1, 5 and 10 voltammetry cycles. Equivalent circuit used for AC-K: $R_e(R_1Q_1)(R_2Q_2)Q_g$. Equivalent circuit used for AC-H: $R_e(R_1Q_1)Q_g$.

Further difference between AC-K and AC-H interphases can be observed by taking into account the overall interphase resistance (R) reported in Table 4.1.4, and plotted in the inset of the corresponding Nyquist plots of Figure 4.1.4b and Figure 4.1.4d, respectively. The figure reveals higher resistance for AC-K compared to AC-H with values of about 33 Ω and 3 Ω, respectively, at the OCV. After 1 CV cycle, the resistance decreases to about 21 Ω for AC-K, while it raises to about 24 Ω for AC-H, to finally increase after 5 and 10 CV cycles to 43 Ω, and 78 Ω for AC-K, and to 32 Ω, and 40 Ω for AC-H, respectively. These trends as well as the different CV responses may be likely ascribed to the nature of each carbon in terms of composition and morphology, which can actually influence the electrochemical behavior of the electrode and the possible side reactions.[55,56]

In this respect, it may be worth noting that the additional decomposition peak at about 1.2 V *vs* Li$^+$/Li observed for AC-H during the first cathodic scan (inset of Fig. 4.1.4c) may actually lead to the initial increase of the interphase resistance observed in inset of Figure 4.1.4d, while CV profile in AC-K (inset of Fig. 4.1.4a) can likely favor the SEI formation as suggested by the initial impedance decrease in the corresponding trend in inset Figure 4.1.4b. On the other hand, the subsequent CV cycles lead for both samples to an increase of the interphase resistance due to the SEI growth.
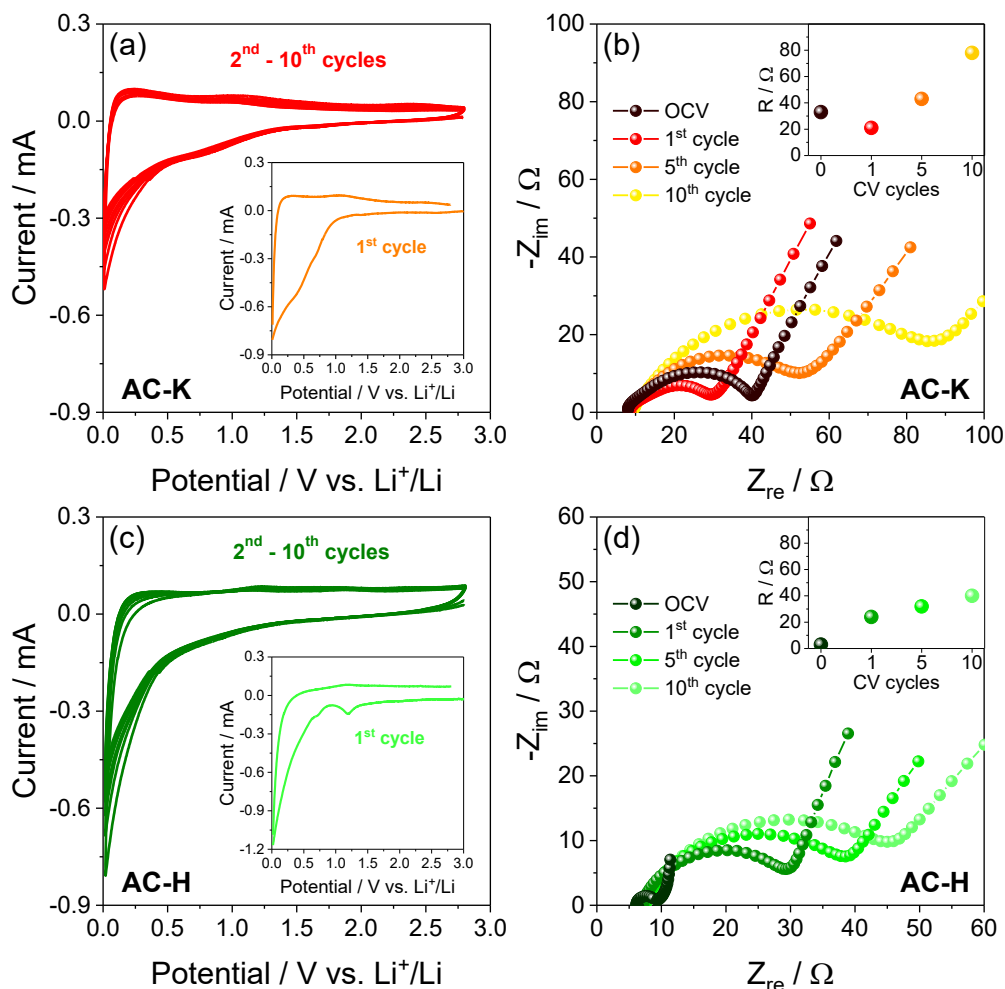
Figure 4.1.4. (a-d) Electrochemical features of the carbon electrodes and characteristics of the electrode/electrolyte interphase. **(a, c)** CV of **(a)** AC-K and **(c)** AC-H in three-electrode T-cell using lithium as counter and reference electrodes at a scan rate of 0.1 mV s^{-1}, from 0.01 V to 2.8 V *vs* Li$^+$/Li, and **(b, d)** corresponding Nyquist plots of the EIS, respectively, at the OCV, after 1, 5 and 10 voltammetry cycles. Alternate voltage signal amplitude: 10 mV. Frequency range: 500 kHz – 100 mHz.

Hence, the characteristic electrode/electrolyte interphase in AC-K and AC-H is expected to influence the electrochemical response of the two materials both in lithium half-cell, and in lithium-ion full cell. Therefore, the applicability of the two electrodes is investigated in lithium cell galvanostatically cycled at different currents by adopting various protocols. Figure 4.1.5 reports the cycling responses of AC-K (red curves), and AC-H (green curves) in lithium cell at a C/3 rate, and their rate capability at C/10, C/5, C/3, C/2, 1C, 2C and 5C (1C = 372 mA g^{-1}). Both AC-H and AC-K show during the initial 20 cycles a capacity decreasing from about 330 mAh g^{-1} to about 200 mAh g^{-1} (Fig. 4.1.5a). This trend, likely expected by progressive decomposition of the impurities in the two carbons, is reflected by the voltage profiles (Fig. 4.1.5c and Fig. 4.1.5e, respectively) which significantly change from the 1st cycle (insets of the figures), to the 2nd, the 10th, and to the 20th

206

cycle. Subsequently, the voltage trends of Figure 4.1.5c and Figure 4.1.5e reflect for both materials the typical sloping shape ascribed to the insertion of lithium into the disordered carbon below 1.2 V.[56] The above side reactions initially depress the delivered capacity, and decrease the coulombic efficiency, which has a value below 50% during the first cycle (Fig. 4.1.5a); however, the same processes lead also to the formation of a very stable interphase during the subsequent cycles[27] with an efficiency approaching 100%, and a reversible trend. This relevant stability is well justified by the inset of Fig. 4.1.5a which shows the trends of the electrode/electrolyte interphase resistance of the lithium half-cells using AC-K (red), and AC-H (green) upon the galvanostatic cycling at C/3 (see Table 4.1.5 for the corresponding NLLS analyses, Nyquist plots not reported). The data reveal a remarkable decrease of the overall electrode/electrolyte resistance for the cells, including both lithium anode, and either AC-K or AC-H, from about 48 Ω and 18 Ω, respectively, to low and constant values ranging between 7 and 9 Ω, thus further accounting for the electrode suitability for prolonged cycling.

Hence, AC-H reveals a decrease of the specific capacity from about 200 at the 20th cycle to about 170 mAh g^{-1} after 200 cycles, while AC-K shows a capacity slightly increasing, i.e., from 200 to about 210 mAh g^{-1}, upon the same number of cycles (Fig. 4.1.5a). The rate capability of the two samples in lithium cell is examined at the current of C/10, C/5, C/3, C/2, 1C, 2C and 5C, and reported in terms of cycling trend (Fig. 4.1.5b), and voltage profile of selected cycles (Fig. 4.1.5d and Fig. 4.1.5f for AC-K and AC-H, respectively). The two samples evidence the initial decay already discussed above, and a different rate capability, with a higher delivered capacity for AC-H compared to AC-K at currents lower than C/2; accordingly, AC-H has an average capacity ranging from about 400 mAh g^{-1} at C/10 to 230 mAh g^{-1} at C/3, while AC-K shows an average value from about 320 mAh g^{-1} at C/10 to 200 mAh g^{-1} at C/3. This trend is reversed at C-rates higher than C/2, with an average capacity ranging from about 120 mAh g^{-1} at 1C to 40 mAh g^{-1} at 5C for AC-H, and a value from about 140 mAh g^{-1} at 1C to 70 mAh g^{-1} at 5C for AC-K.

AC-K					
Cell condition	**Circuit**	**R_1 [Ω]**	**R_2 [Ω]**	**$R=R_1+R_2$ [Ω]**	**χ^2**
OCV	$R_e(R_1Q_1)(R_2Q_2)Q_g$	42 ± 1	5.4 ± 3.5	47.4 ± 3.7	8×10^{-5}
1 cycle at C/3	$R_e(R_1Q_1)(R_2Q_2)Q_g$	2.2 ± 0.4	5.8 ± 0.4	8.1 ± 0.5	8×10^{-5}
10 cycles at C/3	$R_e(R_1Q_1)(R_2Q_2)Q_g$	2.2 ± 0.2	6.5 ± 0.2	8.7 ± 0.3	5×10^{-5}
100 cycles at C/3	$R_e(R_1Q_1)(R_2Q_2)Q_g$	2.4 ± 0.2	6.8 ± 0.2	9.2 ± 0.3	3×10^{-5}
AC-H					
OCV	$R_e(R_1Q_1)(R_2Q_2)Q_g$	10.4 ± 0.2	7.1 ± 0.9	17.5 ± 0.9	5×10^{-5}
1 cycle at C/3	$R_e(R_1Q_1)Q_g$	8.0 ± 0.2	-	8.0 ± 0.2	8×10^{-5}
10 cycles at C/3	$R_e(R_1Q_1)Q_g$	7.2 ± 0.2	-	7.2 ± 0.2	6×10^{-5}
100 cycles at C/3	$R_e(R_1Q_1)(R_2Q_2)Q_g$	5.1 ± 0.2	2.9 ± 0.2	8.0 ± 0.3	4×10^{-5}

Table 4.1.5. Electrode/electrolyte interphase resistance and χ^2 values obtained by NLLS analyses using a Boukamp tool of the EIS data related to AC-K (inset of Fig. 4.1.5a) and AC-H (inset of Fig. 4.1.5b) employed in lithium cell at the OCV, and after 1, 10 and 100 discharge/charge cycles at a C/3 current rate. Alternate voltage signal amplitude: 10 mV. Frequency range: 500 kHz – 100 mHz.

The lower value of the capacity obtained at the higher currents is likely attributed to the increase of the cell polarization, as evidenced by the voltage profiles of the rate capability tests reported in Figure 4.1.5d and Figure 4.1.5f for AC-K and AC-H, respectively. It is worth mentioning that the capacity values of AC-H, estimated by considering the carbon content only, i.e., by excluding 15% of impurity observed above (see discussion of Fig. 4.1.1), may be actually higher than the ones observed in Figure 4.1.5, thus further accounting for the differences observed between the two samples. Therefore, the difference observed between the two samples in terms of reversible capacity, and value of the electrode/electrolyte interphase resistance (Table 4.1.4) may be actually driven by the different nature of impurities, the textural properties, a greater BET surface of AC-H compared to the AC-K, the significant mesopore content interconnected with the micropores in AC-H, and the predominant presence of macropores in the AC-K sample.

In overall, the galvanostatic tests in half-cell evidence the applicability of the two materials as the anode in Li-ion cell. However, the data of Figure 4.1.5 suggest a preliminary treatment of the electrodes before use in full-cell in order to avoid the detrimental effect of the initial capacity decay, and achieve a suitable reversibility for an efficient application. In this respect, several procedures have been proposed, in particular for amorphous carbons and Li-alloy electrodes characterized by relevant irreversible capacity during the initial cycles.
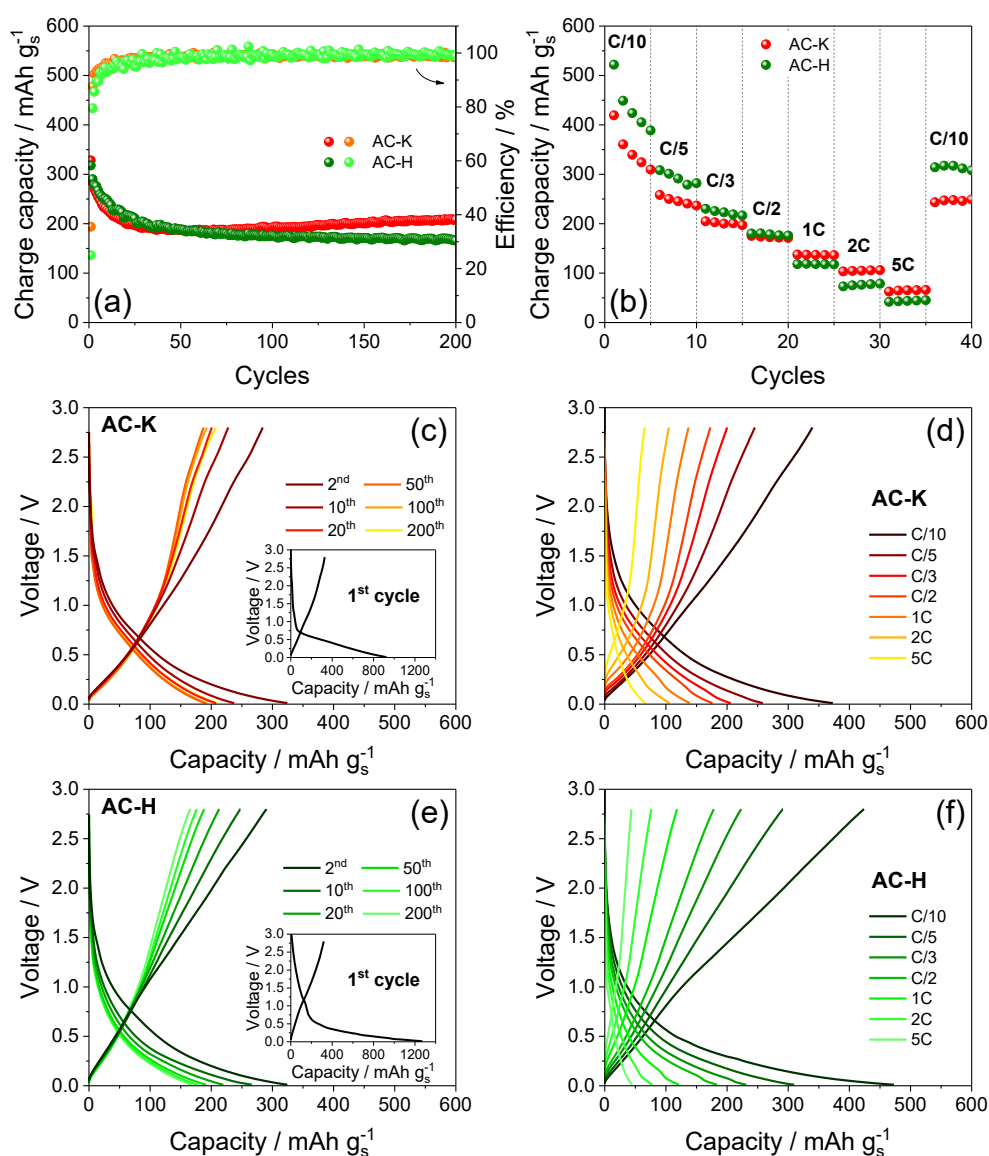
Figure 4.1.5. (a-f) Cycling performances of the carbon electrodes in lithium half-cell. **(a)** Cycling trend with coulombic efficiency (right y-axis) of AC-K (red), and AC-H (green) in a lithium cell galvanostatically cycled at a C/3 rate (1C = 372 mA g⁻¹), and **(c, e)** corresponding voltage profiles, respectively, for selected cycles; inset in panel **(a)** shows the electrode/electrolyte interphase resistance values of the AC-K (red), and AC-H (green) measured by EIS upon the cycling at C/3 (see Table 4.1.5 for the corresponding NLLS analyses). **(b)** Rate capability cycling trend of AC-K (red), and AC-H (green) in a lithium cell galvanostatically cycled at C/10, C/5, C/3, C/2, 1C, 2C and 5C, and **(d, f)** corresponding voltage profiles, respectively, of selected cycles.

Among them, electrochemical activation by pre-cycling of the electrodes in lithium half-cell,[57] via surface modification and coatings,[58] or by direct contact with lithium metal[35] evidenced the most suitable results in terms of stability of the full-cell. Therefore, prior to use AC-K and AC-H in full cell exploiting LiFePO₄ olivine-structure cathode[59] the two electrodes are electrochemically activated in half-cell by 30 galvanostatic cycles at C/3 to achieve the steady state observed in Figure

209

4.1.5 (see *4.1.2 Experimental* section for further details). The cells are balanced by slight anode excess with an N/P capacity ratio of about 1.03, according to the mass loading reported in the *4.1.2 Experimental* section, considering the theoretical capacity of 170 mAh g^{-1} for LiFePO$_4$ and a practical capacity at the steady state of about 200 mAh g^{-1} for the carbon electrodes.

Figure 4.1.6 reports the cycling performances of AC-K (red), and AC-H (green) in the lithium-ion full-cell, both at the constant C-rate of C/3 (1C = 170 mA g^{-1}) for evaluating the cycle life (Fig. 4.1.6a), and at various C-rates to determine the rate capability (Fig. 4.1.6b). After the initial few cycles characterized by some side irreversible processes dealing with electrolyte oxidation at the higher voltages, and possible reduction at the lower voltage values,[60] the two cells remarkably deliver a steady state capacity of about 160 mAh g^{-1}, that is, a value of about 95 % of the theoretical one of LiFePO$_4$. The corresponding voltage profiles, reported in Figure 4.1.6c for AC-K, and Figure 4.1.6e for AC-H, clearly evidence during the initial cycles the above mentioned processes likely occurring at about 3.6 V during charge and at 0.6 V during discharge. Furthermore, the steady state charge/discharge profile reflects the combination between the flat profile typical of the insertion process of the LiFePO$_4$ occurring at about 3.5 V,[59] and the sloping one extending from about 1.5 V until low potential of AC-K, and AC-H (compare with Fig. 4.1.5c, and Fig. 4.1.5e, respectively). Therefore, the cells show at the steady state a capacity approaching 160 mAh g^{-1} delivered with an average working voltage of about 2.8 V, thus a theoretical energy density of about 450 Wh kg^{-1}.[61] Remarkably, both cells evidence high efficiency after the initial cycles, and a relevant stability by the subsequent ones (Fig. 4.1.6a). Hence, the cell using AC-K reveals a coulombic efficiency of about 98 % (upon 20 cycles) leading to a capacity retention of 94 % with respect to the steady state (160 mAh g^{-1}) upon 200 cycles, while the cell using AC-H shows after 20 cycles a coulombic efficiency higher than 99 %, and a capacity retention as high as 96 %. It is worth mentioning that the voltage shape of the cells (Fig. 4.1.6c for AC-K and Fig. 4.1.6e for AC-H) progressively modifies during cycles, in particular during the final stages of the test, likely due to a slight change of the cell balance promoted by the side processes, however without significant change of the delivered capacity.[57] The rate capability of the two full-cells is examined at currents increasing from C/5 to C/3, 1C and 2C (Fig. 4.1.6b). After the initial cycles at C/5 during which the cells undergo side reactions affecting the delivered capacity, the figure shows stable values of about 162, 159, 123, and 79 mAh g^{-1} for the cell using AC-K, and 156, 148, 98, and 67 mAh g^{-1} for the cell using AC-H at C/5, C/3, 1C and 2C, respectively.

Therefore, the cells show the expected decrease of the delivered capacity by raising the current due to the increase of the polarization (Fig. 4.1.6d, and Fig. 4.1.6f for AC-K, and AC-H, respectively), however with an excellent rate capability. Compared to the half-cells, the full cells using the two

carbons reveal less differences, most likely due to the pre-activation process prior to cycling which mitigates the irreversible processes ascribed to the different samples nature, and composition. Despite further insights may be required to fully setup the activation pathway of AC-K and AC-H for achieving a low impurity content, the remarkable performances of the lithium-ion cells reported above actually suggest the two electrodes as alternative electrode materials for a safe, low cost, and environmentally sustainable energy storage system.
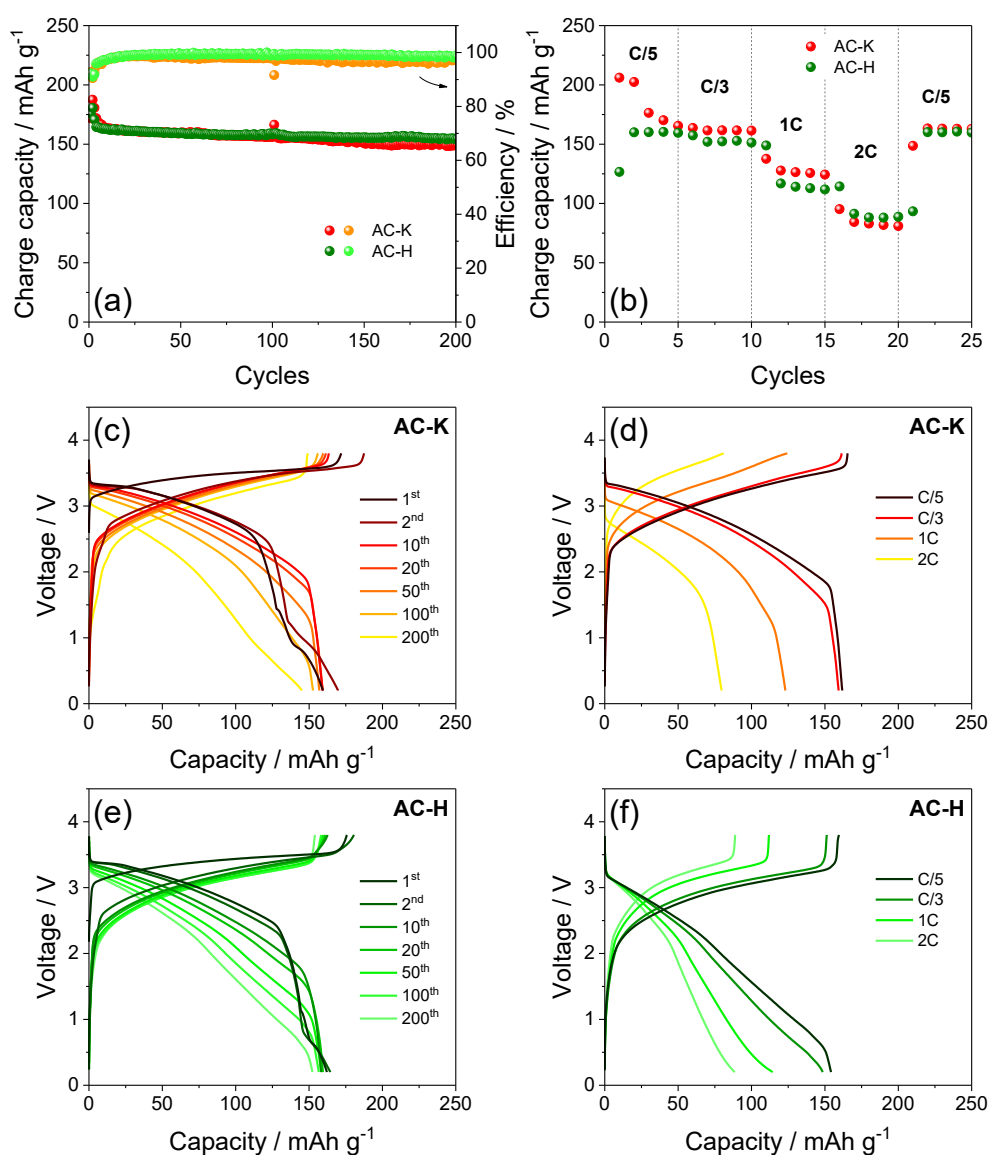
Figure 4.1.6. (a-f) Cycling performances of the carbon electrodes in lithium-ion full-cell using a LiFePO$_4$ cathode. **(a)** Cycling trend with coulombic efficiency (right *y*-axis) of AC-K (red), and AC-H (green) in a lithium-ion cell galvanostatically cycled at a C/3 rate (1C = 170 mA g^{-1}), and **(c, e)** corresponding voltage profiles, respectively, for selected cycles. **(b)** Rate capability cycling trend of AC-K (red), and AC-H (green) in a lithium-ion cell galvanostatically cycled at C/5, C/3, 1C, and 2C, and **(d, f)** corresponding voltage profiles, respectively, of selected cycles.

Following this trend, the AC-H material was selected as carbonaceous precursor to synthetize a sulfur composite to serve as cathode in Li-S and, in particular, in an efficient and safe full lithium-ion-sulfur battery where the reactive lithium metal is substituted by a silicon oxide-based anode. The new sulfur-carbon composite obtained by disproportionation of sodium thiosulfate pentahydrate (AC-H@S, see the *4.1.2 Experimental* section for details on the synthesis) is initially investigated in terms of structure, morphology and thermal behavior. It is worth mentioning that the AC-K material was excluded from the following study due incompatibility with operation in Li-S battery (data not reported).

The structural features of the AC-H@S composite are investigated by means of XRD, and the results are reported in Figure 4.1.7a. The AC-H@S pattern exhibits the sulfur (S_8) signals between 20 and 60° without any crystallographic evidence corresponding to graphite, which is usually observed at about 26°, as expected by the disordered nature of the activated carbon precursor (AC-H).[62] Furthermore, the exclusive presence of the sulfur signals implies the absence of impurities and, thus, the effectiveness of the synthesis pathway.

The disordered nature of the AC-H precursor is maintained in the AC-H@S composite, as further confirmed by Raman spectroscopy reported in Figure 4.1.7b. Indeed, the presence of broad D ($\sim$1350 cm^{-1}) and G ($\sim$1600 cm^{-1}) bands, the related intensity ratios (I_D/I_G) of 0.95, as well as the absence of a defined 2D band generally observed around 2700 cm^{-1} for graphitic structures,[63] evidence the large ratio of structural defects.[64] The Raman spectrum also identifies the sulfur hosted in the composite, which is represented by the narrow peak centered at about 473 cm^{-1}.[65]

The actual amount of sulfur in AC-H@S is detected through TGA carried out under N_2 flow in Figure 4.1.7c, which reveals a sulfur content as high as 75 % that is expected to enable high energy density of lithium-metal and lithium-ion cells. Furthermore, the derivative thermogravimetric (DTG) curve reported in the bottom panel of Figure 4.1.7c evidences that the sulfur weight loss evolves through two subsequent steps, among which the first and major one is centered at 300 °C (51 % of the total sulfur loss) while the second one extends between 300 and 400 °C (24 % of the total sulfur loss). The first step is likely ascribable to sulfur located on the external carbon surface, whereas the second one can be related to the active material hosted within the microporous carbon structure.[66,67] It is worth mentioning that the above electrode architecture may actually enhance the electrical contact between the active material (*i.e.*, sulfur) and the conductive matrix (the carbon frame), thus shortening the electron pathway and enabling the kinetics of the lithium-sulfur electrochemical conversion process and the cell cycling, as discussed in section *2.3* of Chapter 2.

The electron microscopy of the AC-H@S reported in Figure 4.1.7 shows a sample formed by submicron flakes (TEM image in Figure 4.1.7d) aggregated into particles with size ranging from 1

μm or smaller to about 10 μm (SEM image in Figure 4.1.7e). Furthermore, the EDS analyses carried out on the TEM image of Figure 4.1.7f display a uniform elemental distribution of carbon (Fig. 4.1.7g) and sulfur (Fig. 4.1.7h) forming the electrode matrix, as well as the above mentioned traces of phosphorous (Figure 4.1.7i) due to the H_3PO_4 activating agent used for the AC-H precursor synthesis.[30] The observed morphology, characterized by the concomitant presence of sulfur-carbon particles with a wide size range, may actually play an important role in achieving enhanced battery performances of the AC-H@S composite, since the small sulfur particles generally enable high capacity values while the large ones are active material reservoirs allowing stable cycling, as observed in section *2.1* in Chapter 2.
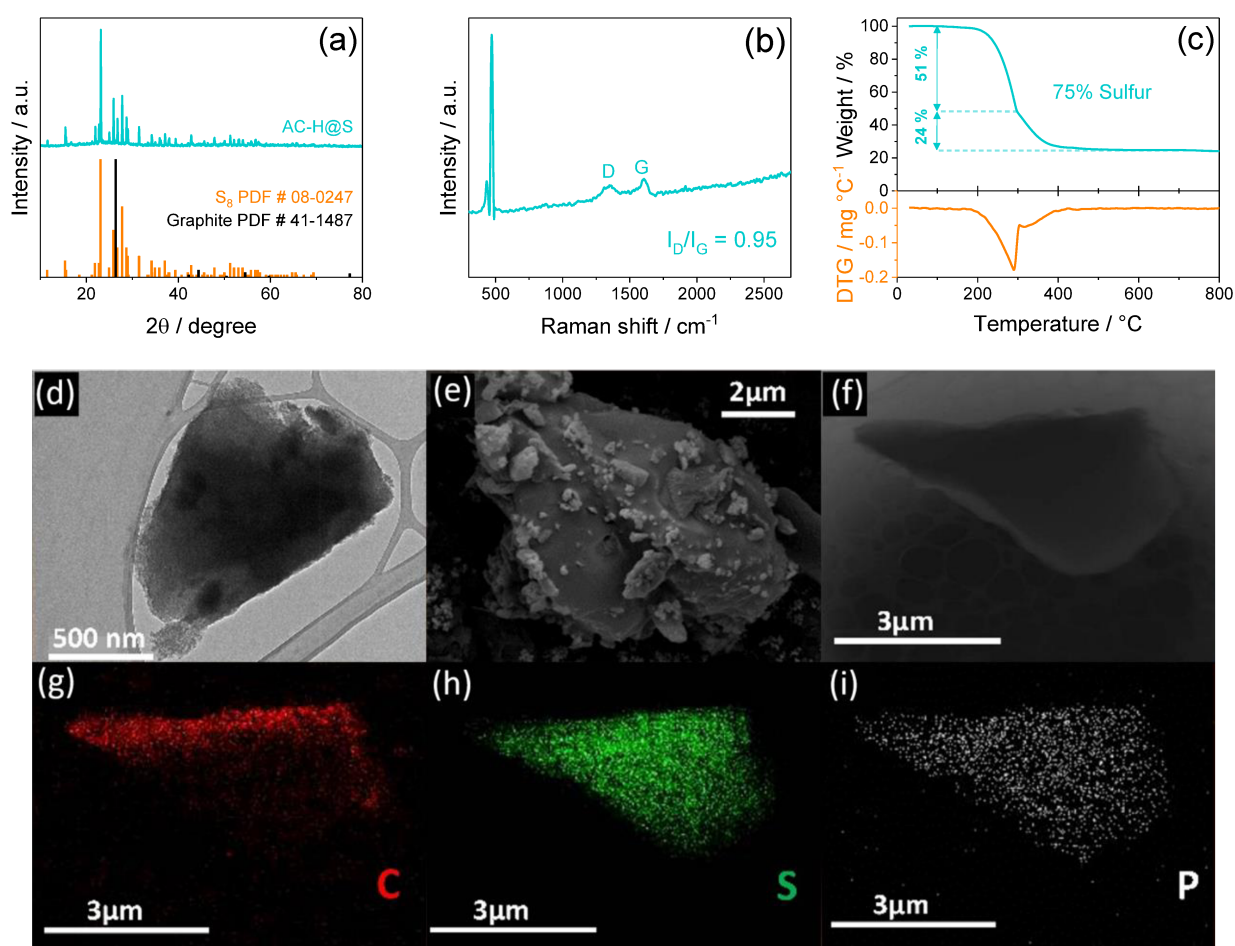
Figure 4.1.7. (a) XRD pattern, **(b)** Raman spectrum, and **(c)** TGA with corresponding DTG curve (bottom panel, orange left *y*-axis) of the AC-H@S composite powder. XRD reference data for elemental sulfur (S_8, PDF # 8–247, orange) and graphite (PDF # 41–1487, black) are also reported for comparison. TGA was carried out under N_2 atmosphere in the 30 - 800 °C temperature range at 10°C min⁻¹. **(d–i)** Morphological analyses of AC-H@S powder samples: **(d)** TEM and **(e)** SEM images; **(f)** additional TEM image; **(g–i)** corresponding EDS elemental maps for **(g)** carbon, **(h)** sulfur, and **(i)** phosphorus.

The electrochemical features of the AC-H@S electrode are investigated in lithium half-cell by CV and EIS, as depicted in Figure 4.1.8. The first CV profile (Fig. 4.1.8a) shows the typical signature of the Li-S conversion process detected by two discharge peaks at 2.25 and 2.0 V *vs* Li^+/Li, corresponding to the formation long-chain lithium polysulfides (Li_2S_8 and Li_2S_6) and short-chain ones (Li_2S_x, $2 \leq x \leq 4$), respectively, reversed in a broad double-peak between 2.3 and 2.5 V *vs* Li^+/Li during charge, which indicates the conversion of the polysulfides back to lithium and sulfur.[68] The subsequent voltammetry cycles reveal a shift of the discharge peaks to higher potential values, suggesting the occurrence of the activation process studied in Chapter 2 that leads to a lower polarization between charge and discharge. Indeed, the activation process is often observed taking place in the first cycles of lithium-sulfur batteries and is usually associated with rearrangements of the sulfur electrode accompanied by a structural reorganization generally leading to the stabilization of the electrode/electrolyte interphase and the enhancement of the electrode conductivity. Furthermore, the narrow discharge/charge signals exhibited by AC-H@S, as well as the notable overlapping of the potential profiles, suggest an efficient conversion process characterized by fast kinetics.

Additional details on the behavior of the AC-H@S electrode in lithium half-cell are provided by the EIS measurements reported in Figure 4.1.8b carried out upon CV. The Nyquist plots are analyzed by NLLS method to obtain the corresponding equivalent circuit formed by resistive (R) and constant phase elements (CPE, Q), and identified by the $R_e(R_iQ_i)Q_w$ model as reported in Table 4.1.6.[33,34] In detail, R_e is the electrolyte resistance, identified by the high-frequency intercept in the Nyquist plots, R_i and Q_i parallel elements (R_iQ_i) represent the single or multiple high-medium-frequency semicircles and account for the electrode/electrolyte interphase, while Q_w indicates the Warburg-type Li^+ ions diffusion which is observed as a tilted line at low-frequency values in the Nyquist plots.[33,34] The results of NLLS analyses reported in Table 4.1.6 reveal that the above mentioned favorable activation process of the AC-H@S electrode upon the first CV cycle is well supported by the decrease of total interphase resistance (R_{tot}, given by the sum of the R_i elements) as well as by the corresponding Nyquist plot shrinks. Indeed, the cell exhibits a total resistance of about 40 Ω at the open-circuit voltage (OCV; inset in Figure 4.1.8b), and a drop down to around 8 Ω after 1 cycle and 6 Ω after 10 cycles (Figure 4.1.8b). Further modifications of the electrode/electrolyte interphase upon CV may be inferred by the change of the Nyquist plot shape and the increase of the (R_iQ_i) elements number in the corresponding equivalent circuit (Table 4.1.6), which is likely ascribed to a change of the electrode morphology.
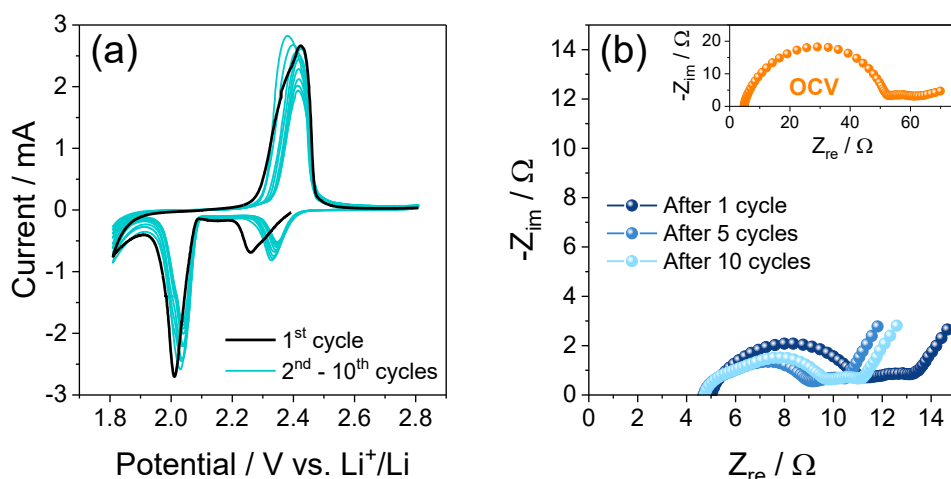
Figure 4.1.8. (a) CV and **(b)** EIS measurements performed on a Li/AC-H@S cell. CV potential range: 1.8 – 2.8 V *vs* Li⁺/Li; scan rate: 0.05 mV s⁻¹. Impedance spectra were recorded in the 500 kHz to 100 mHz frequency range (signal amplitude: 10 mV) at OCV (inset in panel **(b)**) of the cell and after 1, 5, and 10 CV cycles.

Cell condition	Equivalent circuit	R_1 [Ω]	R_2 [Ω]	R_3 [Ω]	R_{tot} $\sum_{i=1}^{3} R_i$ [Ω]	χ^2
OCV	$R_e(R_1Q_1)(R_2Q_2)Q_w$	32 ± 4	8.0 ± 3.8	/	40 ± 8	1×10^{-4}
1 CV cycle	$R_e(R_1Q_1)(R_2Q_2)Q_w$	6.1 ± 0.1	2.3 ± 0.1	/	8.4 ± 0.2	6×10^{-6}
5 CV cycles	$R_e(R_1Q_1)(R_2Q_2)(R_3Q_3)Q_w$	0.8 ± 0.3	3.3 ± 0.3	1.5 ± 0.3	5.6 ± 0.9	8×10^{-5}
10 CV cycles	$R_e(R_1Q_1)(R_2Q_2)(R_3Q_3)Q_w$	1.0 ± 0.1	3.8 ± 0.2	1.3 ± 0.1	6.1 ± 0.4	1×10^{-5}

Table 4.1.6. NLLS analyses carried out on the EIS Nyquist plots reported in Figure 4.1.8b recorded upon CV test performed on a Li/AC-H@S cell. The analyses were carried out through a Boukamp tool.[33,34]

The electrochemical performances of the AC-H@S electrode in lithium half-cell are evaluated in Figure 4.1.9 through galvanostatic tests at increasing current from C/10 (1C=1675 mA g$_S^{-1}$) to C/8, C/5, C/3, C/2, 1C, and 2C (Fig. 4.1.9a, b), and at the constant rate of C/3 for 100 cycles (Fig. 4.1.9c, d). The evolution of the voltage profiles reported in Figure 4.1.9a evidences that the Li/AC-H@S cell at a C-rate lower than 1C operates according to the CV of Figure 4.1.8 with two discharge plateaus centered at 2.3 and 2.0 V due to the reduction of sulfur to lithium polysulfides, and merging charge plateaus between 2.3 and 2.4 V due to the subsequent oxidation. The cell reveals the excepted increase of the discharge/charge polarization by raising the current from C/10 to C/2; however, a further increase to 1C and 2C turns into the deactivation of the electrochemical process due to excessive overvoltage, which is indicated by the concomitant drop of the delivered capacity. Nonetheless, the

cycling trend depicted in Figure 4.1.9b shows for the AC-H@S electrode stable capacity values of 1200, 1180, 1100, and 1000 mAh g_S^{-1} at C/10, C/8, C/5, and C/3, respectively, and between 890 and 780 mAh g_S^{-1} at C/2. After the abrupt decay of the delivered capacity below 300 and 150 mAh g_S^{-1} at 1C and 2C, respectively, the cell recovers about 92 % of the initial value when the C-rate is lowered back to C/10, thus suggesting a good stability of the active material by changing currents. Figure 4.1.9c shows selected voltage profiles related to the Li/AC-H@S cell characterized at the constant current of C/3 for 100 cycles. Interestingly, the poor capacity exhibited during the first cycle (400 mAh g_S^{-1}), as well as the anomalous evolution of the corresponding discharge/charge plateaus, may be attributed to an initial low conductivity of the electrode/electrolyte interphase, which is improved by the activation process after 1 cycle as already discussed in Figure 4.1.8. On the other hand, the electrode exhibits a remarkable capacity, with starting values higher than 1200 mAh g_S^{-1}, and a coulombic efficiency approaching 99 % at the steady state (Figure 4.1.9d). However, the half-cell shows a retention limited to 60 % upon 100 discharge/charge cycles, which may be ascribed to the reaction of the lithium metal with polysulfides or impurities such as phosphorous dissolved from the activated carbon matrix (see EDS and related discussion in Figure 4.1.7). Therefore, it can be assumed that the AC-H@S electrode has suitable performance for battery application, in particular for Li-ion cell in which the above issues ascribed to the presence and reactivity of the lithium metal can be actually mitigated.

The AC-H@S electrode is subsequently coupled with a silicon oxide-based anode (SiO_x-C) in a full lithium-ion-sulfur battery. Prior to using, the SiO_x-C electrode was activated by galvanostatic cycling in lithium cell (see the *4.1.2 Experimental* section) in order to obtain the lithiated Li_ySiO_x-C anode, which is a suitable Li^+ ions reservoir in the full Li-ion-sulfur cell.[69] The voltage profiles of the galvanostatic test performed on the Li_ySiO_x-C/AC-H@S full-cell at the constant current rate of C/5 reported in Figure 4.1.9e reveal an electrochemical process centered at about 1.8 V. The discharge and charge processes evolve according to the combination between the typical voltage shapes associated to the multi-step conversion process of the Li-S battery[70] and the (de-)alloying mechanism of the Li/SiO_x-C cell.[32] During the first cycle, the discharge exhibits two broad plateaus extending in voltage intervals of 1.9 – 2.3 and 1.1 – 1.6 V, which are reversed into a sloping charge profile evolving between 1.5 and 2.35 V. Interestingly, the subsequent cycles exhibit the gradual fragmentation of the charge plateau into three different processes taking place at 1.7, 2.2, and 2.45 V. This trend may be ascribed with structure rearrangements and consolidation of a stable interphase at the surface of both electrodes, as suggested by CV and EIS measurements in Figure 4.1.8 and by previous literature.[71] This complex process is likely reflected into an increase of delivered capacity upon the first cycle, as also evidenced by the cycling trend shown in Figure 4.1.9f.

216
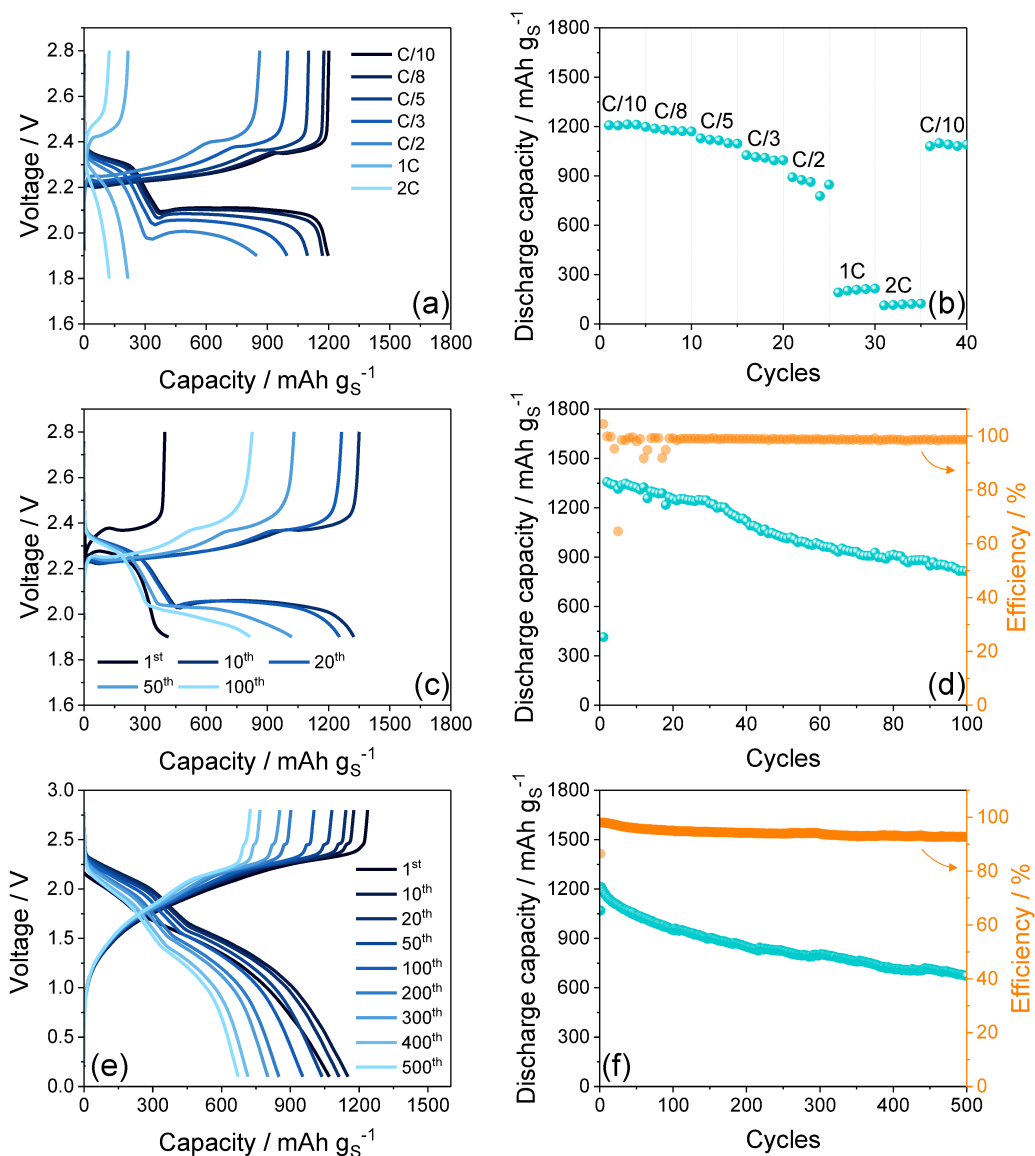
Figure 4.1.9. (a–d) Galvanostatic tests performed on Li/AC-H@S half-cells. In detail: **(a, c)** selected voltage profiles and **(b, d)** corresponding cycling trend (right *y*-axis in panel **(d)** refers to coulombic efficiency) related to tests carried out **(a, b)** at increasing currents employing the C/10, C/8, C/5, C/3, C/2, 1C, and 2C rates and **(c, d)** at the constant current rate of C/3. Voltage ranges: 1.9 – 2.8 V from C/10 to C/2 and 1.8 – 2.8 V for 1C and 2C rates. **(e, f)** Galvanostatic tests performed on Li_ySiO_x-C/AC-H@S full-cell at a C/5 current rate. In detail: **(e)** selected voltage profiles and **(f)** corresponding cycling trend with coulombic efficiency in right y-axis. Voltage range: 0.1 – 2.8 V. The N/P ratio between the Li_ySiO_x-C and AC-H@S electrodes was tuned to a value of 1.04. The anode was electrochemically pre-lithiated at 50 mA g^{-1} for over 30 cycles in the 0.01 – 2.0 V voltage range in lithium half-cell.

Indeed, the Li_ySiO_x-C/AC-H@S cell exhibits 1070 mAh g$_S^{-1}$ during the first cycle that raise up to 1210 mAh g$_S^{-1}$ during the second one. The Li-ion-sulfur cell shows a relevant capacity retention, in particular if compared to the corresponding Li-sulfur half-cell. Hence, the corresponding plots in Figure 4.1.9f (Li-ion cell) and Figure 4.1.9d (Li-S cell) indicate a retention over 100 cycles of about

217

79 % for the former and of 60 % for the latter. Furthermore, the test extended for 500 cycles in the Li-ion cell (Figure 4.1.9f) reveals a residual capacity as high as 670 mAh g_S^{-1} corresponding to a retention of 56 % of the maximum value, and a coulombic efficiency higher than 92 %. Therefore, considering an average operating voltage of about 1.8 V and a capacity of 670 mAh g_S^{-1} after 500 cycles, the Li$_y$SiO$_x$-C/AC-H@S cell can be estimated to still hold upon this challenging test a theoretical specific energy density of about 1200 Wh kg$_S^{-1}$, which could lead to practical value of 400 Wh kg^{-1} by taking in consideration a correction factor of 1/3 that includes all the inactive components of the cell.[72] This stable cycling behavior, the remarkable delivered capacity and energy, and the proper voltage evolution of the cell are herein achieved by tuning the negative-to-positive (N/P) ratio with a very limited anode excess, that is, 1.04. The N/P ratio approaching the unity may in fact favor the achievement of optimized full-cell performances.[61]

  With the aim of further understanding the behavior of the full Li-ion-sulfur cell, the morphological and structural features of the AC-H@S and SiO$_x$-C electrodes were investigated at the pristine state and after cycling. Indeed, an additional full Li$_y$SiO$_x$-C/AC-H@S cell is assembled with an anode achieved by chemical pre-lithiation of the SiO$_x$-C material through direct contacting the electrode disk with a lithium foil soaked with the electrolyte to reach the Li$_y$SiO$_x$-C alloy (see the *4.1.2 Experimental* section for further details). This activation pathway allows a rapid and efficient lithiation of the electrode,[35] as demonstrated by Figure 4.1.10. The selected voltage profiles of lithium half-cells assembled either with a pristine SiO$_x$-C electrode (Figure 4.1.10a) or with Li$_y$SiO$_x$-C electrodes achieved by chemical pre-lithiation at various time regimes, that is, 30 min (Figure 4.1.10b), and 1, 2, and 14 h (Figure 4.1.10c–e, respectively) show that the capacity delivered at the first discharge of the half-cells, corresponding to the charge step in full-cell, decreases by increasing the contact time, thus indicating the progressive lithiation "activation" of the SiO$_x$-C electrode (see histogram in Figure 4.1.10f). The Li$_y$SiO$_x$-C/AC-H@S full-cell is then assembled by coupling a fresh cathode with an anode chemically activated for 48 h to ensure the complete lithiation, and galvanostatically cycled at the constant current rate of C/5 for 20 cycles (Figure 4.1.10g).

  Subsequently, the two electrodes are recovered after disassembling the cycled cell and characterized along with pristine AC-H@S and SiO$_x$-C disks by SEM and XRD as displayed in Figure 4.1.11, while the corresponding elemental distribution is detected by EDS (Figures 4.1.12 and 4.1.13, respectively).
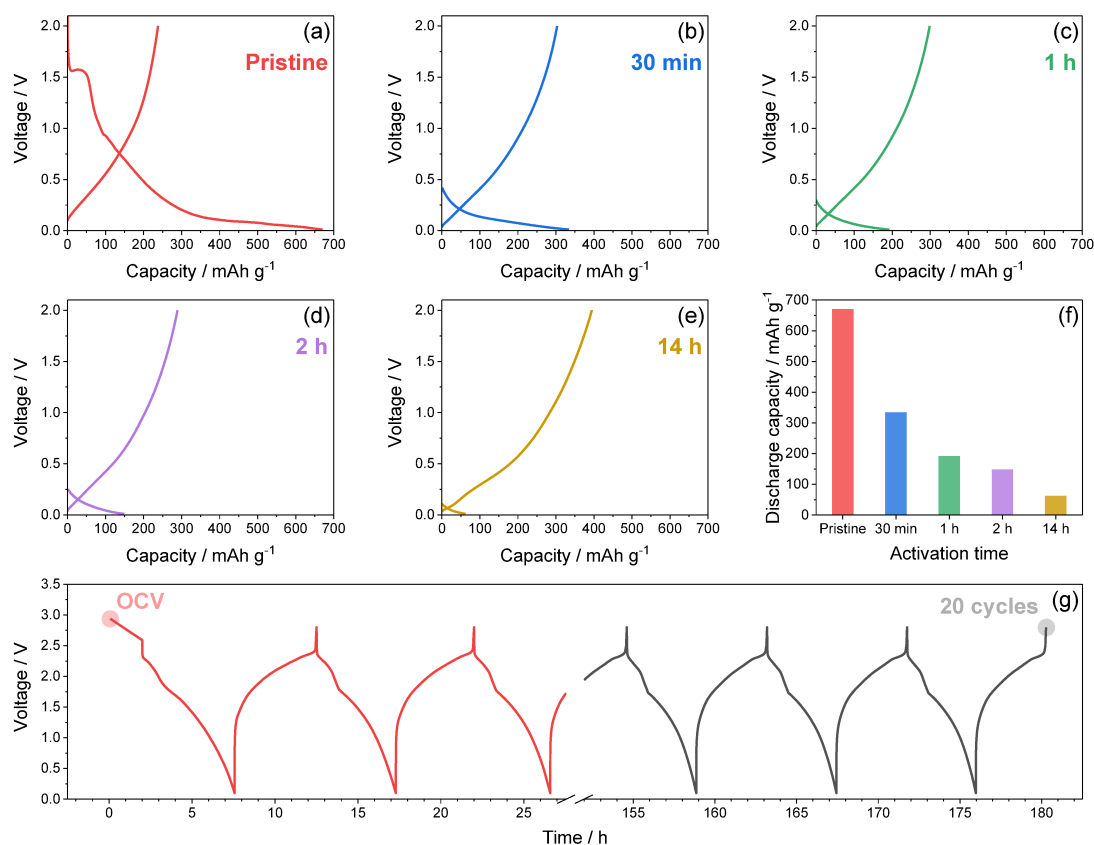
Figure 4.1.10. (a–f) Voltage profiles related to the first cycle of **(a)** a Li/SiO$_x$-C pristine cell and **(b–e)** Li/Li$_y$SiO$_x$-C cells employing Li$_y$SiO$_x$-C electrodes chemically pre-lithiated (activated) at various times: **(b)** 30 min, **(c)** 1 h, **(d)** 2 h, and **(e)** 14 h. **(f)** Histogram representation of the discharge capacity values obtained from the cycling tests reported in panels **(a–e)**. All the cycling measurements were carried out at a current rate of 50 mA g^{-1} (referred to the pristine SiO$_x$-C mass) in the 0.01 – 2 V voltage range. **(g)** Voltage profiles related to the full cell exploiting the Li$_y$SiO$_x$-C/AC-H@S configuration galvanostatically cycled at the constant rate of C/5 in the 0.1 – 2.8 V voltage range. The anode was chemically pre-lithiated by employing an activation time of 48 h.

The SEM image related to the pristine AC-H@S cathode (Figure 4.1.11a) reveals the presence of micrometric sulfur (bright domains) and H$_3$PO$_4$-activated carbon particles (grey domains) uniformly distributed on the electrode surface, as evidenced by the EDS elemental maps of carbon (Figure 4.1.12a), sulfur (Figure 4.1.12b) and phosphorous (Figure 4.1.12c), while the one related to fluorine (Figure 4.1.12d) evidences the polyvinylidene fluoride (PVDF) added to the electrode formulation as the polymer binder (see the *4.1.2 Experimental* section). On the other hand, the pristine SiO$_x$-C shows large particles with size exceeding 20 μm (Figure 4.1.11b) formed by a carbon matrix containing silicon oxide particles, as identified by the EDS elemental maps of C (Figure 4.1.13a), Si (Figure 4.1.13b), and O (Figure 4.1.13c).[35]

219
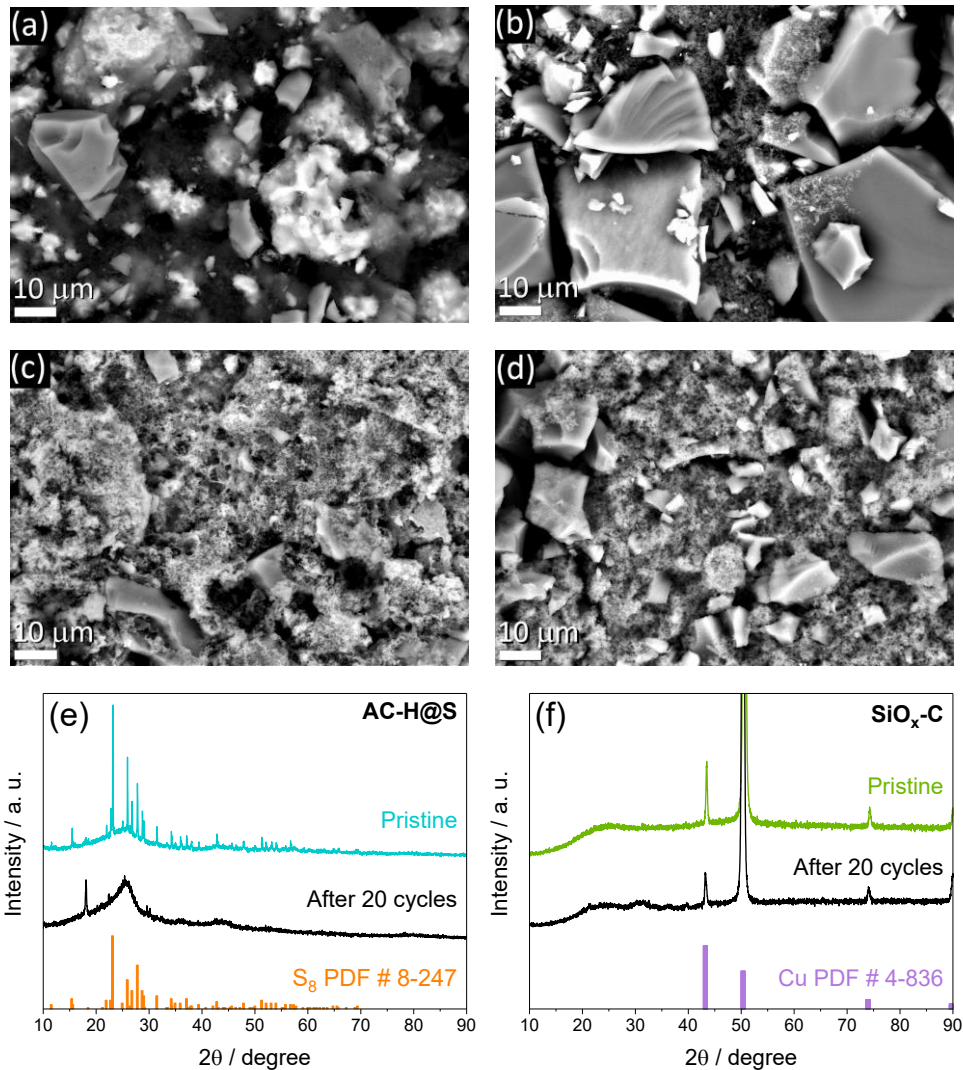
Figure 4.1.11. (a–d) SEM images recorded on **(a,c)** AC-H@S and **(b,d)** SiO$_x$-C electrodes at **(a,b)** the pristine state and **(c,d)** after 20 discharge/charge cycles in a Li$_y$SiO$_x$-C/AC-H@S cell (see the corresponding voltage profiles in Figure 4.1.10g) cycled at a constant current rate of C/5 in the 0.1 – 2.8 V voltage range. **(e–f)** XRD patterns of the **(e)** AC-H@S and **(f)** SiO$_x$-C electrodes before and after cycling. XRD reference data for elemental sulfur (S$_8$, panel **(e)**, PDF # 8–247) and copper (Cu, panel **(f)**, PDF # 4–836) are also reported for comparison.

Substantial modifications of the morphology can be observed in Figure 4.1.11c and d, which displays the SEM images of the AC-H@S and SiO$_x$-C electrodes, respectively, after cycling. Indeed, AC-H@S shows a surface apparently filled by active material or carbon particles different than the pristine one (compare Fig. 4.1.11a and c), while SiO$_x$-C displays particles having similar shape with respect to the pristine state however with smaller size (compare Figure 4.1.11b and d), as likely associated with the unavoidable volume changes due to the Li-Si (de-)alloying process and possible partial fragmentation.
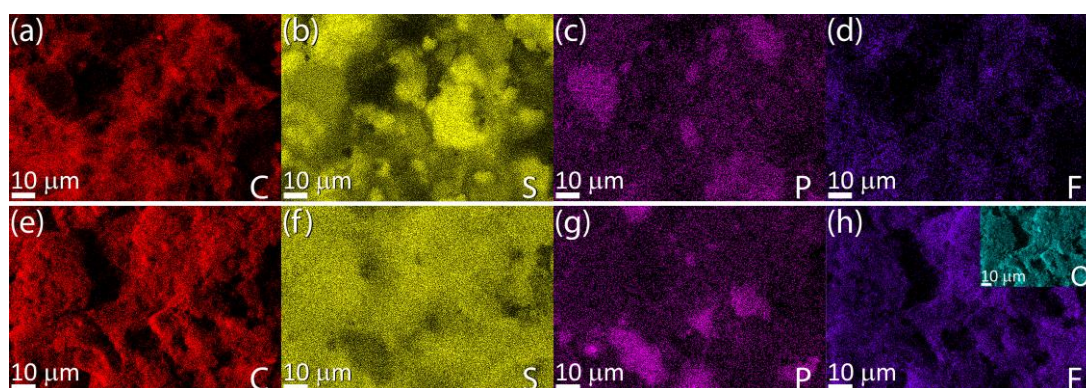
Figure 4.1.12. EDS elemental maps recorded on AC-H@S electrodes surface either **(a-d)** at the pristine state or **(e-h)** upon 20 cycles in a Li$_y$SiO$_x$-C/AC-H@S full-cell at the constant current rate of C/5 in the 0.1 – 2.8 V voltage range (see Fig. 4.1.10g for the corresponding voltage profiles).
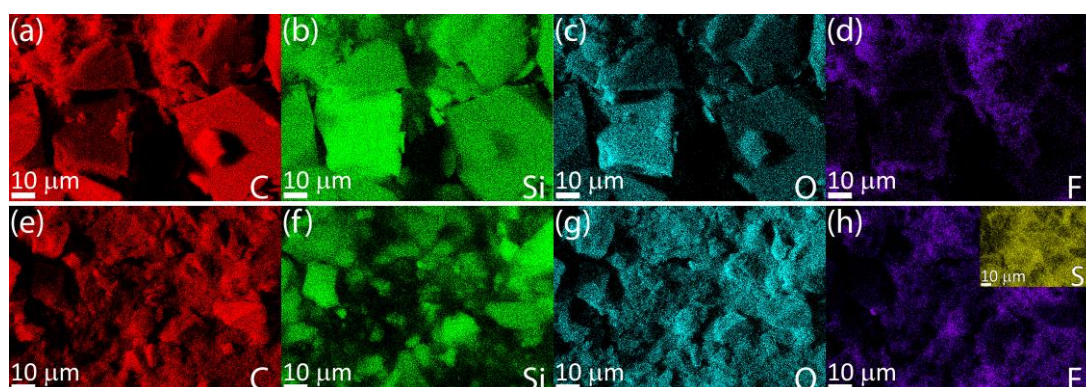
Figure 4.1.13. EDS elemental maps recorded on SiO$_x$-C electrodes surface either **(a-d)** at the pristine state or **(e-h)** upon 20 cycles in a Li$_y$SiO$_x$-C/AC-H@S full-cell at a constant current rate of C/5 in the 0.1 – 2.8 V voltage range (see Fig. 4.1.10g for the corresponding voltage profiles).

Both AC-H@S and SiO$_x$-C exhibit the presence of a bright uniform surface layer suggesting the growth of a SEI formed by carbon (EDS in Figs. 4.1.12e and 4.1.13e), sulfur (Figure 4.1.12f and inset in Figure 4.1.13h), fluorine (Figures 4.1.12h and 4.1.13h), and oxygen (inset in Figure 4.1.12h and Figure 4.1.13g). The above elemental composition of the SEI layer can be attributed to the partial decomposition of the 1,3-dioxolane (DOL) and 1,2-dimethoxyethane (DME) ether chains or the lithium bis(trifluoromethanesulfonyl)imide (LiTFSI) conductive salt in the electrolyte,[73] to the electrodeposition of amorphous sulfur upon charge on the AC-H@S surface, as well as to possible side reaction of lithium polysulfides with the lithiated SiO$_x$-C electrode.[74] Interestingly, the XRD pattern related to the AC-H@S electrode exhibits at the pristine state the broad peak centered at 26°

ascribed to the porous carbon-cloth electrode (see the *4.1.2 Experimental* Section) and the typical crystalline sulfur signals between 20 and 60°, which vanish in the pattern of the cycled electrode (Figure 4.1.11e). Furthermore, both the patterns related to the SiO_x-C electrode (before and after cycling) show exclusive peaks ascribed to the copper support in addition to sulfur impurity detected by EDS (inset in Figure 4.1.13h), as well as the unaltered amorphous structure of the carbon-embedded silicon oxide particles (Figure 4.1.11f). Therefore, the SEM-EDS analyses and the XRD measurements suggest specific morphological modifications and structural stability of the two electrodes upon cycling in full-cell, and the formation of a protecting SEI layer through a series of favorable side reactions at the electrode/electrolyte interphase.

4.2 Sodium metal as sustainable anode

4.2.1 Presentation

The sustainability of Li-S batteries is heavily affected by the use of metallic lithium, due to its low natural availability.[75] This issue also interests the previously studied lithium-ion-sulfur batteries which still relies on lithium despite the absence of a metallic anode. In this scenario, sodium is one of the most abundant elements in the earth crust, hence, it attracts an increasing interest as material for energy storage alternative to lithium.[76] Despite higher weight and less negative redox potential with respect to lithium, *i.e.*, 23 g mol^{-1} compared to 7 g mol^{-1} and -2.7 V compared to -3.0 V *vs* SHE, respectively, sodium is less geo-localized and more available; thus, it may lower the economic impact in view of large-scale production of battery.[77] However, this reactive alkali metal suffers from typical safety issues ascribed to dendrite formation during the electrochemical process, short circuits, and possible thermal runway and venting during batteries operation.[78,79] Therefore, suitable electrolyte media are of key importance for allowing the proper cycling of sodium cell, both using the metal anode and employing the Na-ion configuration.[80] Among possible electrolytes, solutions using end-capped poly-ether (*i.e.*, glyme) solvents and various salts, including sodium trifluoromethanesulfonate ($NaCF_3SO_3$) and sodium bis(trifluoromethanesulfonyl)imide (NaTFSI), revealed very promising characteristics in terms of conductivity, sodium transport number, and electrochemical stability.[80–88] Furthermore, the relatively low flammability of these solutions, particularly for the high-molecular weight glymes, appeared as an important additional bonus for enhancing the battery safety level.[89] Therefore, in this section, a solution formed by dissolving $NaCF_3SO_3$ in triethylene glycol dimethyl ether (TREGDME- $NaCF_3SO_3$) is investigated as suitable electrolyte for sodium battery. The solution is studied by various electrochemical techniques in order to determine its ionic conductivity, charge transport characteristics, and electrochemical and chemical stability. Subsequently, the solution is studied in a room temperature Na-S cell with a composite cathode combining multiwalled carbon nanotubes and sulfur.

4.2.2 Experimental

The TREGDME-$NaCF_3SO_3$ electrolyte was prepared by dissolving sodium trifluoromethanesulfonate ($NaCF_3SO_3$, 98 %, Sigma-Aldrich) in triethylene glycol dimethyl ether (TREGDME, anhydrous, $CH_3O(CH_2CH_2O)_3CH_3$, Sigma-Aldrich) in the 1 mol kg^{-1} ratio. The TREGDME-$NaCF_3SO_3$ solution is liquid according to the melting point of TREGDME (Tm = -40

°C). Both electrolyte components were dried before use. $NaCF_3SO_3$ was heated at 120 °C under vacuum for 3 days, while TREGDME was dehydrated under dry molecular sieves (5 Å, Sigma-Aldrich) until the 10 ppm water content was reached, as determined by an 899 Karl Fischer Coulometer (Metrohm). TREGDME drying, water titration, and electrolyte preparation were carried out in an Ar-filled glovebox (MBraun, O_2 and H_2O content below 1 ppm). The flammability of the TREGDME-$NaCF_3SO_3$ solution was evaluated through exposure to a butane flame for 30 s.

The electrode slurry was prepared by mixing through an agate mortar a sulfur-multiwalled carbon nanotube composite (S-MWCNTs, 60:40 w/w),[90] polyvinilidene fluoride (Solef ® 6020 PVDF) as polymer binder, and a conductive carbon (Super P, Timcal) using the weight proportion of 80:10:10 in N-methyl-2-pyrrolidinone (NMP, anhydrous, Sigma-Aldrich). The slurry was casted by doctor blade on either aluminum (thickness of 15 μm, MTI Corporation) or gas diffusion layer (GDL ELAT LT1400, MTI Corp) foils, which were then dried for 3 h on a hot plate at 70 °C, cut into either 10-mm or 14-mm disks, and heated overnight at 40 °C under vacuum. The final sulfur loading of the electrodes was 0.9 and 2.5 mg cm^{-2} over Al and GDL, respectively. Carbon-coated Al and Cu electrodes were prepared by the doctor blade casting procedure above described using Super P carbon and PVDF binder in the 80:20 weight ratio, cut into 10-mm disks, and dried overnight at 110 °C under vacuum. Sodium-metal electrode disks with diameter of either 10 or 14 mm were prepared from sodium cubes (Sigma-Aldrich) by rolling and pressing.

2032 coin-cells (MTI Corp.) and three-electrode T-type cells were assembled in an Ar-filled glovebox (MBraun, O_2 and H_2O content below 1 ppm), by using sodium metal as the counter and reference electrodes and a Whatman® GF/D glass fiber separator soaked by the TREGDME-$NaCF_3SO_3$ solution. Electrodes having diameter of 10 and 14 mm were employed for preparing T-type cells and coin-cells, respectively.

The ionic conductivity of the TREGDME-$NaCF_3SO_3$ solution was determined by EIS on a symmetrical blocking-electrode coin-cell using stainless steel (SS) electrodes and a Teflon ring as the separator to fix the cell constant to 4.0×10^{-2} cm^{-1}. EIS was performed by applying an alternate voltage signal with amplitude of 10 mV within the 500 kHz – 10 Hz frequency range.

The sodium transference number (t^+) of the TREGDME-$NaCF_3SO_3$ electrolyte solution was evaluated by the method developed by Bruce-Vincent-Evans.[91] Chronoamperometry and EIS measurements were carried out on two Na-Na symmetrical coin-cells using a Whatman® GF/D glass fiber separator soaked by the electrolyte solution. Chronoamperometry was performed by applying to the cell a voltage of 10 mV for 90 min, while impedance spectra were recorded by employing an alternate voltage signal with amplitude of 10mVwithin the 100 kHz – 100 mHz frequency range.

The electrochemical stability window of the TREGDME-NaCF$_3$SO$_3$ solution was evaluated by CV in the cathodic range and linear sweep voltammetry (LSV) in the anodic range on three-electrode T-type cells using Super P carbon electrodes on either Cu or Al substrates, respectively, as the working electrode. All the voltammetry experiments were carried out by using a scan rate of 0.1 mV s^{-1}. The sodium/electrolyte interphase resistance was measured by EIS on symmetrical Na-Na coin-cells throughout 30 days, by applying an alternate voltage signal of 10 mV amplitude in the 100 kHz – 100 mHz frequency range.

Galvanostatic sodium stripping/deposition tests were carried out by applying 0.1 mA cm^{-2} for 1 h of charge/discharge to a Na-Na symmetrical coin-cell.

Galvanostatic cycling tests were performed on sodium coin-cells using the TREGDME-NaCF$_3$SO$_3$ electrolyte and S-MWCNTs over Al or GDL. The Na|TREGDME-NaCF$_3$SO$_3$|S-MWCNTs cells using Al and GDL supports were cycled at a current rate of C/20 (1C = 1675 mA g$_S^{-1}$) within the voltage ranges of 0.5 – 2.1 V and 1.6 – 2.5 V, respectively. The charge capacity of both Na-S cells was limited to 500 mAh g$_S^{-1}$. The capacity values are referred to S in the electrodes. A comparative sodium cell was assembled by using the TREGDME-NaCF$_3$SO$_3$ electrolyte and MWCNTs over GDL as working electrode, and tested by employing the same experimental conditions of the Na/S-MWCNTs (GDL) cell.

CV of a three-electrode T-type sodium cell using Na metal as the counter and the reference electrode was performed using the TREGDME-NaCF$_3$SO$_3$ electrolyte and S-MWCNTs coated over Al. CV was carried out within the potential range 0.5 – 2.1 V vs Na$^+$/Na using a scan rate of 0.1 mV s^{-1}. EIS measurements of the above cell were performed at the open circuit voltage (OCV) and after each voltammetry cycle within 100 kHz – 100 mHz using AC signal amplitude of 10 mV.

EIS, CV, and LSV were performed though a VersaSTAT MC Princeton Applied Research (PAR, AMETEK) instrument, while the galvanostatic measurements were performed through a MACCOR Series 4000 battery test system. All the electrochemical measurements, except for the ionic conductivity ones, were performed at room temperature (25 °C).

4.2.3 Results

Safety has a key role in determining the suitability of the electrolyte for sodium battery. Therefore, a test by direct exposure of the TREGDME-NaCF$_3$SO$_3$ electrolyte to a butane flame under ambient conditions was performed (photographic images in Fig. 4.2.1).[92] The test reveals that the sample does not undergo ignition upon 30 s of exposure (Fig. 4.2.1a, b) as the fire evolution over the solution is missing after the test (Fig. 4.2.1c). Despite further flammability tests in different

experimental conditions are certainly required to evaluate the safety content of the TREGDME-NaCF$_3$SO$_3$ solution,[93] the electrolyte can be considered a promising candidate for a possible employment in battery. The lower flammability of the TREGDME-NaCF$_3$SO$_3$ electrolyte compared to the conventional carbonate-based ones, already observed for analogue solutions used in lithium battery,[89] may be likely attributed to relatively low vapor pressure of the glyme solvents which further decreases by raising the chain length, thus favoring the safety content of the electrolyte.[94] This trend indicates long-chain glymes, such as polyethylene glycol dimethyl ether (PEGDME), as the most suitable candidate for achieving the maximum safety. However, further parameters depending on the chain length determine the applicability of the electrolyte in battery; among them, the most important are the ion transport ability, the chemical and the electrochemical stability.

(A)

(B)

(C)

Figure 4.2.1. (a, b) Photographic images of the TREGDME-NaCF$_3$SO$_3$ electrolyte **(a)** before, **(b)** during, and **(c)** after direct exposure to a butane flame for 30 s under ambient conditions.
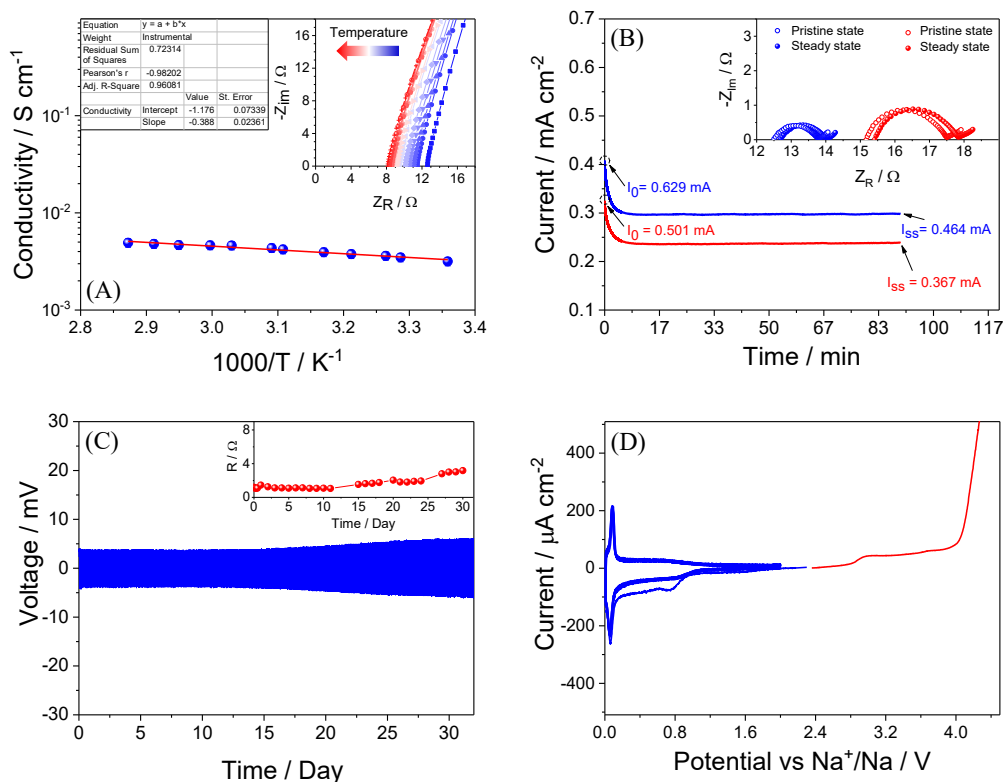
Therefore, ion transport properties and electrochemical characteristics of the TREGDME-NaCF$_3$SO$_3$ electrolyte have been studied and reported in Figure 4.2.2. Panel a of Figure 4.2.2 reports the Nyquist plots of EIS measurements performed on a symmetrical blocking cell using a Teflon O-ring as the separator to fix the cell constant in inset (see the *4.2.2 Experimental* section for further details), and the related Arrhenius plot with linear fit. EIS reveals the typical response attributed to the electrolyte resistance (R$_e$) and the double-layer capacitance (Cdl, see Fig. 4.2.2a inset) and suggests ionic conductivity ranging from 3×10^{-3} S cm^{-1} at the room temperature to 5×10^{-3} S cm^{-1} at about 80 °C. These values are in agreement with previous literature on liquid, glyme-based electrolytes for sodium batteries,[95] and are slightly lower than those attributed to conventional, flammable, alkyl carbonate-based electrolytes,[96] thereby suggesting the TREGDME-NaCF$_3$SO$_3$ solution as adequate electrolyte for low-resistance sodium cells. In addition, the small value of slope obtained by linear fitting of the curve (inset of Fig. 4.2.2a) indicates a limited activation energy for the ion transport likely reflected into a fast Na$^+$ diffusion into the electrolyte, which may possibly lead to high rate capability in non-blocking electrode cell.[97] As seen previously for lithium, the sodium transference number (t$^+$) is an important characteristic of the electrolyte solution since it strongly influences the interphase resistance during the electrochemical process and the associated charge transfer features; in fact, high values of t$^+$ likely lead to small resistance and fast electrochemical process at the electrode/electrolyte interlayer.[80] Figure 4.2.2b shows the chronoamperometric profiles and EIS Nyquist plots (inset) before and after polarization of two symmetrical sodium cells employed to evaluate the t$^+$ by the Bruce-Vincent-Evans equation (4.2.1):[91]

$$t^+ = \frac{i_{ss}}{i_0} \frac{\Delta V - R_0 i_0}{\Delta V - R_{ss} i_{ss}}$$

(4.2.1)

where i$_0$ and i$_{ss}$ are the initial and the steady-state currents, ΔV is the applied signal, R$_0$ and R$_{ss}$ are the electrode/electrolyte interphase resistances before and after polarization. Both cells exhibit similar response in terms of current and impedance features. Although slight differences due to cell assembly are observed, both experiments provide a sodium transference number of 0.72, thus further confirming the reliability of the method adopted for the measurement.[91] This value is considered very suitable for efficient application in low-resistance sodium cells.[80]

Further important characteristics of the electrolyte solution are the electrochemical and chemical stability of the Na/electrolyte interphase, which are herein determined by galvanostatic stripping/deposition tests (Fig. 4.2.2c) and EIS measurements throughout 30 days of storage (Fig. 4.2.2c, inset), respectively, performed on sodium symmetrical cells. Figure 4.2.2c reveals that the

electrolyte has a charge/discharge polarization as low as 4 mV, which slightly increases to about 5 mV and stabilizes by the ongoing of the test due to a modest growth and consolidation of the SEI film as the electrochemical process of Na occurs.[95]

Figure 4.2.2. (a–d) Ion transport properties and electrochemical characteristics of the TREGDME-NaCF$_3$SO$_3$ electrolyte. **(a)** Arrhenius plots of the ionic conductivity with corresponding linear fit and Nyquist plots (inset). Electrolyte resistances for the calculation determined by EIS within 500 kHz – 10 Hz by using AC signal amplitude of 10 mV. **(b)** Chronoamperometric profile and EIS Nyquist plots (inset) before and after polarization of two Na/Na symmetrical cells employed for the determination of Na$^+$ transference number (t$^+$) by the Bruce-Vincent-Evans equation (4.2.1).[91] Chronoamperometry performed by applying to the cell a voltage of 10 mV for 90 min. EIS performed within 100 kHz – 100 mHz using AC signal amplitude of 10 mV. **(c)** Galvanostatic sodium stripping/deposition test performed at 0.1 mA cm^{-2} for 1 h of charge/discharge and interphase resistance evolution during time (inset) determined by EIS within 100 kHz – 100 mHz with AC signal amplitude of 10 mV on Na/Na symmetrical cells. **(d)** CV (cathodic region) and LSV (anodic region) performed for determining the electrochemical stability window of the electrolyte in sodium. Scan rate 0.1 mV s^{-1}.

Similar trend is evidenced by the EIS test of the symmetrical cell (Fig. 4.2.2c inset), which shows very low impedance (about 1 Ω) at the initial stages of the measurement, and a still very low value of about 3 Ω after 30 days of storage as the SEI is fully formed.[95] Such an excellent trend is generally reflected into an optimal electrolyte performance in sodium cell, characterized by long life cycle and remarkable stability.[98] The electrochemical stability window of the electrolyte is determined in

sodium cells using Super P carbon as the working electrode by CV in the cathodic region and LSV in the anodic region (Fig. 4.2.2d). The figure evidences typical cathodic profile (blue curve), characterized by an irreversible peak at about 0.8 V *vs* Na^+/Na associated with the reductive decomposition of the electrolyte and formation of a protective SEI at the electrode surface, as well as by a remarkably reproducible CV response during the subsequent cycles, in which only reversible (de-)insertion and deposition/dissolution of sodium over the SP carbon electrode at about 0.9 and 0V *vs* Na^+/Na, respectively, are observed.[95] Concerning the anodic scan (red curve in Fig. 4.2.2d), a small increase of the current may be observed at about 3 V *vs* Na^+/Na, most likely due to a partial oxidation of the electrolyte, while the full oxidative decomposition may be detected only at about 4 V *vs* Na^+/Na. It is noteworthy that undesired electrolyte decomposition processes are generally mitigated by the addition to the electrolyte solution of film-forming additives,[80] such as $NaNO_3$.[95] It is important to mention however that the S-MWCNTs material operates within the above-determined stability window of the TREGDME-$NaCF_3SO_3$ electrolyte, *i.e.*, within 0 and 3 V *vs* Na^+/Na. Based on the low bulk and sodium/electrolyte interphase resistances of TREGDME-$NaCF_3SO_3$ at room temperature, the subsequent tests were performed in sodium cells at 25 °C.

The sulfur electrode is characterized by high specific capacity in sodium cell due to its electrochemical process involving multiple-ion exchange.[99] Herein, an S-MWCNTs material was selected as the working electrode for a sodium battery operating at the room temperature. Figure 4.1.3 shows the voltage profile (a), and the cycling trend with the Coulombic efficiency (b) of a Na|TREGDME-$NaCF_3SO_3$|S-MWCNTs cell studied at a current of C/20 (1C = 1675 mA gs^{-1}). The S-MWCNTs electrode used for the test is coated on a conventional Al support.

The first discharge of the cell (Fig. 4.1.3a) is characterized by various voltage plateaus which may be divided into three main groups, thereby suggesting a different reaction mechanism compared to the one widely accepted for lithium-sulfur batteries. The attribution of each plateau to a specific phenomenon occurring in the cell is not unambiguous, since various voltage fingerprints and corresponding reaction mechanisms have been reported so far for similar Na/S systems.[86–88,100] The voltage curve here observed is consistent with literature studies on sodium-sulfur batteries,[86] which have revealed the reversible multi-step conversion reaction of sulfur into long-chain and short-chain sodium polysulfides by electrochemical measurements, X-ray photoelectron, and UV/Vis spectroscopy. Accordingly, the first group of reactions, ranging from 2.1 to 1.8 V, may be attributed to the formation of long-chain polysulfides; the second one, occurring at constant voltage of about 1.8 V, to the formation of polysulfides with intermediate-length chain; and the third one, characterized by a profile with rather constant slope from 1.8 to 0.4 V, to the formation of short-chain polysulfides along with possible Na^+ insertion into the MWCNTs.[86,100] Despite that a full understanding of the

conversion reaction mechanism is beyond the scope of the work, it is worth mentioning that the electrochemical behavior of Na-S batteries in terms of reversible capacity and working voltage may be strongly affected by both cathode characteristics and cell configuration.[87,88] The subsequent charge evolves according to two, rather constant, plateaus at about 1.8 and 2.2 V and leads to the reverse oxidation of the polysulfides likely to sulfur and sodium, with a capacity approaching the one obtained during discharge, *i.e.*, about 500 mAh g^{-1}. However, the second and third cycles reveal a remarkable decrease of the delivered capacity accompanied by a reduction of the efficiency, as most likely due to a process involving polysulfide dissolution from the electrode into the electrolyte and precipitation at the anode side, with a significant loss of the active material and resistance increase.[101] *Ex situ* analyses of sodium-sulfur cells employing glyme-based electrolyte revealed large polysulfide dissolution throughout discharge and charge, which depended on the molar concentration of sulfur.[101] Apparently, the proposed electrolyte mitigates neither the polysulfide dissolution nor the polysulfide shuttle, thereby leading to fast capacity fading and large irreversible capacity. Thus, it can be reasonably expected that the use of SEI film-forming additives, such as $NaNO_3$, might address the reaction of the dissolved polysulfides at the anode side. However, recent reports have evidenced possible adverse effects of $NaNO_3$ on the stability of the sodium-metal anode in polysulfide-containing, glyme-based electrolytes.[102]

The deterioration process is further evidenced by the cycling trend of the cell reported in Figure 4.2.2b, which shows the decay of the specific capacity to about 150 mAh g$_S^{-1}$ after 10 discharge/charge cycles. In order to further shed light on the detrimental phenomena affecting the electrode stability, an EIS study of a Na|TREGDME-NaCF$_3$SO$_3$|S-MWCNTs cell cycled by voltammetry within the potential range from 0.5 and 2.1 V was performed. Panels c and d of Figure 4.2.3 report the related voltammetry profiles for three cycles and the Nyquist plots of EIS carried out at the OCV and after each cycle. In agreement with the voltage profiles of panel a and the literature,[101] Figure 4.2.3c shows two cathodic peaks at 1.6 and 2.2 V as well as two weak current signals at 1.9 and 0.8 V, which reflect the multi-step reaction of sulfur with sodium. These processes are partially reversed upon charge through an anodic peak at about 2.0 V. The profiles partially overlap during the subsequent cycles, being characterized by cathodic processes mainly at 1.6 and 0.8 V, and an anodic peak at 2.0 V. According to the galvanostatic cycling results (see panels a and b of Fig. 4.2.3), cyclic voltammetry reveals a decrease of the peak intensity by cycling, thereby suggesting worsening kinetics at electrode/electrolyte interphase. This trend is confirmed by EIS, which indicates an electrode/electrolyte interphase resistance as low as 10 Ω at the OCV, as revealed by Figure 4.2.3d inset, remarkably increasing after three cycles to about 130 Ω (see Fig. 4.2.3d).
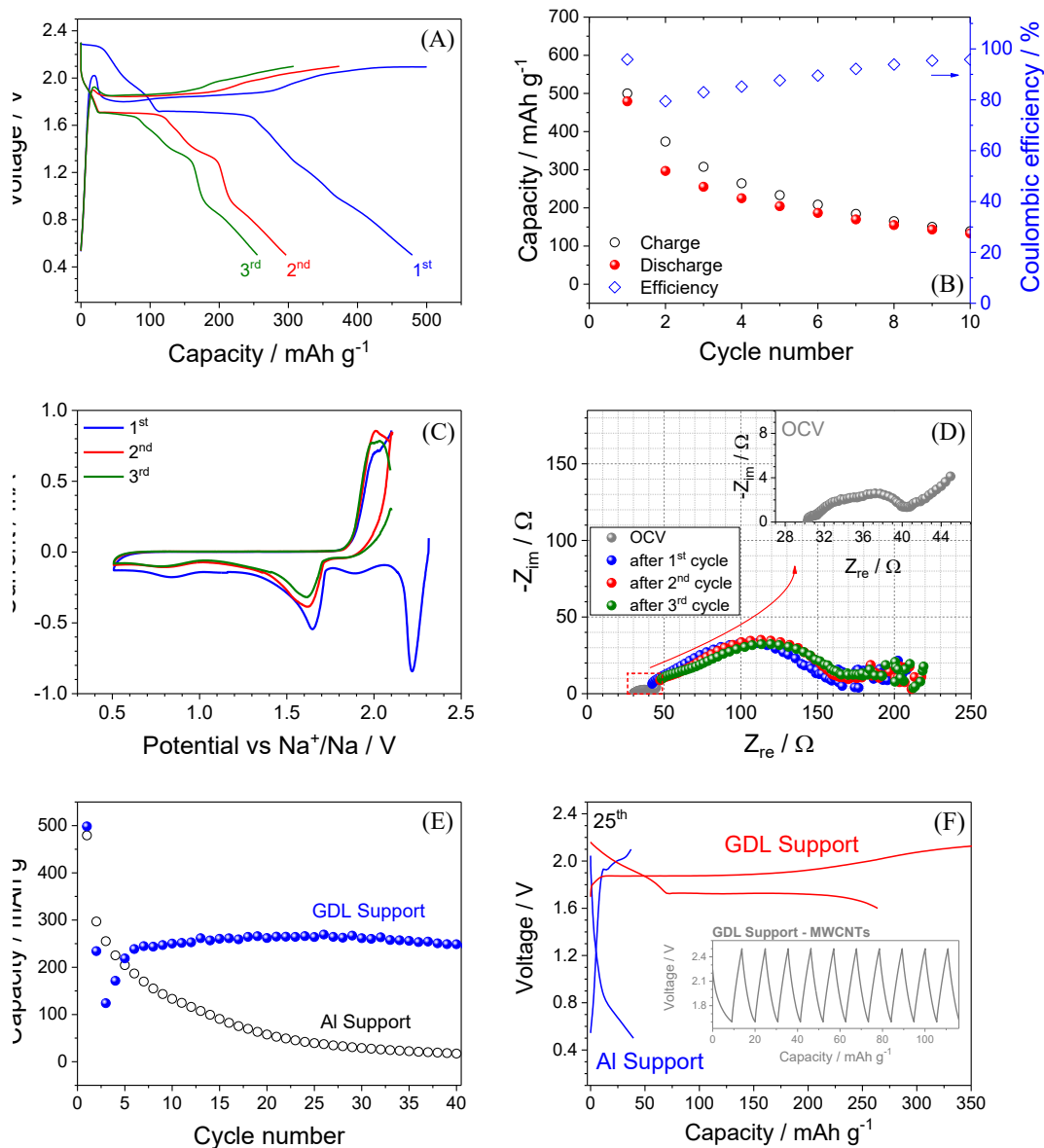
Figure 4.2.3. (a) Voltage profiles and **(b)** cycling trend with Coulombic efficiency of a Na/S-MWCNTs cell galvanostatically studied at a current of C/20. Voltage limits 0.5 – 2.1 V. Charge capacity limited to 500 mAh g^{-1}. S-MWCNTs cast on Al support. **(c)** CV of a Na/S-MWCNTs cell and **(d)** related Nyquist plots of EIS measurements performed at the OCV and after the 1st, 2nd, and 3rd CV cycles. Potential limits 0.5 – 2.1 V *vs* Na$^+$/Na. Scan rate 0.1 mV s^{-1}. EIS performed within 100 kHz – 100 mHz using AC signal amplitude of 10 mV. S-MWCNTs cast on Al support. **(e)** Comparison of cycling trends and **(f)** voltage profiles of the 25th cycle at C/20 of two sodium cells using the TREGDME-NaCF$_3$SO$_3$ electrolyte and the SMWCNTs working electrode cast on conventional Al and GDL supports. Voltage limits 0.5 – 2.1 V for aluminum, 1.6 –2.5 V for GDL. Charge capacity limited to 500 mAh g^{-1}. Inset of panel **(f)**: voltage profiles of a comparative sodium cell using the TREGDME-NaCF$_3$SO$_3$ electrolyte and MWCNTs over GDL as working electrode; cell tested by employing the same experimental conditions of the Na/S-MWCNTs (GDL) cell. Room temperature (25 °C).

Therefore, the S-MWCNTs material was cast on the GDL support instead of the conventional aluminum support previously used, in order to improve the sodium cell stability. Such an improvement by changing the current collector has been observed on lithium–sulfur batteries and attributed to the microporous texture of the carbon cloth, leading to an optimal electric contact with the active material, as well as to its favorable chemical composition and wetting ability (see Chapter 2). Indeed, Figure 4.2.3e compares the cycling trends at C/20 of two sodium cells using the TREGDME-NaCF$_3$SO$_3$ electrolyte and the S-MWCNTs working electrode cast on either conventional Al or GDL supports. After a first cycle evolving at about 500 mAh g^{-1}, the cell using the sulfur electrode on GDL reveals a fast drop of the capacity by two cycles and a subsequent rapid increase up to about 250 mAh g^{-1}. This behavior is most likely attributed to partial dissolution and rapid reorganization of the active material at the electrode/electrolyte interface. Furthermore, the charge/discharge test prolonged up to 40 cycles indicates a very stable performance of the electrode using GDL, which still delivers a capacity of about 250 mAh g^{-1}, that is, a remarkably higher value compared to the material coated on Al. The GDL support actually mitigates capacity fading and cell degradation. Sodium ions are expected to (co-)intercalate within carbon cloth below 0.9 V vs Na$^+$/Na, and possible electrolyte decomposition at low voltage promoted by high surface area of the GDL support cannot be excluded. It is worth mentioning that the discharge was limited to 1.6 V in order to avoid Na$^+$ insertion into the GDL support. Figure 4.2.3f compares the steady-state voltage profiles of Na/S-MWCNTs cells employing either aluminum or carbon cloth. The last cell exhibits a voltage curve attributed to the reversible conversion of sulfur into short-chain sodium polysulfides,[86,100] while the former cell shows poor electrochemical activity. A comparative galvanostatic measurement with a sodium cell using a MWCNTs electrode coated on GDL support was performed, by employing the same cycling conditions of the Na/SMWCNT cell (the capacity has been normalized with respect to the MWCNTs mass). The related results, reported in Figure 4.2.3f inset, exclude significant contribution of the MWCNTs and GDL materials, as revealed by capacitive profiles and very low specific capacity values. Thus, the promising results of the Na/S-MWCNTs cell employing the GDL support pave the way for further works aimed at cathode optimization. Considering the observed capacity value, an average working voltage of about 1.7 V, and the sulfur content (see the *4.2.2 Experimental* section), a theoretical energy density with respect to the sulfur mass of about 425 Wh kg^{-1} can be estimated, leading a practical value of 140 Wh kg^{-1} by roughly considering a correction factor of 1/3 which takes into account the weight of electrolyte, anode, and inactive components of the cell. These values are considered well suitable for sustainable energy storage applications.[61] However, it is worth mentioning that an excess of electrolyte was employed, which may affect the actual energy density.

4.3 Summary

In section *4.1*, two carbon materials derived from cherry pits and differing by the activation pathway have been fully characterized in terms of applicability in lithium battery. The two materials evidenced slightly different structure and morphology and, in particular, a different content and nature of impurity depending on the adopted activation method. Indeed, the material treated by KOH (indicated by AC-K) revealed notable organic fraction, while the material activated by H_3PO_4 (indicated by AC-H) mostly showed an inorganic residual. The two samples have also shown significant differences of the textural properties. AC-H sample evidenced a BET surface 40 % higher than that of AC-K, and a micro-/mesopore system rather than micro-/macropore one. These differences have been reflected into characteristic electrochemical behaviors in lithium cell in terms of voltage profiles shape, rate capability, and delivered capacity. However, upon the initial irreversible cycles due to the above mentioned impurities, the two materials operated according to stable and reversible trends, with steady state capacity approaching 200 mAh g^{-1}, which suggested the applicability in lithium-ion full cell upon electrochemical pre-treatment. Therefore, electrochemically pre-cycled AC-K and AC-H electrodes have been used in a full cell in combination with a $LiFePO_4$ electrode. The Li-ion cells delivered a very stable capacity approaching the theoretical value of the cathode with a cycle life extended over 200 cycles, an efficiency approaching 100 % upon the initial cycles, a retention exceeding 90 %, and a rate capability extending over 2C. Subsequently, the AC-H material was selected and used as precursor to synthetize a sustainable sulfur-carbon composite (AC-H@S) for application in Li-S and lithium-ion-sulfur battery. X-ray diffraction (XRD) measurement performed on the composite powder evidenced the absence of side products and the predominant presence of sulfur, as well as the disordered nature of the carbon frame which was confirmed by Raman spectroscopy. Thermogravimetric analysis of the ACH@S powder detected a sulfur content as high as 75 %, which is allowed by the microporous structure of the activated carbon. Cyclic voltammetry (CV) and electrochemical impedance spectroscopy (EIS) performed on lithium half-cell suggested fast kinetics of the Li-S electrochemical conversion process and a remarkable conductivity of the electrode/electrolyte interphase upon activation. Galvanostatic cycling tests carried out on lithium half-cells have shown maximum capacity values exceeding 1200 mAh g_S^{-1}, coulombic efficiency approaching 99 %, and a rate capability extending up to C/2. Despite the suitability of the AC-H@S for battery application, the half-cell suffered by an excessive capacity decay by cycling due to side reactivity of the lithium metal with polysulfides and phosphorous impurities possibly dissolved into the electrolyte upon cathode operation. Therefore, the lithium electrode was replaced by a Li-alloy anode based on silicon oxide embedded into amorphous carbon

to achieve the Li$_y$SiO$_x$-C/AC-H@S cell exploiting the Li-ion configuration and environmentally friendly materials. The new battery revealed at C/5 a sloped voltage signature centered at about 1.8 V in line with the combination of the multi-step sulfur conversion and the (de-)alloying process of the Li$_y$SiO$_x$-C anode. Furthermore, the Li$_y$SiO$_x$-C/AC-H@S full-cell delivered a maximum capacity of about 1200 mAh g$_S^{-1}$, retained slightly below 60 % over 500 cycles. The electrodes structural retention and the formation of a SEI layer have been actually observed by performing *ex-situ* XRD, SEM, and EDS measurements on pristine electrodes and cycled ones recovered from the Li$_y$SiO$_x$-C/AC-H@S cell upon cycling.

It is worth noting that the promising lithium-ion-sulfur configuration studied in section *4.1* would certainly benefit from optimization on both electrodes and electrolyte as seen in Chapters 2 and 3, *e.g.*, the addition of metal nanoparticles to increase the cathode conductivity or the dissolution of lithium polysulfides into the electrolyte to buffer the sulfur loss and improving the SEI. On the other hand, the combination of novel research techniques requires *ad-hoc* and extensive studies which fall out the objective of the present work, although the development of a high-performance full lithium-ion-sulfur battery exploiting the strategies investigated in this and previous Chapters is presently pursued.

Section *4.2* proposed an alternative configuration for room temperature Na-S batteries benefitting from the combination between a non-flammable glyme-based electrolyte (TREGDME-NaCF$_3$SO$_3$) and a porous GDL current collector at the cathode side. The characterization of the glyme-based electrolyte evidenced several characteristics well adequate for the use of the electrolyte in sodium cell, including an expected high safety content due to relatively low flammability, an ionic conductivity ranging from 3×10^{-3} to 5×10^{-3} S cm^{-1} depending on the temperature, and a Na-transference number higher than 0.7. In addition, the electrolyte shown a remarkable chemical and electrochemical stability of the Na/electrolyte interface, with maximum impedance value limited to 3 Ω, and Na-stripping/deposition polarization as low as 5 mV. Furthermore, the electrolyte revealed an excellent cathodic stability, well suitable for Na-ion cell, while demonstrating low anodic stability. Afterwards, the room-temperature Na-S cell using the TREGDME-NaCF$_3$SO$_3$ electrolyte in combination with an S-MWCNTs composite electrode cast on a gas diffusion layer (*i.e.*, GDL) support has revealed a stable capacity of about 250 mAh g$_S^{-1}$ and an average voltage of 1.7 V, thus leading to an expected practical energy of the order of 140 Wh kg$_S^{-1}$. Importantly, the data revealed a great enhancement of the capacity retention upon switching from the conventional Al current collector to the GDL one, thereby proving the suitability of a carbon-based porous cathode support for the Na-S battery in according with the results achieved in this work on Li-S cells.

4.4 References

[1]   B. Meyer, *Chem. Rev.* **1976**, *76*, 367.

[2]   A. Manthiram, Y. Fu, S.-H. Chung, C. Zu, Y.-S. Su, *Chem. Rev.* **2014**, *114*, 11751.

[3]   Z. Li, H. Bin Wu, X. W. (David) Lou, *Energy Environ. Sci.* **2016**, *9*, 3061.

[4]   C. Liang, N. J. Dudney, J. Y. Howe, *Chem. Mater.* **2009**, *21*, 4724.

[5]   G. Hu, C. Xu, Z. Sun, S. Wang, H.-M. Cheng, F. Li, W. Ren, *Adv. Mater.* **2016**, *28*, 1603.

[6]   J. Guo, Y. Xu, C. Wang, *Nano Lett.* **2011**, *11*, 4288.

[7]   H. Shi, W. Lv, C. Zhang, D.-W. Wang, G. Ling, Y. He, F. Kang, Q.-H. Yang, *Adv. Funct. Mater.* **2018**, *28*, 1800508.

[8]   Y. Wu, S. Zhang, J. Hao, H. Liu, X. Wu, J. Hu, M. P. Walsh, T. J. Wallington, K. M. Zhang, S. Stevanovic, *Sci. Total Environ.* **2017**, *574*, 332.

[9]   J. Chen, C. Li, Z. Ristovski, A. Milic, Y. Gu, M. S. Islam, S. Wang, J. Hao, H. Zhang, C. He, H. Guo, H. Fu, B. Miljevic, L. Morawska, P. Thai, Y. F. LAM, G. Pereira, A. Ding, X. Huang, U. C. Dumka, *Sci. Total Environ.* **2017**, *579*, 1000.

[10]   J. Wang, P. Nie, B. Ding, S. Dong, X. Hao, H. Dou, X. Zhang, *J. Mater. Chem. A* **2017**, *5*, 2411.

[11]   S. Dühnen, J. Betz, M. Kolek, R. Schmuch, M. Winter, T. Placke, *Small Methods* **2020**, *4*, 2000039.

[12]   F. Wang, D. Ouyang, Z. Zhou, S. J. Page, D. Liu, X. Zhao, *J. Energy Chem.* **2021**, *57*, 247.

[13]   A. Benítez, J. Amaro-Gahete, Y.-C. Chien, Á. Caballero, J. Morales, D. Brandell, *Renew. Sustain. Energy Rev.* **2022**, *154*, 111783.

[14]   L. Carbone, S. G. Greenbaum, J. Hassoun, *Sustain. Energy Fuels* **2017**, *1*, 228.

[15]   L. Liu, F. Xie, J. Lyu, T. Zhao, T. Li, B. G. Choi, *J. Power Sources* **2016**, *321*, 11.

[16]   M. Ge, C. Cao, G. M. Biesold, C. D. Sewell, S. Hao, J. Huang, W. Zhang, Y. Lai, Z. Lin, *Adv. Mater.* **2021**, *33*, 2004577.

[17]   K. Zhao, L. Zhang, R. Xia, Y. Dong, W. Xu, C. Niu, L. He, M. Yan, L. Qu, L. Mai, *Small* **2016**, *12*, 588.

[18]   H.-W. Yang, D. I. Lee, N. Kang, J.-K. Yoo, S.-T. Myung, J. Kim, S.-J. Kim, *J. Power Sources* **2018**, *400*, 613.

[19]   J. Ge, Q. Tang, H. Shen, F. Zhou, H. Zhou, W. Yang, J. Hong, B. Xu, J. Saddique, *Appl. Surf. Sci.* **2021**, *552*, 149446.

[20]   G. Wang, F. Li, D. Liu, D. Zheng, C. J. Abeggien, Y. Luo, X.-Q. Yang, T. Ding, D. Qu, *Energy Storage Mater.* **2020**, *24*, 147.

[21] S. Thieme, J. Brückner, A. Meier, I. Bauer, K. Gruber, J. Kaspar, A. Helmer, H. Althues, M. Schmuck, S. Kaskel, *J. Mater. Chem. A* **2015**, *3*, 3808.

[22] Y. Yao, H. Wang, H. Yang, S. Zeng, R. Xu, F. Liu, P. Shi, Y. Feng, K. Wang, W. Yang, X. Wu, W. Luo, Y. Yu, *Adv. Mater.* **2020**, *32*, 1905658.

[23] M. Shahbandeh, "Cherry production worldwide from 2000 to 2017, 2019-02- 01," can be found under https://www.statista.com/statistics/577489/world-cherryproduction/, **2019**.

[24] Q. Jiang, Z. Zhang, S. Yin, Z. Guo, S. Wang, C. Feng, *Appl. Surf. Sci.* **2016**, *379*, 73.

[25] Z. Li, Z. Xu, X. Tan, H. Wang, C. M. B. Holt, T. Stephenson, B. C. Olsen, D. Mitlin, *Energy Environ. Sci.* **2013**, *6*, 871.

[26] K. Hong, L. Qie, R. Zeng, Z. Yi, W. Zhang, D. Wang, W. Yin, C. Wu, Q. Fan, W. Zhang, Y. Huang, *J. Mater. Chem. A* **2014**, *2*, 12733.

[27] Y. Zhang, L. Chen, Y. Meng, J. Xie, Y. Guo, D. Xiao, *J. Power Sources* **2016**, *335*, 20.

[28] L. Tao, Y. Huang, X. Yang, Y. Zheng, C. Liu, M. Di, Z. Zheng, *RSC Adv.* **2018**, *8*, 7102.

[29] M. Olivares-Marín, C. Fernández-González, A. Macías-García, V. Gómez-Serrano, *Appl. Surf. Sci.* **2006**, *252*, 5980.

[30] M. Olivares-Marín, C. Fernández-González, A. Macías-García, V. Gómez-Serrano, *Energy & Fuels* **2007**, *21*, 2942.

[31] M. M. Dubinin, **1975**, pp. 1–70.

[32] G. A. Elia, J. Hassoun, *ChemElectroChem* **2017**, *4*, 2164.

[33] B. A. Boukamp, *Solid State Ionics* **1986**, *20*, 31.

[34] B. A. Boukamp, *Solid State Ionics* **1986**, *18–19*, 136.

[35] J. Hassoun, K. S. Lee, Y. K. Sun, B. Scrosati, *J. Am. Chem. Soc.* **2011**, *133*, 3139.

[36] W. Ruland, B. Smarsly, *J. Appl. Crystallogr.* **2002**, *35*, 624.

[37] A. K. Kercher, D. C. Nagle, *Carbon N. Y.* **2003**, *41*, 15.

[38] G. A. Zickler, B. Smarsly, N. Gierlinger, H. Peterlik, O. Paris, *Carbon N. Y.* **2006**, *44*, 3239.

[39] C. Hernández-Rentero, R. Córdoba, N. Moreno, A. Caballero, J. Morales, M. Olivares-Marín, V. Gómez-Serrano, *Nano Res.* **2018**, *11*, 89.

[40] D. Hulicova-Jurcakova, A. M. Puziy, O. I. Poddubnaya, F. Suárez-García, J. M. D. Tascón, G. Q. Lu, *J. Am. Chem. Soc.* **2009**, *131*, 5026.

[41] M. Jagtoyen, F. Derbyshire, *Carbon N. Y.* **1998**, *36*, 1085.

[42] A. Kumar, H. M. Jena, *Results Phys.* **2016**, *6*, 651.

[43] F. Quesada-Plata, R. Ruiz-Rosas, E. Morallón, D. Cazorla-Amorós, *Chempluschem* **2016**, *81*, 1349.

[44] L. Wang, X. Hu, *Chem. - An Asian J.* **2018**, *13*, 1518.

[45] F. Yu, S. Li, W. Chen, T. Wu, C. Peng, *ENERGY Environ. Mater.* **2019**, *2*, 55.

[46] D. Aurbach, B. Markovsky, G. Salitra, E. Markevich, Y. Talyossef, M. Koltypin, L. Nazar, B. Ellis, D. Kovacheva, *J. Power Sources* **2007**, *165*, 491.

[47] P. Verma, P. Maire, P. Novák, *Electrochim. Acta* **2010**, *55*, 6332.

[48] X. Zhang, J. Hu, X. Chen, M. Zhang, Q. Huang, X. Du, Y. Liu, X. Li, *J. Porous Mater.* **2019**, *26*, 1821.

[49] M. Winter, J. O. Besenhard, M. E. Spahr, P. Novák, *Adv. Mater.* **1998**, *10*, 725.

[50] M. B. Pinson, M. Z. Bazant, *J. Electrochem. Soc.* **2013**, *160*, A243.

[51] C. J. Wen, C. Ho, B. A. Boukamp, I. D. Raistrick, W. Weppner, R. A. Huggins, *Int. Mater. Rev.* **1981**, *26*, 253.

[52] C. Ho, I. D. Raistrick, R. A. Huggins, *J. Electrochem. Soc.* **1980**, *127*, 343.

[53] D. Aurbach, M. D. Levi, E. Levi, *Solid State Ionics* **2008**, *179*, 742.

[54] D. Aurbach, *J. Power Sources* **2000**, *89*, 206.

[55] S. L. Candelaria, Y. Shao, W. Zhou, X. Li, J. Xiao, J.-G. Zhang, Y. Wang, J. Liu, J. Li, G. Cao, *Nano Energy* **2012**, *1*, 195.

[56] E. Buiel, J. . Dahn, *Electrochim. Acta* **1999**, *45*, 121.

[57] D. Di Lecce, S. Levchenko, F. Iacoviello, D. J. L. Brett, P. Shearing, J. Hassoun, *ChemSusChem* **2019**, 1.

[58] D. Molina Piper, S.-B. Son, J. J. Travis, Y. Lee, S. S. Han, S. C. Kim, K. H. Oh, S. M. George, S.-H. Lee, C. Ban, *J. Power Sources* **2015**, *275*, 605.

[59] A. Eftekhari, *J. Power Sources* **2017**, *343*, 395.

[60] J. Vetter, P. Novák, M. R. Wagner, C. Veit, K.-C. Möller, J. O. Besenhard, M. Winter, M. Wohlfahrt-Mehrens, C. Vogler, A. Hammouche, *J. Power Sources* **2005**, *147*, 269.

[61] D. Di Lecce, R. Verrelli, J. Hassoun, *Green Chem.* **2017**, *19*, 3442.

[62] P. Lian, X. Zhu, S. Liang, Z. Li, W. Yang, H. Wang, *Electrochim. Acta* **2010**, *55*, 3909.

[63] A. C. Ferrari, J. C. Meyer, V. Scardaci, C. Casiraghi, M. Lazzeri, F. Mauri, S. Piscanec, D. Jiang, K. S. Novoselov, S. Roth, A. K. Geim, *Phys. Rev. Lett.* **2006**, *97*, 187401.

[64] T. Xing, L. H. Li, L. Hou, X. Hu, S. Zhou, R. Peter, M. Petravic, Y. Chen, *Carbon N. Y.* **2013**, *57*, 515.

[65] G. Li, J. Sun, W. Hou, S. Jiang, Y. Huang, J. Geng, *Nat. Commun.* **2016**, *7*, 10601.

[66] W. G. Wang, X. Wang, L. Y. Tian, Y. L. Wang, S. H. Ye, *J. Mater. Chem. A* **2014**, *2*, 4316.

[67] M. Chen, S. Jiang, S. Cai, X. Wang, K. Xiang, Z. Ma, P. Song, A. C. Fisher, *Chem. Eng. J.* **2017**, *313*, 404.

[68] C. Barchasz, F. Molton, C. Duboc, J.-C. Leprêtre, S. Patoux, F. Alloin, *Anal. Chem.* **2012**,

84, 3973.

[69]   C. Shen, M. Ge, A. Zhang, X. Fang, Y. Liu, J. Rong, C. Zhou, *Nano Energy* **2016**, *19*, 68.

[70]   A. Manthiram, S.-H. Chung, C. Zu, *Adv. Mater.* **2015**, *27*, 1980.

[71]   M. Agostini, J. Hassoun, J. Liu, M. Jeong, H. Nara, T. Momma, T. Osaka, Y. K. Sun, B. Scrosati, *ACS Appl. Mater. Interfaces* **2014**, *6*, 10924.

[72]   J. Hassoun, D. J. Lee, Y. K. Sun, B. Scrosati, *Solid State Ionics* **2011**, *202*, 36.

[73]   Q. Liu, A. Cresce, M. Schroeder, K. Xu, D. Mu, B. Wu, L. Shi, F. Wu, *Energy Storage Mater.* **2019**, *17*, 366.

[74]   M. R. Busche, P. Adelhelm, H. Sommer, H. Schneider, K. Leitner, J. Janek, *J. Power Sources* **2014**, *259*, 289.

[75]   S. Zhang, Y. Yao, Y. Yu, *ACS Energy Lett.* **2021**, *6*, 529.

[76]   D. Kundu, E. Talaie, V. Duffort, L. F. Nazar, *Angew. Chemie Int. Ed.* **2015**, *54*, 3431.

[77]   J.-Y. Hwang, S.-T. Myung, Y.-K. Sun, *Chem. Soc. Rev.* **2017**, *46*, 3529.

[78]   I. Hasa, J. Hassoun, S. Passerini, *Nano Res.* **2017**, *10*, 3942.

[79]   Q. Wang, P. Ping, X. Zhao, G. Chu, J. Sun, C. Chen, *J. Power Sources* **2012**, *208*, 210.

[80]   H. Che, S. Chen, Y. Xie, H. Wang, K. Amine, X.-Z. Liao, Z.-F. Ma, *Energy Environ. Sci.* **2017**, *10*, 1075.

[81]   J. Serra Moreno, M. Armand, M. B. Berman, S. G. Greenbaum, B. Scrosati, S. Panero, *J. Power Sources* **2014**, *248*, 695.

[82]   H. Kim, J. Hong, Y.-U. Park, J. Kim, I. Hwang, K. Kang, *Adv. Funct. Mater.* **2015**, *25*, 534.

[83]   P. K. Dutta, S. Mitra, *J. Power Sources* **2017**, *349*, 152.

[84]   Y.-E. Zhu, L. Yang, X. Zhou, F. Li, J. Wei, Z. Zhou, *J. Mater. Chem. A* **2017**, *5*, 9528.

[85]   B. Jache, J. O. Binder, T. Abe, P. Adelhelm, *Phys. Chem. Chem. Phys.* **2016**, *18*, 14299.

[86]   X. Yu, A. Manthiram, *ChemElectroChem* **2014**, *1*, 1275.

[87]   H. Ryu, T. Kim, K. Kim, J.-H. Ahn, T. Nam, G. Wang, H.-J. Ahn, *J. Power Sources* **2011**, *196*, 5186.

[88]   S. Wei, S. Xu, A. Agrawral, S. Choudhury, Y. Lu, Z. Tu, L. Ma, L. A. Archer, *Nat. Commun.* **2016**, *7*, 11722.

[89]   D. Di Lecce, L. Carbone, V. Gancitano, J. Hassoun, *J. Power Sources* **2016**, *334*, 146.

[90]   L. Carbone, T. Coneglian, M. Gobet, S. Munoz, M. Devany, S. Greenbaum, J. Hassoun, *J. Power Sources* **2018**, *377*, 26.

[91]   J. Evans, C. A. Vincent, P. G. Bruce, *Polymer (Guildf).* **1987**, *28*, 2324.

[92]   A. Benítez, D. Di Lecce, Á. Caballero, J. Morales, E. Rodríguez-Castellón, J. Hassoun, *J. Power Sources* **2018**, *397*, 102.

[93] S. Hess, M. Wohlfahrt-Mehrens, M. Wachtler, *J. Electrochem. Soc.* **2015**, *162*, A3084.

[94] S. Tobishima, H. Morimoto, M. Aoki, Y. Saito, T. Inose, T. Fukumoto, T. Kuryu, *Electrochim. Acta* **2004**, *49*, 979.

[95] L. Carbone, S. Munoz, M. Gobet, M. Devany, S. Greenbaum, J. Hassoun, *Electrochim. Acta* **2017**, *231*, 223.

[96] K. Xu, *Chem. Rev.* **2014**, *114*, 11503.

[97] M. A. Ratner, D. F. Shriver, *Chem. Rev.* **1988**, *88*, 109.

[98] D. J. Lee, J. W. Park, I. Hasa, Y. K. Sun, B. Scrosati, J. Hassoun, *J. Mater. Chem. A* **2013**, *1*, 5256.

[99] D.-H. Lim, M. Agostini, J.-H. Ahn, A. Matic, *Energy Technol.* **2018**, *6*, 1214.

[100] D. Kumar, S. K. Rajouria, S. B. Kuhar, D. K. Kanchan, *Solid State Ionics* **2017**, *312*, 8.

[101] I. Kim, J.-Y. Park, C. Kim, J.-W. Park, J.-P. Ahn, J.-H. Ahn, K.-W. Kim, H.-J. Ahn, *J. Electrochem. Soc.* **2016**, *163*, A611.

[102] H. Wang, C. Wang, E. Matios, W. Li, *Angew. Chemie Int. Ed.* **2018**, *57*, 7734.

Chapter 5.

Conclusions and general remarks

The work presented herein proposed various approaches for the optimization of sulfur-based rechargeable batteries, with particular focus on the Li-S system. The study involved the characterization of alternative configurations of the three main components of the device, that is, cathode, electrolyte and anode. Cathodes based on sulfur-carbon composites sharing the same compositions revealed unique morphologies depending on the adopted synthesis pathway, which strongly affected the electrochemical performance in lithium cell as well. The novel multi-disciplinary investigative approach suggested X-ray computed tomography (CT) as a fundamental technique to obtain crucial insights on the morphological features of sulfur-carbon composites and related electrodes. X-ray CT was also successively employed in the study of sulfur-metal nanocomposites, which were proposed as an alternative to conventional sulfur-carbon formulations due to the superior conductivity of metals with respect to carbon that may lead to higher sulfur content and improved energy densities. Tin, nickel and gold were employed as conductive additive allowing remarkable electrochemical performances of sulfur composites in which the amount of active material was increased to about 85 % for tin and nickel and 97 % for gold nanoparticles. X-ray CT revealed microstructural reorganizations of the sulfur electrodes upon cycling involving infiltration of sulfur into the porous carbon-cloth current collector (*i.e.*, GDL) and deposition near the metallic centers during charge that led to enhancements of the cathode conductivity, as already suggested by other techniques such as cyclic voltammetry and electrochemical impedance spectroscopy. Thus, the combination of sulfur-metal nanocomposites benefitting from simple and scalable synthesis pathway with porous carbon collectors may represent a viable strategy to achieve Li-S batteries of practical interest. Nonetheless, further studies are certainly required to optimize amounts and nature of the conductive additive and to develop suitable porous current collectors, as noble metals can hardly represent a practical solution due to the elevated cost and porous current collectors need careful tuning of weight and thickness to not affect the energy density of the battery.

Glyme-based electrolytes relying on $CH_3O(CH_2CH_2O)_nCH_3$ lowly flammable solvents were identified as promising media for electrodes communication in Li-S batteries. Solutions employing lithium salts in concentrations approaching the saturation limit exhibited notable performances upon optimization of the practical conditions. Indeed, despite high viscosity and density, a DEGDME-based concentrated electrolyte allowed long Li-S cycling at temperature slightly above the room one

(35 °C) at relatively high current rate, that is, 1C. A solid composite polymer electrolyte using a crystalline PEGDME (molecular weight of 2000 g mol^{-1}) demonstrated remarkable Li$^+$ transport properties already at 50 °C, that is, a lower operative temperature with respect to the ones associated to conventional PEO-based solid polymer electrolytes usually approaching 65 °C. Indeed, the novel PEGDME-based Li-S polymer battery exhibited promising electrochemical performances in terms of capacity and cycle life thank to the formation of a suitable electrode/electrolyte interphase driven by partial amorphization of the polymer structure at 50 °C. The presence of SiO_2 particles acting as ceramic fillers prevents the reorganization and recrystallization of the polymer chains, allowing controlled dissolution of lithium polysulfides into the electrolyte and correct occurring of the conversion electrochemical process. Semi-liquid Li-S batteries using catholytes consisting of DEGDME-based solutions revealed fine electrochemical activity of the dissolved Li_2S_8 with no necessity of solid sulfur at the cathode. The use of the $LiNO_3$ sacrificial agent effectively mitigated the "shuttle" mechanism associated to the polysulfides dissolved in the electrolyte, and the application of a polar porous Cr_2O_3-carbon composite at the cathode side suggested increased retention of the polysulfide intermediates, thus preventing massive active material loss. In summary, glymes are versatile solutions to obtain variegated configurations of efficient, safe and sustainable electrolytes for sulfur-based batteries. The compatibility with lithium salts and protective sacrificial agents leads to formation of suitable passivation layers and stable electrode/electrolyte interphases which, together with remarkable transport abilities, low flammability and negligible volatility, satisfy some of the key requirements for practical battery application.

Sustainable electrode materials were considered for boosting low cost Li-S and Na-S batteries. An advanced lithium-ion-sulfur battery was obtained by combining a biomass-derived sulfur-carbon cathode and a lithiated silicon oxide anode. The substitution of lithium metal with a non-reactive and environmentally friendly anode promoted stable performances of the cell which were formerly impeded by side reactivity of the lithium electrode with the impurities deriving from the activated carbon substrate of the sulfur composite. Indeed, the lithium-ion-sulfur cell managed to deliver 500 discharge/charge cycles with notable capacity retention. Finally, a room temperature Na-S battery was also evaluated in terms of safety of the electrolyte solution and electrochemical behavior of the sulfur cathode. The data displayed the suitability of the non-flammable TREGDME-based electrolyte for battery application and the substitution of conventional aluminum current collector with a GDL foil revealed great enhancement of the capacity retention, suggesting this configuration as a step towards a viable application of sulfur-based batteries employing sustainable, yet challenging, Na-based anodes.

Related papers

1) High capacity semi-liquid lithium sulfur cells with enhanced reversibility for application in new-generation energy storage systems.

Daniele Di Lecce, Vittorio Marangon, Almudena Benítez, Álvaro Caballero, Julián Morales, Jusef Hassoun.
Journal of Power Sources **2019**, *425,* 575 – 585.
DOI: 10.1016/j.jpowsour.2018.11.068

2) Triglyme-based electrolyte for sodium-ion and sodium-sulfur batteries.

Daniele di Lecce, Luca Minnetti, Daniele Polidoro, Vittorio Marangon, Jusef Hassoun.
Ionics **2019**, *25,* 3129 – 3141.
DOI: 10.1007/s11581-019-02878-w

3) Sulfur Loaded by Nanometric Tin as a New Electrode for High-Performance Lithium/Sulfur Batteries.

Vittorio Marangon, Jusef Hassoun.
Energy technology **2019**, *7*, 1900081.
DOI: 10.1002/ente.201900081

4) An alternative composite polymer electrolyte for high performances lithium battery.

Vittorio Marangon, Yoichi Tominaga, Jusef Hassoun.
Journal of Power Sources **2020**, *449,* 227508.
DOI: 10.1016/j.jpowsour.2019.227508

5) Investigating high-performance sulfur-metal nanocomposites for lithium batteries.

Vittorio Marangon, Daniele Di Lecce, Fabio Orsatti, Dan J.L. Brett, Paul R. Shearing, Jusef Hassoun.
Sustainable Energy & Fuels **2020**, *4*, 2907 – 2923.
DOI: 10.1039/d0se00134a

6) Alternative lithium-ion battery using biomass-derived carbons as environmentally sustainable anode.

Celia Hernández-Rentero, Vittorio Marangon, Mara Olivares-Marín, Vicente Gómez-Serrano, Álvaro Caballero, Julián Morales, Jusef Hassoun.
Journal of Colloid and Interface Science **2020**, *573*, 396 – 408.
DOI: 10.1016/j.jcis.2020.03.092

7) Porous Cr$_2$O$_3$@C composite derived from metal organic framework in efficient semi-liquid lithium-sulfur battery.

Almudena Benítez, Vittorio Marangon, Celia Hernández-Rentero, Álvaro Caballero, Julián Morales, Jusef Hassoun.
Materials Chemistry and Physics **2020**, *255*, 123484.
DOI: 10.1016/j.matchemphys.2020.123484

8) The role of synthesis pathway on the microstructural characteristics of sulfur-carbon composites: X-ray imaging and electrochemistry in lithium battery.

Daniele Di Lecce, Vittorio Marangon, Wenjia Du, Dan J.L. Brett, Paul R. Shearing, Jusef Hassoun.
Journal of Power Sources **2020**, *472*, 228424.
DOI: 10.1016/j.jpowsour.2020.228424

9) Lithium-Oxygen Battery Exploiting Highly Concentrated Glyme-Based Electrolytes.

Vittorio Marangon, Celia Hernández-Rentero, Stanislav Levchenko, Giacomo Bianchini, Davide Spagnolo, Álvaro Caballero, Julián Morales, Jusef Hassoun.
ACS Applied Energy Materials **2020**, *3*, 12263 – 12275.
DOI: 10.1021/acsaem.0c02331

10) A Stable High-Capacity Lithium-Ion Battery Using a Biomass-Derived Sulfur-Carbon Cathode and Lithiated Silicon Anode.

Vittorio Marangon, Celia Hernández-Rentero, Mara Olivares-Marín, Vicente Gómez-Serrano, Álvaro Caballero, Julián Morales, Jusef Hassoun.
ChemSusChem **2021**, *14*, 3333 – 33343.
DOI: 10.1002/cssc.202101069

11) Lithium-Metal Batteries Using Sustainable Electrolyte Media and Various Cathode Chemistries.

Vittorio Marangon, Luca Minnetti, Matteo Adami, Alberto Barlini, Jusef Hassoun.
Energy & Fuels **2021***, 35,* 10284 − 10292.
DOI: 10.1021/acs.energyfuels.1c00927

12) Novel Lithium-Sulfur Polymer Battery Operating at Moderate Temperature.

Vittorio Marangon, Daniele Di Lecce, Luca Minnetti, Jusef Hassoun.
ChemElectroChem **2021***, 8*, 3971 – 3981.
DOI: 10.1002/celc.202101272

13) Characteristics of a gold-doped electrode for application in high-performance lithium-sulfur battery.

Vittorio Marangon, Daniele Di Lecce, Dan J.L. Brett, Paul R. Shearing, Jusef Hassoun.
Journal of Energy Chemistry **2022***, 64,* 116 – 128.
DOI: 10.1016/j.jechem.2021.04.025

Acknowledgements